

**THÈSE DE DOCTORAT  
DE SORBONNE UNIVERSITÉ**

Spécialité : Physique

École doctorale n°564: Physique en Île-de-France

réalisée sous la direction de Alberto BRAMATI

**au Laboratoire Kastler Brossel**



présentée par

**Kevin FALQUE**

Sujet de la thèse :

**Experimental study of stimulated Hawking radiation and  
Bogoliubov modes correlations in a quantum fluid of  
polaritons.**

soutenue le 4 juillet 2025

devant le jury composé de :

M. RICHARD Maxime,	DR,	CNRS,	Rapporteur
M. FABBRI Alessandro,	MCF,	Univ. de Valencia,	Rapporteur
M <sup>me</sup> DIEDERICH Carole,	PR,	ENS Paris,	Examinateuse
M. WESTBROOK Chris,	DR,	Institut d'optique,	Examinateur
M. PAVLOFF Nicolas,	PR,	Univ. de Paris Saclay,	Examinateur
M. BRAMATI Alberto,	PR,	SU,	Directeur de thèse



# Contents

<b>Contents</b>	<b>iii</b>
<b>Remerciements</b>	<b>vii</b>
<b>1 Introduction</b>	<b>1</b>
<b>I Theory of Microcavity Exciton Polaritons</b>	<b>3</b>
<b>2 Microcavity Exciton Polaritons</b>	<b>5</b>
2.1 Microcavity Photons . . . . .	5
2.2 Excitons in Semiconductors . . . . .	9
2.2.1 Band theory structure . . . . .	9
2.2.2 Band structure of semiconductors . . . . .	9
2.2.3 Exciton phenomenological approach . . . . .	10
2.2.4 Electron-hole interactions and exciton formation . . . . .	12
2.2.5 Exciton-photon interaction in bulk semiconductor: . . . . .	18
2.2.6 Exciton in 2D quantum well . . . . .	19
2.2.7 Exciton-exciton interaction . . . . .	23
2.3 Excitons-polaritons . . . . .	24
2.3.1 Polariton interactions . . . . .	31
2.4 Polariton dynamics . . . . .	33
2.4.1 Mean field approximation . . . . .	34
2.4.2 Driven dissipative Gross-Pitaevskii Equation. . . . .	35
2.4.3 Excitation scheme . . . . .	37
2.5 Conclusion . . . . .	43
<b>3 Hawking radiation in a polariton quantum fluid</b>	<b>45</b>
3.1 The hydrodynamical analogy . . . . .	45
3.2 Elementary excitations of the fluid : Bogoliubov theory . . . . .	48
3.2.1 Linearization of the Gross-Pitaevskii equation . . . . .	48
3.3 Homogeneous fluid . . . . .	54
3.3.1 Bogoliubov spectrum characterization . . . . .	57
3.4 Hawking radiation in a transcritical fluid . . . . .	64
3.4.1 Inhomogeneous pumping . . . . .	64
3.4.2 Modes quantization . . . . .	68

3.4.3	Spontaneous emission . . . . .	71
3.4.4	Stimulated emission . . . . .	73
3.5	Numerical study of stimulated emission . . . . .	74
3.6	Conclusion . . . . .	74
<b>4</b>	<b>Optical generation and spectroscopy of arbitrary acoustic horizons</b>	<b>77</b>
4.1	Optical generation of an arbitrary fluid velocity field . . . . .	77
4.1.1	Waterfall configuration . . . . .	78
4.1.2	Target velocity profile . . . . .	78
4.1.3	Effective 1D fluid . . . . .	81
4.2	Experimental spectroscopy of the collective excitation spectrum . . . . .	82
4.2.1	High resolution pump-probe spectroscopy method . . . . .	82
4.3	Experimental setup . . . . .	84
4.4	Experimental results . . . . .	85
4.4.1	Homogeneous fluid . . . . .	85
4.4.2	Smooth transition geometry . . . . .	90
4.4.3	Steep horizon geometry . . . . .	98
4.4.4	Quasi-normal mode configuration . . . . .	99
4.5	Conclusion . . . . .	101
<b>5</b>	<b>Experimental observation of stimulated Hawking radiation in a polariton quantum fluid</b>	<b>103</b>
5.1	Interferometric measurement of the scattering matrix . . . . .	103
5.1.1	Challenges of the measurement . . . . .	105
5.1.2	Interferometric reconstruction of the scattered field . . . . .	107
5.2	Experimental implementation . . . . .	109
5.2.1	Ballistic configuration . . . . .	109
5.2.2	Measurement of the Bogoliubov spectrum . . . . .	111
5.2.3	Observation of stimulated Hawking radiation . . . . .	115
5.2.4	Toward the measurement of the scattering matrix . . . . .	117
5.3	Conclusion . . . . .	126
<b>6</b>	<b>Bogoliubov modes correlations in a polariton quantum fluid</b>	<b>127</b>
6.1	Quantum noise of an electromagnetic field . . . . .	127
6.1.1	Standard quantum limit . . . . .	127
6.1.2	Intensity and phase fluctuations . . . . .	129
6.1.3	Squeezed states . . . . .	129
6.2	Photodetection . . . . .	130
6.3	Balanced detection . . . . .	131
6.3.1	Difference measurement . . . . .	132
6.4	Correlations in continuous-variables quantum optics . . . . .	133
6.4.1	Correlation function . . . . .	133
6.4.2	Bogoliubov modes correlations . . . . .	134
6.5	Experimental implementation . . . . .	135
6.5.1	Bogoliubov coefficients measurement . . . . .	136
6.5.2	Bogoliubov modes correlations . . . . .	139
6.6	Conclusion . . . . .	146

<b>7 Conclusion</b>	<b>149</b>
<b>Appendices</b>	<b>151</b>
<b>A Mean field shaping and monitoring</b>	<b>153</b>
A.1 Phase printing . . . . .	153
A.1.1 Spatial light modulator. . . . .	153
A.1.2 Phase measurement . . . . .	154
A.1.3 Off axis interferometry . . . . .	154
A.1.4 Controlling the local intensity . . . . .	154
<b>Bibliography</b>	<b>157</b>



# **Remerciements**

Merci à tous



# Chapter 1

## Introduction

Studying quantum effects in gravitational systems remains one of the most challenging endeavors in modern physics. The extreme conditions required to probe such phenomena, such as those near black holes, make direct experimental investigations practically impossible. Among these quantum effects, Hawking radiation stands out as a cornerstone prediction of quantum field theory in curved spacetime. Proposed by Stephen Hawking in 1974, this radiation arises from the interplay between quantum mechanics and general relativity, predicting the emission of thermal radiation from the event horizon of black holes. Despite its profound implications, Hawking radiation has yet to be observed directly due to the faintness of the signal and the difficulty of accessing black hole horizons. The obvious difficulty to test this prediction experimentally is double. First, the blackness of such an object makes it hard to spot with a telescope meaning one have to rely rather on the peculiar behavior of visible object moving in its gravitational field. The optical observation of a black hole took almost one century since the first prediction of gravitational collapse by Subrahmanyan Chandrasekhar in 1920. It required the synchronization of nine telescope across the world to obtain an optical system whose optical aperture is the diameter of earth. Then the black body temperature of a black hole is inversely proportional to its mass and falls below the temperature of the cosmic microwave background, rendering it effectively undetectable. In principle, primordial black holes with much smaller masses could exhibit higher temperatures, but such objects remain hypothetical and have yet to be observed.

To circumvent these challenges, William Unruh introduced the concept of analog gravity in 1981, proposing that certain fluid systems could mimic the behavior of spacetime near a black hole. This analogy relies on the mathematical equivalence between the propagation of sound waves in a moving fluid and scalar fields in curved spacetime. Since then, numerous classical analog gravity experiments have been conducted, demonstrating phenomena such as horizons and superradiance in systems ranging from water waves to optical fibers. While these experiments have provided valuable insights into the classical aspects of analog gravity, they fall short of capturing the quantum nature of effects like Hawking radiation.

In recent years, the focus has shifted toward quantum fluids, which offer the unique advantage of enabling the observation of quantum effects in analog gravity systems. Among these, quantum fluids of light have emerged as particularly promising candidates. These systems, formed by the interaction of photons with a nonlinear medium, combine the advantages of quantum fluids—such as coherence and tunability—with the accessibility of optical techniques. Quantum fluids of polaritons, which arise from the strong coupling

between photons and excitons in semiconductor microcavities, are especially well-suited for analog gravity experiments. Their out-of-equilibrium nature, combined with their ability to form horizons and exhibit quantum fluctuations, makes them ideal platforms for studying phenomena like Hawking radiation.

This thesis explores the theoretical and experimental investigation of analog Hawking radiation in polariton quantum fluids. By leveraging the unique properties of these systems, we aim to bridge the gap between classical analog gravity experiments and the quantum realm, providing new insights into the interplay between quantum mechanics and curved spacetime physics.

In the **second chapter**, we introduce polariton fluids, which result from the strong coupling between photons and excitons in semiconductor microcavities. We present the fundamental properties of these systems, including their out-of-equilibrium nature, coherence, and ability to form analog horizons. These characteristics make them ideal candidates for analog gravity experiments. We also establish the theoretical framework based on the Gross-Pitaevskii equation, which describes the collective dynamics of polariton fluids.

**Chapter 3: Theory of Analog Hawking Radiation** This chapter develops the theoretical framework for understanding analog Hawking radiation in polariton fluids. By deriving the Bogoliubov spectrum of collective excitations, we highlight the role of positive- and negative-energy modes in particle creation. We analyze the mixing of these modes at the transcritical interface, which is the key mechanism behind Hawking radiation emission. Finally, we discuss the theoretical implications of this phenomenon and the conditions required for its observation.

**Chapter 4: Experimental Realization of a Transcritical Flow** In this chapter, we describe the experimental realization of a transcritical flow in a polariton fluid. Through precise optical pump shaping, we successfully created a transcritical region, essential for the emergence of a sonic horizon. We also present an experimental method to detect negative-energy modes in this region, confirming the necessary conditions for observing analog Hawking radiation.

**Chapter 5: Experimental Observation of Stimulated Hawking Radiation** This chapter focuses on the experimental observation of stimulated Hawking radiation in a polariton fluid. By injecting a coherent state into the upstream region and measuring the scattered modes, we provide evidence of positive-negative energy mixing at the interface. While our results do not yet constitute a complete quantitative measurement of amplification, they demonstrate the power of optical techniques for reconstructing the fluctuation field and analyzing scattered modes.

**Chapter 6: Measurement of Correlations between Bogoliubov Modes** In this chapter, we present the first measurement of correlations between Bogoliubov modes in a polariton fluid. By analyzing the intensity correlations between Bogoliubov modes on a homogeneous static fluid. While not demonstrating quantum correlations, this work represents a significant step toward understanding how quantum optics measurement methods can be applied to study correlations in analog horizons.

## **Part I**

# **Theory of Microcavity Exciton Polaritons**



## Chapter 2

# Microcavity Exciton Polaritons

Microcavity polaritons arise from the strong coupling between photons confined in a microcavity and quantum wells excitons in a semiconductor. Due to their hybrid nature, polaritons inherit properties from both photons and excitons and are often referred as a fluid of light since they can be seen as photons dressed by the medium interactions.

In general, whenever an electromagnetic field is shone on a material, the dipoles of the medium oscillate and change the refractive index seen by the field. At high intensity, the change in the refractive index can depend on the square of the electric field, which is then called the Kerr effect. Since a local variation of the refractive index deflects light, a high-intensity region in the material can modify the trajectory of an incoming beam leading to self-focusing or defocusing. From this point of view, one can see how photon-photon interaction can arise in a nonlinear medium.

In the present case, the light matter coupling is achieved in a semiconductor microcavity by inserting two-dimensional quantum wells at the antinode of the electromagnetic field of a high-quality factor optical microcavity. In such devices, polaritons arise from the coupling between the cavity photons and the excitons of the quantum wells.

This chapter is dedicated to describe photons and excitons separately before showing how they couple in the sample to form polaritons. Then, from a microscopic description, we will derive the macroscopic equations of motion of the fluid and show that polaritons can be described with a driven dissipative Gross-Pitaevskii equation.

### 2.1 Microcavity Photons

**Planar microcavity parameters:** First, let us consider an electromagnetic field incident at an angle  $\theta$  on a planar microcavity made with two mirrors with reflectivities  $R_1$  and  $R_2$ , separated by a distance  $L$ . The z-axis is normal to the mirrors as shown in [Figure 2.1](#). The phase shift acquired during a single round trip in the cavity is  $\Delta\phi(\theta) = 2nk_0L \cos(\theta)$ , with  $n$  the refractive index of the medium and  $k_0 = 2\pi/\lambda$  the wave vector of the field in vacuum. The interference between the multiple reflections sets the resonance condition of the cavity, and the transmission of the field can be written as:

$$T(\theta) = \frac{R_1 R_2}{1 + R_1 R_2 - \sqrt{R_1 R_2} \cos(\Delta\phi(\theta)/2)} \quad (2.1)$$

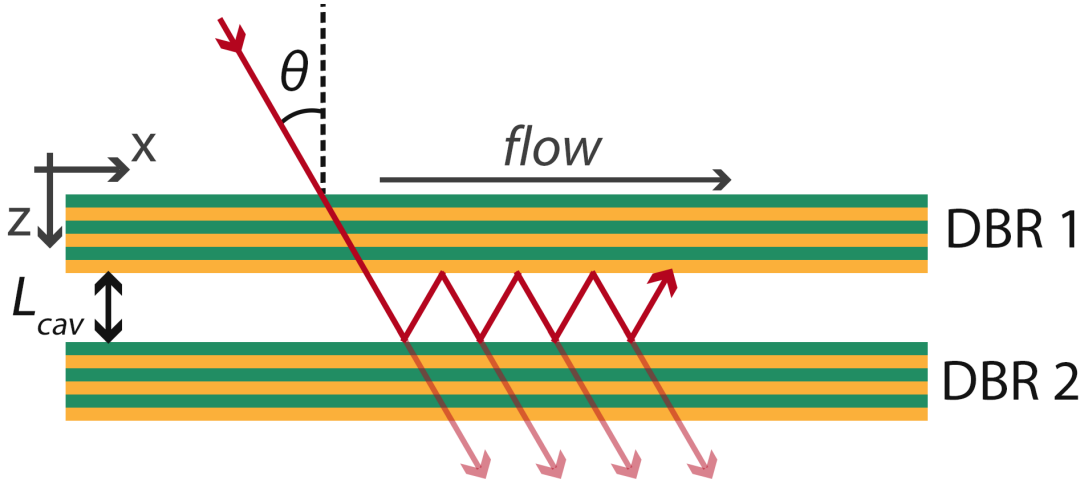


Fig. 2.1 Photon in a planar microcavity. Distributed Bragg Reflectors (DBR) mirrors are used to reflect the light and trap it in the cavity. The  $z$ -axis is normal to the mirrors, and the  $x$  and  $y$  axes are in the plane of the mirrors. The angle  $\theta$  is defined as the angle of incidence of the electromagnetic field on the mirrors. The field is confined in a region of length  $L$  between the two mirrors.

From this, one can define the decay rate of the field oscillation known as the quality factor:

$$Q = \frac{\omega_\gamma}{\delta\omega_\gamma} \quad (2.2)$$

with  $\omega_\gamma$  the resonance frequency of the cavity and  $\delta\omega_\gamma$  the linewidth of the resonance, which sets the lifetime of the photon in the cavity through  $\tau_\gamma = 1/\Delta\omega_\gamma$  and depends on the mirrors' reflectivities. Another important parameter describing the cavity is its frequency resolution, which is encoded in the cavity finesse through:

$$\mathcal{F} = \pi \frac{\Delta\omega_\gamma}{\delta\omega_\gamma} = \pi \frac{\sqrt{R_1 R_2}}{1 - R_1 R_2} \quad (2.3)$$

where  $\Delta\omega_\gamma = c/2L_{cav}$  is the Free Spectral Range (FSR) representing the frequency difference between two successive longitudinal modes of the cavity. To achieve strong coupling with the nonlinear medium, the photon needs to stay trapped in the cavity long enough to interact with the medium. In other words, the quality factor of the cavity must be very high, which means using mirrors with high reflectivities. This can be achieved with Distributed Bragg Reflectors (DBR) mirrors.

**Distributed Bragg Reflectors.** These reflectors consist of a series of  $N$  alternating layers composed of two materials with different refractive indices  $n_1 < n_2$ . This configuration causes partial reflection of the electromagnetic field at each of the  $N$  interfaces, resulting in a very high overall reflection coefficient,  $R$ , which is expressed as follows:

$$R = \left[ \frac{(n_2/n_1)^{2N} - n_f/n_0}{(n_2/n_1)^{2N} + n_f/n_0} \right]^2, \quad (2.4)$$

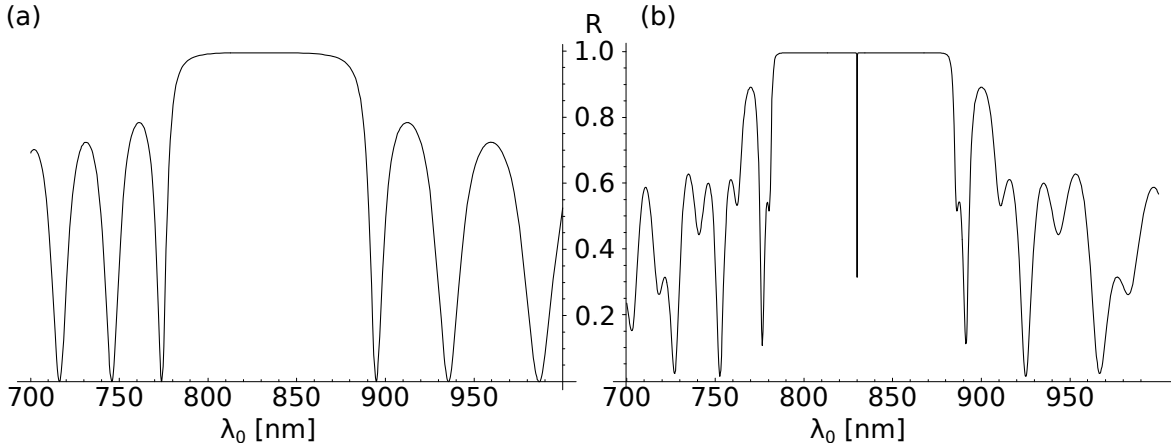


Fig. 2.2 **DBR and Fabry-Perot cavity reflectivity.** (a) Reflectivity  $R$  of a Bragg mirror of 20 pairs of  $\text{Ga}_{0.9}\text{Al}_{0.1}\text{As}/\text{AlAs}$ , illuminated at normal incidence for different wavelengths  $\lambda$ . The DBR has a reflectivity close to 1 over a large range of wavelengths called the stop-band, centered on  $\lambda_0 = 836$  nm by tuning the thickness of each of the mirror layers. (b) Corresponding reflectivity of the optical cavity built from the facing of two DBR mirrors identical to that in (a) and separated by a distance  $L_{\text{cav}} = 2\lambda_0/n_{\text{cav}}$ , leading to the appearance of a very narrow resonance at  $\lambda_0$ . Adapted from [21].

with  $n_0$  and  $n_f$  representing the refractive indices of the media before and after the mirrors. Figure 2.2 illustrates the evolution of  $R$  in relation to the wavelength of the electromagnetic field for a single DBR mirror used in our system. This mirror is constructed with 20 pairs of  $\text{Ga}_{0.9}\text{Al}_{0.1}\text{As}/\text{AlAs}$  layers, having refractive indices  $n_2 = 3.48$  and  $n_1 = 2.95$  respectively. The reflection coefficient  $R$  is 0.9985 across a broad wavelength range, known as the stop-band, centered around a wavelength of  $\lambda_0 = 836$  nm. This central wavelength is achieved by setting the thickness of the layers to  $d_{1,2} = \lambda_0/4n_{1,2}$ . The microcavity used in the experiments is built by facing two of those DBR mirrors separated by a distance  $L_{\text{cav}} = 3\lambda_0/2n_{\text{cav}}$ . The front mirror is made of 40 stacks while the output mirror is made of 53 stacks which gives reflectivities of  $R_{in} = 99.85\%$  and  $R_{out} = 99.95\%$  respectively. It gives rise to a very narrow resonance at  $\lambda_0$  with three field antinodes within the cavity. The parameters of the cavity are summarized in Equation 2.1.

Fabry-Perot cavity parameters					
$R_1$	$R_2$	$n_1$	$n_2$	$n_{\text{cav}}$	$\lambda_0$ (nm)
0.9992	0.9985	2.95	3.48	3.54	836

With the above-described DBR, the cavity has a finesse  $\mathcal{F} = 2850$  from which we can infer the photon lifetime:

$$\delta\omega_\gamma = \pi \frac{\Delta\omega_\gamma}{\mathcal{F}} = \frac{c}{n_{\text{cav}}L_{\text{eff}}} \frac{1 - R_{in}R_{out}}{\sqrt{R_{in}R_{out}}}, \quad (2.5)$$

where  $L_{\text{eff}} = L_{\text{cav}} + L_{\text{bragg}}$  is the effective length of the sample taking into account the

penetration of the field in the mirrors.

$$L_{\text{Bragg}} = \frac{\lambda_0}{2} \frac{n_1 n_2}{n_{\text{cav}}(n_2 - n_1)} \quad (2.6)$$

which gives  $\tau_\gamma = \frac{1}{\delta\omega_\gamma} = 5 \text{ ps}$ .

**Transverse dynamics of the photon.** The energy of the photon within the sample can be written as:

$$E_\gamma = \frac{\hbar c}{n_{\text{cav}}} \sqrt{k_x^2 + k_y^2 + k_z^2}. \quad (2.7)$$

The resonance condition of the cavity fixes the photon wavevector along the z component.

$$k_z = \frac{2\pi n_{\text{cav}}}{\lambda_0}. \quad (2.8)$$

In the paraxial approximation  $k_x, k_y \ll k_z$ , one can expand (2.7) in terms of  $\frac{\|\mathbf{k}_\parallel\|}{\|\mathbf{k}_z\|}$  as:

$$E_\gamma = \frac{\hbar c}{n_{\text{cav}}} \sqrt{k_z^2 + k_\parallel^2} = E_0 \left( 1 + (\hbar k_\parallel)^2 \frac{c^2}{2(n_{\text{cav}} E_0)^2} \right). \quad (2.9)$$

where  $\mathbf{k}_\parallel = \mathbf{k}_x + \mathbf{k}_y$  is the wavevector in the transverse plane and  $E_0 = hc/\lambda_0$  is the photon energy in vacuum. We can identify the effective mass of the photon by writing (2.9) with the usual form of the kinetic energy of a massive particle:

$$E_\gamma = E_0 + \frac{p_\parallel^2}{2m_\gamma} = E_0 + \frac{\hbar^2 k_\parallel^2}{2m_\gamma}, \quad (2.10)$$

where we identify  $m_\gamma = \frac{hn_{\text{cav}}^2}{\lambda_0 c}$  which is inversely proportional to the second derivative of the energy with respect to  $k_\parallel$ :

$$\frac{1}{m_\gamma} = \frac{1}{\hbar^2} \frac{\partial^2 E_\gamma}{\partial k_\parallel^2} \quad (2.11)$$

**Momentum conservation:** we mentioned the necessity to have a high quality factor to achieve strong coupling. One could then ask why do we stick to planar designs, which are generally not the best solution to get a high Q factor since they are known to be unstable except for plane waves. The answer lies in the calculation just above. Indeed, the advantage of having a planar design is the translational invariance in the  $xy$ -plane, which brings  $\mathbf{k}_\parallel$  conservation. As a consequence, if one shines a laser with a given  $\mathbf{k}_\parallel$ , light will behave in the cavity as a massive particle moving at velocity  $v_\gamma = \hbar \mathbf{k}_\parallel / m_\gamma$ . In the picture of creating a fluid whose flow is controlled, the planar design then appears as a wise choice.

**A direct link between incidence angle and in plane momentum  $k_{\parallel}$ :** as shown in [Figure 2.1](#) the incidence angle  $\theta = (\theta_x, \theta_y)$  of the incoming field is related to the in-plane momentum  $k_{\parallel}$  as :

$$k_x = k_0 \sin(\theta_x) \quad (2.12)$$

$$k_y = k_0 \sin(\theta_y) \quad (2.13)$$

Controlling the in plane momentum of photons and latter that of polaritons then reduces to control the local incidence angle of the field, in other words, the transverse phase of the incoming beam. This is a crucial point for the experiments as it allows to control the flow of the fluid by changing the laser phase.

**Conclusion:** This section showed how trapping light in a planar microcavity grants it effective mass and lifetime. The next section will explore the semiconducting media that are inserted into these cavities, especially the bound electron-hole pairs called excitons that can be addressed by the trapped light.

## 2.2 Excitons in Semiconductors

### 2.2.1 Band theory structure

Applying the Schrodinger equation to an atom shows that the electrons energies can only take discrete values. However, N atoms sufficiently close to each other interact which lift the degeneracy and turns each energy state in a set of N separated levels (see [Figure 2.3](#)). Within a solid material, the density is so high (typically  $10^{22}$  atoms per  $\text{cm}^3$ ) that the spacing between energy levels tends to zero forming a continuous band of energy. The electrons fill the band from the lowest energy level up to the Fermi energy. The latter is the energy of the highest occupied state at zero temperature. The band structure of a material is then defined by the energy of the valence band, the conduction band and the band gap between them. The valence band is the first energy band that is fully occupied at zero temperature, while the conduction band is the lowest energy band that is empty at zero temperature. The band gap is the energy difference between the conduction band and the valence band. Determining if a material is a metal, a semiconductor or an insulator is then a matter of comparing the band gap to the Fermi energy. For metals the conduction band and the valence band overlap, any electric potential difference puts then the electron into motion and create a current. For insulators and semiconducting materials the Fermi energy is in the band gap. For insulators the band gap is typically  $\sim 3$  eV making the promotion of an electron to the conduction band highly energy demanding. Finally, the semiconductors gap energy is accessible with photons in the visible domain making these materials perfect candidates for controlled light-matter interactions.

### 2.2.2 Band structure of semiconductors

Finding the exact band structure of a material can be done by solving the Schrodinger equation for an electron in periodic potential [81]. The Bloch theorem states that the wave function of such an electron can be written as a plane wave modulated by a periodic function.

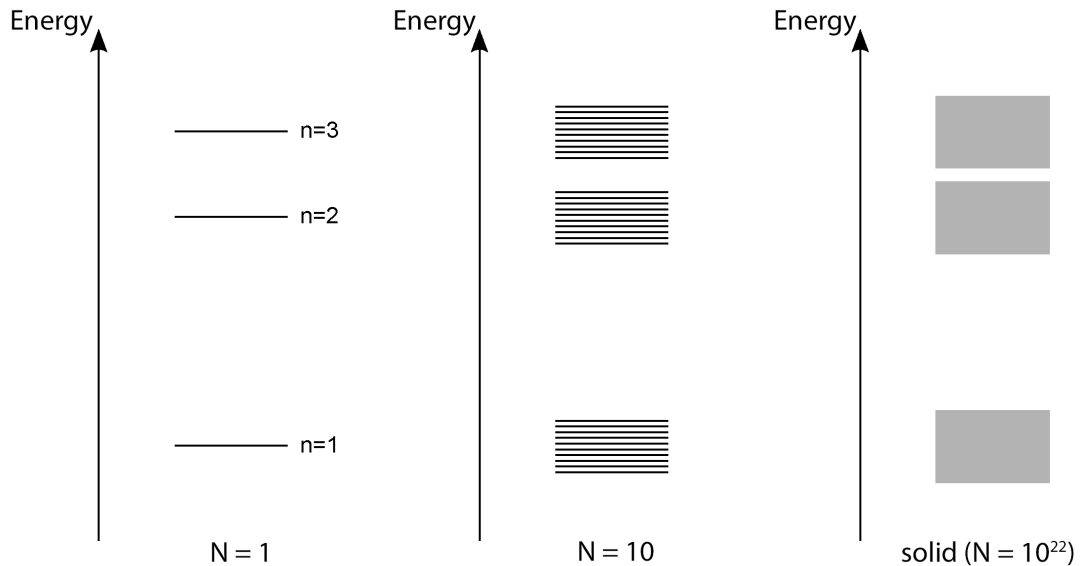


Fig. 2.3 **Energy levels of a set of  $N$  atoms.** As  $N$  increase the spacing between two successive levels tends to zero and eventually form a continuous band of energy.

The periodic function is then expanded in a Fourier series and the Schrodinger equation is solved for each Fourier component. The exact band structure can be rather complicated but a simplified version can be obtained by considering the effective mass approximation [47]. In this picture, the dispersion relation of the electron in the material is typically represented in [Figure 2.4](#). In this case the minimum of the conduction band and the maximum of the valence band are located at the same point in the Brillouin zone. The material is then said to have a direct band gap [81].

### 2.2.3 Exciton phenomenological approach

This section is dedicated to the description of excitons and is strongly inspired by the work of Combescot et al. [26]. As shown in [Figure 2.4](#) shining a photon whose energy exceed the gap energy can promote an electron from the valence band to the conduction band through the absorption of a photon. The disappearance of the electron in the valence band can be described equivalently as the creation of a virtual particle of opposite charge called hole [26]. If one shine a laser on a semiconductor and ramp up its frequency a narrow absorption peak is observed below the gap energy. The presence of this peak originates from the Coulomb interaction between the excited electron and the hole creating a bound state of the material. In terms of energy it is as if the gap energy is reduced by the binding energy of the exciton and the electron lies in a virtual band below the conduction band as represented by the red dashed lines in [Figure 2.4](#). The exciton energy can then be written as :

$$E_X = E_g - E_b + \frac{\hbar^2 K^2}{2m_X} \quad (2.14)$$

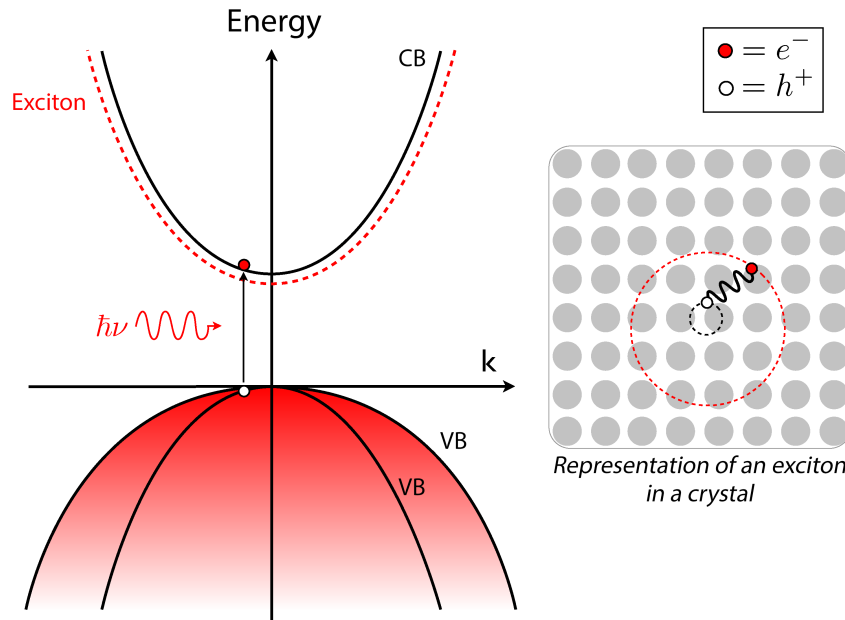


Fig. 2.4 **Band structure of a direct gap semiconductor.** The black solid line represent the conduction and valence band in a bulk semiconductor. The red dashed lines represent the dispersion relation of an exciton. The filling of the valence band by electrons is represented by the shaded red color.

where  $E_g$  is the gap energy,  $E_b$  the binding energy,  $\hbar\vec{K}$  is the exciton momentum defined as the electron-hole pair center of mass momentum and  $m_X$  the exciton effective mass which is the sum of the electron and hole effective mass. Since  $E_b$  is the interaction energy between a electron and a hole it is, as we will see in the next section, very similar to the Rydberg energy series of the hydrogen atom, the hole playing the role of the proton. As a consequence, the same electronic structure exist for the exciton : 1s, 2s, 2p, etc state can be observed in the absorption spectrum of the material. However, the hole is quite different from the proton in the sense that it is actually a collective excitation of all the valence band electrons. Furthermore, the exciton is a weakly bound state as the binding energy is typically a few meV. In GaAs or AlGaAs heterostructures which are the materials used in the present work,  $E_b$  is around 4 meV due to their high dielectric constant  $\epsilon_r \sim 12$ . In these kinds of samples, excitonic resonances can only be observed at cryogenic temperatures since the binding needs to exceed the thermal energy  $k_B T$  in order to survive to the thermal fluctuations. For the above mentionned structures we obtain the condition  $T < 10$  K for excitons stability. Another important excitons characteristic is their huge Bohr Radius  $a_X = \frac{\epsilon_r \hbar^2}{m_X e^2} = 11.6$  nm in GaAs which is much larger then the typical size of a crystalline unit cell  $a_0 = 5.651$  Å. This means that the exciton wavefunction is delocalized over many unit cells. Such excitons, are called Wannier-Mott and contrast with Frenkel excitons which are localized on a single unit cell and are typically found in organic materials.

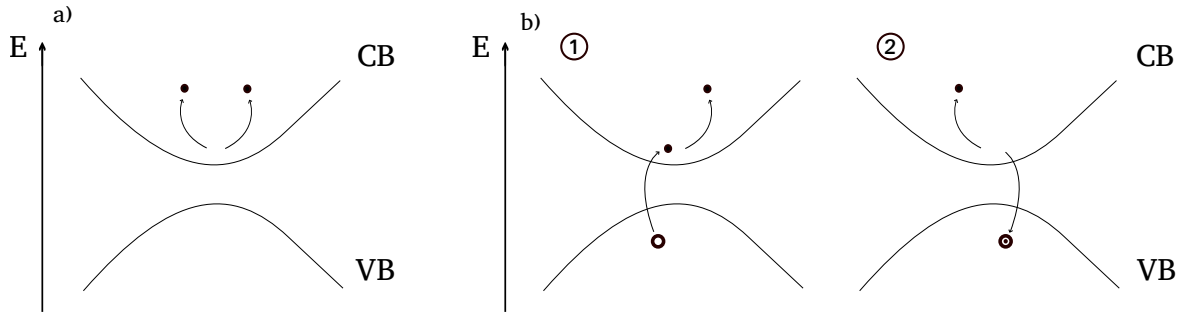


Fig. 2.5 **Schematic representing the scattering between two conduction band electrons.** a) Direct intraband scattering. Filled black dots represent conduction band electrons while the arrows represent a scattering process. b) Two steps scattering involving an electron-hole exchange or creation and annihilation of an exciton, referred as interband scattering. The empty black circle represent a valence band hole while the same circle with a small black dot inside stands for a valence band hole filled with an electron which is equivalent to a valence electron. a) and b) share the same final state which is a full valence band and two scattered conduction band electrons. Drawing inspired from [26].

## 2.2.4 Electron-hole interactions and exciton formation

Excitons were presented as made of an electron and a hole bound by Coulomb interactions. However, all the interactions in the material are ultimately mediated by valence and conduction band electrons. The rising of a bound state in such a material is therefore not obvious. In other words moving from a conduction-valence band electrons to a electron-hole picture is not trivial and reveals interesting feature about the electron-hole interactions that will at the end enable exciton formation. In this section we will first describe all the possible interactions between the electrons of the semiconductor before showing how they can be recasted in terms of electron-hole interactions [26]

### 2.2.4.1 Electron scattering in semiconductors

**Intraband scattering.** To start with let us consider the direct scattering between two conduction band electrons as presented in Figure 2.5 a). This simple process is referred as intraband scattering since each electron stays in its own band. In the small momentum limit  $\mathbf{q} \rightarrow 0$  it yields a potential of the form [26]:

$$V_{\mathbf{q}} \simeq \frac{4\pi e^2}{L^3 q^2} \quad (2.15)$$

in a sample of size L. This form of potential also holds for the scattering between two valence electrons or between a valence and a conduction band electron that stay in their respective bands.

**Interband scattering.** Processes in which one or two electrons change band are also possible and are referred as interband scattering. In the case of a single interband jump the potential reads  $(\frac{q}{\kappa}) \times V_q = 4\pi e^2 / L^3 q \kappa$  where  $\kappa$  is a factor dimensionally equivalent to a wavevector that depends on the material crystalline structure. It then behaves as  $1/q$ . When both electrons change band the potential is then  $(\frac{q}{\kappa})^2 V_q$  proportionnal to  $q^0$  and thus remaining finite when  $q \rightarrow 0$ . Remarkably, in both the single and two interband jump scenarios, the number of electrons in each band changes by one and two respectively, making these transitions less likely to occur compared to number-conserving processes.

Indeed, in second order perturbation theory the transition amplitude between an initial state  $|i\rangle$  and a final state  $|f\rangle$  may be written as :

$$\Gamma_{i \rightarrow f}^{(2)} = \frac{2\pi}{\hbar} \left| \sum_m \frac{\langle f | V_q | m \rangle \langle m | V_q | i \rangle}{E_f - E_i - E_m} \right|^2 \delta((E_f - E_i) - E_g) \quad (2.16)$$

Whenever an electron undergo a band jump the energy cost is of the order of the band gap  $E_f - E_i \simeq E_g$ . As a consequence the corresponding transition amplitude gets reduced by a factor  $\frac{1}{E_g}$  and appears to be negligible. However a direct intraband scattering can happen in several interband jumps that will dress the direct Coulomb scattering as shown in [Figure 2.5 b\)](#) for the case of two jumps. When summing over all possible intermediate states as in [\(2.16\)](#) we end up with the same potential as the direct intraband scattering but reduced by dielectric constant factor  $\epsilon_{sc}$  that depend on the material.

To clarify this idea let us now consider the scattering between a conduction and a valence band electron. The same scattering process can also occur in two steps. First, a conduction band electron is scattered in its band while a valence band electron is promoted to the conduction band. Since an electron changes band, it brings a potential  $(q/\kappa) \times V_q$ . Secondly, the excited electron goes back to the valence band while a valence band electron is scattered in its band yielding again a potential  $(q/\kappa) \times V_q$ . This two steps interaction end up with the same initial and final states as direct intraband scattering and the number of electrons in each band is conserved. In terms of energy, the two scatterings behaving as  $1/q$  potentials the overall potential behaves also as  $1/q^2$  but with an additionnal  $1/E_g$  factor coming from the intermediate interband jumps. More specifically the two steps contribution is :  $(4\pi e^2 / L^3 q^2) [(e^2 / L^3 \kappa^2) / E_g]$ .

It is also possible to make it a three steps scattering by adding an intermediate interband exchange after the first step : the previously excited conduction band electron returns to the valence band while a valence band electron is promoted to the conduction band. More explicitly the process is as follows :

- **Step 1 :** a valence band electron is promoted to the conduction band while a conduction band is scattered in its band. The potential reads  $(q/\kappa) \times V_q \propto \frac{1}{q}$  and the energy cost is of the order of  $E_g$ .
- **Step 2 :** the previously excited conduction band electron returns to the valence band while another valence band electron is excited to the conduction band. The potential read  $V_q (q/\kappa)^2 \propto q$  and the energy cost is of the order of  $2E_g$ .

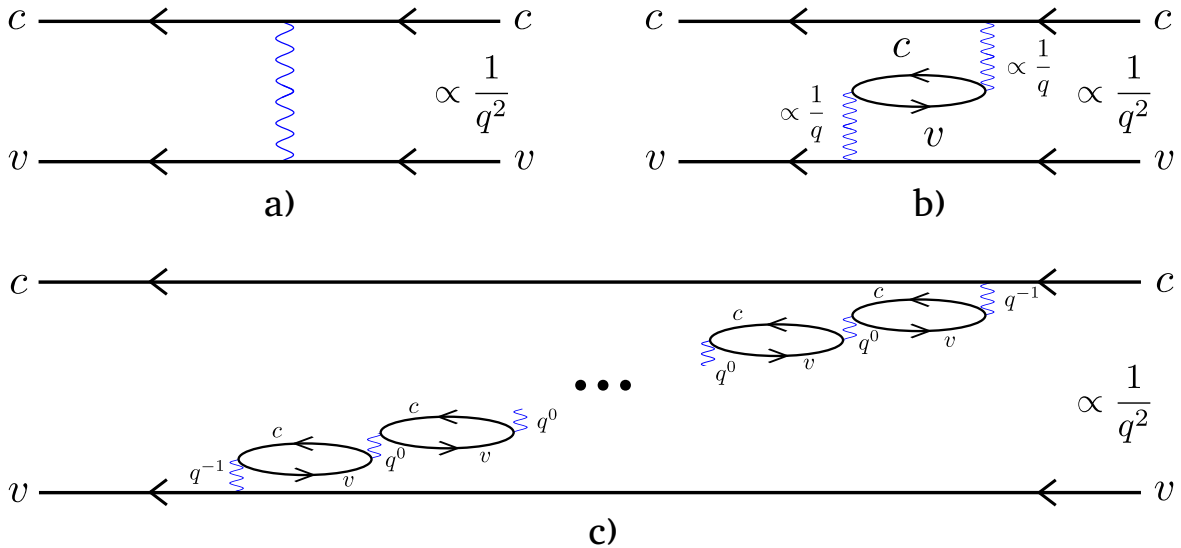


Fig. 2.6 **Feynman diagrams representing an intraband scattering between a conduction and a valence band electron.** a) Direct intraband scattering. The blue wavy lines represent the Coulomb interaction that make the electrons to change states. b) Two steps scattering involving an intermediate interband exchange that is represented by the bubble in the middle. c) Multiple steps scattering involving several interband exchanges represented by the numerous bubbles. Drawing inspired from [26].

- **Step 3 :** the excited electron goes back to the valence band while a valence band electron is scattered in its band. The potential read again  $(q/\kappa) \times V_q \propto \frac{1}{q}$  and the energy cost is of the order of  $E_g$ .

The total energy budget is then :  $(4\pi e^2/L^3 q^2) [(e^2/L^3 \kappa^2)/E_g]^2$ . Remarkably, one might expect the overall potential to scale as  $1/E_g^3$  since each step requires at least one electron to change band. However, the structure of perturbation theory ensures that the total energy denominator accounts for the number of coupled interband transitions, rather than treating each step independently. Step 2 effectively "couples" the transitions in such a way that two energy denominators are introduced, rather than three independent ones, which explains the  $1/E_g^2$  dependence. This coupling reflects the fact that intermediate states are shared between adjacent steps in the perturbative sequence.

Finally, the number of intermediate states can be arbitrarily increased by adding 'bubbles' of exchange interaction, as illustrated in the Feynman diagram in Figure 2.6 b). Each pair of adjacent bubbles represents an interband interaction similar to the one described in Step 2 above. While it conserves the number of electrons in each band, it involves two interband jumps. The interaction between two bubbles is then  $\propto q^0$  and is finite in the small momentum limit. By summing the contributions of processes with all possible numbers of bubbles, we obtain an effective Coulomb potential:

$$V_q = \frac{4\pi e^2}{L^3 q^2 \epsilon_{sc}} \quad (2.17)$$

where  $\epsilon_{sc}$  is a dielectric constant stemming from the infinite sum over the number of bubbles. The discussion that we just made also holds for the intraband scattering between two conduction band electrons or two valence band electrons. Indeed, it reduces to change the letter of the bands in the Feynman diagrams of [Figure 2.6](#) which doesn't change the overall energy budget of the process. Consequently, the potential (2.17) is valid for all intraband scattering processes. Based on the previous discussion we restrict the Coulomb potential that describes any scattering process to interactions that conserve the number of particles in each band, namely the intraband scattering potential between conduction and valence band electrons derived above. The general form of the potential is then in second quantization formalism:

$$V_{coul} \simeq \frac{1}{2} \sum_{\mathbf{q} \neq 0} \frac{4\pi e^2}{L^3 q^2 \epsilon_{sc}} \sum_{\mathbf{k}_1, \mathbf{k}_2} \sum_{i_1, i_2} a_{i_1, \mathbf{k}_1 + \mathbf{q}}^\dagger a_{i_2, \mathbf{k}_2 - \mathbf{q}}^\dagger a_{i_2, \mathbf{k}_2} a_{i_1, \mathbf{k}_1} \quad (2.18)$$

where  $i_1, i_2 \in (c, v)$ . The creation operators  $a_{c, \mathbf{k}}^\dagger$  and  $a_{v, \mathbf{k}}^\dagger$  create respectively a conduction and a valence band electron with momentum  $\mathbf{k}$ . The  $\mathbf{q} = 0$  contribution is not included and treated separately by the wise choice of an average electron-electron potential  $V_{e-e}$  that cancels it. More details can be found in the Appendix of [26]. It is worth noting that, in the conduction-valence electron framework, all intraband interactions are identical and repulsive. From this it is not obvious how a bound state like an exciton can arise in the material. However, as we will see in the next section, transitioning to the electron-hole description transforms one of these scattering interactions into an attractive interaction. This feature is central to the energy splitting between two types of excitons: bright excitons, which couple to light, and dark excitons, which do not as we will see later.

#### 2.2.4.2 From the conduction-valence electrons to the electron-hole picture

So far we described the scattering processes within the semiconductor using valence and conduction electrons. However, the exciton results form the binding between a conduction band electron and the absence of a valence band electron that we usually describe as a hole. While the conduction electron description stays the same, moving from one picture to the other requires to define the hole creation operator that account for the removal of a valence band electron or equivalently the creation of a hole in the valence band.

$$a_{c, \mathbf{k}}^\dagger = a_{\mathbf{k}}, \quad (2.19a)$$

$$a_{v, \mathbf{k}}^\dagger = h_{-\mathbf{k}}^\dagger, \quad (2.19b)$$

where  $h_{-\mathbf{k}}^\dagger$  creates a hole in the valence band with momentum  $-\mathbf{k}$ . The  $-$  sign is imposed by energy and momentum conservation laws. When we substitute the full valence band with a missing electron with momentum  $\mathbf{k}_v$  by a hole, the hole needs to have opposite charge  $+|e|$ , momentum  $\mathbf{k}_h = -\mathbf{k}_v$  and energy  $E_h(\mathbf{k}) = -E_v(\mathbf{k})$  to account for the "absence" of

the valence electron. In the small momentum limit we have  $E_v(\mathbf{k}) = E_{v_0} + \frac{\hbar^2 k_v^2}{2m_v}$  with  $m_v$  the valence electron effective mass that is negative as visible in [Figure 2.4](#). The constraint on the energy  $E_h = -E_v$  then imposes  $\frac{\hbar^2 k_h^2}{2m_h} = -\frac{\hbar^2 k_v^2}{2m_v}$  making the effective mass of the hole positive. Its charge and mass being positive it can then undergo attractive interactions with a conduction band electron and eventually form an exciton. We already see how describing the valence band with hole instead of electrons can predict the formation of bound state. Let us now look how this feature arises from a microscopic point of view. The full crystal hamiltonian is :

$$\mathcal{H} = \mathcal{H}_0 + V_{coul} \quad (2.20)$$

with  $\mathcal{H}_0$  the free electron hamiltonian and  $V_{coul}$  the Coulomb interaction between electrons. The free electron hamiltonian reads :

$$\mathcal{H}_0 = \sum_{\mathbf{k}} E_c(\mathbf{k}) a_{c,\mathbf{k}}^\dagger a_{c,\mathbf{k}} + \sum_{\mathbf{k}} E_v(\mathbf{k}) a_{v,\mathbf{k}}^\dagger a_{v,\mathbf{k}} \quad (2.21)$$

where  $E_c(\mathbf{k})$  and  $E_v(\mathbf{k})$  are the conduction and valence band energies respectively. The Coulomb interactions part can be decomposed in the following way :

$$V_{coul} = V_{cc} + V_{vv} + V_{cv} \quad (2.22)$$

Using the newly defined operators [\(2.19\)](#) together with fermionic commutation relation  $a_{i,\mathbf{k}}^\dagger a_{i,\mathbf{k}} = 1 - a_{i,\mathbf{k}} a_{i,\mathbf{k}}^\dagger$  the different scattering potentials are modified as we now show.

- The one body hamiltonian reads :

$$\mathcal{H}_0 = \sum_{\mathbf{k}} E_v(\mathbf{k}) + \sum_{\mathbf{k}} E_c(\mathbf{k}) a_{\mathbf{k}}^\dagger a_{\mathbf{k}} + \sum_{\mathbf{k}} -E_v(\mathbf{k}) h_{\mathbf{k}}^\dagger h_{\mathbf{k}}. \quad (2.23)$$

- The scattering between two conduction band electron is the same as before :

$$V_{cc} = \frac{1}{2} \sum_{\mathbf{q} \neq 0} V_{\mathbf{q}} \sum_{\mathbf{k}_1, \mathbf{k}_2} a_{\mathbf{k}_1 + \mathbf{q}}^\dagger a_{\mathbf{k}_2 - \mathbf{q}}^\dagger a_{\mathbf{k}_2} a_{\mathbf{k}_1} \equiv V_{ee} \quad (2.24)$$

- The scattering between two valence band electrons splits into three terms :

$$V_{vv} = -\frac{N_v}{2} \sum_{\mathbf{k} \neq 0} V_{\mathbf{k}} + \sum_{\mathbf{k}} \hat{h}_k^\dagger \hat{h}_k \sum_{\mathbf{k}' \neq \mathbf{k}} V_{\mathbf{k}' - \mathbf{k}} + V_{hh}. \quad (2.25)$$

The first term is constant and account for repulsive exchange interaction between all valence electrons. The second term comes from the scattering between a valence electron with wavevector  $\mathbf{k}$  and all the other valence electrons. It adds a shift to the hole kinetic energy  $E_h = -E_v$  that appears in the one body hamiltonian  $\mathcal{H}_0$ . The last term is the hole-hole interaction that is repulsive and is the same as the valence electron-electron interaction with opposite wavevectors :

$$V_{hh} = \frac{1}{2} \sum_{\mathbf{q} \neq 0} V_{\mathbf{q}} \sum_{\mathbf{k}_1, \mathbf{k}_2} h_{\mathbf{k}_1 + \mathbf{q}}^\dagger h_{\mathbf{k}_2 - \mathbf{q}}^\dagger h_{\mathbf{k}_2} h_{\mathbf{k}_1} \quad (2.26)$$

- Finally, scattering between a conduction and a valence band electron is :

$$V_{cv} = \sum_{\mathbf{q} \neq 0} V_{\mathbf{q}} \sum_{\mathbf{k}_1, \mathbf{k}_2} a_{c, \mathbf{k}_1 + \mathbf{q}}^\dagger a_{v, \mathbf{k}_2 - \mathbf{q}}^\dagger a_{v, \mathbf{k}_2} a_{c, \mathbf{k}_1}. \quad (2.27)$$

Using that for non zero momentum transfer  $[a_{v, \mathbf{k}_2 - \mathbf{q}}^\dagger, a_{v, \mathbf{k}_2}] = 0$  and introducing  $\mathbf{k}'_2 = -(\mathbf{k}_2 - \mathbf{q})$  the potentials in terms of electron-hole reads :

$$V_{cv} = - \sum_{\mathbf{q} \neq 0} V_{\mathbf{q}} \sum_{\mathbf{k}_1, \mathbf{k}'_2} a_{\mathbf{k}_1 + \mathbf{q}}^\dagger h_{\mathbf{k}'_2 - \mathbf{q}}^\dagger h_{\mathbf{k}'_2} a_{\mathbf{k}_1} \equiv V_{eh}. \quad (2.28)$$

The latter requires a special attention since it exhibits an attractive interaction and reveals the possibility of excitons formation which was not obvious in the conduction-valence electron picture.

**Spin conservation in electron scattering.** Scattering processes mediated by the Coulomb interaction conserve the spin of the electron for both interband and intraband scatterings due to the rotationnal symmetry of the Coulomb force. As a consequence, the interactions between electrons and holes that we just exhibited are also spin preserving. The latter has important consequences to determine selection rules when looking at optical excitation of an electron-hole pair.

To summarize this section, we demonstrated that replacing the full valence band by a hole looks quite convenient since it allow to forget about all the valence band electrons and exhibits the possibility of bound state formation. However, it must be done with caution since the remaining valence band electrons undergo the many intraband scattering processes described in the section and reduce the effective Coulomb intraband interaction by a factor  $1/\epsilon_{sc}$ . Remarkably, the intraband scatterings between valence and conduction band electrons  $V_{cv}$  are at the origin of the attractive electron-hole interactions while valence-valence interactions are responsible for the shift in the hole kinetic energy as expressed by [Equation 2.25](#). Let us now explain how the aforementioned electron-hole attractive interactions can lead to exciton formation.

#### 2.2.4.3 The electron-hole hamiltonian

If we restrict the previous description to a one pair subspace namely to the interactions between a single electron and a single hole, electron-electron and hole-hole interactions can be safely dropped since they require two holes or electrons. The one pair hamiltonian then reads :

$$\mathcal{H}_{eh} = \mathcal{H}_e + \mathcal{H}_h + V_{eh}, \quad (2.29)$$

$$= \sum_{\mathbf{k}} E_c(\mathbf{k}) a_{\mathbf{k}}^\dagger a_{\mathbf{k}} + \sum_{\mathbf{k}} E_h(\mathbf{k}) h_{\mathbf{k}}^\dagger h_{\mathbf{k}} - \sum_{\mathbf{q} \neq 0} V_{\mathbf{q}} \sum_{\mathbf{k}_1, \mathbf{k}_2} a_{\mathbf{k}_1 + \mathbf{q}}^\dagger h_{\mathbf{k}_2 - \mathbf{q}}^\dagger h_{\mathbf{k}_2} a_{\mathbf{k}_1}. \quad (2.30)$$

Wannier exciton are the solutions  $|x\rangle$  of the eigenproblem :

$$(\mathcal{H}_e + \mathcal{H}_h + V_{eh}) |i\rangle = E_i |i\rangle \quad (2.31)$$

with eigenvalue  $E_i$ . At this level the hamiltonian is very general and describe two coupled harmonic oscillators. Without going into details, this problem can be solved by following the same procedure as in classical mechanics. The core of the derivation consists in decoupling the two oscillators by introducing new coordinates that are the center of mass and relative coordinates [26; 33]. Since Coulomb interaction conserve momentum, the total momentum of the electron-hole pair  $k_e + k_h$  stays constant and is equal to the exciton center of mass momentum  $\mathbf{Q}$ . Namely, we define :

$$\mathbf{Q} = \mathbf{k}_e + \mathbf{k}_h, \quad (2.32a)$$

$$\mathbf{q} = \gamma_h \mathbf{k}_e - \gamma_e \mathbf{k}_h, \quad (2.32b)$$

where  $\gamma_e = 1 - \gamma_h = m_e / (m_e + m_h)$  is the reduced mass ratio and  $\mathbf{q}$  is the relative motion momentum. We then define the creation operator that creates an exciton  $|x\rangle$  in state  $(\mathbf{Q}_i, \nu_i)$  in terms of electron and hole operators :

$$b_{\mathbf{Q}_i, \nu_i}^\dagger = \sum_{\mathbf{p}} f_{\mathbf{p}}^{\nu_i} a_{\gamma_e \mathbf{Q}_i + \mathbf{p}}^\dagger h_{-\mathbf{p} + \gamma_h \mathbf{Q}_i}^\dagger \quad (2.33)$$

where  $f_{\mathbf{p}}^{\nu_i} = \langle \mathbf{p} | \nu_i \rangle$  is the relative motion wave function. Let us show that the states  $|\nu_i\rangle$  are the eigensolutions of a Hydrogen like problem  $\nu_i$  being then related to the first quantum number of an electron orbital. Injecting  $|x\rangle = b_{\mathbf{Q}_i, \mathbf{q}_i}^\dagger |0\rangle$ ,  $|0\rangle$  being the vacuum state in [Equation 2.31](#) we obtain  $\mathcal{H}_{eh}$  in a diagonal form :

$$\mathcal{H}_{eh} b_{\mathbf{Q}_i, \nu_i}^\dagger |0\rangle = \sum_{\mathbf{p}} \left\{ \left( E_g + \frac{\mathbf{Q}_x^2}{2m_X} + \frac{\mathbf{p}_x^2}{2\mu_X} \right) f_{\mathbf{p}}^{\nu_i} - \sum_{\mathbf{q} \neq 0} V_{\mathbf{q}} f_{\mathbf{p}-\mathbf{q}}^{\nu_i} \right\} a_{\mathbf{p} + \gamma_e \mathbf{Q}_i}^\dagger h_{-\mathbf{p} + \gamma_h \mathbf{Q}_i}^\dagger |0\rangle \quad (2.34)$$

whose eigenstates are  $b_{\mathbf{Q}_i, \nu_i}^\dagger |0\rangle$  with energy  $E_{X_i} = E_g + \frac{\mathbf{Q}_i^2}{2M_X} + E_b^i$  if and only if  $f_{\mathbf{p}}^{\nu_i}$  are solution of the Hydrogen-like problem :

$$\frac{\mathbf{p}^2}{2\mu_X} f_{\mathbf{p}}^{\nu_i} - \sum_{\mathbf{q} \neq 0} V_{\mathbf{q}} f_{\mathbf{p}-\mathbf{q}}^{\nu_i} = E_b^i f_{\mathbf{p}}^{\nu_i} \quad (2.35)$$

where  $\mu_X^{-1} = m_e^{-1} + m_h^{-1}$  is the relative motion mass and  $m_X = m_e + m_h$  the total mass. The exciton then appears as a bound state of the electron-hole pair with a binding energy  $E_b^i$  whose center of mass is delocalized as a plane wave with momentum  $\mathbf{Q}$ . The binding energies  $E_b^i$  follows a Rydberg series  $E_b^i = -\frac{R_X}{i^2}$  where  $R_X$  is the Rydberg constant of the exciton as defined in [subsection 2.2.3](#) In the following section we will see how the excitons interact with light.

## 2.2.5 Exciton-photon interaction in bulk semiconductor:

The creation of an exciton can be mediated by the absorption of a photon by the material. On the other hand the annihilation of a exciton can lead to photon emission. As a starting point, we describe this interaction with an usual electron-photon Hamiltonian in first quantization:

$$\mathcal{H}_{dip} = -e \frac{\mathbf{p}_e \cdot \mathbf{A}}{m_e}, \quad (2.36)$$

with  $\mathbf{p}_e$  the momentum operator of the electron and  $\mathbf{A}$  the potential vector of the electromagnetic field. Before going further let us have a look at what the symmetries of this Hamiltonian imply based on the Noether theorem.

- **Total momentum conservation :** translational invariance of the system implies that the total momentum of the system is conserved. The absorption of a photon with momentum  $\hbar\vec{k}_c$  will create an exciton with the same momentum.
- **Total angular momentum conservation :** rotational invariance of the system implies that the total angular momentum of the system is conserved along the interaction.

The second point raises the question of the possible values that the exciton angular momentum can assume. To answer this question we need to get back to its microscopic constitutive particles : a conduction band electron and a hole in the valence band. In usual semiconductors a conduction band electron has an orbital angular momentum ( $L = 0, L_z = 0$ ) while a valence band electron yields ( $L = 1, L_z = (+1,0, -1)$ ) (see [47]). Since  $J_z = L_z + S_z$  and the electron spin is  $S_z = \pm 1/2$  we obtain for the valence band  $J_z^v = (3/2, 1/2, -1/2, -3/2)$  and for the conduction band  $J_z^c = \pm 1/2$ . If we now move to the electron-hole picture the electron angular momentum remains unchanged  $J_z^e = J_z^c = \pm 1/2$  while the hole angular momentum is the opposite of the valence band electron  $J_z^h = -J_z^v = (3/2, 1/2, -1/2, -3/2)$ . The exciton angular momentum is then  $J_z = J_z^e + J_z^h = (-2, -1, 0, 1, 2)$ . We can thus distinguish **bright** excitons with  $J_z = (-1, 0, 1)$  that couple to light with polarization  $\sigma_-, \pi, \sigma_+$  and **dark** excitons with  $J_z = (-2, 2)$  that do not couple to light. In the latter case the spin of the electron and the hole are aligned :  $J_z = \pm 2$  excitons are made of  $\pm 1/2$  electrons and  $\pm 3/2$  holes. It means it corresponds to a situation in which the valence band electron flipped spin when it got promoted to the electron band. Yet, dark excitons can subsequently not undergo interband transitions that are spin preserving as mentionned in [subsubsection 2.2.4.2](#). On the other hand, bright excitons result from interband transitions since both photon absorption and emission involve an electron changing band. In the framework of polaritons which involves excitons creation through light absorption, one could think that since Coulomb inter and intraband scatterings are spin preserving, dark excitons are of no interest and will not play any role in the system. However, we will see that dark excitons can be created from bright excitons thanks to exchange carrier.

## 2.2.6 Exciton in 2D quantum well

Let us now get closer to the situation encountered in the sample used in the experiment. In such microcavities, excitons are confined in planar quantum wells which are made by stacking layers of semiconductor materials with different band gaps. The confinement in the plane is then ensured by the potential barrier between the layers. In our case a quantum well is made of InGaAs placed in between two layers of GaAs. InGaAs has a smaller band gap than the bulk GaAs because of the p-fraction of InAs doping as shown in [Figure 2.7](#) (b). Both electrons and holes then remain confined in the region where the band gap is the smallest

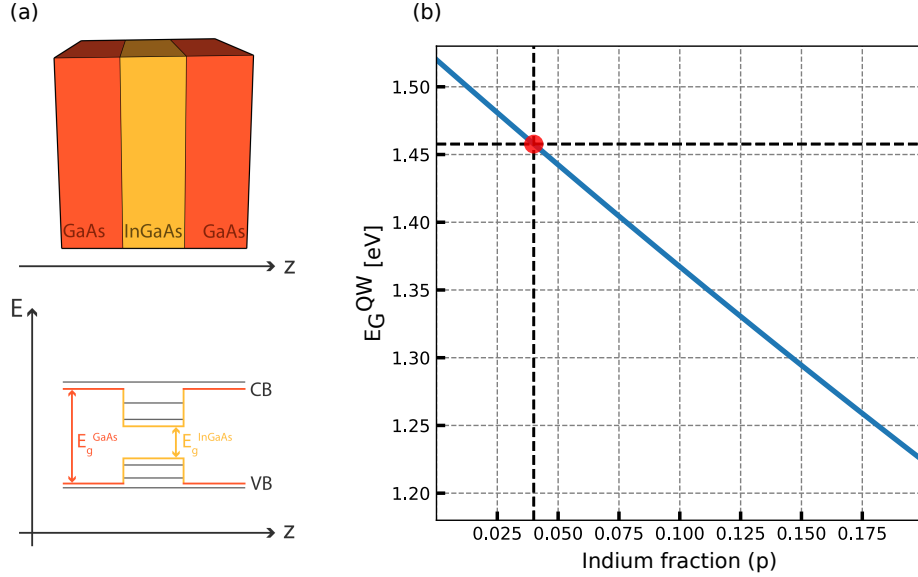


Fig. 2.7 **Schematic representation of a quantum well heterostructure.** a) Representation of a planar quantum well made of InGaAs placed in between two layers of GaAs. The confinement in the plane is ensured by the gap energy difference between the layers. b) Gap energy of the InGaAs quantum well as a function of the doping fraction of Indium. The red dot represent the doping of the sample used in the experiment :  $E_g^{InGaAs} = 1.46\text{eV} < E_g^{GaAs} = 1.52\text{eV}$ .

(see Figure 2.7 (a)). By repeating this "sandwiching" procedure it is possible to create many QW heterostructures as we shall see later.

Assuming the same geometry as in the above figure, the electron-hole hamiltonian taking into account the potential barrier is written in first quantization as :

$$\mathcal{H} = E_g^{QW} + \frac{\mathbf{p}_e^2}{2m_e} + \frac{\mathbf{p}_h^2}{2m_h} - \frac{e^2}{\epsilon_{sc}|r_e - r_h|} + V_e(z_e) + V_h(z_h) \quad (2.37)$$

where  $z$  is the growth axis of the quantum well and  $V_e(z_e)$  and  $V_h(z_h)$  are the potential barriers felt by the electron and the hole respectively,  $r_e$  and  $r_h$  are the electron and hole spatial coordinates. The system is invariant under translation in the  $xy$ -plane meaning the exciton in plane wavevector  $k_{\parallel}$  can take any value of  $k_x, k_y$  while the confinement in the  $z$ -direction quantizes the corresponding component of the wavevector  $k_z$ . This problem is treated by writing the exciton wavefunction  $\Psi(x,y,z)$  as a two components product :

$$\Psi(x,y,z) = \psi(x,y)\phi(z). \quad (2.38)$$

The Schrödinger equation is then solved separately for  $\psi(x,y)$  and  $\phi(z)$ . The confinement in  $z$ -direction is treated as a standard quantum box problem. The electron and hole energies are then quantized as :

$$E_n^{e,h} = \frac{\pi^2 n^2 \hbar^2}{2m_{e,h} L_z^2} \quad (2.39)$$

where  $L_z$  is the width of the quantum well.

To determine the in-plane wavefunction we follow the same procedure than for the exciton eigenproblem in the 3D case. The exciton is again a correlated pair whose center of mass is delocalized as a plane wave with momentum  $\mathbf{Q} = \hbar \mathbf{k}_{\parallel}$ . The corresponding energy is then :

$$E_X^{xy} = E_g^{QW} + \frac{\hbar \mathbf{k}_{\parallel}^2}{2m_X} - \frac{R_X^{QW}}{n^2} \quad (2.40)$$

provided that we define a new Rydberg constant  $R_X^{QW}$  taking into account the confinement in the  $z$ -direction. Remarkably, due to confinement the Bohr radius  $a_X^{QW}$  of the QW exciton is twice smaller than the bulk exciton Bohr radius. This is a direct consequence of the enhancement of the electron-hole wavefunctions overlap which increases the exciton binding energy [81]. The exciton total energy is then :

$$E_X(\mathbf{k}_{\parallel}) = E_g^{QW} + E_n^e + E_n^h + \frac{\hbar \mathbf{k}_{\parallel}^2}{2m_X} - \frac{R_X^{QW}}{n^2}. \quad (2.41)$$

The design of the sample used in the experiment is done such as the  $n=1$  level is sufficiently far from the next level that we can restrict our description to the first 1s exciton state. In the following we will therefore drop the  $n$  index by setting it to one.

**Bosonic nature of excitons.** Since an exciton is made of two fermions its pseudo spin is an integer. However, when reaching regimes of high exciton densities the fermionic nature of their microscopic components can no longer be neglected [25]. The composite nature of excitons can be safely dropped provided that the exciton density per unit area is such as  $n_X(a_X^{QW})^2 \ll 1$ . This condition states that the average distance between excitons is much larger than the exciton Bohr radius. In this regime the excitons can be treated as bosons, namely :

$$[b_{\mathbf{k}}, b_{\mathbf{k}}^\dagger] = 1 + O(n_X(a_X^{QW})^2) \simeq 1 \quad (2.42)$$

**Optical selection rules in planar quantum wells.** In bulk semiconductors, a single exciton mode couples exclusively to a single photon mode. In quasi-two-dimensional systems, due to the breaking of translational invariance in the growth direction  $z$  the momentum conservation during a photon absorption or emission remains valid only for the in-plane component, the  $z$ -component being fixed by the quantum well width. Accordingly, an exciton with wavevector  $\mathbf{k}_X = (\mathbf{k}_{\parallel}^X, k_z^X)$  will interact with a photon with the same in plane wavevector but with any value of  $k_z^Y$ . If we consider a photon of wavevector frequency  $\omega$ , there is thus a density of states for radiative decay given by [81]:

$$\rho_{2D}(\mathbf{k}_{\parallel}, \hbar\omega) \equiv \sum_{k_z} \delta(\hbar\omega - \frac{\hbar c}{n_{QW}} \sqrt{\mathbf{k}_{\parallel}^2 + k_z^2}) \propto \frac{\hbar\omega}{\sqrt{(k_0^2 - \mathbf{k}_{\parallel}^2)}} \Theta(k_0 - |\mathbf{k}_{\parallel}|) \quad (2.43)$$

where  $n_{QW}$  is the refractive index in the QW,  $k_0 = n_{QW}\omega/c$  is the wavevector of the photon in the material and  $\Theta$  is the Heaviside step function. Only states with  $|\mathbf{k}_{\parallel}| < k_0$  can couple to light giving rise again to two class excitons.

- States with  $|\mathbf{k}_{\parallel}^X| < k_0$  that couple to light. These states have a finite radiative lifetime  $1/\gamma_X$  given by the Fermi Golden rule. They lie on the left of the light cone in the  $\mathbf{k}_{\parallel} - \omega$  plane.
- States with  $|\mathbf{k}_{\parallel}^X| > k_0$  that do not decay radiatively. They lie on the right of the photon line in the the  $\mathbf{k}_{\parallel} - \omega$  plane. They are analog to surface modes as they have a vanishing electric field far from the QW. These states join the previously described excitons that could not couple to light because of their spin configuration to form a wider class of "dark" excitons.

This stands in contrast to bulk semiconductors, where a single exciton mode couples exclusively to a single photon mode. Nevertheless, if we also impose energy conservation between the exciton and the photon mode the maximum in-plane wavevector of radiative excitons gets modified and depend on the exciton energy. To see this let us consider an initial state made of an exciton of overall energy  $E_X(\mathbf{k}_{\parallel}^X)$  and zero photon and a final state made of a single photon with energy  $E_{\gamma}(\mathbf{k}_{\parallel}^{\gamma}) = \frac{\hbar c}{n_{QW}} \sqrt{(\mathbf{k}_{\parallel}^{\gamma})^2 + (k_z^{\gamma})^2}$  and no exciton. The energy conservation of this process reads :

$$E_X(\mathbf{k}_{\parallel}^X) = E_{\gamma}(\mathbf{k}_{\parallel}^{\gamma}) \quad (2.44a)$$

$$E_X^{QW} + \frac{(\hbar\mathbf{k}_{\parallel}^X)^2}{2m_X} = \frac{\hbar c}{n_{QW}} \sqrt{(\mathbf{k}_{\parallel}^{\gamma})^2 + (k_z^{\gamma})^2}, \quad (2.44b)$$

in which we set  $E_X^{QW} = E_g^{QW} + E_X^{1s} = E_g^{QW} + E_1^e + E_1^h - R_X^{QW}$ . Injecting the in-plane momentum conservation and imposing  $k_z^{\gamma 2} \geq 0$  for the photon field to be propagative, the above condition restricts the exciton that can couple to light to :

$$|\mathbf{k}_{\parallel}^X| \leq \frac{cm_X}{n_{QW}\hbar} \left( 1 + \sqrt{1 - \frac{4n_{QW}E_X^{QW}}{m_Xc^2}} \right). \quad (2.45)$$

Since  $E_X^{QW}$  can be neglected with respect to the exciton mass energy  $m_Xc^2$  the above condition taken at first order gives :

$$|\mathbf{k}_{\parallel}^X| \leq \frac{n_{QW}E_X^{QW}}{\hbar c}. \quad (2.46)$$

Excitons with higher wavevector are then forbidden to exchange energy with light. However, in our case we have  $E_X^{QW} \simeq 1.485$  meV and  $n_{QW} \simeq 3.5$  leading to  $|\mathbf{k}_{\parallel}^X| \leq 30$  pm which is way beyond the values adressed in the experiment. Now that the exciton formation is well established let us have a look at the mechanisms that can lead them to interact.

### 2.2.7 Exciton-exciton interaction

The scope of this section is to answer the question of what can lead two excitons in states  $(i,j)$  to end up in states  $(f,g)$ . Obviously, direct Coulomb interactions between the excitons constitutive is an unambiguous valid answer. Nonetheless, an interaction giving the same result can also occur in the absence of any Coulomb interactions via pure carrier exchange [25]. Namely, excitons  $i$  and  $j$  can exchange either their electron or hole. The latter is a direct consequences of the Pauli exclusion principle stating that two fermions cannot occupy the same quantum state.

#### 2.2.7.1 Coulomb interaction

As explained in the previous section, holes and electrons undergo Coulomb interaction. As a consequence, the interaction between two excitons  $(e_1,h_1)$  and  $(e_2,h_2)$  consist of  $V_{e_1e_2} + V_{h_1h_2} + V_{e_1h_2} + V_{h_1e_2}$ . However, if the exciton were made of  $(e_1,h_2)$  and  $(e_2,h_1)$  the cross term in the interaction potential would be replaced by  $V_{e_1h_1} + V_{e_2h_2}$ . Because there are different possible ways to form excitons, the total interaction energy depends on the specific pairing choice. This makes it impossible to define a single, clean exciton-exciton interaction potential that works in all cases. Hence, treating them as pure bosons with a simple interaction potential fails because the effective exciton-exciton potential is not unique and depends on the microscopic way the excitons are formed. Nevertheless, it is clear that, through Coulomb interaction, excitons can change states and thus interact in the most general sense. This being said, as experimentalist, we will focus on the most important scattering process that is actually coming from exchange carrier among excitons and that is a unique feature of composite particles [17; 26].

#### 2.2.7.2 Fermionic exchange interaction

Let us consider two excitons  $X_1 = |\mathbf{k}_e, \mathbf{k}_h\rangle$  and  $X_2 = |\mathbf{k}'_e, \mathbf{k}'_h\rangle$ . If their wavefunctions start to overlap, the two electrons might see their quantum state becoming almost equal which is forbidden by the Pauli exclusion principle. To regularize this situation the exciton can exchange their carrier to form  $X'_1 = |\mathbf{k}'_e, \mathbf{k}_h\rangle$  and  $X'_2 = |\mathbf{k}_e, \mathbf{k}'_h\rangle$ . This is might look counterintuitive since exchanging two particles in the same quantum state doesn't seem to solve the problem. However, it is truly the exchange process itself put together with wavefunction symmetries that modifies the quantum state configuration to avoid Pauli principle violation. Take two indistinguishable particles, in state  $\psi_a$  and  $\psi_b$  in a 1D system [23]. Normalization consideration aside, the wavefunction of the system can be written in two ways :  $\psi_{ab} = \psi_a(x_1)\psi_b(x_2) \pm \psi_a(x_1)\psi_b(x_2)$ . Depending on the plus or minus sign, the wavefunction is symmetric or antisymmetric under position exchange. The two different configurations imply different physics. For instance the mean value of the particle interdistance is :

$$\langle (x_1 - x_2)^2 \rangle = \langle x_1^2 \rangle + \langle x_2^2 \rangle \mp 2\langle x_1 x_2 \rangle, \quad (2.47)$$

provided the wavefunctions overlap  $\langle x_1 x_2 \rangle \neq 0$ , the expected value is decreased for bosons and increased for fermions. Although, it seems to act as a force repelling or attracting particles, it is rather a geometrical constraint arising from the Pauli principle and the quantum nature

of the particle at stake. This is precisely what happens during carrier exchange and can, at the end, lead to scattering processes between excitons. Forgetting about this interaction and trying to fully bosonize excitons would then be a mistake [17]. As an example, some features experimentally measured like exciton Stark effect, precisely needs to put exchange carrier on the table to be understood [45; 49; 56]. Furthermore, in a 2D quantum well system this scatterings are dominant at larger scale while direct Coulomb interactions are dominant at scales smaller than the Bohr radius of excitons. Therefore, by considering only radiative modes, i.e. dynamics occurring on scales much larger than the Bohr radius of excitons  $ka_X \ll 1$ , Coulomb interactions can be neglected. Despite all the differences with true bosons above mentionned and the hot debates still going on about polaritons interactions [25; 34] this enable us, to escape from ambiguity and focus on the main exciton-exciton potential that will be relevant in the experiment reported in this work. Written in momentum space this exciton-exciton potential  $V_{XX}(\mathbf{k})$  appears as a four body contact interaction [64]. The corresponding hamiltonian follows as :

$$\mathcal{H}_{XX} = \frac{1}{2} \sum_{\mathbf{k}, \mathbf{k}', \vec{q}} V_{XX}(\vec{q}) \hat{b}_{\mathbf{k}+\vec{q}}^\dagger \hat{b}_{\mathbf{k}'-\vec{q}}^\dagger \hat{b}_{\mathbf{k}} \hat{b}_{\mathbf{k}'} . \quad (2.48)$$

The potential  $V_{XX}(\vec{q})$  is a function of the exchanged momentum  $\vec{q}$ . However, it can be approximated by a constant in the limit of low wavevectors since excitons, being four order of magnitude heavier than microcavities photons, their energy varies only slightly with  $\mathbf{k}$  in the range of the photon wavevector that excite them. Therefore  $V_{XX}$  can be assumed constant. The numerical calculation gives  $A \times V_{XX} \simeq 3 \text{ } \mu\text{eV}\cdot\mu\text{m}^2$  for our InGaAs system.

$$V_{XX} = \frac{e^2 a_X^{QW}}{\epsilon A}, \quad (2.49)$$

with  $A$  the quantization area equal to the quantum well surface. The numerical calculation gives  $A \times V_{XX} \simeq 3 \text{ } \mu\text{eV}\cdot\mu\text{m}^2$  in our GaAs-InGaAs system.

**Dark excitons creation through carrier exchange.** As discussed in subsection 2.2.5 electron-hole pairs with a total spin of  $\pm 1$  are coupled to  $\sigma \pm$  photons, meaning that photon absorption leads to the creation of only bright exciton states  $\pm 1$ . However, dark exciton states can also be present in the system, arising from fermion exchange processes. Namely, fermion exchange between two bright excitons  $(+1, 1)$  made of  $(\mp 1/2)$  electrons and  $(\pm 3/2)$  holes leads to dark excitons  $(+2, -2)$ . Hence, even though photon absorption only creates bright excitons, excitons not coupled to light are likely to be indirectly excited and participate to the overall interactions of the system. This being said, we will in the following only tackle this problem from a phenomenological point of view and consider the exciton-exciton interaction as a unique potential  $V_{XX}$  whereas dark excitons will be accounted for through a reservoir.

## 2.3 Excitons-polaritons

So far we described separately microcavity photons and excitons both in bulk and 2D systems. Microcavity polaritons arise from the strong coupling between these two components. Remarkably, the half light half matter nature of polaritons allows them to inherit the best

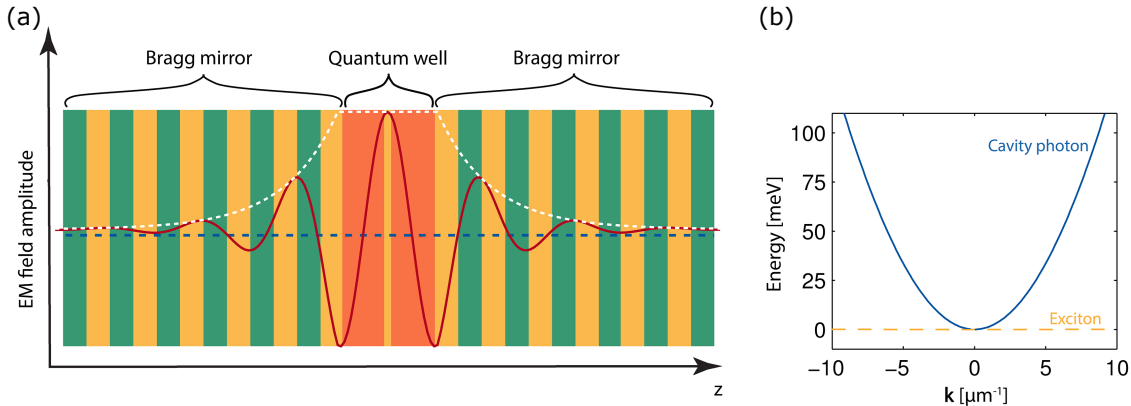


Fig. 2.8 **Schematic representation of a quantum well embedded in an optical microcavity.** The quantum wells are placed at the antinode of the electric field of the cavity. The cavity is designed to have a longitudinal mode that matches the exciton energy. (b) Dispersions relation of the exciton (yellow) and photon (blue) modes in a typical microcavity. Since the exciton effective mass  $m_X$  is  $10^4$  times larger than the photon mass the exciton dispersion looks flat with respect to the photon. The cavity has been designed so the  $\mathbf{k}_{\parallel} = 0$  energies are matched.

of both worlds namely the low photon effective mass and the strong excitons non linear interactions. In this section we will describe the formation of polaritons by describing how placing a 2D semiconducting quantum well in an optical microcavity to enhance the light-matter interactions. To start with let us have a look again at the Fermi Golden rule giving the spontaneous emission rate from a level  $|i\rangle$  to a level  $|f\rangle$  in a continuum of states per unit time in the presence of a weak coupling  $W$  :

$$\Gamma_{i \rightarrow f} = \frac{2\pi}{\hbar} \left| \langle f | W | i \rangle \right|^2 \rho(E_f) \delta(E_f - E_i - \hbar\omega), \quad (2.50)$$

where  $\rho(E_f)$  is the density of states at energy  $E_f$ ,  $\delta(E_f - E_i - \hbar\omega)$  ensures energy conservation between the initial and final states, and the matrix element  $|\langle f | W | i \rangle|^2$  is the typical frequency at which this emission occur, also denoted  $\Omega_R$  and called vacuum Rabi frequency. In order to achieve strong coupling between excitons and photons the challenge is to enhance the probability than an exciton recombine in a given photonic state ( $\hbar\mathbf{k}_{\parallel}, \hbar\omega$ ). Solving this problem reduces to changing the density of state  $\rho$  in order to suppress spontaneous emission in all unwanted modes. As usually done in cavity quantum electrodynamics, this problem is tackled by embedding the quantum well in an high finesse optical microcavity as shown in Figure 2.8 (a).

The role of the cavity is to create a set of resonant modes that will act as a "filter" for the exciton recombination. The quantization axis of the optical microcavity is chosen to be the same as the quantum well and the light-matter interactions are optimized by placing the quantum well at the antinode of the electric field. The cavity length is chosen so that a single photonic mode can be equal to the excitonic energy. This matching can be seen by looking simultaneously at the exciton and photon dispersion relation as a function of

the in plane wavevector and check that they cross each other at a finite wavevector. For instance in the case of [Figure 2.8](#) (b) the cavity has been designed so that the exciton and photon energies are equal at  $\mathbf{k}_{\parallel} = 0$ . Several quantum wells can then be stacked in the cavity to enhance the interactions provided that they are once again located at antinodes of the photonic field. In the experiment we use a  $3\lambda/2$  made of two planar DBR in which are placed three *InGaAs/GaAs* quantum wells. An extended description of the fabrication procedure to built such a sample can be found in [53]. However, the main features mentionned so far can be summarized in a few points.

### Summary

- The cavity is made by embedding semiconducting quantum wells in between two distributed bragg reflectors forming a high finesse optical microcavity.
- The length of the cavity and of the wells are chosen in a way that a single longitudinal mode of the electric field is resonant with the 1s state of the exciton.
- The excitons are confined in the  $xy$ -plane in each quantum well and the exciton density can be tuned by changing the number of quantum wells.
- Momentum conservation still holds in the plane of the cavity. Namely, an incoming photon with wavevector  $\mathbf{k}_{\parallel}$  will create an exciton with the same in-plane wavevector.

It appears then that the relevant motion of the interacting particles at stake lies in the  $xy$ -plane since the wavevectors in the  $z$ -direction are fixed by the cavity parameters. Consequently, for sake of clarity, we will only refer to the in-plane wavevector in the following by dropping the  $\parallel$  label and just write  $\mathbf{k}$ . Let us now see the different coupling regimes that can be reached in such samples.

**Coupling regimes.** At first approximation the problem can be thought as two bath of particles exchanging quanta at a rate  $\Omega_R$ . Depending on the efficiency of this exchange compared to the damping rate of each bath  $\gamma_X$  and  $\gamma_\gamma$  one has to revisit the way to describe the system. Indeed, when  $\Omega_R \ll \gamma_X, \gamma_\gamma$  the system is said to be in the weak coupling regime. It can be understood in terms of lifetimes : both excitons and photons lifetimes are too short compared to the characteristic time of the exchange  $1/\Omega_R$ . The energy leaks out of the system before it can change from one state to the other. The exciton-photon interaction is in this case irreversible. If  $\Omega_R \gg \gamma_X, \gamma_\gamma$  the system is said to be in the strong coupling regime. In a given photonic (or excitonic) lifetime  $1/\gamma_{cav}$ , the energy have had enough time to coherently go back and forth between exciton and photon states plenty of times. Translating this in quantum mechanics language means that the system is in a superposition of exciton and photon states. Polariton then rise in this regime as a supersposition of microcavity photons and excitons exchanging energy at the so called Rabi frequency  $\Omega_R$ .

**Linear Hamiltonian.** Let us write formally the coupling between excitons and photons described above. First we tackle the weak optical excitation scheme in which non linear

interactions among excitons can be neglected. The corresponding linear Hamiltonian is given by :

$$\mathcal{H}_{lin} = \sum_{\mathbf{k}} \left[ E_X(\mathbf{k}) b_{\mathbf{k}}^\dagger b_{\mathbf{k}} + E_\gamma(\mathbf{k}) a_{\mathbf{k}}^\dagger a_{\mathbf{k}} + \frac{\hbar\Omega_R}{2} a_{\mathbf{k}}^\dagger b_{\mathbf{k}} + a_{\mathbf{k}} b_{\mathbf{k}}^\dagger \right] \quad (2.51)$$

where  $b_{\mathbf{k}}^\dagger$  and  $a_{\mathbf{k}}^\dagger$  are the creation operators of the exciton and photon modes respectively. The first two terms account for the energies of the excitons and the photons while the terms  $b_{\mathbf{k}}^\dagger a_{\mathbf{k}}$  and  $a_{\mathbf{k}}^\dagger b_{\mathbf{k}}$  account for the linear exciton-photon coupling yielding an interaction energy  $\hbar\Omega_R$ . Obviously this hamiltonian is not diagonal in the excitons-photons operators basis. Excitons-polaritons then arise as the two eigenstates of  $\mathcal{H}_{lin}$  : the upper and the lower polaritons whose creation and annihilation operators are  $(u_{\mathbf{k}}^\dagger, u_{\mathbf{k}})$  and  $(p_{\mathbf{k}}^\dagger, p_{\mathbf{k}})$  respectively. These operators can be found by an unitary transformation on the exciton-photon basis that was extensively used by Hopfield [42] :

$$\begin{bmatrix} p_{\mathbf{k}} \\ u_{\mathbf{k}} \end{bmatrix} = \begin{bmatrix} C_{\mathbf{k}} & X_{\mathbf{k}} \\ X_{\mathbf{k}} & -C_{\mathbf{k}} \end{bmatrix} \begin{bmatrix} \hat{a}_k \\ \hat{b}_k \end{bmatrix}, \quad (2.52)$$

where  $C_{\mathbf{k}}$  and  $X_{\mathbf{k}}$  are the Hopfield coefficients for photons and excitons respectively. The unitarity of the transformation is reflected by the relation  $C_{\mathbf{k}}^2 + X_{\mathbf{k}}^2 = 1$ . As a consequence, they can be interpreted as the fractions of excitons and photons in both modes. More precisely they depend on the excitons/photons energies and the Rabi frequency as :

$$C_{\mathbf{k}}^2 = \frac{\sqrt{\Delta E_{X-\gamma}^2 + \hbar^2\Omega_R^2} - \Delta E_{X-\gamma}}{2\sqrt{\Delta E_{X-\gamma}^2 + \hbar^2\Omega_R^2}}, \quad (2.53a)$$

$$X_{\mathbf{k}}^2 = \frac{\sqrt{\Delta E_{X-\gamma}^2 + \hbar^2\Omega_R^2} + \Delta E_{X-\gamma}}{2\sqrt{\Delta E_{X-\gamma}^2 + \hbar^2\Omega_R^2}}. \quad (2.53b)$$

where  $\Delta E_{X-\gamma}(\mathbf{k}) = E_\gamma(\mathbf{k}) - E_X(\mathbf{k})$  is the detuning between the exciton and the photon energies at  $\mathbf{k}$ . In this basis the linear hamiltonian can be written in its diagonal form.

$$\mathcal{H}_{lin} = \sum_{\mathbf{k}} \left[ E_{LP}(\mathbf{k}) p_{\mathbf{k}}^\dagger p_{\mathbf{k}} + E_{UP}(\mathbf{k}) u_{\mathbf{k}}^\dagger u_{\mathbf{k}} \right] \quad (2.54)$$

where the eigenvalues  $E_{LP}(\mathbf{k})$  and  $E_{UP}(\mathbf{k})$  are the lower and upper polariton dispersion relation. Their analytical expressions are given by :

$$E_{LP}(\mathbf{k}) = \frac{E_X(\mathbf{k}) + E_\gamma(\mathbf{k})}{2} - \frac{\sqrt{\Delta E_{X-\gamma}^2 + \hbar^2\Omega_R^2}}{2}, \quad (2.55)$$

$$E_{UP}(\mathbf{k}) = \frac{E_X(\mathbf{k}) + E_\gamma(\mathbf{k})}{2} + \frac{\sqrt{\Delta E_{X-\gamma}^2 + \hbar^2\Omega_R^2}}{2}. \quad (2.56)$$

**Tuning the exciton-photon fraction.** As it can be seen the weight of photon and exciton in a given polaritonic state can be then tuned by changing the exciton-photon detuning  $\Delta E_{X-\gamma}$ . Particularly, when  $\Delta E_{X-\gamma} = 0$  we have  $C_{\mathbf{k}}^2 = X_{\mathbf{k}}^2 = \frac{1}{2}$  meaning that the exciton and the photon are equally mixed in the polariton states. In practice, there are two ways to change the exciton-photon detuning. The first tuning knob, which is the most obvious, is the wavevector  $\mathbf{k}$ . Since the exciton dispersion is flat with respect to the photon it reduces to move on the photon dispersion curve. Still, exciting a polariton state with a given set of Hopfield coefficients will fix the wavevector and, in some case might not be even possible. For instance if the photonic dispersion is above the exciton energy at all wavevector as in [Figure 2.9 b<sub>1</sub>](#)), it is impossible to reach the purely hybrid configuration  $\Delta E_{X-\gamma} = 0$ . Creating an arbitrary polaritonic state thus require a second knob to tune  $\Delta E_{X-\gamma}$ . It is generally done by introducing a small wedge between the two DBR that will change the photon resonance condition as shown in [Figure 2.9 a\)](#) : a change in the cavity length  $L$  will shift vertically the photon dispersion. This can be done with the usual Molecular Beam Epitaxy method used to grow the sample.

The principle is to heat the target material to its sublimation temperature to produce a molecular beam that is then deposited on a substrate to form thin atomic layers that stack on top of each other. In practice, the substrate is located on a spinning disk to avoid the molecule to clusterise. If the spinning disk is stopped, molecules will accumulate in the center of the beam and form a "hill". By taking advantage of this features it is possible to change progressively the thickness of the layer and thus the cavity resonance condition. A given sample then has a wide range of exciton-photon detuning that can be addressed in the lab by changing the working point on the cavity.

In general, when the exciton-photon detuning is too positive the UP branch recovers the excitons curve while the LP branch recovers the photons curve. Conversely, when the exciton-photon detuning is negative the UP branch recovers the photons curve while the LP branch recovers the excitons curve. This is not very surprising since a large detuning means that the exciton and the photon are far from each other making the coupling less efficient. At the zero detuning point  $\Delta E_{X-\gamma} = 0$  the coupling is maximum and the splitting between the lower and upper polariton branch is equal to the Rabi energy  $\hbar\Omega_R$ . Besides, the anticrossing between the two branches is a direct consequence of the strong coupling regime and can be found even in classical systems like coupled springs or pendulums.

The suitable range of detuning for which the polariton concept is still relevant and that we can address in the experiment is shown in [Figure 2.10](#)

**Relaxation.** The strong coupling condition  $\Omega_R \gg \gamma_X, \gamma_{cav}$  can also be seen by directly taking into account the finite lifetime of excitons and photons, introducing complex energies  $E_\gamma - i\gamma_{cav}$  and  $E_X - i\gamma_X$  as in [24]. Doing so, the polariton dispersions relation become :

$$E_{UP,LP}(\mathbf{k}) = \frac{E_\gamma(\mathbf{k}) + E_X(\mathbf{k})}{2} - i\hbar \frac{\gamma_{cav} + \gamma_X}{2} \pm \frac{1}{2} \sqrt{[\hbar\Omega_R]^2 + [\Delta E_{X-\gamma} - i\hbar(\gamma_{cav} - \gamma_X)]^2}. \quad (2.57)$$

At zero detuning we obtain :

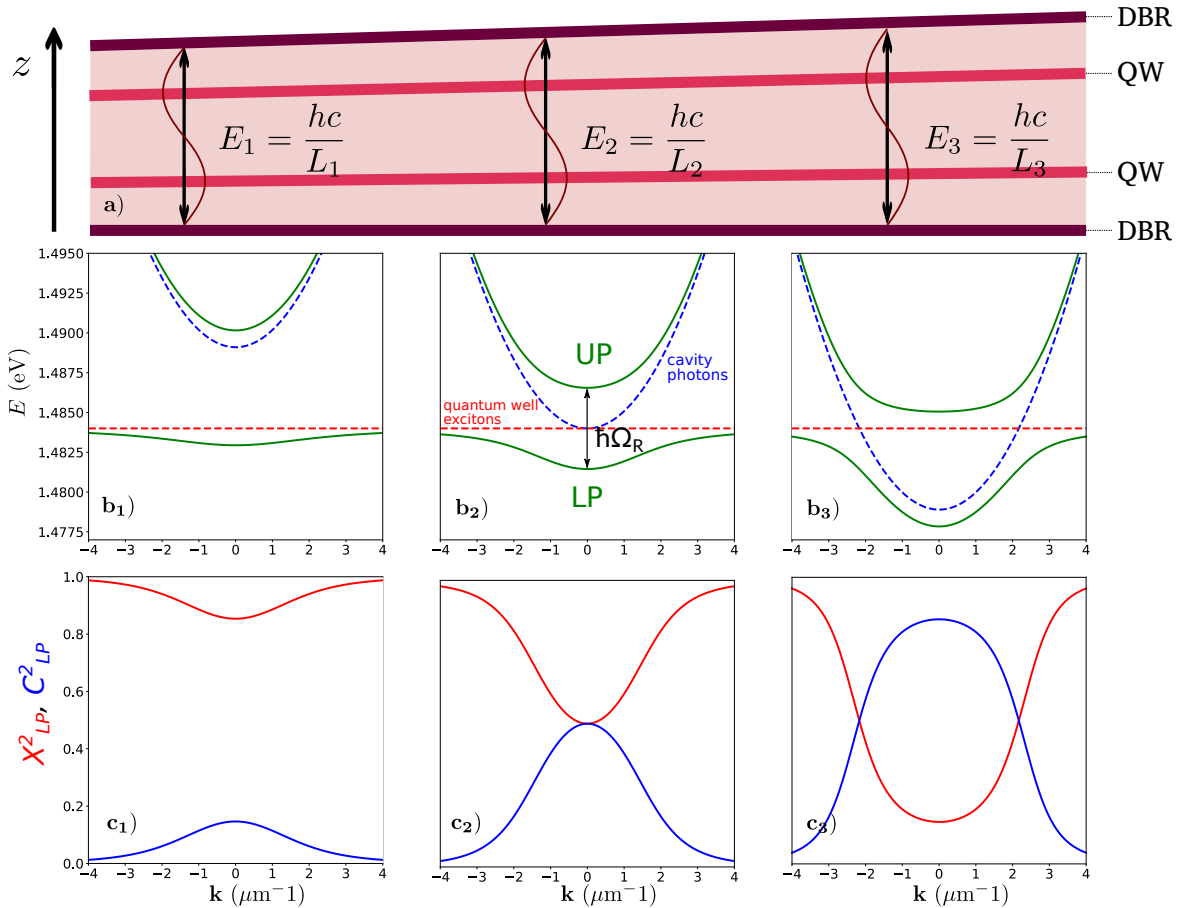


Fig. 2.9 **Scheme of an optical microcavity with a wedge, polaritons dispersion relations and Hopfield coefficients.** a) Side view of a double quantum well semiconducting microcavity. From left to right the photon resonant energy decreases as the length of the cavity increases. The exciton energy remains constant since it is fixed by the width of the quantum well. We take as example three point in the sample  $i = 1,2,3$  with increasing cavity length. At each point the wavy lines represent the optical standing wave stemming from the resonance conditions  $\lambda_i = L_i$ . The corresponding energies  $E_i$  illustrate the three different regimes namely :  $\Delta E_{X-\gamma}^{(1)}(\mathbf{k} = 0) > 0$ ,  $\Delta E_{X-\gamma}^{(2)}(\mathbf{k} = 0) = 0$ ,  $\Delta E_{X-\gamma}^{(3)}(\mathbf{k} = 0) < 0$ . Each  $E_i$  corresponds to the subplots b<sub>i</sub>) and c<sub>i</sub>). b<sub>1</sub>), b<sub>2</sub>), b<sub>3</sub>) Dispersion relations of the lower (LP) and upper polaritons (UP) in a typical microcavity for each value of  $\Delta E_{X-\gamma}^{(i)}$ . The exciton energy is the yellow dashed line while the photon energy is the blue dashed line. Depending on the location on the sample  $i = 1,2,3$  the photon dispersion curve gets shifted vertically yielding different values of the Hopfield coefficient. c<sub>1</sub>), c<sub>2</sub>), c<sub>3</sub>) Corresponding Hopfield coefficients as a function of the in-plane wavevector for the three different regimes. Adapted from [21].

$$E_{UP,LP}(\mathbf{k}) = E_X(\mathbf{k}) - i\hbar \frac{\gamma_{cav} + \gamma_X}{2} \pm \frac{1}{2} \sqrt{(\hbar\Omega_R)^2 + (\hbar\gamma_{cav} - \hbar\gamma_X)^2}. \quad (2.58)$$

The existence of two distinct energies for the two polaritons modes thus depends on the relative values of  $\Omega_R$  and  $|\gamma_{cav} - \gamma_X|$ . If the coupling constant  $\Omega_R$  is smaller than the difference between the relaxation constants, the two eigenenergies share the same real part, and the degeneracy between the exciton and the cavity mode remains unbroken. Being a supersposition of excitons and photons the polaritons also have a relaxation rate that can then be inferred from the imaginary part of their energy :

$$\gamma_{UP}(\mathbf{k}) = X_{\mathbf{k}}^2 \gamma_{cav} + C_{\mathbf{k}}^2 \gamma_X, \quad (2.59a)$$

$$\gamma_{LP}(\mathbf{k}) = X_{\mathbf{k}}^2 \gamma_X + C_{\mathbf{k}}^2 \gamma_{cav}. \quad (2.59b)$$

Once again, the Hopfield coefficients have a strong impact on the polariton relaxation rate. In the range of detuning available in our sample we measure relaxation rates of the order of  $70 \mu\text{eV}$  which correspond to a lifetime  $\tau \sim 12 \text{ ps}$ . This value is beyond the time response of a wide class of instruments and require generally both pulsed lasers and ultrafast detection devices to be resolved as in [77]. The present work is not dedicated to time resolved experiments as we rather use a continuous wave laser to constantly compensate for the losses and reach a steady state from which we extract observable quantities. This system is then highly out of equilibrium. Although this feature seems limiting at first sight it can actually turn into an asset whenever one wants to study dynamical instabilities. Indeed, in conservative systems, instabilities are difficult to study precisely because they tend to make the system unstable. In the case of polaritons, the losses can reduce their effect while keeping their signature visible in the steady state of the system [19].

**Effective mass.** By analogy with what was done for the photons in section 2.1 it is possible to attribute an effective mass to the polaritons by taking the second derivative at the bottom of the polariton dispersion relation, namely :

$$\frac{1}{m_{UP}} = \frac{X_0^2}{m_X} + \frac{C_0^2}{m_\gamma}, \quad (2.60a)$$

$$\frac{1}{m_{LP}} = \frac{X_0^2}{m_\gamma} + \frac{C_0^2}{m_X}. \quad (2.60b)$$

Reminding that  $C_0^2 + X_0^2 = 1$  and that  $\frac{m_\gamma}{m_X} \ll 1$ . It can effectively be cast in the following form :

$$m_{UP} \approx \frac{m_\gamma}{C_0^2} \quad (2.61a)$$

$$m_{LP} \approx \frac{m_X}{X_0^2} \quad (2.61b)$$

It can be seen that polaritons inherit the low effective mass of the photons making their transport easier than for excitons and their Bose-Einstein condensation possible to occur at higher temperatures. This is particularly interesting for the realisation of polaritonic circuits in the framework of quantum information processing [52]. The excitonic part of the polariton also brings its own features to the table. In particular, the strong exciton-exciton non linear interactions that will turn light into a fluid of interacting particles. This is the subject of the next section.

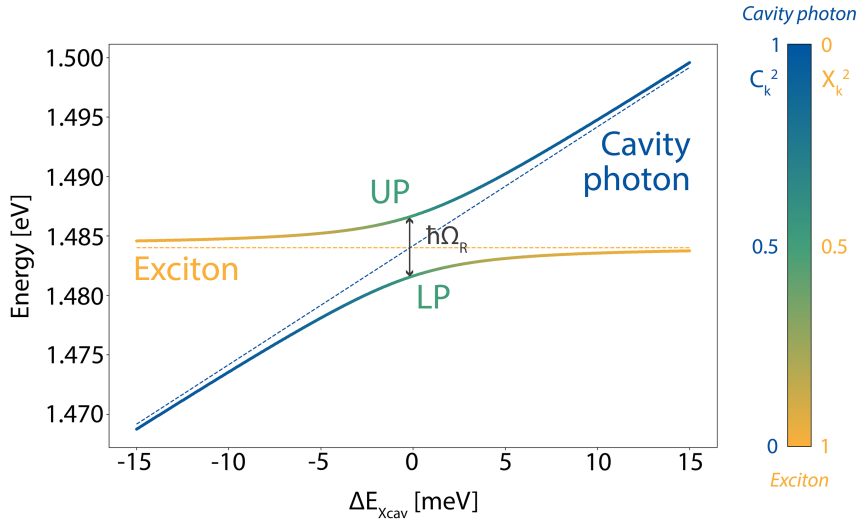


Fig. 2.10 **Anticrossing in the strong coupling regime.** Energies of the upper (UP) and lower (LP) polariton branches at  $\mathbf{k} = 0 \mu\text{m}^{-1}$ , with respect to the exciton-photon detuning at zero wavevector  $\Delta E_{X-\gamma}(\mathbf{k} = 0)$  and the color-coded squared modulus of the Hopfield coefficient  $X^2$  (exciton) and  $C^2$  (photon). The yellow and blue dashed lines are respectively the bare exciton and photon energies. At  $\Delta E_{X-\gamma} = 0$  meV, the coupling is the better yielding an energy splitting equal to the Rabi energy  $\hbar\Omega_R$ . Adapted from [53]

### 2.3.1 Polariton interactions

It is now clear that shinning a strong laser with the right frequency on a semiconductor microcavity will create many polaritons. Since they have an excitonic part, they may undergo many body effects that were not taken into account in the linear hamiltonian model derived above. More precisely, polaritons experience all the exciton-exciton interactions described in subsection 2.2.7 as well as additional features coming from their coupling with light. Remarkably, in high density regime the Pauli principle has to apply again on the electrons and the holes leading to carrier exchanges. In the absence of light these fermionic exchanges are actually the dominant scatterings processes while the direct Coulomb scattering is negligible as was explained in subsection 2.2.7. We remind the expression of the resulting exchange hamiltonian :

$$\mathcal{H}_{XX} = \frac{1}{2} \sum_{\mathbf{k}, \mathbf{k}', \mathbf{q}} V_{XX} \left[ p_{\mathbf{k}+\mathbf{q}}^\dagger p_{\mathbf{k}'-\mathbf{q}}^\dagger p_{\mathbf{k}} p_{\mathbf{k}'} \right] \quad (2.62)$$

When the excitons are strongly coupled to cavity photon these carrier exchanges give rise to an additional saturation potential describing what is called a "photon-assisted exchange scattering" in [25].:

$$\mathcal{H}_{sat} = \frac{1}{2} \sum_{\mathbf{k}, \mathbf{k}', \mathbf{q}} V_{sat} [a_{\mathbf{k}+\mathbf{q}}^\dagger b_{\mathbf{k}'-\mathbf{q}}^\dagger b_{\mathbf{k}} b_{\mathbf{k}'} + h.c.] , \quad (2.63)$$

where  $V_{sat}$  is the saturation potential that can be computed by applying an Usui transformation on the quantum wells [76]. This transformation aim is to transform the fermionic Hamiltonian above into an Hamiltonian expressed in the basis of exciton states. Following what is done in [65]

$$V_{sat} = \frac{\hbar\Omega_R}{An_{sat}}, \quad (2.64)$$

in which  $n_{sat}$  is the saturation density computed from the 2D exciton Bohr radius as  $n_{sat} = 1/a_X^{QW}$  and  $A$  the macroscopic quantization area. To end up with a description of interactions in the polariton basis we invert the unitary transformation in [Equation 2.52](#) :

$$\hat{b}_k = X_k p_{\mathbf{k}} - C_k u_{\mathbf{k}}, \quad (2.65a)$$

$$\hat{a}_k = C_k p_{\mathbf{k}} + X_k u_{\mathbf{k}}, \quad (2.65b)$$

and inject these expressions into  $\mathcal{H}_{XX}$  and  $\mathcal{H}_{sat}$ . We end up with a single polariton-polariton potential that is a combination of Hopfield coefficients,  $V_{sat}$  and  $V_{XX}$ . For the lower polaritons, which are excited in the experiment and to which we will restrict in the following, we obtain an effective polariton-polariton potential  $V_{pp}$  as :

$$V_{pp} = |X_{\mathbf{k}}|^4 V_{XX} + 2|X_{\mathbf{k}}|^2 X_{\mathbf{k}} C_{\mathbf{k}} V_{sat}. \quad (2.66)$$

Once again it depends on the exciton-photon fraction through the Hopfield coefficients, and, in the purely hybrid situation  $\Delta E_{X-\gamma}=0$ , the quantity  $A \times V_{pp}$  is theoretically expected to be of the order of  $1 \text{ } \mu\text{eV } \mu\text{m}^{-2}$  [13] while no precise experimental value has been reported so far.

**Non linear LP hamiltonian.** Finally, taking into account the polariton-polariton interactions abovementioned the linear hamiltonian for Lower Polaritons can be completed as follows :

$$\mathcal{H}_{LP} = \sum_{\mathbf{k}} \hbar\omega_{LP}(\mathbf{k}) p_{\mathbf{k}}^\dagger p_{\mathbf{k}} + \frac{1}{2} \sum_{\mathbf{k}, \mathbf{k}', \mathbf{q}} V_{pp} [p_{\mathbf{k}+\mathbf{q}}^\dagger p_{\mathbf{k}'-\mathbf{q}}^\dagger p_{\mathbf{k}} p_{\mathbf{k}'}]. \quad (2.67)$$

**Energy renormalization.** As it can already be seen in the LP non linear hamiltonian, the bare polariton energies are no longer eigenvalues of the system in the presence of interactions. To give a simple picture of this feature let us restrict the description to two polariton modes  $p_{\mathbf{k}_1}$  and  $p_{\mathbf{k}_2}$ . If the system is prepared in such a way as to populate one of the two modes,  $\mathbf{k}_2$ , this macroscopic reservoir of polaritons acts as an external potential for the polaritons in the weakly populated mode  $\mathbf{k}_1$ . Consequently, the energy of the polaritons in mode  $\mathbf{k}_1$  increases by an amount corresponding to the potential created by the polaritons in mode  $\mathbf{k}_2$ . This is the phenomenon of energy renormalization.

To be more quantitative, we can write the Hamiltonian of the system while restricting it to these two modes. In this case,  $\mathcal{H}_{int}$  is the sum of  $p_{\mathbf{k}_1}^\dagger p_{\mathbf{k}_2}^\dagger p_{\mathbf{k}_1} p_{\mathbf{k}_2}$  and  $p_{\mathbf{k}_2}^\dagger p_{\mathbf{k}_1}^\dagger p_{\mathbf{k}_2} p_{\mathbf{k}_1}$ . Since  $p_{\mathbf{k}_2}$  and  $p_{\mathbf{k}_1}$  are eigenstates of the system, they commute, meaning that the two previous terms account for the same scattering. The time evolution of  $p_{\mathbf{k}_1}$  can then be described by the Heisenberg equation :

$$i\hbar \frac{d}{dt} p_{\mathbf{k}_1} = [p_{\mathbf{k}_1}, \mathcal{H}_{LP}] = [p_{\mathbf{k}_1}, \mathcal{H}_{lin}] + [p_{\mathbf{k}_1}, \mathcal{H}_{int}]. \quad (2.68)$$

the interacting term being :

$$[p_{\mathbf{k}_1}, \mathcal{H}_{int}] = \frac{V_{pp}}{2} p_{\mathbf{k}_2}^\dagger p_{\mathbf{k}_1} = \frac{\hbar g_{LP}}{A} \hat{N}_2 p_{\mathbf{k}_1}. \quad (2.69)$$

$\hat{N}_2$  is the number operator in mode  $\mathbf{k}_2$  and  $\hbar g_{LP} = V_{pp}A/2$  is the polariton-polariton interaction constant. Since, the mode  $\mathbf{k}_2$  is macroscopically populated, we can replace  $\hat{N}_2$  by its expectation value  $\langle \hat{N}_2 \rangle$ , which gives the polariton density in mode  $\mathbf{k}_2$ ,  $n_2 = \langle \hat{N}_2 \rangle / A$ . As a result, the master equation for the  $\mathbf{k}_1$  gets renormalized by interactions with the  $\mathbf{k}_2$  mode as :

$$i\hbar \frac{d}{dt} p_{\mathbf{k}_1} = [\hbar\omega_{LP}(\mathbf{k}_1) + \hbar g_{LP}n_2] p_{\mathbf{k}_1}. \quad (2.70)$$

where  $\hbar\omega_{LP}(\mathbf{k}_1) = E_{LP}(\mathbf{k}_1)$  is the bare energy of the polariton with wavevector  $\mathbf{k}_1$ . Although this is a simplified model with only two modes, the equation demonstrates how interactions between polaritons can lead to the renormalization of their energies. More generally, this phenomenon takes place between all modes in the system, including self-interactions of individual modes. The latter closely resembles the optical Kerr effect, where a field modifies the refractive index of the medium through which it propagates.

## 2.4 Polariton dynamics

To summarize, microcavity exciton-polaritons are hybrid light-matter quasiparticles that combine characteristics of both components. Their photonic part endows them with an exceptionally low effective mass and allows us to manipulate them using light. Conversely, their excitonic part provides them with the nonlinearities associated with electrons in semiconductors. Although the resulting interactions are various and stem from different origins, they can, to a first approximation, be described by a single four-body contact potential,  $V_{pp}$ .

In this framework, polaritons can be viewed as weakly interacting bosons, distinguished by their inherent losses, making their behavior an out-of-equilibrium problem. In the following, we will explore their dynamics when one or a few modes are macroscopically populated, revealing remarkable phenomena typically associated with many-body bosonic systems, such as superfluidity and Bose-Einstein condensation (BEC). However, whenever necessary, we will return to their composite fermionic nature to account for unique features that may not be captured by the mean field approximation.

### 2.4.1 Mean field approximation

In order to describe the dynamics of the polariton fluid, it is convenient to use the mean field approximation as it is usually done for quantum fluids [60]. This assumption is valid when the number of particles is large  $N \sim N + 1$  and when the major part of them occupy the same quantum state. Obviously, the latter can happen only in bosonic systems since fermions obey the Pauli exclusion principle. In atomic systems, the macroscopic occupation occurs in the ground state of the system, and, provided that the temperature is low enough, happens spontaneously due to bosonic stimulation. In the case of polaritons, the situation is dramatically different since the system is out of equilibrium and the particles have to be continuously pumped to compensate for the losses. The mean field of the system is then rather a steady state than a ground state at equilibrium. This being said, it is still possible to define a macroscopic occupation of a given mode in the system. Whenever this happens, the theoretical procedure reduces to replacing the field operator  $\hat{\psi}(\mathbf{r},t) = \sum_k \varphi_{\mathbf{k}} \hat{p}_{\mathbf{k}}$  that annihilates particles at  $(\mathbf{r},t)$ , by its expectation value  $\langle \hat{\psi}(\mathbf{r},t) \rangle$ . This idea is supported by the fact that, in such situations, adding or removing a particle from the system does not change its state. The system is then described by a single classical wavefunction whose square modulus gives the density of particles in the system  $|\psi(\mathbf{r},t)|^2 = n(\mathbf{r},t)$  and with a well defined phase accounting for long range coherence. However, it doesn't mean that the system has become fully classical. Indeed, its quantum nature is present in the fluctuations around the mean field and often manifest itself through collective behavior. Accounting for these fluctuations is done by adding a small perturbation to the mean field :

$$\hat{\psi}(\mathbf{r},t) = \langle \psi(\mathbf{r},t) \rangle + \delta\psi(\mathbf{r},t). \quad (2.71)$$

For now let us focus on the description of the mean field dynamics and justify more quantitatively the relevance of describing a polariton fluid with a single wavefunction.

**One wavefunction to rule them all.** A pioneering result in the early stages of quantum mechanics is the so called wave-particle duality proposed by Louis de Broglie [27] in 1924. It states that particles can exhibit both wave and particle properties. More precisely, to any particle with momentum  $\mathbf{p}$  can be associated a wavelength  $\lambda = h/|\mathbf{p}|$ . This wavelength is the characteristic of the wave associated with the particle and is called the de Broglie wavelength. As a result, if two particles are separated by a distance smaller than their de Broglie wavelength their corresponding wavefunction will overlap and possibly give rise to wave like effect as interferences. In fact, it can happen with a single particle that is in superposition of two paths the same way as two coherent laser beams superimposed on a screen can interfere. This idea was later confirmed by the famous double slit experiment in which single electrons were sent through a double slit and displayed an interference pattern as the experiment was repeated many times.

If one applies this idea to a large number of particles in the same quantum states whose inter-particle distance is smaller than  $\lambda$  it is no longer possible to distinguish them and they can be described by a single wavefunction. At thermal equilibrium the momentum of a particle follows a Maxwell Boltzmann distribution and the de Broglie wavelength is of the

order of the thermal de Broglie wavelength :

$$\lambda_T = \frac{h}{\sqrt{2\pi m k_B T}}, \quad (2.72)$$

where  $T$  is the temperature  $m$  the particle mass and  $k_B$  the Boltzmann constant. From this simple formula, one can see why reaching long range coherence in a system often requires trapping and cooling procedures. In the case of polaritons, a typical polariton-polariton inter-distance is about  $0.1 \mu\text{m}$  while the small polaritons effective mass and the cryogenic temperature ( $\sim 4K$ ) yields a thermal de Broglie wavelength of the order of  $1 \mu\text{m}$  which validates the mean field approximation. Now that we have a single order parameter to describe the system, let us see how it evolves in time.

#### 2.4.2 Driven dissipative Gross-Pitaevskii Equation.

In the context of Bose gas this problem was first tackled by Gross [37] and Pitaevskii [59] to describe the structure of quantized vortices in liquid Helium. The resulting equation is known as the *Gross-Pitaevskii equation* or non-linear Schrödinger equation :

$$i\hbar \frac{\partial}{\partial t} \psi(\mathbf{r}, t) = \left( -\frac{\hbar^2}{2m} \nabla_{\mathbf{r}}^2 + V_{ext}(\mathbf{r}) + \hbar g |\psi(\mathbf{r}, t)|^2 \right) \psi(\mathbf{r}, t), \quad (2.73)$$

where  $g$  is the interaction constant,  $\nabla_{\mathbf{r}}$  the kinetic energy and  $V_{ext}(\mathbf{r})$  is the external potential experienced by the particles. To extend this equation to the out of equilibrium polariton case, a first formulation in terms of exciton and photon enable to identify the various corrections that must be considered. Losses are incorporated through the relaxation rates  $\gamma_X$  and  $\gamma_{cav}$  while the continuous injection of photons in the system is accounted for by a pumping term  $F_p(\mathbf{r}, t)$  in the photon field master equation. Considering these terms we end up with a set of coupled equation for the exciton and photon fields  $\psi_X(\mathbf{r}, t)$ ,  $\psi_{\gamma}(\mathbf{r}, t)$  :

$$i\hbar \frac{d}{dt} \begin{bmatrix} \psi_{\gamma}(\mathbf{r}, t) \\ \psi_X(\mathbf{r}, t) \end{bmatrix} = \begin{bmatrix} \hbar F_p(\mathbf{r}, t) \\ 0 \end{bmatrix} + \left( \mathcal{H}_{lin}(\mathbf{r}) + \begin{bmatrix} V_{\gamma}(\mathbf{r}) - i\hbar \frac{\gamma_{cav}}{2} & 0 \\ 0 & V_X(\mathbf{r}) - i\hbar \frac{\gamma_X}{2} + \hbar g_{XX} n_X(\mathbf{r}, t) \end{bmatrix} \right) \begin{bmatrix} \psi_{\gamma}(\mathbf{r}, t) \\ \psi_X(\mathbf{r}, t) \end{bmatrix}, \quad (2.74)$$

where  $V_{\gamma}(\mathbf{r})$  and  $V_X(\mathbf{r})$  are the mean external potentials felt by photons and excitons respectively,  $g_{XX} = AV_{XX}/2\hbar$  is the exciton interaction strength and  $n_X = |\psi_X|^2$  is the exciton density. Additionally,  $\mathcal{H}_{lin}(\mathbf{r})$  corresponds to the linear Hamiltonian from [Equation 2.54](#), expressed in real space by substituting  $\mathbf{k}$  with  $i\nabla_{\mathbf{r}}$ .

$$\mathcal{H}_{lin}(\mathbf{r}) = \begin{bmatrix} \hbar\omega_X & \hbar\Omega_R/2 \\ \hbar\Omega_R/2 & \hbar\omega_{\gamma}(-i\nabla_{\mathbf{r}}) \end{bmatrix}. \quad (2.75)$$

as explained earlier, the exciton dispersion relation can be safely considered constant with respect to the photon one,  $\hbar\omega_X(\mathbf{k}) = \hbar\omega_X(0)$ . We can then make a transition to the polariton basis, obtaining two decoupled equations for the lower and upper polariton fields,  $\psi_{LP}(\mathbf{r},t)$  and  $\psi_{UP}(\mathbf{r},t)$ . Focusing on the lower polariton branch, this leads to the so-called *driven-dissipative Gross-Pitaevskii equation*:

$$i\hbar \frac{\partial}{\partial t} \psi_{LP}(\mathbf{r},t) = \left[ \hbar\omega_{LP}^0 - \frac{\hbar^2}{2m_{LP}} \nabla_{\mathbf{r}}^2 + V_{LP}(\mathbf{r}) + \hbar g n(\mathbf{r},t) - i\hbar \frac{\gamma_{LP}}{2} \right] \psi_{LP}(\mathbf{r},t) + \hbar \eta_{LP} F_p(\mathbf{r},t) \quad (2.76)$$

$$:= \mathcal{H}_{LP} \psi_{LP}(\mathbf{r},t) + \hbar \eta_{LP} F_p(\mathbf{r},t), \quad (2.77)$$

where  $V_{LP}$  is the external potential experienced by the polaritons which depends on those felt by photons and excitons through the Hopfield coefficients  $V_{LP}(\mathbf{r}) = C_{\mathbf{k}}^2 V_{\gamma} + X_{\mathbf{k}}^2 V_X$ ,  $\mathbf{k}$  being here the pump wavevector. The term  $\hbar\omega_{LP}^0$  is the polaritons energy at zero wavevector while the  $\hbar^2 \nabla_{\mathbf{r}}^2 / 2m_{LP}$  is again the kinetic energy. Finally, the prefactor  $\eta_{LP}$  account for the coupling efficiency of the pump photons whithin the system. Since the presence of a fluid in the sample changes the optical resonance through non linear interaction this term is generally not constant. However, in first approximation it is linked to the reflectivity of the sample front mirror and can be considered as a constant. A full derivation of this equation as well as a complete discussion on its validity can be found in [13].

**Dark reservoir.** In our description of excitons we mentionned the presence of dark excitons that are not directly coupled to light because of spin selection rules. As a consequence, one could think that they are not involved in the polariton dynamics. It is actually not the case. Indeed, even though they do not interact with photons they can still interact with bright excitons through the many complex electron-hole interactions described in [subsection 2.2.7](#). More precisely, they participate to the overall energy renormalization of the polariton fluid outlined by [Equation 2.70](#). Forgetting them in the description of the polariton dynamics would then be a mistake [54; 71]. To derive a single master equation starting from the many microscopic interactions between photons, dark and bright excitons would require a full spin resolved description and is beyond the scope of this manuscript. Nevertheless, we will account for their presence phenomenologically by considering them as a reservoir of density  $n_r$  with characteristic decay rate  $\gamma_r$ . The latter is coupled to polaritons through an energy renormalization term  $g_r n_r$  and a bright to dark excitons decay rate  $\gamma_{in}$ . In terms of equations it reads as :

$$i\hbar \frac{\partial}{\partial t} \psi_{LP}(\mathbf{r},t) = \left[ \hbar\omega_{LP}^0 - \frac{\hbar^2}{2m_{LP}} \nabla_{\mathbf{r}}^2 + V_{LP}(\mathbf{r}) + \hbar g n(\mathbf{r},t) + \hbar g_r n_r(\mathbf{r},t) - i\hbar \frac{\gamma_{LP} + \gamma_{in}}{2} \right] \psi_{LP}(\mathbf{r},t) + \hbar \eta_{LP} F_p(\mathbf{r},t), \quad (2.78)$$

$$\frac{\partial}{\partial t} n_r = -\gamma_r n_r + \gamma_{in} n. \quad (2.79)$$

A derivation of this equation as well as en extended experimental investigation can be found in [71]. As it will be shown in the following the presence of a dark reservoir is of great importance when it comes to describing the quantum fluctuations of the polariton fluid.

### 2.4.3 Excitation scheme

So far, the derivation of the master equation was initiated by stating that a polaritonic state could be macroscopically populated through optical pumping. However, the pump term was not yet defined in the sense that we did not specify the frequency of the pump photons with respect to the polariton dispersion relation. The latter is crucial to determine what are the mechanisms leading to long range coherence.

#### 2.4.3.1 Off resonance excitation

In the off resonant case the pump laser is highly blue detuned with respect to the polariton energy, close to a reflectivity minimum above the stop band of the DBRs (see [Figure 2.2](#)). The rise of a macroscopic population then occurs in the bottom of the LP branch through polaritons relaxation. More precisely, the injected photons create highly excited electron-hole pairs that relax through the emission of phonons. Lowering their energy they can emit photons and, at some point, eventually strongly couple to them to form polaritons. At this stage the polaritons are incoherent since the coherence of the pump laser got lost in the many relaxation processes. Then, the incoherent polaritons undergo scatterings and relax toward the minimum energy states available. If the pump intensity is increased, the population in the minimum of the LP branch will stimulate the relaxation of the other polaritons through bosonic stimulations. If the stimulation is efficient enough with respect to the losses, the bottom of the LP branch gets macroscopically populated and obtains a long range order which can be seen on [Figure 2.11](#). Like in atomic systems, the phase of the condensate wave function is chosen randomly through  $U(1)$  symmetry breaking and is not inherited from the pump laser. Such a phase transition in polariton planar microcavity was first observed in 2006 by Kasprzak et al. [46].

Some major differences with atomic BECs are worth mentioning. First, the temporal phase of an atomic BEC is defined by the chemical potential and is related to the number of atoms in the system while the polaritonic system can never reach equilibrium. Its temporal phase results from a complex interplay between the pump laser and the losses of the system : the phase transition is driven by the pump intensity rather than the temperature.

#### 2.4.3.2 Resonant excitation.

In the resonant case, the pump laser is tuned near the polariton energy. The population of the polaritons is then directly driven by the pump laser. In particular due to momentum and energy conservation, the spatial and temporal coherence of the pump laser are transferred to the polaritons fluid. In that case the phase of the fluid is fixed by the pump and therefore is not randomly chosen. In this excitation scheme the fluid should then not be called a condensate. However, it can still exhibit superfluidity and other quantum fluid properties because it possesses the required properties, namely : a macroscopic occupation of a single quantum state, long range coherence and weak interactions. The first experimental evidence of superfluid-like flows in a resonant excitation scheme was reported in 2009 in this group [3]. Then, many works showed that superfluid features as dark solitons [53] or quantized vortices streams [50] could be observed in such systems. Finally, the experimental measurement of the Bogoliubov collective excitation spectrum [18; 19; 71] confirmed that in many aspect

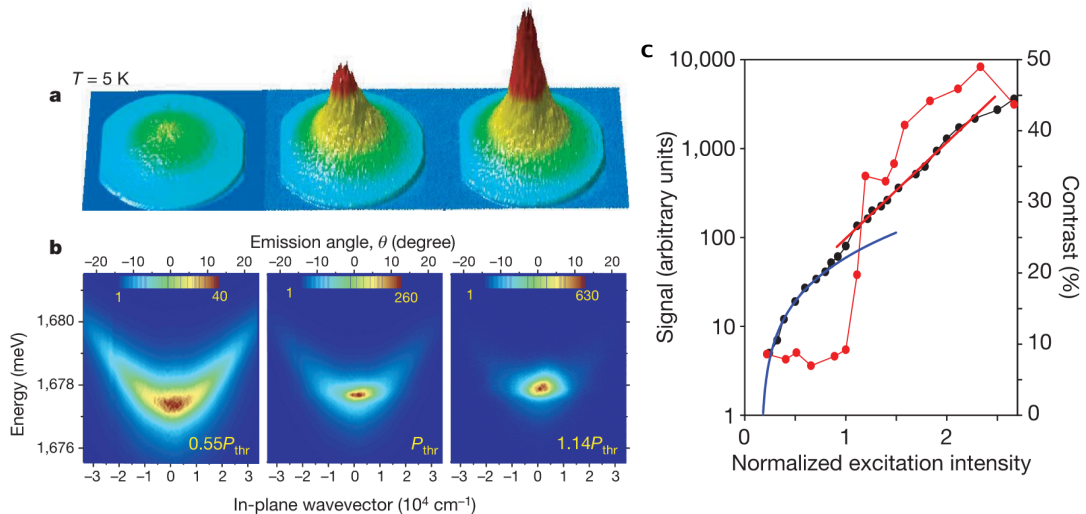


**Fig. 2.11 Bose-Einstein condensation of polaritons.** **a)** Far field emission of the fluid for increasing pump intensity. Above threshold, a strong emission in the zero wavevector mode is observed. **b)** Polariton dispersion for increasing pump intensities. Above threshold the bottom of the LP branch is macroscopically populated. **c)** First order coherence using a Michelson interferometer. Solid red circles indicate correlations between two spots separated by 6mm (2.5 times the thermal de Broglie wavelength) within the condensate as a function of the excitation power. The correlation exhibits a threshold-like behaviour. The variation of the ground-state emission intensity, normalized to the excitation power, is shown for comparison (solid black circles). The solid blue line is a quadratic fit of the data demonstrating the occurrence of particle-particle interaction below threshold. Above threshold, the solid red line is an exponential fit demonstrating the strong stimulation of the relaxation by the high occupancy factor of the ground state. Adapted from [46].

a resonantly driven polariton fluid behaves as a superfluid. In this work we will only use the resonant scheme to take advantage of the tunability of the pump to create fluid with arbitrary densities and velocity profiles. Before detailing the great versatility of this system, let us first discuss a consequence of the resonant excitation scheme which will be of great interest in the following.

**Optical bistability.** Consider a Fabry-Pérot cavity filled with a non-linear Kerr medium, through which a weak resonant laser beam is shone. As the laser intensity is low, the refractive index within the cavity is the same as the bare medium. It means that the optical length of the cavity is an integer multiple of half the laser wavelength. If the laser intensity is increased, the non-linear Kerr effect turns on and the refractive index decreases or increases depending on the medium. The laser is then no longer resonant with the cavity which reduces the intensity of the intracavity field and counteracts on the refractive index. This interplay between non-linearities and resonance conditions is at the heart of what is called optical bistability. Since this phenomenon is not specific to polaritonic system, we will, to understand it more in details, follow the very general derivation done in [38].

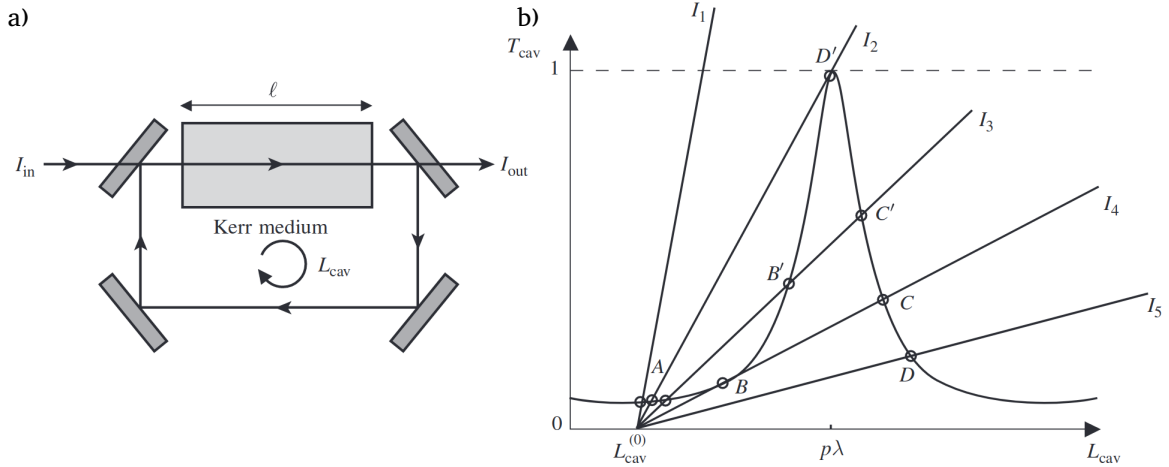


Fig. 2.12 **Optical bistability.** a) Schematic of a ring cavity filled with a Kerr medium. The cavity has a length  $L_{cav}^{(0)}$  and the Kerr medium a length  $l$ . b) Transmission of the cavity as a function of the optical length of the cavity  $L_{cav}$ . The straight lines represent the values  $T_{cav}$  as a function of  $L_{cav}$  for different values of  $I_{in}$ . The operating points lie at the intersections of the cavity resonance curve and the straight lines. Depending on  $I_{in}$  one or three operating points can be found. Adapted from [38].

To avoid first complications due to cross Kerr effect and standing wave establishment we consider a ring cavity of geometrical length  $L$  filled with Kerr medium of length  $l$  as shown in Figure 2.12 a). The optical length of such a cavity is :

$$L_{cav} = L + (n_0 - 1)l + n_2 I_{cav} l, \quad (2.80)$$

where  $n_0$  is the refractive index of the medium,  $n_2$  the non linear refractive index and  $I_{cav}$  the intracavity intensity. As explained for a planar cavity in section 2.1, the cavity has transmission peaks whenever the optical path of a round trip in the cavity (a photon going back and forth) is an integer multiple of the laser wavelength  $\lambda$ . In the case of a ring cavity this condition reads as :

$$T_{cav} = \frac{1}{1 + \frac{4F^2}{\pi^2} \sin^2 \left( \frac{kL_{cav}}{2} \right)}, \quad (2.81)$$

where  $F$  is the cavity finesse and  $k = 2\pi/\lambda$  the wavevector of the laser. The transmission of the cavity as a function of  $L_{cav}$  is plotted in Figure 2.12 b). On the other hand the transmission of the cavity is defined as :

$$T_{cav} = \frac{I_{out}}{I_{in}} = T \frac{I_{cav}}{I_{in}} = \frac{T}{n_2 l} \frac{L_{cav} - L_{cav}^{(0)}}{I_{in}}, \quad (2.82)$$

where  $T$  is the transmission of the outport mirror and  $L_{cav}^{(0)}$  the optical length of the cavity at low intensity  $I_{cav} \approx 0$ . An operating point is then defined as the intersection of the transmission curve [Equation 2.81](#) and the straight line of [Equation 2.82](#). Graphically the slope of the linear relation between  $T_{cav}$  and  $L_{cav}$  depends on the value of  $I_{in}$ . As a consequence several regimes are possible depending on the value of the input intensity as shown in [Figure 2.12 b\)](#). For low intensity as  $I_1$ , the operating point is unique and the system is in a stable regime but exhibits a low transmission. For higher input intensity like  $I_3$ , the system exhibits three operating points. However, it can be shown that the intersection points with a negative derivative between B and D are unstable. At even higher intensity the system has again a single operating point and a poor transmission. When the input intensity lies between  $I_2$  and  $I_4$  the system is said to be in a bistable regime.

In the case of microcavity-polaritons the same behavior can be observed as the exciton-exciton non-linear interactions are of the same nature as the Kerr effect. Analytically, polariton bistability can be found by looking at the steady state of the driven-dissipative Gross-Pitaevskii equation in the presence of a driving pump term nearly resonant with the LP branch. In first approximation, it can be written as a plane wave  $F_p(\mathbf{r},t) = F_p e^{i\mathbf{k}_p \cdot \mathbf{r} - i\omega_p t}$ . As it is usually done for equations including a resonant forcing term, we look for solutions of the same form, namely plane wave with the same phase,  $\psi(\mathbf{r},t) = \sqrt{n_0} e^{i\mathbf{k}_p \cdot \mathbf{r} - i\omega_p t}$ . Inserting this ansatz into [Equation 2.4.2](#) in the absence of external potential  $V_{LP} = 0$  one obtain the steady state equation :

$$\left[ \omega_p - \omega_{LP} - \frac{\hbar k_p^2}{2m_{LP}} - gn_0 - g_r n_r + i \frac{\gamma_{LP}}{2} \right] \sqrt{n_0} = \eta_{LP} F_p^0, \quad (2.83)$$

while the reservoir rate equation gives :

$$n_r = \frac{\gamma_{in}}{\gamma_r} n_0. \quad (2.84)$$

To eliminate the reservoir density we follow the procedure done in [71] and introduce an effective interaction strength  $g_e = g + g_r \frac{\gamma_{in}}{\gamma_r}$  so that  $g_r n_r + gn = g_e n$ . We can then rewrite [Equation 3.13](#) as :

$$\left[ \omega_p - \omega_{LP} - \frac{\hbar k_p^2}{2m_{LP}} - g_e n_0 + i \frac{\gamma_{LP}}{2} \right] \sqrt{n_0} = \eta_{LP} F_p^0. \quad (2.85)$$

It is the equivalent of the equation of state of a conservative system with the difference that, in this case, it results of a complex equilibrium between interactions, pumping and losses. Notice that the contribution of the dark reservoir just appears as a correction on the interaction strength and thus does not change significantly the phenomenology discussed earlier. Nonetheless, it has quantitative consequences on the hysteresis cycle—it reduces the pump power bistable range—that can be used to probe polariton-dark excitons interactions with optical means, notably through two photon excitation to overcome spin forbidden transitions [69].

To end up with an equation linking the pump intensity to the polariton density one can multiply this equation by its complex conjugate which gives :

$$n \left[ \frac{\gamma_{LP}^2}{4} + (\delta(k_p) - g_e n)^2 \right] = \eta_{LP}^2 I, \quad (2.86)$$

where  $\delta(k_p)$  is the effective detuning between the pump laser and the LP branch at the pump wavevector in a parabolic approximation,  $\delta(k_p) = \omega_p - \omega_{LP} - \hbar k_p^2 / 2m_{LP}$  and  $I$  the pump intensity. Being a polynomial of degree 3 in the polariton density, this equation have up to three solutions. Three distinct real solutions can be found only if  $\delta > \sqrt{3/2}\gamma_{LP}$ , as explained in the previous paragraph, one of this solution is known to be unstable. This being said, we do not take the latter into account this solution in the present work since the dimension of the fluid will always be 2D.

The evolution of  $n$  as a function of  $I$  in this regime is plotted in [Figure 2.13](#). The system is in a bistable regime when the curve exhibits two stable solutions for a given intensity : one at low density and one at high density. It is worth noticing that the actual state in which the system depends on its past history. More precisely, if the incident intensity is initially low, since the laser is blue detuned with the polariton energy, the photon injection within the sample is poor and few polariton are created. However, their presence in the cavity tends to blueshift their own resonance energy as explained in [subsection 2.3.1](#). As the intensity is ramped up, the system will follow the low density branch until the energy renormalisation is sufficient to reach the point B. At this point the system is compelled to jump to the high density branch and will suddenly move from point B to point C. If the pump intensity is then decreased, the situation is rather different since many polaritons are already present in the sample and support the laser injection and thus polariton creation. The system will follow the high density branch until it reaches the point D' where interactions can no longer compensate for the losses making it fall again on the low density branch. A particular attention must be given to this so called turning point D'. Indeed, as it can be seen on [Figure 2.12](#) it is the only point at which the laser is exactly resonant with the cavity filled with non linearities. This point can only be reached by ramping down the pump power for a system already operating on the high density branch. The corresponding density can be determined by solving  $\frac{dn}{dI} = 0$  which gives the discriminants :

$$\Delta = g_e^2 \left( \delta^2 - \frac{3\gamma_{LP}^2}{2} \right). \quad (2.87)$$

The bistable regime requires two distinct solution for  $\frac{dn}{dI} = 0$  which requires  $\Delta > 0$  and provides the aforementioned condition  $\delta > \sqrt{3/2}\gamma_{LP}$ . From this one can find that the density corresponding to the turning point fulfills  $\delta(k_p) = g_{eff}n = gn_0 + grn_r$ .

Conversely, when the detuning is too small with respect to the system losses the system is monostable and said to be in the optical limiter regime.

**All optical control.** In the context of hydrodynamical experiments and especially in the analog gravity framework, the ability to easily control and monitor the fluid of light is a great asset. Indeed, the study of Hawking radiation in a quantum fluid requires the creation of an acoustic horizon as well as the possibility to measure what is emitted by the latter. In particular, it is crucial to achieve two goals.

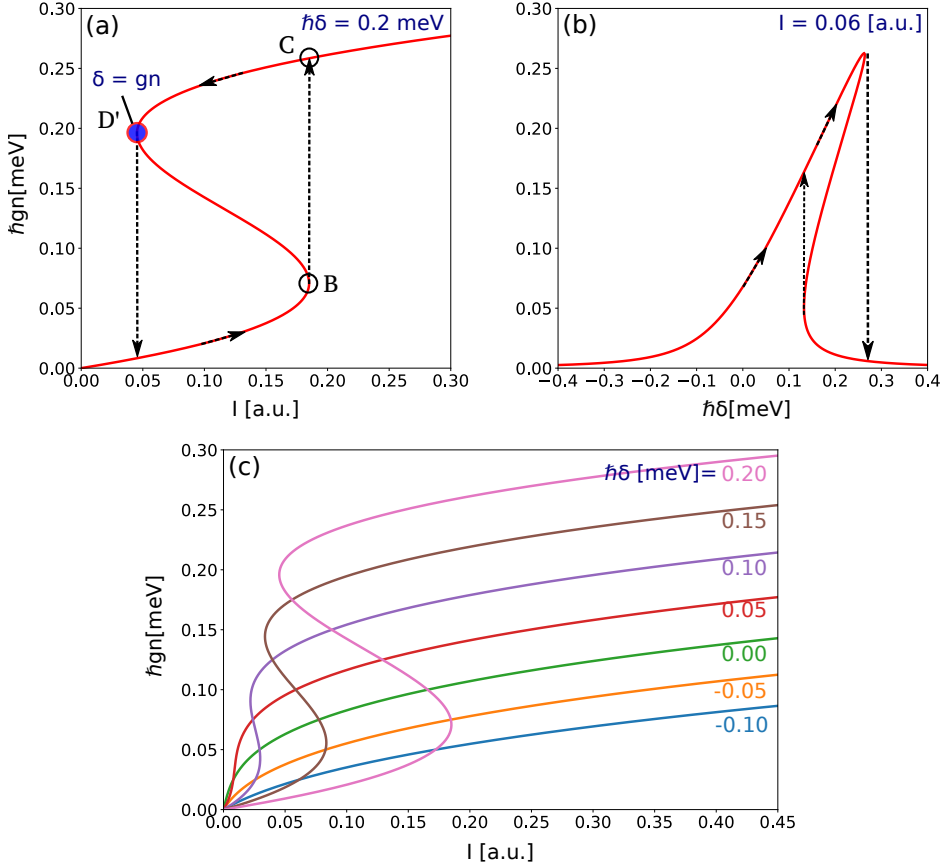


Fig. 2.13 **Optical bistability in a polariton fluid.** a) The polariton density as a function of the pump intensity when  $\delta > \frac{\sqrt{3}\gamma_{LP}}{2}$ . The blue point represents the so called turning point at which the detuning is exactly equal to the interaction energy. b) Polariton density as a function of  $\delta$  for a fixed pump intensity. c) Polariton density as a function of the pump intensity for different values of  $\delta$ , bistability is observed when  $\delta > \frac{\sqrt{3}\gamma_{LP}}{2}$ .

- 1. To create and monitor a stable fluid with an arbitrary flow profile and density since the mean field and especially its velocity profile are the analog of the curved spacetime we want to study.
- 2. To probe the fluid collective excitations. These small perturbations on top of the mean field are the fluid counterpart of the quantum fields fluctuations considered in the Hawking radiation theory.

With planar microcavity polaritons this is done fully optically since the fluid is created by the pump laser and is monitored by collecting the photons leaving the sample. The first point is allowed by the resonant excitation scheme. The velocity of a polariton being  $\mathbf{v}_{LP} = \frac{\hbar \mathbf{k}_{LP}}{m_{LP}}$  momentum conservation enables to create a fluid with a given velocity by just changing the pump incidence angle (see section 2.1). This correspondence also holds for the light outgoing the sample : the recombination of a polariton with wavevector  $\mathbf{k}$  produces a

photon with the same wavevector. Although the relation between the pump intensity and the polariton density is not trivial as we shall see in the next section, it is also a practical control knob that can be used to tune the fluid speed of sound. The second point can again be tackled with optics means since the struture of collective excitations is ultimately hidden in the fluctuations of the photonic field outgoing the sample. As a consequence, the large variety of tools and methods developped in the field of optics can be used to probe the fluid. Microcavity polaritons, are liying at the crossroad of optics and quantum fluids, definitely justifying the designation "quantum fluid of light".

## 2.5 Conclusion

In this chapter, we have explored the theoretical foundations of microcavity exciton-polaritons, emphasizing their hybrid nature as light-matter quasiparticles. By combining the low effective mass and coherence of photons with the strong nonlinear interactions of excitons, polaritons emerge as a unique platform for studying quantum fluids. We have detailed the mechanisms behind their formation, interactions, and dynamics, highlighting the versatility of these systems.

A key feature of polariton fluids is their fully optical control, which allows for precise manipulation of their density, velocity, and flow profiles. This capability, enabled by the resonant excitation scheme, makes polariton fluids particularly well-suited for analog gravity experiments. In the following chapters, we will build on this theoretical foundation to investigate the experimental realization and observation of analog Hawking radiation in polariton fluids.



## Chapter 3

# Hawking radiation in a polariton quantum fluid

After introducing the polariton system that will be used for quantum simulations, we present the theoretical framework that describes Hawking radiation in a polariton quantum fluid. In this chapter, we will first establish the original hydrodynamical analogy between the propagation of acoustic waves in a moving fluid and scalar fields in curved spacetime. This analogy is at the heart of what motivated the study of Hawking radiation in analog systems, leading to a first generation of experiment in classical systems such as water tanks. These experiments [68; 80] demonstrated positive to negative frequency conversion of shallow surface waves in the vicinity of a sonic horizon. However the temperature of classical fluids is too high to observe quantum effects. More precisely, Hawking radiation is expected to create entanglement between the emitted modes which can not be tested with water waves. Quantum fluids appear then as promising candidate since the fluctuations around the ground or steady state require a quantum treatment to be understood. In fact, we will see that describing a fluid with trans-critical flow in the framework of the Bogoliubov theory also predicts particle creation from vacuum. Studying the effect from this point of view will reveal a strong robustness of the effect beyond the original hydrodynamical approach and widen the range of regimes where Hawking radiation can be observed.

### 3.1 The hydrodynamical analogy

In the previous chapter, we established that the dynamics of microcavity polaritons can be described by a driven dissipative Gross-Pitaevskii equation. By writing the wavefunction in terms of phase and density, this equation can be cast into a continuity equation and an Euler equation for a non-barotropic fluid in the pump rotating frame. Starting from the GPE, a polariton system resonantly pumped by a laser of the general form  $F_p e^{i\phi(x,t)}$  leads the fluid to a state described by the wavefunction  $\psi(x,t) = \sqrt{n_0} e^{i\phi(x,t)}$ . The phase and modulus  $\psi$  :

$$\partial_t \phi + \frac{m_{LP} v_0^2}{2\hbar} + \frac{\hbar}{2m_{LP}} \frac{\partial_x^2 \sqrt{n_0}}{\sqrt{n_0}} + V_{LP} + gn + g_r n_r + \frac{\Re[F_p e^{-i\theta}]}{m_{LP}} = 0 \quad (3.1)$$

$$\partial_t n_0 + \partial_x(n_0 v) = \gamma n_0 - 2\Im[F_p e^{-i\theta}] \sqrt{n_0} \quad (3.2)$$

If we neglect the drive and dissipation terms which is the situation of a conservative fluid, we recover the original equation describing sound waves in a moving flow. This is precisely the equation that was used in the initial analogy made by W. Unruh [73]. However, the out of equilibrium nature of the microcavity polaritons brings different phenomenology. In particular, perturbations propagating in the fluid are not necessary sound waves as we will see later. It means that the dispersion of these perturbations is not linear and can remarkably exhibit a gap which can be associated to massive excitations. To avoid making approximations it is convenient to make the same calculations in the pump rotating frame. It equivalently means that all frequencies will be taken with respect to the pump. In practice this is done by writing the pump  $F_p(x) = F_p e^{i\theta_p(x)}$  with  $\theta_p(x) = k_p x$  and looking for steady state wavefunction of the same form  $\psi(x,t) = \sqrt{n_0} e^{i\theta_p(x)}$ . Plugging this into the GPE we obtain that the phase and density of the fluid must fulfill the following equation :

$$\left[ -\frac{\hbar}{2m_{LP}} \nabla^2 - i\frac{\hbar}{2} (\boldsymbol{\nabla} \cdot \mathbf{v}_0) - i\hbar(\mathbf{v}_0 \cdot \boldsymbol{\nabla}) - \delta(v_0) + g_r n_r + gn_0 - i\frac{\hbar\gamma}{2} \right] \sqrt{n_0} + |F_p| = 0 \quad (3.3)$$

with  $\hbar\delta(v_0) = \hbar\omega_p - \hbar\omega_0 - m_{LP}v_0^2/2$  (note that this is just  $\delta(k_p)$  in a homogeneous configuration where  $\mathbf{v}_0 = \hbar\mathbf{k}_p/m_{LP}$ ). To study the low energy collective perturbations of the fluid state we linearize the system around the steady state by writing the wavefunction  $\psi(x,t) = (\sqrt{n_0} + e^{-\gamma t/2} \delta\psi(x)) e^{i\theta_p(x)}$  where the term  $e^{-\gamma t/2}$  account for the losses as we will see later. Injecting this expression in [Equation 2.79](#) and using [Equation 3.3](#) we obtain to linear order in  $\delta\psi$  :

$$i\hbar(\partial_t + \mathbf{v}_0 \cdot \boldsymbol{\nabla}) \delta\psi = \left[ -\frac{\hbar}{2m_{LP}} \nabla^2 + \rho - i\sigma \right] \delta\psi + gn_0 \delta\psi^*, \quad (3.4)$$

where

$$\rho := 2gn_0 - \delta(v_0) + g_r n_r \quad \text{and} \quad \sigma := \hbar/2\boldsymbol{\nabla} \cdot \mathbf{v}_0.$$

The term  $\sigma$  encodes the gradient of the fluid velocity field and is zero for a homogeneous velocity background. Note that here we have assumed that there is no external potential without loss of generality since it can be included in the definition of  $\rho$ .

The above equation and its complex conjugate can be seen as a system of two coupled partial differential equations (PDEs) of first order in time-derivatives and second order in space-derivatives. A way to solve this system is by rewriting it as a single PDE of second order in time and fourth order in space. To that end, we solve  $\delta\psi^*$  in terms of  $\delta\psi$  from the above equation to obtain

$$\delta\psi^* = \frac{1}{gn_0} \left[ i\hbar(\partial_t + \mathbf{v}_0 \cdot \boldsymbol{\nabla}) + \frac{\hbar}{2m_{LP}} \nabla^2 - \rho + i\sigma \right] \delta\psi. \quad (3.5)$$

Plugging this into the complex conjugate equation of (3.4) we find

$$\begin{aligned} i\hbar(\partial_t + \mathbf{v}_0 \cdot \boldsymbol{\nabla}) \frac{1}{gn_0} \left[ i\hbar(\partial_t + \mathbf{v}_0 \cdot \boldsymbol{\nabla}) + \frac{\hbar}{2m_{LP}} \nabla^2 - \rho + i\sigma \right] \delta\psi = \\ \left[ \left( \frac{\hbar}{2m_{LP}} \nabla^2 - \rho - i\sigma \right) \frac{1}{gn_0} \left( i\hbar(\partial_t + \mathbf{v}_0 \cdot \boldsymbol{\nabla}) + \frac{\hbar}{2m_{LP}} \nabla^2 - \rho + i\sigma \right) - gn_0 \right] \delta\psi \end{aligned} \quad (3.6)$$

For homogeneous backgrounds we have  $\sigma = 0$  and  $\delta(v_0) = \delta(k_p)$ . Hence, the above equation (3.6) can be simplified to

$$\left[ (\partial_t + \mathbf{v}_0 \cdot \nabla)^2 + \left( \frac{\xi^2}{4} \nabla^2 - 1 \right) \frac{\rho}{m_{LP}} \nabla^2 + \frac{\rho^2 - g^2 n_0^2}{\hbar^2} \right] \delta\psi = 0, \quad (3.7)$$

where we have defined the healing length

$$\xi := \frac{\hbar}{\sqrt{m_{LP}\rho}} = \frac{\hbar}{\sqrt{m_{LP}(2gn_0 + g_r n_r - \delta(k_p))}}. \quad (3.8)$$

This length scale is the limit of the hydrodynamical regime. Indeed, for large wavelength perturbations  $\lambda \gg \xi$  (low wavenumber  $k \ll \xi^{-1}$ ), we can set  $\xi^2 \nabla^2 / 4 - 1 \approx -1$ . This is called the hydrodynamic approximation, because neglecting this term corresponds to neglecting the effect of the quantum pressure, so that the fluid becomes barotropic in that regime. Indeed, under this approximation, the above 4th order PDE for  $\delta\psi$  reduces to a 2nd order PDE of the form

$$\left[ -(\partial_t + \mathbf{v}_0 \cdot \nabla)^2 + c_B^2 \nabla^2 - \frac{m_{det}^2 c_B^4}{\hbar^2} \right] \delta\psi = 0. \quad (3.9)$$

where

$$\begin{aligned} c_B &= \sqrt{\frac{\rho}{m_{LP}}} = \sqrt{\frac{2gn_0 - \delta(k_p) + g_r n_r}{m_{LP}}}, \\ m_{det} &= \frac{\sqrt{(\rho^2 - g^2 n_0^2)}}{c_B^2} = m_{LP} \frac{\sqrt{(gn_0 - \delta(k_p) + g_r n_r)(3gn_0 - \delta(k_p) + g_r n_r)}}{(2gn_0 - \delta(k_p) + g_r n_r)}. \end{aligned} \quad (3.10)$$

These two quantities have a well defined physical meaning as follows. On the one hand,  $m_{det} c_B^2$  is the energy of  $k = 0$  modes of  $\delta\psi$ , introducing a mass gap. On the other hand, Eq. (3.9) is a hyperbolic PDE whose characteristic curves in a fluid at rest are given by  $|\mathbf{x}| = c_B t$ . These characteristics limit the speed at which acoustic excitations  $\delta\psi$  can propagate information, defining the soundcones in full analogy to light cones. However, due to the mass gap, the speed of propagation of excitations of  $\delta\psi$  is  $v_g = d\omega/dk \leq c_B$ . The latter can be seen as the limiting speed of propagation of  $k \rightarrow \infty$  perturbations. This is also in full analogy to propagation of modes of a massive relativistic scalar field, which travel at subluminal speeds, reaching only the speed of light in the limit of infinite momentum.

Indeed, this analogy can be extended beyond the fluid rest frame, as Eq. (3.9) can always be written as a Klein-Gordon equation for a massive real scalar field in a curved spacetime, which takes the form

$$\left[ \frac{1}{\sqrt{|q|}} \partial_\mu \sqrt{|q|} q^{\mu\nu} \partial_\nu - \frac{m_{det}^2}{\hbar^2} \right] \delta\psi = 0 \quad (3.11)$$

where the acoustic metric  $q_{\mu\nu}$  is given by the line element

$$ds^2 = c_B^2 \left[ (v_0^2 - c_B^2) dt^2 - 2\mathbf{v}_0 \cdot d\mathbf{x} dt + d\mathbf{x} \cdot d\mathbf{x} \right]. \quad (3.12)$$

Thus, we see that, in the hydrodynamic regime, collective excitations of a polariton fluid are described by a massive relativistic scalar field, which becomes massless if the polariton fluid is pumped at the turning point of the bistability loop.

Note that Eq. (3.11) with the above form of the acoustic metric is exactly our [Equation 3.5](#). This acoustic metric coincides with the one that describes sound waves in an inviscid, irrotational and barotropic fluids according to the Theorem of section 2.3 in [6]. However, perturbations in isolated inviscid, irrotational and barotropic fluids are described by a massless Klein-Gordon equation. The breaking of the isolation condition, due to the driven-dissipative nature of polaritons, modifies the result of that Theorem by introducing a mass term, whose value can be experimentally controlled at will (and even made to vanish) through the detuning  $\delta(k_p)$  as we will see in the next section.

## 3.2 Elementary excitations of the fluid : Bogoliubov theory

Unlike in classical systems, where Hawking radiation can only be triggered by external disturbances, its analog in quantum fluids may instead arise from vacuum fluctuations. In this context, perturbations of the quantum fluid are emitted at the analog horizon and propagate in opposite directions, mirroring the behavior expected near a gravitational event horizon. However, while the analogy with black hole physics is supported by the fact that the systems can be described by the same equation, derived in the hydrodynamical context, it should be noted that the systems are very different in nature and that analog systems are rather a way to study Quantum Field Theory in curved spacetime than strict black hole simulations.

Indeed, treating the collective excitations of a transonic Bose-Einstein condensate within the framework of Bogoliubov theory already predicts the spontaneous emission of modes at the horizon from vacuum fluctuations. Fundamentally, both Stephen Hawking's original calculation and its quantum fluid analog rely on a Bogoliubov transformation between two sets of operators [41], which ultimately leads to the mixing of creation and annihilation operators.

This section will establish the structure of the collective excitation spectrum and demonstrate how specific fluid configurations can give rise to mode emission from vacuum. Furthermore, we will show that the Hawking effect remains robust even when deviating from the original hydrodynamical analogy, and it does not necessarily require the excitations to be sound waves. In fact, the intrinsically out-of-equilibrium nature of the polariton system reveals a phenomenology far richer than that of conservative systems, extending the possibility of observing Hawking radiation to massive excitations.

### 3.2.1 Linearization of the Gross-Pitaevskii equation

Let us consider a monochromatic pump described by a plane wave  $F_p(\mathbf{r},t) = F_p e^{i(\mathbf{k}_p \cdot \mathbf{r} - \omega_p t)}$ . As explained in the previous chapter, this will drive the system to a steady state of the form  $\psi_0(\mathbf{r},t) = \psi_0 e^{i(\mathbf{k}_p \cdot \mathbf{r} - \omega_p t)}$  and satisfying :

$$\left[ \omega_p - \omega_{LP} - \frac{\hbar k_p^2}{2m_{LP}} - g |\psi_{LP}^0|^2 + i \frac{\gamma_{LP}}{2} \right] \psi_{LP}^0 = \eta_{LP} F_p^0. \quad (3.13)$$

We now look for the elementary excitations following the Bogoliubov prescription which consists in linearizing the GPE around  $\psi_0$ . We write the wavefunction as :

$$\psi(\mathbf{r},t) = \left[ \psi_0(\mathbf{r}) + \delta\psi(\mathbf{r},t) \right] e^{i(\mathbf{k}_p \cdot \mathbf{r} - \omega_p t)}. \quad (3.14)$$

The second term in this equation can be interpreted as the polaritons that are not in the steady state and therefore have a global phase different from the pump. This implies that they can have different energy and momentum than the fluid and undergo scattering processes or spontaneous effects since their dynamics is not fixed by the pump. It is worth noticing that this term does not originate from the out of equilibrium nature of the system and would be non-zero even at zero temperature due to interactions. In the case of Bose Einstein condensates, this linearization process actually introduces a state that is not physical in the sense that this writing implicitly provide the wavefunction with a well defined phase and thus suggests the breaking of the  $U(1)$  symmetry of the system [15]. However, the correct physical state can be recovered through a statistical mixtures of all these "symmetry broken states" which then rather appear as intermediate state convenient for calculation. In the case of a polariton fluid pumped quasi resonantly, the situation is different since the mean field phase is fixed by the pump.

Injecting [Equation 3.14](#) in the GPE, using [Equation 3.13](#) and keeping only the linear terms in  $\delta\psi$  we obtain :

$$\begin{aligned} i\hbar\partial_t\delta\psi = & \left( \hbar\omega_{LP}^0 - \hbar\omega_p - \frac{\hbar^2}{2m_{LP}} [\nabla^2 + 2i\mathbf{k}_p \cdot \nabla - \mathbf{k}_p^2] + \hbar g_r n_r + 2\hbar g |\psi_0|^2 + \frac{i\hbar\gamma}{2} \right) \delta\psi \\ & + \hbar g\psi_0^2 \delta\psi^*. \end{aligned} \quad (3.15)$$

Yet, this equation is not strictly speaking linear in  $\delta\psi$  since it contains a term involving its complex conjugate  $\delta\psi^*$ . A way to solve this problem is to decompose  $\delta\psi$  in its real and imaginary part and to obtain two independent equations. An equivalent procedure, more common in the literature [58], is to find an equation on the complex conjugate and consider  $\delta\psi^*$  as an independent variable. This is the approach we will follow here. The equation on  $\delta\psi^*$  is obtained by simple complex conjugation of [Equation 3.15](#) :

$$\begin{aligned} -i\hbar\partial_t\delta\psi^* = & \left( \hbar\omega_{LP}^0 - \hbar\omega_p - \frac{\hbar^2}{2m_{LP}} [\nabla^2 - 2i\mathbf{k}_p \cdot \nabla - \mathbf{k}_p^2] + \hbar g_r n_r + 2\hbar g |\psi_0|^2 - \frac{i\hbar\gamma}{2} \right) \delta\psi^* \\ & + \hbar g\psi_0^{*2} \delta\psi. \end{aligned} \quad (3.16)$$

For the sake of clarity we define the operator :

$$\mathcal{H}_{bog} = \hbar\omega_{LP}^0 - \hbar\omega_p - \frac{\hbar^2}{2m_{LP}} [\nabla^2 + 2i\mathbf{k}_p \cdot \nabla - \mathbf{k}_p^2] + \hbar g_r n_r + 2\hbar g |\psi_0|^2. \quad (3.17)$$

We can now write the fully linearized problem under its matrix form :

$$i\hbar\partial_t \begin{pmatrix} \delta\psi \\ \delta\psi^* \end{pmatrix} = (\mathcal{L}_B + \frac{i\hbar\gamma}{2}\mathbf{I}_2) \begin{pmatrix} \delta\psi \\ \delta\psi^* \end{pmatrix} \quad (3.18)$$

where  $\mathcal{L}_B$  is the Bogoliubov matrix defined as :

$$\mathcal{L}_B = \begin{pmatrix} \mathcal{H}_{bog} & \hbar g \psi_0^2 \\ -\hbar g \psi_0^{*2} & -\mathcal{H}_{bog}^* \end{pmatrix} \quad (3.19)$$

Since  $\mathcal{L}_B$  is time independent the usual procedure to solve [Equation 3.18](#) is to diagonalize the Bogoliubov matrix and write any generic solution in the basis of eigenmodes defined by :

$$\mathcal{L}_B \begin{pmatrix} u_i \\ v_i \end{pmatrix} = (\hbar\omega_i + \frac{i\hbar}{2}) \begin{pmatrix} u_i \\ v_i \end{pmatrix}. \quad (3.20)$$

As the entire the spectrum is fully determined by the eigenvalues of  $\mathcal{L}_B$  we will drop the loss term in the following for the sake of simplicity and take them into account at the end of the calculation by multiplying the solutions by  $\exp(-\gamma t/2)$ .

**Bogoliubov matrix symmetries.** As in general for quadratic hamiltonian of bosonic systems [15], the Bogoliubov matrix is not hermitian. Therefore, its eigenvalues are not necessarily real and  $\mathcal{L}_B$  is not even ensured to be diagonalizable. However, it can easily be shown that the following symmetry is respected :

$$\mathcal{L}_B^\dagger = \eta^{-1} \mathcal{L}_B \eta \quad \text{with} \quad \eta = \eta^{-1} = \begin{pmatrix} 1 & 0 \\ 0 & -1 \end{pmatrix}. \quad (3.21)$$

It means that the Bogoliubov operator is "hermitian" for the inner product :

$$\langle \vec{X}_1, \vec{X}_2 \rangle = (\vec{X}_1^*)^T \eta \vec{X}_2. \quad (3.22)$$

For any vectors  $\vec{X}_1$  and  $\vec{X}_2$  we thus have  $\langle \vec{X}_1, \mathcal{L}_B \vec{X}_2 \rangle = \langle \mathcal{L}_B \vec{X}_1, \vec{X}_2 \rangle$ . Consequently, the inner product between two modes  $|\phi\rangle = (u_\phi, v_\phi)^T$  and  $|\psi\rangle = (u_\psi, v_\psi)^T$  :

$$\langle \psi | \phi \rangle_B := \int d\mathbf{r} [\psi^\dagger(\mathbf{r}) \eta \psi(\mathbf{r})] = \int d\mathbf{r} [u_\psi^*(\mathbf{r}) u_\phi(\mathbf{r}) - v_\psi^*(\mathbf{r}) v_\phi(\mathbf{r})], \quad (3.23)$$

is conserved in time. This product induces a modified norm for the modes :

$$\|\psi\|_B := \langle \psi | \psi \rangle_B. \quad (3.24)$$

It's worth noticing that since the inner product defined in [Equation 3.23](#) is neither positive nor definite, the induced norm of a given mode  $|\psi\rangle$  can be positive, negative or zero. Let us now see what the symmetry of [Equation 3.21](#) implies on the spectrum of  $\mathcal{L}_B$ . Consider an eigenvector  $|\psi\rangle = (u_k, v_k)^T$  of  $\mathcal{L}_B$  with eigenvalue  $\hbar\omega_k$  :

$$\mathcal{L}_B \begin{pmatrix} u_k \\ v_k \end{pmatrix} = \hbar\omega_k \begin{pmatrix} u_k \\ v_k \end{pmatrix}. \quad (3.25)$$

Direct substitution of [Equation 3.21](#) in the eigenvalue equation gives :

$$\mathcal{L}_B^\dagger \begin{pmatrix} u_k \\ -v_k \end{pmatrix} = \hbar\omega_k \begin{pmatrix} u_k \\ -v_k \end{pmatrix}. \quad (3.26)$$

From this, we obtain that  $\hbar\omega_k^*$  is also an eigenvalue of  $\mathcal{L}_B$  since we have the relation :

$$\det(\mathcal{L}_B - \hbar\omega_k^* \mathbf{I}_d) = [\det(\mathcal{L}_B^\dagger - \hbar\omega_k \mathbf{I}_d)]^* = 0. \quad (3.27)$$

The Bogoliubov matrix as well as its adjoint operator also respect the symmetry :

$$\mathcal{L}_B^* = -\sigma^{-1} \mathcal{L}_B \sigma \quad \text{with} \quad \sigma = \sigma^{-1} = \begin{pmatrix} 0 & 1 \\ 1 & 0 \end{pmatrix}, \quad (3.28)$$

The latter implies that  $-\hbar\omega_k^*$  is also an eigenvalue of  $\mathcal{L}_B$  :

$$\mathcal{L}_B \begin{pmatrix} v_k^* \\ u_k^* \end{pmatrix} = -\hbar\omega_k^* \begin{pmatrix} v_k^* \\ u_k^* \end{pmatrix}, \quad (3.29)$$

which can be again obtained by direct substitution. Putting together all this properties we find that  $\hbar\omega_k$ ,  $-\hbar\omega_k$ ,  $\hbar\omega_k^*$  and  $-\hbar\omega_k^*$  are simultaneously eigenvalues of  $\mathcal{L}_B$ . A special attention must be given to the fact that if  $|\psi\rangle = (u_k, v_k)^T$  is an eigenvector of  $\mathcal{L}_B$  with eigenvalue  $\hbar\omega_k$  the eigenvector  $|\phi\rangle = (v_k^*, u_k^*)^T$  linked to  $-\hbar\omega_k^*$  has opposite norm.

$$\langle \psi | \psi \rangle_B = \langle u_k | u_k \rangle - \langle v_k | v_k \rangle = -\langle \phi | \phi \rangle_B. \quad (3.30)$$

**Orthogonality condition.** An orthogonality condition can be derived by calculating the quantity  $\langle \psi_i | \eta \mathcal{L}_B | \psi_j \rangle - \langle \psi_j | \eta \mathcal{L}_B | \psi_i \rangle^*$ . On one hand we find this term to be zero because the symmetry of [Equation 3.21](#) equivalently means that  $\eta \mathcal{L}_B$  is hermitian. On the other hand we find :

$$\langle \psi_i | \eta \mathcal{L}_B | \psi_j \rangle - \langle \psi_i | \eta \mathcal{L}_B | \psi_j \rangle^* = \hbar\omega_i \langle \psi_i | \eta | \psi_j \rangle - \hbar\omega_j^* \langle \psi_i | \eta | \psi_j \rangle, \quad (3.31)$$

$$= (\hbar\omega_i - \hbar\omega_j^*) \langle \psi_i | \eta | \psi_j \rangle, \quad (3.32)$$

which gives the orthogonality condition :

$$(\hbar\omega_i - \hbar\omega_j^*) \langle \psi_i | \eta | \psi_j \rangle = 0 \quad (3.33)$$

showing that the modified scalar product  $\langle \cdot | \cdot \rangle_B$  between two eigenvectors with different eigenvalues is zero and that eigenmodes with complex eigenvalues have a vanishing norm. The modes with non-zero norm are then associated to non-zero real eigenvalues.

At the end, if we normalize the eigenvectors to unity in absolute value, the spectrum of  $\mathcal{L}_B$  can be split in three parts :

- The  $S_+$  family of modes  $|\delta\psi_k^+\rangle = (u_k, v_k)^T$  with positive norm :  $\langle u_k|u_k\rangle - \langle v_k|v_k\rangle = +1$  and real eigenvalues  $\hbar\omega_k > 0$
- The  $S_-$  family of modes  $|\delta\psi_k^-\rangle = (v_k^*, u_k^*)^T$  with negative norm :  $\langle v_k^*|v_k^*\rangle - \langle u_k^*|u_k^*\rangle = -1$  and real eigenvalues  $-\hbar\omega_k > 0$
- The  $S_0$  family of modes with zero norm :  $\langle u_k|u_k\rangle - \langle v_k|v_k\rangle = 0$  and zero or complex eigenvalues.

Note that the eigenvectors of the  $S_-$  subspace are expressed in terms of the  $u_k$  and  $v_k$  component of the  $S_+$  vectors to reflect the dual structure of the solution space. The modes with zero norm are usually related to abnormal modes [15]. One of them is the vector whose components are  $\psi_0$  and  $-\psi_0$  which satisfy the Bogoliubov equations with a zero eigenvalue because  $\psi_0$  obeys the Gross Pitaevskii equation. It corresponds to a global change of the phase condensate and is very similar to the appearance of the Goldstone modes when the  $U(1)$  phase symmetry of the system is broken. Other modes of  $S_0$  are related to dynamical instabilities due to non-zero imaginary part of their eigenvalues.

**Dynamical stability.** The free evolution of a mode is given by  $\exp(-i\omega_k t)$  so it remains bounded in time provided that the imaginary part of  $\hbar\omega_k$  is negative or zero. This is known as the dynamical stability condition. In fact, this condition must be refined in the polaritonic case since as one can see from [Equation 3.18](#), the eigenvalues already contain a non-zero imaginary part due to the intrinsic losses of the system. Since eigenvalues come in pairs of complex conjugate values the stability condition applies both on  $\Im(\hbar\omega_k)$  and  $\Im(\hbar\omega_k^*) = -\Im(\hbar\omega_k)$  which gives :

$$|\Im(\hbar\omega_k)| \leq \frac{\hbar\gamma}{2} \quad \text{for all } k. \quad (3.34)$$

In practice, the losses can damp the dynamical instabilities that would destroy a conservative system while still exhibiting precursors of the instabilities which makes polariton systems very useful for the study of such phenomena [19]. This being said, the present experiment always takes place in a regime in which the system is stable.

Finally, if we restrict our description to modes with non-zero norm, a general solution of the Bogoliubov equation can be written as :

$$|\delta\psi\rangle = \begin{pmatrix} \delta\psi \\ \delta\psi^* \end{pmatrix} = \sum_{\mathbf{k} \in S_+} b_{\mathbf{k}} \begin{pmatrix} u_k \\ v_k \end{pmatrix} e^{-i\omega_k t} + b_{\mathbf{k}}^* \begin{pmatrix} v_k^* \\ u_k^* \end{pmatrix} e^{i\omega_k t} \quad (3.35)$$

where

$$b_{\mathbf{k}} = \int d\mathbf{r} u_k^*(\mathbf{r}) \delta\psi(\mathbf{r}) - v_k^*(\mathbf{r}) \delta\psi(\mathbf{r}). \quad (3.36)$$

The redundancy of the first line of (3.35) being the complex conjugate of the second is the price we pay now for our initial assumption that considered  $\delta\psi$  and  $\delta\psi^*$  as independent

variables. The advantage of the procedure followed here is the natural emergence of the inner product of [Equation 3.23](#) from the symmetries of  $\mathcal{L}_B$ . It allows for the definition of a norm and the establishment of orthogonality among the eigenvectors, thereby revealing the structure of the solution space as the direct sum of two dual subspaces. This decomposition results in norms with opposite signs and paired complex-conjugate eigenvalues. Another possible approach would have been to directly look for solutions as linear combinations of plane waves with opposite frequencies as it is done in [58]. This method however does not provide a natural way to define a norm and, as we shall see later, it is the sign of the norm and not the sign of the eigenvalues that is relevant for mode classification. The last advantage of the approach followed here is that the derivation is closer to the full quantum derivation and will ease the later quantization of the classical fields obtained here. Taking into account the dissipative part of [Equation 3.18](#) and dropping the redundancy, a generic expression for the fluctuations of the order parameter is :

$$\delta\psi(\mathbf{r},t) = \sum_{\mathbf{k} \in S_+} \left[ A_{\mathbf{k}} u_k(\mathbf{r}) e^{-i\omega_k t} + A_{\mathbf{k}}^* v_k^*(\mathbf{r}) e^{i\omega_k t} \right] e^{-\gamma t/2}. \quad (3.37)$$

**Particle-hole symmetry.** Under this form one might be tempted to interpret the fluctuations order parameter has a superposition of independent plane waves with opposite directions and frequencies. This would be a mistake. Indeed, the coefficient  $u_k$  and  $v_k^*$  are coupled through the Bogoliubov matrix and respect the particle hole symmetry of [Equation 3.28](#). The first term can be interpreted as the addition of a particle with energy  $\hbar\omega_k$  and momentum  $\hbar\mathbf{k}$  while the second term can be interpreted as the addition of a hole with energy  $-\hbar\omega_k^*$  and momentum  $-\hbar\mathbf{k}$ . The coupling between the two terms reflects that a fluctuation of the system is a particle-hole hybrid excitation, while the norm  $\langle \cdot | \cdot \rangle_B$  of the mode reflects the relative weight of the particle and hole components.

- If  $\int d\mathbf{r} \|u_k\|^2 - \|v_k\|^2 > 0$  the mode is mostly made of  $u_k$  and can be interpreted as a particle excitation.
- If  $\int d\mathbf{r} \|u_k\|^2 - \|v_k\|^2 < 0$  the mode is mostly made of  $v_k^*$  and can be interpreted as a hole excitation.

In conservative systems this symmetry is often related to the fluctuation of the number of particles in the condensed state. When the system is out of equilibrium this interpretation seems less straightforward since the number of particles in the mean field is not strictly speaking conserved in time. However, these modes still account for small deviation from the pump mode  $(\mathbf{k}_p, \omega_p)$  both in frequency and wavevector. To elucidate this point, consider the possibility of simultaneously monitoring both the incident laser and its counterpart transmitted through the microcavity. Given that the laser's linewidth is significantly narrower than the microcavity resonance, the latter does not act as a filter. Hence, one would first notice that the two beams share the stochastic features associated with the shot noise inherent to the laser source. Then, one would observe that the polariton field exhibits additional fluctuations, arising from the spontaneous emission of photons with frequencies and wavevectors distinct from those of the pump. These photons originate from the Bogoliubov modes of the fluid

due to the interactions. The photonic nature of this system then appears again as a great asset because the fluctuations of the system are translated in the noise spectrum of the beam transmitted by the cavity.

### 3.3 Homogeneous fluid

So far, the description of the collective excitations spectrum remained quite general and we did not use the homogeneity of system. In this case  $\psi_0$  is invariant under translation meaning the eigenvectors of  $\mathcal{L}_B$  are just plane waves. The  $S_+$  vectors then can be written as :

$$u_k(\mathbf{r}) = U_k \cdot \exp(i\mathbf{k}\mathbf{r}) \quad (3.38a)$$

$$v_k(\mathbf{r}) = V_k \cdot \exp(i\mathbf{k}\mathbf{r}). \quad (3.38b)$$

Before going further in the calculation, let us comment the ansatz of the total field including the fluctuations in terms of reference frame. To obtain the Bogoliubov matrix we set our description in the rotating frame of the pump by factorizing the total field :  $\psi(r,t) = (\psi_0 + \delta\psi)e^{i(\mathbf{k}_p\mathbf{r} - \omega_p t)}$ . Consequently, all the dynamics on  $\delta\psi$  we might extract from the equation derived earlier happen in the moving frame where the fluid is at rest. However, in practice all the accessible observables are measured in the laboratory frame and are consequently dressed by the motion of the fluid. To directly predict the excitation spectrum as we expect to measure it in the experiment, we explicitly write the wavefunction as a function of the wavevector measured in the lab frame  $\mathbf{k}$  as :  $\psi(r,t) = \psi_0 e^{i(\mathbf{k}_p\mathbf{r} - \omega_p t)} + u_k e^{i\mathbf{k}\mathbf{r}}$  and look for their dynamics in the pump rotating frame by writing again  $\psi(r,t) = (\psi_0 + u_k e^{i(\mathbf{k} - \mathbf{k}_p)\mathbf{r}})e^{i(\mathbf{k}_p\mathbf{r} - \omega_p t)}$ . Under this form the wavevector  $\delta k = \mathbf{k} - \mathbf{k}_p$  appears as the wavevector of the fluctuations in the moving frame. To obtain the corresponding Bogoliubov matrix we first express the action of  $\mathcal{H}_{bog}$  on the fluctuations plane wave :  $u_k e^{i((\mathbf{k} - \mathbf{k}_p)\mathbf{r})}$  :

$$\mathcal{H}_{bog} u_k(\mathbf{r}) = \left[ \hbar\omega_{LP}^0 - \hbar\omega_p - \frac{\hbar^2}{2m_{LP}} \left[ -(\mathbf{k} - \mathbf{k}_p)^2 - 2\mathbf{k}_p(\mathbf{k} - \mathbf{k}_p) - \mathbf{k}_p^2 \right] + \hbar g_r n_r + 2\hbar g n_0 \right] U_k e^{i(\mathbf{k} - \mathbf{k}_p)\mathbf{r}} \quad (3.39)$$

$$= \left[ -\hbar\delta(k_p) + \frac{\hbar^2(\mathbf{k} - \mathbf{k}_p)^2}{2m_{LP}} + \hbar g_r n_r + 2\hbar g n_0 \right] U_k e^{i(\mathbf{k} - \mathbf{k}_p)\mathbf{r}} + \frac{\hbar^2 \mathbf{k}_p(\mathbf{k} - \mathbf{k}_p)}{m_{LP}} U_k e^{i(\mathbf{k} - \mathbf{k}_p)\mathbf{r}}. \quad (3.40)$$

where  $\delta(k_p) = \omega_p - \omega_{LP}^0 - \frac{\hbar k_p^2}{2m_{LP}}$  is the detuning between the pump and the LP polariton dispersion at  $\mathbf{k}_p$  provided we stay in the low wavevector parabolic approximation. The second term proportional to  $(\mathbf{k} - \mathbf{k}_p)^2$  is the kinetic energy. It shows that due to the fluid motion, the Bogoliubov spectrum observed in the lab frame is centered at the fluid wavevector. The last term describes the Doppler frequency shift due to the fluid motion  $\Delta\omega = \hbar^2 \mathbf{k}_p(\mathbf{k} - \mathbf{k}_p)/m_{LP} = \hbar \mathbf{v}_0(\mathbf{k} - \mathbf{k}_p)$  where  $\mathbf{v}_0 = \hbar \mathbf{k}_p/m_{LP}$  is the fluid velocity. Doing the same procedure for the complex conjugate the Bogoliubov matrix can be written as :

$$\begin{aligned}\mathcal{L}_B &= \begin{pmatrix} -\hbar\delta(k_p) + \frac{\hbar^2(\mathbf{k} - \mathbf{k}_p)^2}{2m_{LP}} + \hbar g_r n_r + 2\hbar g n_0 & \hbar g n_0 e^{2ik_p} \\ -\hbar g n_0^{-2ik_p} & \hbar\delta(k_p) - \frac{\hbar^2(\mathbf{k} - \mathbf{k}_p)^2}{2m_{LP}} - \hbar g_r n_r - 2\hbar g n_0 \end{pmatrix} \\ &\quad + \begin{pmatrix} \hbar \mathbf{v}_0(\mathbf{k} - \mathbf{k}_p) & 0 \\ 0 & \hbar \mathbf{v}_0(\mathbf{k} - \mathbf{k}_p) \end{pmatrix} \\ &= \mathcal{L}'_B + \hbar \mathbf{v}_0(\mathbf{k} - \mathbf{k}_p) \mathbf{I}_2\end{aligned}\tag{3.41}$$

where the Doppler effect appears in the second diagonal matrix and shifts the spectrum of  $\mathcal{L}'_B$  in the fluid rest frame. Looking at the roots of the  $\det(\mathcal{L}'_B - X\mathbf{I}_2) = 0$  we find the eigenvalues in the fluid frame through :

$$(\hbar\omega'_k)^2 = \left( \frac{\hbar^2(k - k_p)^2}{2m_{LP}} - \hbar\delta(k_p) + \hbar g_r n_r + 2\hbar g n_0 \right)^2 - (\hbar g n_0)^2,\tag{3.42}$$

From this we obtain the two branches of the so called Bogoliubov dispersion relation in the fluid frame :

$$\begin{aligned}\omega'_B^\pm(k) &= \pm \sqrt{\left( \frac{\hbar(k - k_p)^2}{2m_{LP}} - \delta(k_p) + g_r n_r + 2g n_0 \right)^2 - (g n_0)^2} \\ &= \pm \sqrt{\left( \frac{\hbar\delta k^2}{2m_{LP}} - \delta(k_p) + g_r n_r + 2g n_0 \right)^2 - (g n_0)^2}.\end{aligned}\tag{3.43}$$

while in the laboratory frame it yields :

$$\begin{aligned}\omega_B^\pm(k) &= \mathbf{v}_0 \cdot (\mathbf{k} - \mathbf{k}_p) + \omega'_B^\pm(k) \\ &= \mathbf{v}_0 \cdot (\mathbf{k} - \mathbf{k}_p) \pm \sqrt{\left( \frac{\hbar(k - k_p)^2}{2m_{LP}} - \delta(k_p) + g_r n_r + 2g n_0 \right)^2 - (g n_0)^2}.\end{aligned}\tag{3.44}$$

This expression is exactly what we would have obtained by directly applying a Galilean transformation to the spectrum in the fluid frame. With this form the dual structure of the solution space exhibited earlier appears less clear. In fact, the motion of the fluid breaks the symmetry and the Bogoliubov matrix no longer respects [Equation 3.28](#). However, while changing the reference frame Doppler shifts the eigenvalues, it leaves the eigenvectors untouched. More precisely, if  $(u_{k'}, v_{k'})^T$  is an eigenvector with eigenvalues  $\hbar\omega'_k$  in the fluid frame it is also an eigenvector in the lab frame for the shifted frequency. As a consequence, the norm of the eigenvectors is the same and our description of the solution space remains correct.

### 3.3.0.1 Bogoliubov mode energy

The gravitational Hawking effect involves the emission of particles with opposite energy and momentum at the horizon. In our analog system, we demonstrated the existence of modes with opposite frequency and norm. However, the concept of "opposite" is in our case only relative to the fluid energy and momentum. Consequently, what we called negative frequencies so far are actually positive frequencies that can be measured in the lab. The concept of negative energy can nevertheless be understood following Landau description of phonons emission in a superfluid [48]. Consider a fluid in motion with a velocity  $\mathbf{v}_0$  and a Bogoliubov spectrum  $\omega'_B(k)$  in the fluid frame. In the moving frame, the total energy of the system before any excitations are created is just the internal energy of the superfluid, while in the lab frame it is the sum of the internal energy and the kinetic energy of the fluid. Landau's criterion arises from analyzing the conditions under which excitations can be spontaneously generated without an increase in the system's total energy. The fundamental requirement for this process is:

$$v_0 > v_c = \min_k \frac{\omega'_B(k)}{k} \quad (3.45)$$

When  $v_0 > v_c$  certain excitations become energetically favorable, meaning that their spontaneous creation extracts energy from the bulk flow. From an external observer it seems that these modes carry energy away from the bulk motion or in other words, that the fluid is loosing energy.

Let us clarify this more quantitatively for the modes of interest here. To compute the energy of a given mode we introduce the energy functional of the system [15]:

$$E = \int d\mathbf{r} \left( \frac{\hbar^2}{2m_{LP}} |\nabla \psi|^2 + \frac{g_e}{2} |\psi|^4 \right) \quad (3.46)$$

where we set the external potential to zero. Inserting the expression of the total field including the fluctuations it is possible to expand the energy in terms of the fluctuations  $E = E^{(0)} + E^{(1)} + E^{(2)}$ . The first order vanishes because  $\psi_0$  minimizes the energy functional. The second order term is given by :

$$E^{(2)} = \int d\mathbf{r} \left( \frac{\hbar^2}{2m_{LP}} |\nabla \delta\psi|^2 + [2g_e|\psi_0|^2 - \delta(k_p)] |\delta\psi|^2 + \frac{g_e}{2} (\psi_0^*)^2 \delta\psi^2 + \frac{g_e}{2} \psi_0^2 (\delta\psi^*)^2 \right) \quad (3.47)$$

which can be cast in the vectorial form

$$E^{(2)} = \frac{1}{2} \langle \delta\psi | \eta \mathcal{L}_B | \delta\psi \rangle \quad (3.48)$$

where

$$\eta \mathcal{L}_B = \begin{pmatrix} -\hbar\delta(k_p) + \frac{\hbar^2(\mathbf{k} - \mathbf{k}_p)^2}{2m_{LP}} + \hbar g_r n_r + 2\hbar g n_0 & \hbar g n_0 e^{2ik_p} \\ \hbar g n_0^{-2ik_p} & -\hbar\delta(k_p) + \frac{\hbar^2(\mathbf{k} - \mathbf{k}_p)^2}{2m_{LP}} + \hbar g_r n_r + 2\hbar g n_0 \\ + \begin{pmatrix} \hbar \mathbf{v}_0(\mathbf{k} - \mathbf{k}_p) & 0 \\ 0 & -\hbar \mathbf{v}_0(\mathbf{k} - \mathbf{k}_p) \end{pmatrix}. \end{pmatrix} \quad (3.49)$$

Expanding the fluctuations in the eigenvectors basis of  $\mathcal{L}_B$  we obtain :

$$\begin{aligned} E^{(2)} &= \frac{1}{2} \sum_{k,l} \langle \delta\psi_k | \eta \mathcal{L}_B | \delta\psi_l \rangle = \frac{1}{2} \sum_k \langle \delta\psi_k | \eta | \delta\psi_k \rangle \hbar\omega_k \\ &= \frac{1}{2} \sum_k \langle \delta\psi_k | \eta | \delta\psi_k \rangle (\hbar\omega'_k + \hbar \mathbf{v}_0(\mathbf{k} - \mathbf{k}_p)). \end{aligned} \quad (3.50)$$

Let us analyze the case of a static fluid or equivalently what we obtain in the co moving frame. Setting  $\mathbf{k}_p = 0$  the energy contribution is :

$$\frac{1}{2} \langle \delta\psi_k | \eta \mathcal{L}'_B | \delta\psi_k \rangle = \frac{1}{2} \hbar\omega'_k \langle \delta\psi_k | \delta\psi_k \rangle_B. \quad (3.51)$$

When the system operates on the high density branch of the bistability loop one can show that the operator  $\eta \mathcal{L}'_B$  is positive definite [2]. This means that the left-hand side of [Equation 3.51](#) is real and strictly positive which imposes that  $\langle \delta\psi_k | \delta\psi_k \rangle_B$  is not zero. We can thus divide the whole expression by the norm and deduce that the  $\hbar\omega'_k$  is also real. Finally, the positivity of  $\eta \mathcal{L}'_B$  implies that the norm and the eigenvalue of a mode share the same sign. Hence, in the frame where the fluid is at rest the energy of a mode is always positive even if the corresponding frequency is negative.

In the lab frame, the eigenvalue must be replaced by its counterpart in the lab frame  $\hbar\omega_k = \hbar\omega'_k + \hbar \mathbf{v}_0(\mathbf{k} - \mathbf{k}_p)$  while the norm remains unchanged. If the fluid velocity is large enough one can see that the Doppler shift can give rise to negative energies which reminds the above discussion on the Landau criterion. Indeed, above a certain velocity, a mode emitted in the fluid with positive energy can appear as a negative contribution for an external observer sat in the lab frame.

### 3.3.1 Bogoliubov spectrum characterization

#### 3.3.1.1 Static fluid

Let us continue our description with the case of a static fluid. The dispersion is the same in both reference frames which can be seen by setting  $\mathbf{k}_p = 0$  in [Equation 3.44](#) :

$$\begin{aligned} \omega_B^\pm(k) &= \pm \sqrt{\left( \frac{\hbar k^2}{2m_{LP}} - \delta(0) + g_r n_r + 2g n_0 \right)^2 - (g n_0)^2 - \frac{i\gamma}{2}} \\ &= \pm \sqrt{\left( \frac{\hbar k^2}{2m_{LP}} - \delta(0) + g_r n_r + 3g n_0 \right) \left( \frac{\hbar k^2}{2m_{LP}} - \delta(0) + g_r n_r + g n_0 \right) - \frac{i\gamma}{2}}. \end{aligned} \quad (3.52)$$

Where we put the losses term back in the expression. This expression is in general drastically different from conservative systems where the Bogoliubov spectrum is linear. This feature is a direct consequence of interactions and thermodynamical equilibrium which imposes that the energetic cost of adding a particle to the system  $\mu$  is equal to the interaction energy due to the presence of the other bosons  $gn_0$ . Whenever the system is perturbed, it is thus more energetically favorable to dissipate energy through a collective excitation – phonons – rather than to add a particle to the condensate.

The polaritons dynamics is instead dictated by the interplay between losses, pumping and interactions which can give rise to optical bistability. As a consequence, the collective excitations are not necessarily sound waves and can be massive or even energetically unstable. Indeed, one can see from the second line of [Equation 3.52](#) that one of the terms in the square root might be negative depending on the values of the parameters. In the following, we will discuss the modifications of elementary excitations depending on the fluid excitation regime.

**Interplay with the bistability.** As demonstrated in the previous chapter, the system exhibits two distinct density regimes depending on the value of  $\delta(k_p)$  :

1. *Optical bistability*, when  $\delta(k_p) > \sqrt{3}\gamma_{LP}/2$ , which allows for two different interaction regimes depending on the pump intensity: a high-density regime characterized by strong interactions and a low-density regime with weak interactions.
2. *Optical limiter*, when  $\delta(k_p) < \sqrt{3}\gamma_{LP}/2$ . This case will not be considered here, as the various types of elementary excitations it entails are also present in the bistable regime.

To explore the different regimes of collective excitation along the bistability loop, we fix the detuning to be  $\delta(0) = 0.2\text{meV}$  and vary the pump intensity. The corresponding values that  $gn_0$  can take are plotted in [Figure 3.0 a\)](#). At each operating point the collective excitation spectrum is calculated using [Equation 3.52](#) and the results are shown in the subpanel b) of [Figure 3.0](#). Note that for the discussion we set the reservoir contribution to  $g_r n_r = \alpha gn_0$  with  $\alpha = 1.84$  based on previous measurement in the team [21]. The value of  $\alpha$  is expected to depend on sample parameters and more specifically on the exciton-photon detuning  $\omega_X - \omega_\gamma$ . In practice, the value we chose does not change much the discussion since the only relevant effect the reservoir has on the spectrum is to increase the total blueshift due to interaction. However, it must be taken into account whenever one wants to extract quantitative value from a measured spectrum as we shall see in the next chapter.

**Linear spectrum.** Let us first examine the most distinctive regime, which establishes a direct connection with conservative systems and was, in fact, the primary motivation for exploring this platform in the context of analog gravity experiments [19]. When the fluid operates at the turning point of the bistability (D) we demonstrated in the previous chapter that the detuning compensates the total interaction blueshift  $\delta(0) = g_r n_r + gn_0$ . Plugging this constraint in [Equation 3.52](#) we obtain :

$$\omega_B(k) = \pm \sqrt{\frac{\hbar k^2}{2m_{LP}} \left( \frac{\hbar k^2}{2m_{LP}} + gn_0 \right)}. \quad (3.53)$$

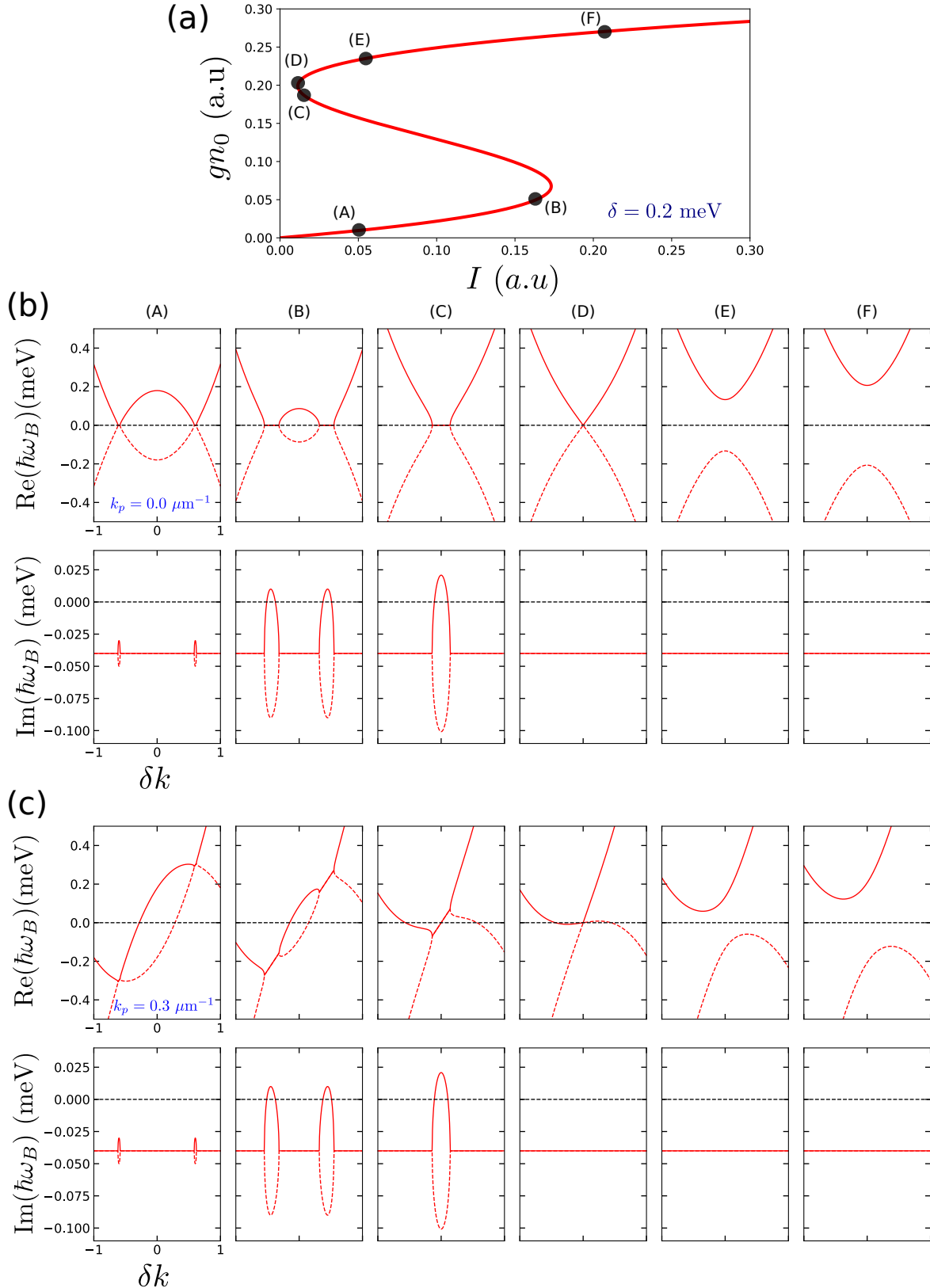


Fig. 3.0 **Analytical Bogoliubov dispersion relations.** (a) Bistability curve of the fluid density  $n_0$  as a function of the pump intensity  $I$ , calculated from [Equation 3.13](#), for a pump detuning  $\hbar\delta = 0.2$  meV. (b) Positive (solid red lines) and negative (dashed red lines) solutions of the Bogoliubov dispersion relation in the fluid reference frame, computed from [Equation 3.44](#), at the pump wavevector  $\mathbf{k}_p = 0$  (zero flow velocity), at the pump detuning  $\delta(0) = 0.2$  meV and for pump intensities indicated by the points A, ..., F in (a). Upper line: real part of the energy of elementary excitations. The black dotted line highlights the pump energy. Lower line: imaginary part of the energy of the elementary excitations. As long as it remains negative (below the black dashed line), the Bogoliubov solutions are dynamically stable. Note that near and all along the negative slope branch of the bistability, the modes are unstable, giving rise at the point B and C respectively to modulation instabilities (coupling of the positive solution with the negative solution at  $\mathbf{k} \neq 0$ ) and Kerr instabilities (coupling of the positive and the negative solutions with the pump mode at  $\mathbf{k} = 0$ ). At the other points A, D, E, F, the system losses fix the imaginary part at  $-\gamma_{LP}/2$ , stabilizing the fluid. (c) Same considerations as for (b) but for a pump wavevector  $k_p = 0.5 \mu\text{m}^{-1}$ . The fluid speed of flow is no longer zero, leading to an asymmetrization of the Bogoliubov solutions. In both (a) and (b) cases, the linearization of the solutions at low- $k$ , relating the generation of phonon-type elementary excitations, appears only at the turning point D. Adapted from [21]

We introduce the healing length  $\xi = \sqrt{\hbar^2/mgn_0}$  which is the characteristic length scale of the system below which the collective description of the fluid breaks down and microscopic effects must be taken into account. The spectrum exhibits two trends depending whether  $k$  is smaller or larger than  $1/\xi$  as shown on the (D) plot of [Figure 3.0 b\)](#). At low wavevector  $k \ll 1/\xi$  the spectrum is linear, for the normal branch we have :

$$\Re(\omega_B^+(k)) \sim c_s |k| \quad (3.54)$$

where  $c_s = \sqrt{\hbar g n_0 / m_{LP}}$  is the speed of sound in the fluid. For the ghost branch, represented by the red dashed line  $c_s$  is replaced by  $-c_s$ . At this operating point the driving laser is forcing the system exactly at its proper energy or said differently it is perfectly resonant with microcavity. In this regime, the long range interactions are dominated by collective deformations of the fluid –phonons– that propagate with the same group velocity  $\partial\omega/\partial k = c_s$  regardless their wavevector. The idea of having –in the low wavevector limit – a fixed velocity at all frequencies reminds the light cone with the difference that the sound velocity is not the same in all the reference frames. The linearity is a typical feature of quantum fluids and gives rise to spectacular collective behavior such as superfluidity [3] as well as topological protection of quantized vortices and dark solitons [53]. The Bogoliubov spectrum was reported in several experiments [71; 78] with different experimental methods while the linearity has been measured with an unprecedented resolution in the group [19]. The latter experiment was performed with a spectroscopy method recently developed [18] that we will describe and use in the next chapter.

In the high wavevector limit,  $k \gg 1/\xi$ , we recover the standard parabolic dispersion

blueshifted by the interaction.

$$\Re \epsilon(\omega_b^+(k)) \sim \frac{\hbar k^2}{2m_{LP}} + gn. \quad (3.55)$$

It's worth noticing that at even higher wavevector the parabolic approximation is not valid anymore and the full LP dispersion must be plugged in the Bogoliubov matrix. In this case one would observe that the Bogoliubov spectrum is flattened by the exciton line at large wavevector [34].

**Massive excitations regime.** If the system is brought further along the upper bistability branch ie if  $gn_0 + g_r n_r > \delta(0)$  a gap opens in the spectrum and linearity is lost as it can be seen in plots (E) and (F). A limited development of the spectrum around  $k = 0$  gives the parabolic approximation:

$$\Re \epsilon(\omega_b^+(k)) \sim \omega_B^+(0) + \frac{\hbar k^2}{2m_{LP}} \frac{(2gn_0 + g_r n_r - \delta(0))}{\sqrt{(2gn_0 + g_r n_r - \delta(0))^2 - (gn_0)^2}}. \quad (3.56)$$

This enables to provide the Bogoliubov modes with an effective mass :

$$m_{\text{det}} = m_{LP} \frac{\sqrt{(2gn_0 + g_r n_r - \delta(0))^2 - (gn_0)^2}}{(2gn_0 + g_r n_r - \delta(0))}. \quad (3.57)$$

Note that in the limit  $gn_0 + g_r n_r \rightarrow \delta(0)$ , the system recovers the massless scenario described earlier. The emergence of a gap in the spectrum can be understood as a form of "rigidity" in the fluid's phase, since introducing a phase fluctuation into the system requires a minimum energy.

In both the previous regimes, the terms in the square root of [Equation 3.52](#) remain positive at all wavevectors meaning the imaginary part of full dispersion never deviates from  $\gamma/2$  as shown in the subpanels of [Figure 3.0 b\)](#) ensuring the stability of the system.

**Low density regime.** Conversely, when the system is operating on the lower branch of the hysteresis loop, the amount of interaction is not sufficient to compensates for the detuning. Equivalently, it means that for some value of the wavevector the term in the square root of [Equation 3.52](#) becomes negative giving rise to additional contribution to the imaginary part of the spectrum. Note that it does not necessarily mean that the system is unstable. Indeed, an instability requires that the overall imaginary part of  $\omega_B^\pm$  is positive. At very low density like in (A), the inherent losses of the system are sufficient to dump the instability and the imaginary part remains negative at all  $k$ . If the pump strength is ramped up near the lower branch turning point (B) the imaginary part of the spectrum might become positive at some wavevector and makes the system unstable. Note that the point at which this happens depends on the experimental parameters. Finally, the point (C), located between the two branches, has an imaginary part that is highly positive at low wavevectors. This is the reason why this branch of excitation is often referred as unstable and can not be observed.

The discussion above also holds for the case of a moving fluid provided we set our description in the comoving frame and replace  $k$  by  $\delta k = k - k_p$  in [Equation 3.52](#).

### 3.3.1.2 Moving polaritons at finite $k_p$

In this section we consider again a fluid in motion at  $\mathbf{k}_p \neq 0$  that we describe in the lab frame. In terms of regime of collective excitations, the phenomenology is similar to the one described above and the discussion can be carried out in the same way. The only difference is that the dispersion relation is now centered around the fluid wavevector  $\mathbf{k}_p$  and "tilted" by the Doppler effect. Consequently, the Bogoliubov spectrum graphically loses an axis of symmetry which is a graphical manifestation that  $\mathcal{L}_B$  no longer respects the symmetry of [Equation 3.21](#). Again we set  $\delta(k_p) = 0.2\text{meV}$  and we plot the dispersion relation for the same operating points as in the static case, the results are presented in the subpanels of [Figure 3.0 c](#)). Note that the spectra are displayed as functions of the wavevector in the fluid frame since [Equation 3.44](#) mathematically depends only on  $\delta k$  enabling to compare the spectra in the two reference frames.

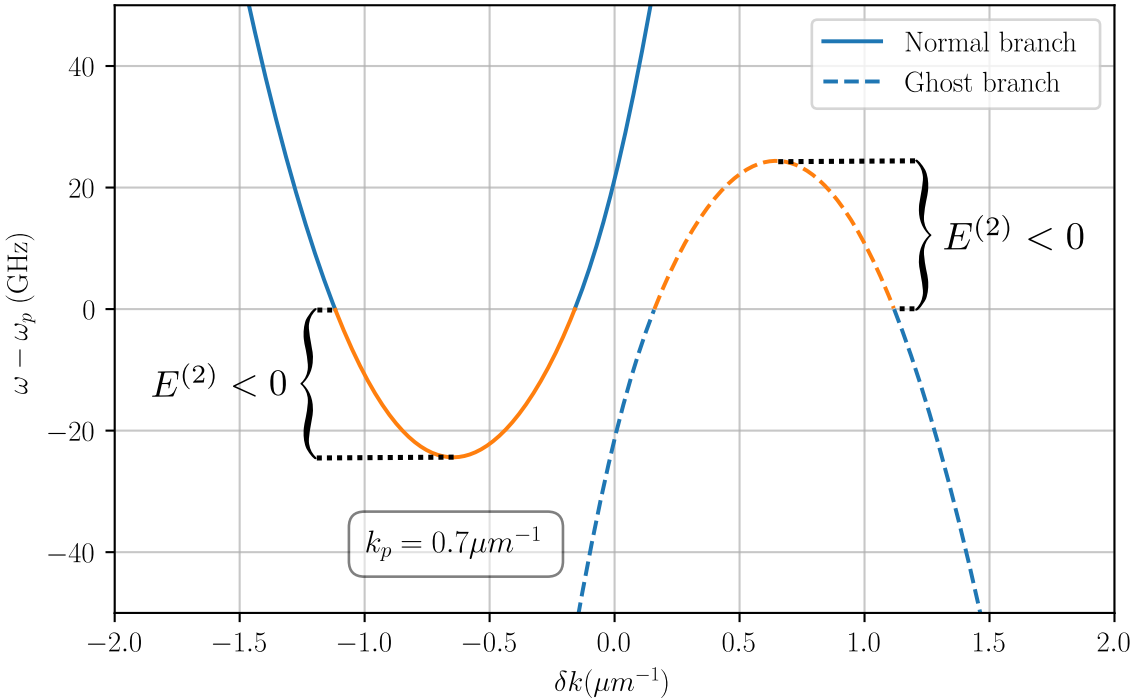


Fig. 3.1 Bogoliubov spectrum for a fluid in motion at  $k_p = 0.7\mu\text{m}^{-1}$  and  $\delta(k_p) = 0.2\text{ meV}$ . The dashed line represents the ghost branch ie the negative norm branch while the solid line represents the normal branch ie the positive norm branch. The blue color represents the positive energy modes while the orange represent the negative energy modes resulting from the product of a norm and a frequency with opposite signs.

In the linear case  $gn_0 + g_r n_r = \delta(k_p)$ , the low wavevector slope is modified by the fluid

velocity :

$$\begin{aligned}\Re(\omega_b^+(\delta k)) &\sim (c_s + \mathbf{v}_0)|\delta k| \quad \text{for } \delta k > 0 \\ \Re(\omega_b^+(\delta k)) &\sim (c_s - \mathbf{v}_0)|\delta k| \quad \text{for } \delta k < 0\end{aligned}\tag{3.58}$$

From this, one can see that when the fluid is supersonic  $\mathbf{v}_0 > c_s$  as in plot (D) some modes of the normal branch –the positive norm modes– are pulled down to the negative frequency domain. Symmetrically, some ghost branch modes –the negative norm modes– are pulled up to the positive frequency domain. In both cases, the excitations carry negative energy as explained in [subsubsection 3.3.0.1](#). In this regime, superfluidity is lost and any defect in the fluid flow can create excitations [3]. If the pump intensity is increased further like in (E) and (F), a gap opens again in the spectrum, the excitations are massive while the negative energy modes may disappear due to the gap opening. However, it does not mean that the possibility to create excitations with negative energy is lost as soon as the spectrum is no longer linear. Indeed, increasing further the pump velocity can lead to situations where the spectrum is massive but still has negative energy modes. A typical example of this case is presented in [Figure 3.1](#), where the pump wavevector was set to  $k_p = 0.7\mu\text{m}^{-1}$  and the other parameters stayed the same. A gap is present but the Doppler effect is strong enough to excite negative energy modes on both branches which are represented by the orange lines. Unlike the linear case, it is not possible to define a sound velocity for the low wavevector excitations. Consequently, the critical velocity to exceed for the appearance of negative energy modes does not match the velocity  $\sqrt{\hbar g n_0 / m_{LP}}$  that we still refer to as the sound velocity by analogy with linear case. Moreover, since the velocity affects the dispersion itself through the detuning  $\delta(k_p)$ , the usual procedure of applying the Landau criterion—where the energy of excitations is modified solely through a Doppler shift  $\omega_B(k) \rightarrow \omega'_B(k) + v_0 k$ —is no longer valid. By that, we mean that changing the pump wavevector while keeping all the other parameters equals (the pump power and frequency) will affect the interaction energy since the bistability loop is modified through the detuning. In this case, the spectrum itself is inherently altered by the fluid motion, meaning that the flow velocity does not simply act as a shift parameter but fundamentally changes the nature of the excitations. As a result, the criterion to observe negative energy waves must be modified to account for this direct dependence. In practice, the knowledge of an analytical expression for the critical velocity is not necessary and knowing that there exist one is sufficient as we will see in the experimental section.

It is now clear that depending on its velocity and parameters the fluid can exhibit a rich variety of collective excitations. Let us summarize what we reviewed so far in this chapter.

### Summary

- The polariton fluid exhibits a rich variety of collective excitations depending on the pump intensity and detuning through the bistability curve. The different modes are characterized by their norm and frequency.
- There exist a peculiar operating point at which the spectrum is linear allowing for the definition of a sound velocity  $c_s = \sqrt{\hbar g n_0 / m_{LP}}$ .
- The spectrum can also be massive if the system is pumped further along the high density branch and the effective mass depend on the detuning and the pump intensity.
- In the low density regime, the spectrum can become unstable and exhibit a positive imaginary part.
- Putting the fluid in motion can lead to the appearance of negative energy modes. The critical velocity for this to happen is a complex function of the detuning and the interactions. It does not match the speed of sound  $c_s$  as soon as the system does not operate at the turning point of the hysteresis loop.

In particular, if we restrict ourselves to high density regime where, inherent losses apart, the Bogoliubov dispersion remains real, the fluid can be either subcritical –all the modes carry positive energy– or supercritical –some modes carry negative energy. This discussion on the different collective excitation regimes paves the way to already understand how Hawking radiation can be observed in a polariton fluid. Indeed, creating an interface between a subcritical and a supercritical region will mix positive and negative energy modes just as a gravitational event horizon would. Then, showing that it can lead to paired correlated emission from vacuum will require to quantize the modes as we will see in the next section.

## 3.4 Hawking radiation in a transcritical fluid

### 3.4.1 Inhomogeneous pumping

We consider a driving pump defined as follow :

$$F_p(r,t) = \begin{cases} F_u e^{i(k_u x - \omega_p t)} & \text{if } x < x_h \\ F_d e^{i(k_d x - \omega_p t)} & \text{if } x > x_h \end{cases} \quad (3.59)$$

where  $x_h$  is an arbitrary position that will define the interface between the two regions. The wavevectors are chosen so that  $0 < k_u < k_d$  and  $k_d$  is sufficiently high to create a supercritical flow. The fluid is flowing toward the  $x > 0$  direction and the label "u" and "d" refer respectively to "upstream" and "downstream" region of the fluid with respect to the interface. We want to study Hawking emission of propagating modes so we set the laser frequency in order to ensure bistability in both regions namely  $\delta(k_u), \delta(k_d) > \sqrt{3}\gamma_{LP}/2$ , and the pump amplitudes  $F_u$  and  $F_d$  in such a way that the fluids operate on the high density branch of their respective hysteresis cycle. Note that the pump is two dimensional but only

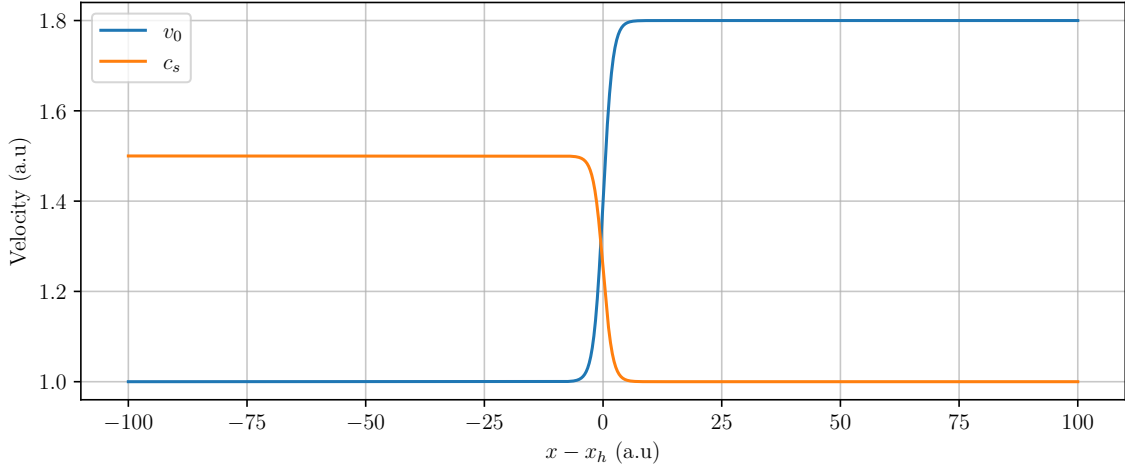


Fig. 3.2 **Typical fluid and sound velocity profiles of a transcritical flow.** The blue line represents the fluid velocity  $v_0(x)$  while the orange line represents the sound velocity  $c_s(x)$ .

depends on  $x$ . As we will justify it in the experimental section, the sample is in some extent also translationally invariant in the  $y$  direction. Henceforth, we restrict our description to an effective 1D model. Solving the GPE far from the interface gives two homogeneous regions with different asymptotic velocities  $v_u = \hbar k_u / m_{LP}$  and  $v_d = \hbar k_d / m_{LP}$ , and different densities  $n_u$  and  $n_d$ . We also account for fluctuations around each of these solutions the same way we did in the previous section which gives the asymptotic wavefunctions :

$$\psi(x,t) = \begin{cases} (\sqrt{n_u} + \delta\psi_u)e^{i(k_u x - \omega_p t)} & \text{if } x \ll x_h \\ (\sqrt{n_d} + \delta\psi_d)e^{i(k_d x - \omega_p t)} & \text{if } x \gg x_h. \end{cases} \quad (3.60)$$

While continuity conditions at  $x_h$  makes the definition of the wavefunction near the interface unclear for now. Typical density and velocity profiles are shown in Figure 3.2. For the sake of clarity, the speed of sound rather than the density is plotted allowing direct comparison with the fluid velocity. We remind nonetheless that the previous section made clear that the relevant velocity to cross generally differs from  $c_s$ .

We wish to solve the scattering problem for the Bogoliubov modes at the interface ie determine how a perturbation impinging on the analog horizon is scattered. In each homogeneous region, fluctuations are plane wave oscillating at  $\omega$  of the form :

$$\begin{pmatrix} u_k(x) \\ v_k(x) \end{pmatrix} = \begin{pmatrix} U_k^u \\ V_k^u \end{pmatrix} e^{i(k+k_{u,d})x}. \quad (3.61)$$

The wavevector  $k$  and frequency  $\omega$  satisfy the Bogoliubov dispersion relation  $\omega = \omega_B(k)$  that we remind here :

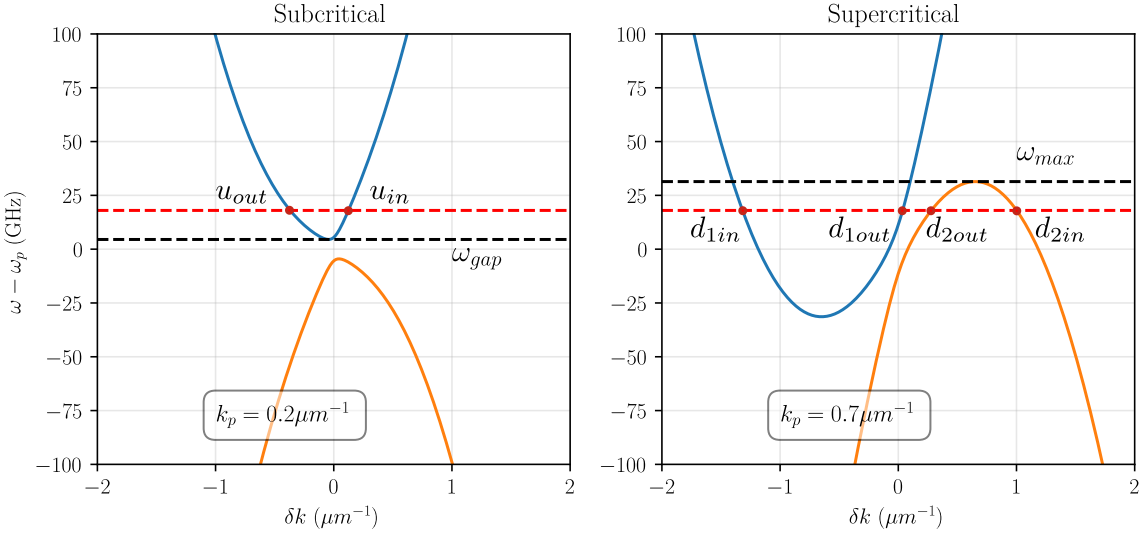


Fig. 3.3 **Bogoliubov spectrum in the upstream and downstream regions.** The Bogoliubov spectrum in the asymptotic upstream region (a) and downstream region (b) of the fluid, calculated from Equation 3.44 with  $\delta(0) = 30$  (GHz),  $k_u = 0.2 \mu\text{m}^{-1}$  and  $k_d = 0.7 \mu\text{m}^{-1}$ .

$$\omega_B(k) = v_{u,d}k \pm \sqrt{\left(\frac{\hbar k^2}{2m_{LP}} - \delta(k_{u,d}) + g_r n_r + 2gn_0\right)^2 - (gn_0)^2 - \frac{i\gamma}{2}} \quad (3.62)$$

where  $v_{u,d} = \hbar k_{u,d}/m_{LP}$  are the fluid velocities in the upstream and downstream regions. The corresponding dispersions are plotted in Figure 3.3. We see that, in the subcritical region ( $x < x_h$ ), positive- and negative-norm modes are still found exclusively at positive and negative frequency, respectively. However, in the supercritical region ( $x > x_h$ ), some positive-norm modes are dragged to negative frequencies (and reciprocally for negative-norm modes) by the Doppler effect.

Since there is redundancy of the information with respect to the zero frequency line let us fix  $\omega > 0$  and look for the wavevectors  $k$  satisfying  $\omega = \omega_B(k)$  in each region.

**Subcritical region.** In the upstream region  $x < x_h$ , for any  $\omega > \omega_{gap}$  where  $\omega_{gap} = \min \omega_B^+(k)$  there always exist two real solutions corresponding to positive norm modes as visible on the left panel of Figure 3.3. Depending on the sign of their group velocity  $v_g = \partial\omega/\partial k$ , we label the solution '*out*' if it propagates away from the interface and '*in*' if it goes toward the interface. Taking the square of Equation 3.62 the problem can be cast under a real coefficient polynomial equation of degree 4 in  $k$ . As a consequence, there exist two additional complex conjugate solutions. Depending on the sign of their imaginary part, they are either exponentially growing or decaying. Note that for  $0 < \omega < \omega_{gap}$ , the four solutions are non propagating with imaginary wavevectors.

**Supercritical region.** In the downstream region  $x > x_h$ , the situation is different and requires a different analysis. If  $\omega > \omega_{max}$  where  $\omega_{max} = \max \omega_B^-(k)$ , the situation is the same as in the upstream region. There exists two propagating solutions  $d_{1in}$  and  $d_{1out}$  lying on the normal branch with opposite group velocity as well as two non propagating modes. When  $\omega < \omega_{max}$ , in addition to the positive norm solution, the Doppler shift pulls two negative norm solutions  $d_{2in}$  and  $d_{2out}$  inherited from  $\omega = \omega_B^-(k)$

So far, the modes we have identified are defined locally, in the sense that a Bogoliubov plane wave that is a solution to the equations of motion in the upstream region is not a solution in the downstream region, and vice versa. Let us now see how we can construct global modes (GM) that are defined everywhere in the system and satisfy the equations of motion in both regions.

**Scattering solutions-in global modes** A general function to describe the fluctuations at  $\omega$  is obtained by the linear combination of all the possible propagating solutions :

$$\begin{pmatrix} u_k(x) \\ v_k(x) \end{pmatrix}_{u,d} = \left( \sum_{i \in \text{in}} \beta_i^{\text{in}} e^{ik_i^{\text{in}} x} \begin{pmatrix} U_{k_i^{\text{in}}} \\ V_{k_i^{\text{in}}} \end{pmatrix} + \sum_{i \in \text{out}} \beta_i^{\text{out}} e^{ik_i^{\text{out}} x} \begin{pmatrix} U_{k_i^{\text{out}}} \\ V_{k_i^{\text{out}}} \end{pmatrix} \right)_{u,d} \quad (3.63)$$

From this expression we can form the so-called scattering solutions. Such a solution reflects how a given local mode impinging on the interface is scattered into the other channels. For instance, for the case of an incoming mode from the upstream region, the scattering solution is a piece-wise function given by :

$$\begin{pmatrix} u_k(x) \\ v_k(x) \end{pmatrix}_u = \beta_u^{\text{in}} e^{ik_u^{\text{in}} x} \begin{pmatrix} U_{k_u^{\text{in}}} \\ V_{k_u^{\text{in}}} \end{pmatrix} + \beta_u^{\text{out}} e^{ik_u^{\text{out}} x} \begin{pmatrix} U_{k_u^{\text{out}}} \\ V_{k_u^{\text{out}}} \end{pmatrix} \quad \text{for } x \leq x_h \quad (3.64)$$

$$\begin{pmatrix} u_k(x) \\ v_k(x) \end{pmatrix}_d = \beta_{d2}^{\text{out}} e^{ik_{d2}^{\text{out}} x} \begin{pmatrix} U_{k_{d2}^{\text{out}}} \\ V_{k_{d2}^{\text{out}}} \end{pmatrix} + \beta_{d1}^{\text{out}} e^{ik_{d1}^{\text{out}} x} \begin{pmatrix} U_{k_{d1}^{\text{out}}} \\ V_{k_{d1}^{\text{out}}} \end{pmatrix} \quad \text{for } x \geq x_h. \quad (3.65)$$

A given solution and its derivative has to be continuous in space which imposes matching conditions at the interface. This condition will fix the coefficients  $\beta_i^{\text{in}}$  and  $\beta_i^{\text{out}}$  that can be interpreted as reflexion and transmission coefficients of the incoming wave at the interface. These modes are defined over the entire space and satisfy the equations of motion everywhere. From the three *in* local modes— $u_{in}$ ,  $d_{1in}$  and  $d_{2in}$ —in the  $\omega_{gap} < \omega < \omega_{max}$  regime it is possible to construct three global scattering solutions by following the same reasoning. At a given frequency  $\omega$  one can verify that these solutions are orthonormal with respect to the Bogoliubov inner product :

$$\begin{aligned} \langle \delta\psi_i^{\text{in}}(\omega) | \delta\psi_j^{\text{in}}(\omega') \rangle_B &= \int dx [u_{i,\omega}^*(x) u_{j,\omega'}(x) - v_{i,\omega}^*(x) v_{j,\omega'}(x)] \\ &= \text{sign}(\langle \psi_i^{\text{in}} | \psi_i^{\text{in}} \rangle_B) \delta_{ij} \delta(\omega - \omega'), \end{aligned} \quad (3.66)$$

where  $i,j \in \{u_{in}, d_{1in}, d_{2in}\}$  and sign is the sign function. As defined, the *in* global modes (GM) form a basis of the Bogoliubov problem valid at any  $x$  in the system.

**Outgoing global modes.** It is also possible to define the global solution of an outgoing wave. Take the outgoing mode  $d_{1out}$  in the downstream region : in the scattering picture it

originates from the transmission of an ingoing upstream mode  $u_{in}$  and the reflexion of the two ingoing downstream modes  $d_{2in}$  and  $d_{1in}$ . Doing this procedure in the  $\omega_{gap} < \omega < \omega_{max}$  range, the three *out* modes define three outgoing GM. Just as the *in* solutions, the *out* ones form an orthonormal basis of the solution space.

Since we found two basis describing the same set it is possible to express the *out* modes in terms of the *in* modes. Each three *out* modes are linear combination of the three *in* modes which define the so called  $3 \times 3$  scattering matrix  $S(\omega)$  :

$$\begin{pmatrix} \beta_u^{\text{out}}(\omega) \\ \beta_{d1}^{\text{out}}(\omega) \\ \beta_{d2}^{\text{out}}(\omega) \end{pmatrix} = S(\omega) \begin{pmatrix} \beta_u^{\text{in}}(\omega) \\ \beta_{d1}^{\text{in}}(\omega) \\ \beta_{d2}^{\text{in}}(\omega) \end{pmatrix}. \quad (3.67)$$

Note that in  $\omega > \omega_{max}$  case the  $d_{2out}$  mode is not present and the scattering matrix should be  $2 \times 2$ . However, to keep the notation the same everywhere, we also take into account the evanescent modes and allow some coefficient to be zero in the scattering matrix.

Since the orthonormal structure of the Bogoliubov modes was built with the modified norm  $\langle \cdot | \cdot \rangle_B$  it implies that  $S$  is unitary for the corresponding extended metric  $\nu$  :

$$S^\dagger(\omega) \eta S(\omega) = \eta. \quad (3.68)$$

where  $\eta = \text{diag}(1, 1, -1)$ . The unitary condition ensures energy conservation even in the presence of negative energy modes. Indeed, the  $-1$  sign in the third diagonal term account for norm conversion and originate from the scattering of positive norm modes into negative norm modes. The square modulus of a given coefficient  $|S_{ij}|^2$  gives the probability of reflexion or transmission of the mode  $i$  into the mode  $j$ .

To make this point clear, let us consider the example of the scattering of an incoming mode  $u_{in}$  with energy  $\hbar\omega$  in the upstream region. There is a probability  $|S_{uu}|^2$  that the mode gets reflected in  $u_{out}$  and a probability  $|S_{d1u}|^2$  that it gets transmitted into  $d_{1out}$  : both these modes have the same energy. The remaining term  $|S_{u2}|^2$  is the probability of transmission into a negative norm mode  $d_{2out}$  with the opposite energy  $-\hbar\omega$ . The unitary condition [Equation 3.68](#) ensures that the total energy is conserved  $1 = |S_{uu}|^2 + |S_{d1u}|^2 - |S_{d2u}|^2$ . Note that a complete derivation of the scattering matrix in an ideal step like case as well as a numerical study case was done for conservative systems in [63] and [30] respectively.

It is interesting to stress that the asymptotic classification of modes as *in* or *out* mirrors the procedure used in the study of quantum fields in black hole spacetimes, where a causal, time-oriented interpretation is adopted: *in* modes represent incoming configurations in the remote past, while *out* modes correspond to outgoing configurations in the distant future. This structure forms the basis of the Bogoliubov transformation formalism, which relates the two bases and captures the mixing between positive and negative frequency components that underlies processes such as particle production.

### 3.4.2 Modes quantization

So far, we described the fluctuations of the order parameter as classical fields. This approach shows that the Bogoliubov modes can exist in the system as solutions to the equations of motion. The scattering matrix tells us how an incoming wavepacket is scattered at the

interface [63]. Yet, our classical description requires an external perturbation to inject a given mode. Hence, it does not predict what would happen with highly non-classical state as an input, like the vacuum state. To achieve this, we need to quantize the modes.

**Quadratic Hamiltonian.** The first step is to write the field operator :

$$\hat{\psi}(x,t) = \psi_0(x,t)\hat{a}_{\psi_0} + \delta\hat{\psi}(x) \quad (3.69)$$

where  $\hat{a}_{\psi_0}$  is the operator that annihilates a polariton in the mean field state and  $\delta\hat{\psi}(x)$  is the fluctuation operator that annihilates a fluctuation particle. Plugging this ansatz into the GPE in its second quantization form 2.67 and going to first order in the fluctuations, one finds that the hamiltonian has a quadratic form in the fluctuation operator. As a consequence, the Heisenberg equations of motion for the Bogoliubov operator are linear in the fluctuations [15]. This property is of great importance. Indeed, it allows using a very simple quantization procedure. The fully quantum decomposition of the fluctuation operator is obtained from its classical counterpart 3.35 by promoting the coefficients  $b_k$  to bosonic operators. A  $u$  coefficient is associated to an annihilation operator while a  $v$  coefficient is associated to a creation operator. Under this prescription—whose validity is rigorously justified in [16]—the classical fluctuations field becomes :

$$\delta\hat{\psi}(x,t) = \sum_k \left[ u_k(x)\hat{b}_k e^{-i\omega_k t} + v_k^*(x)\hat{b}_k^\dagger e^{i\omega_k t} \right] \quad (3.70)$$

with the commutation relation

$$\|\phi_i\|_B \|\phi_j\|_B [\hat{b}_i, \hat{b}_j^\dagger] = \|\phi_i\|_B \delta_{ij} \quad (3.71)$$

which is the usual bosonic commutation relation for positive norm modes while for negative norm modes the annihilation operator and the creation operator are exchanged. To encode this property in a convenient way in the notation we rewrite the fluctuation field in a such a way that for negative norm modes an annihilation operator is associated to the  $v$  component as :

$$\delta\hat{\psi}(x,t) = \sum_{k \in S_+} \left[ u_k(x)\hat{b}_k e^{-i\omega_k t} + v_k^*(x)\hat{b}_k^\dagger e^{i\omega_k t} \right] + \sum_{k \in S_-} \left[ u_k(x)\hat{b}_k^\dagger e^{-i\omega_k t} + v_k^*(x)\hat{b}_k e^{i\omega_k t} \right] \quad (3.72)$$

This formulation has the advantage of making explicit that for negative norm modes the frequency  $\omega_k$  is associated to annihilation operators reflecting the particle-hole symmetry : the creation of a particle a yields the same contribution as the annihilation of a hole.

This procedure remains valid regardless the basis initially chosen and can especially be applied to the global modes exhibited earlier. The fully quantized fluctuations field can then be expressed in terms of *in* global operators as [63]:

$$\delta\hat{\psi}(x,t) = \int d\omega \sum_{j \in \{u_{in}, d_{1in}\}} [\hat{a}_j(\omega)u_{j,\omega}(x) + \hat{a}_j^\dagger(\omega)v_{j,\omega}^*(x)] + \int d\omega [\hat{a}_{d_2}^\dagger(\omega)u_{d_2,\omega}(x) + \hat{a}_{d_2}(\omega)v_{d_2,\omega}^*(x)] \quad (3.73)$$

where the operator  $\hat{a}_j(\omega)$  is the operator that annihilates a global *in* mode in channel  $j$  at frequency  $\omega$ . An equivalent expression can be written for the *out* global modes noted  $\hat{b}_i$ . The two sets of operators are again related by the scattering matrix :

$$\begin{pmatrix} \hat{b}_u(\omega) \\ \hat{b}_{d1}(\omega) \\ \hat{b}_{d2}^\dagger(\omega) \end{pmatrix} = S(\omega) \begin{pmatrix} \hat{a}_u(\omega) \\ \hat{a}_{d1}(\omega) \\ \hat{a}_{d2}^\dagger(\omega) \end{pmatrix} \quad (3.74)$$

Few comments can be done at this stage. First, since we deal with quadratic Hamiltonian, the matrix is exactly the same as that obtained in the classical case. From an experimental point of view this property is a crucial asset. Indeed, it means one can reconstruct the full matrix and hence all its quantum properties by just solving the scattering problem for classical modes which are much easier to engineer than quantum state. Any quantum correlations between the modes are in fact encoded in the matrix coefficients under phase and amplitude values. Of course, solving the scattering problem would only be a way to infer correlations between the modes but not to measure them. Still, it gives information about what you can expect from a given analog horizon.

Secondly, while the *in* and *out* operators describe the same physical system they generate two different Fock states and thus two distinct vacuum states  $|0_{\text{in}}\rangle$  and  $|0_{\text{out}}\rangle$ . Indeed, the vacuum is ultimately defined by the Hamiltonian and thus of the operators used to describe the system. This raises the question of whether a preferential basis can be found to provide an unequivocal description of the system. In fact, when a system does not exhibit time or space symmetries it is generally not the case [79]. In quantum field theory on curved spacetime, the Hamiltonian is typically time-dependent, which makes it difficult to define a unique set of operators and an unambiguous vacuum state. For instance, in the Unruh effect [74], an accelerating observer detects thermal radiation whereas an inertial observer perceives the 'standard' vacuum. This ambiguity lies at the core of particle creation processes in general.

This being said, the *in* and *out* basis remain, in the present case, wise choices to describe the system since they are natural basis to infer what can be measured in the lab.

Finally, we reminded at the beginning of this chapter that the wave equation describing the fluctuations on top of a moving polariton fluid could be casted under Klein-Gordon equation for a massive real scalar field in a curved spacetime. Treating the polariton fluid with the Bogoliubov theory showed that the formal equivalence with black hole equations could be pushed one step further by the presence of a Bogoliubov transformation between the *in* and *out* basis induced by the scattering matrix.

To say this in one sentence : while being very different, these two systems have in common the presence of a horizon that mixes positive and negative energy modes. The polariton platform is then an interesting system to study quantum field theory predictions –initially made for gravitational event horizons– through the universality of the underlying mathematical structure, a Bogoliubov transformation [40; 75]. This universality allows studying a wide classe of "superradiant" phenomena [11] sharing the common feature of creating entanglement [28].

### 3.4.3 Spontaneous emission

Now that we have a fully quantized description of the system, expectation values of physical observables can be straightforwardly computed by plugging the desired input quantum state and look how it is modified by the scattering matrix. Let us start with the most spectacular effect, that Stephen Hawking demonstrated in his original work [41] : spontaneous emission of correlated pairs from vacuum.

We are interested in the expectation value of the outgoing mode that is radiated by the interface away from the supercritical region  $\hat{b}_u$ . Its decomposition in terms of the *in* modes is :

$$\hat{b}_u = S_{uu}\hat{a}_u + S_{ud_1}\hat{a}_{d_1} + S_{ud_2}\hat{a}_{d_2}^\dagger. \quad (3.75)$$

The corresponding number operator  $\hat{N}_u^{out} = \hat{b}_u^\dagger \hat{b}_u$  then reads :

$$\begin{aligned} \hat{N}_u^{out} = & |S_{uu}|^2 \hat{a}_u^\dagger \hat{a}_u + |S_{ud_1}|^2 \hat{a}_{d_1}^\dagger \hat{a}_{d_1} + |S_{ud_2}|^2 \hat{a}_{d_2} \hat{a}_{d_2}^\dagger \\ & + S_{uu}^* S_{ud_1} \hat{a}_u^\dagger \hat{a}_{d_1} + S_{uu}^* S_{ud_2} \hat{a}_u^\dagger \hat{a}_{d_2}^\dagger + S_{ud_1}^* S_{uu} \hat{a}_u^\dagger \hat{a}_{d_1}^\dagger \\ & + S_{ud_1}^* S_{ud_2} \hat{a}_{d_1}^\dagger \hat{a}_{d_2}^\dagger + S_{ud_2}^* S_{uu} \hat{a}_{d_2} \hat{a}_u + S_{ud_2}^* S_{ud_1} \hat{a}_{d_2} \hat{a}_{d_1}. \end{aligned} \quad (3.76)$$

Using the bosonic commutation relation for the negative norm term  $|S_{ud_2}|^2 \hat{a}_{d_2} \hat{a}_{d_2}^\dagger = |S_{ud_2}|^2 (1 + \hat{a}_{d_2}^\dagger \hat{a}_{d_2})$ , the expectation value of the number operator in the *in* vacuum state  $|0_{in}\rangle$  is :

$$\langle 0_{in} | \hat{N}_u^{out} | 0_{in} \rangle = |S_{ud_2}|^2 \quad (3.77)$$

In the  $\omega \notin [\omega_{gap}, \omega_{max}]$  frequency range, the  $d_2$  mode is not present and there is no emission. Conversely, when  $\omega_{gap} < \omega < \omega_{max}$  the negative energy mode  $d_2$  is present and yields a non-zero emission from vacuum. This is the so-called Hawking effect. In fact, this radiation is correlated with all the other outgoing modes and one could even show tripartite entanglement among them [43]. Nonetheless, this is beyond the scope of this work and we will not go into the details of this calculation.

**State of the art.** Usually in the literature, correlations at the horizon between the out mode are inferred by computing the two points density correlation function [57; 63] :

$$g^{(2)}(x, x') = \frac{\langle \delta\hat{\psi}^\dagger(x) \delta\hat{\psi}^\dagger(x') \delta\hat{\psi}(x) \delta\hat{\psi}(x') \rangle}{\langle \delta\hat{\psi}^\dagger(x) \delta\hat{\psi}(x) \rangle \langle \delta\hat{\psi}^\dagger(x') \delta\hat{\psi}(x') \rangle} \quad (3.78)$$

Several numerical studies have been performed first in conservative systems [14] and then in polariton platforms [44; 57] demonstrating that the horizon of a transcritical flow can indeed exhibit Hawking radiation signature in its density correlation map. A typical  $g^{(2)}(x, x')$  map is shown in [Figure 3.4](#).

An experimental measurement of this correlation map has already been performed in Bose Einstein Condensate of Rb atoms [70]. In this experiment, the same analog black hole is created 7400 times, each shot providing a realization of the density fluctuation map.

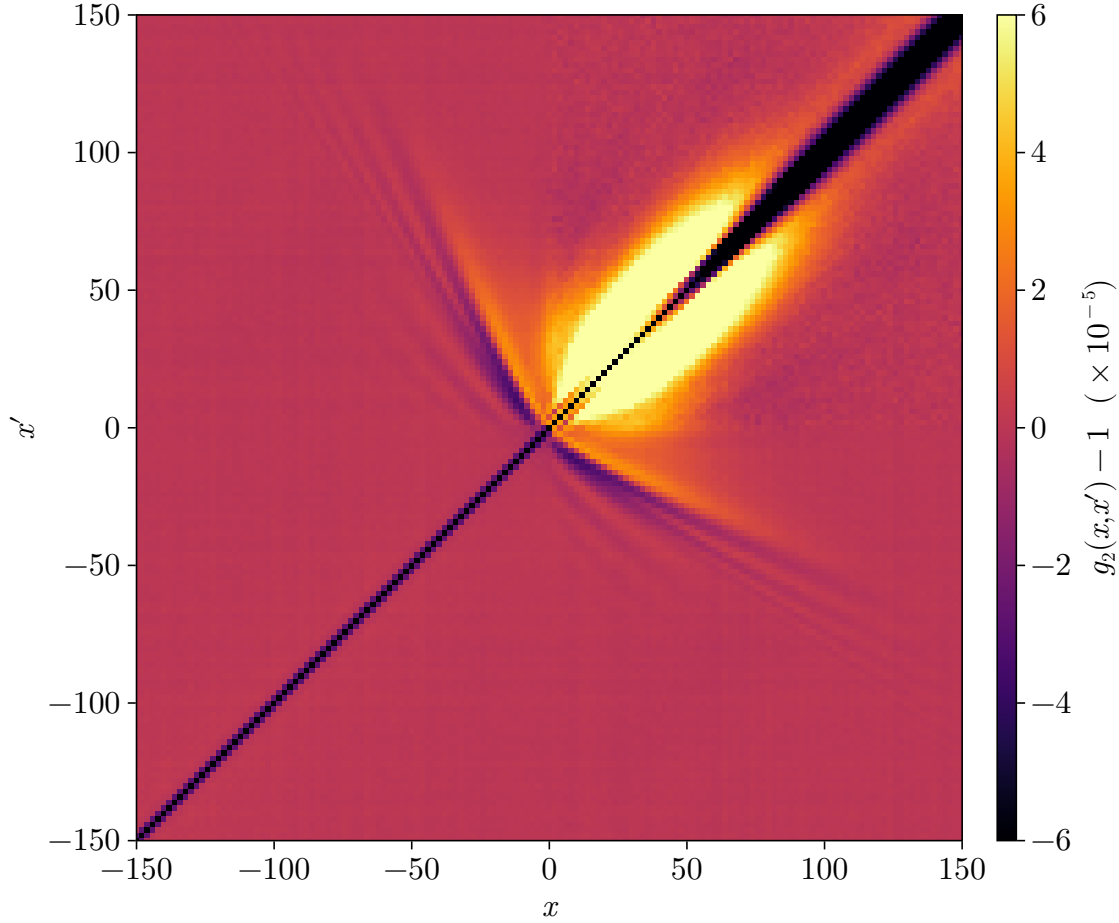


Fig. 3.4 **Density correlation map.** Two points density correlation function  $g^{(2)}(x, x')$  of a 1D transcritical polariton fluid. The correlation signal in the  $x > 0$  and  $x' < 0$  region (top-left panel) is the signature of the correlated Hawking emission at the horizon position  $x = 0$ .

The two points density correlation function is then computed by taking the average of  $\hat{\delta}\psi^\dagger(x)\hat{\delta}\psi^\dagger(x')\hat{\delta}\psi(x)\hat{\delta}\psi(x')$ . In the case of a polariton fluid the density fluctuations map is harder to obtain due to the out of equilibrium nature of the system. Indeed, due to the finite lifetime of the polaritons  $1/\gamma \sim 10$  ps, a single image of the fluid, even with the fastest camera, is already the result of many realizations of the fluctuations which hence average to zero. In the conservative case, a given shot of the experiment limits the condensate time evolution on a finite time interval when the trap is released. Therefore, looking for spontaneous emission in the polariton fluid is not a trivial task. However, the photonic nature of the polariton system allows to use many quantum optics techniques to look for correlation into other observables. For instance, a homodyne detection should in principle be able to detect the horizon effect on the vacuum quadrature since it acts as a two mode squeezer [9]. As a first approach one can look for a stimulated version of the experiment which, in the light of the previous section, can be theoretically grasped by injecting a coherent state in the scattering problem. As we

will see in [chapter 5](#), the polariton platform is better suited to look for signatures of Hawking radiation in momentum space and is closer to the theoretical proposal of [\[31\]](#).

### 3.4.4 Stimulated emission

Consider a coherent state input state  $|\alpha_{in}\rangle$  in the upstream region, eigenstate of the annihilation operator  $\hat{a}_u$  with eigenvalue  $\alpha_u \in \mathbb{C}$ . All the other input modes are left in the vacuum state which gives the overall input state :

$$|\alpha_{in}\rangle = |\alpha_u\rangle \otimes |0_{d_1}\rangle \otimes |0_{d_2}\rangle. \quad (3.79)$$

Using that  $\hat{a}_u |\alpha_{in}\rangle = \alpha_u |\alpha_{in}\rangle$  the expectation value in this state is straightforwardly computed as :

$$\langle \alpha_{in} | \hat{N}_u^{out} | \alpha_{in} \rangle = |S_{uu}|^2 |\alpha_u|^2 + |S_{ud_2}|^2 |\alpha_u|^2 \quad (3.80)$$

The presence of a coherent input state gives rise to an additional term  $|S_{uu}|^2 |\alpha_u|^2$  which is the "classical" reflexion of the input mode at the interface. To obtain a full scattering picture we also compute what is transferred in the other outgoing modes. The calculations are similar and we find :

$$\langle \alpha_{in} | \hat{N}_{d_1}^{out} | \alpha_{in} \rangle = |S_{d_1u}|^2 |\alpha_u|^2 + |S_{d_1d_2}|^2 \quad (3.81)$$

for the  $d_1$  outgoing mode and

$$\langle \alpha_{in} | \hat{N}_{d_2}^{out} | \alpha_{in} \rangle = |S_{d_2u}|^2 |\alpha_u|^2 + |S_{d_2d_2}|^2 \quad (3.82)$$

for the  $d_2$  outgoing mode. This negative energy mode can be interpreted as the Hawking partner of the positive energy mode  $u_{out}$ . If we assume that  $|\alpha_u|$  is large enough, the first term in each of the above equation dominates the second one which gives :

$$\frac{\langle \alpha_{in} | \hat{N}_i^{out} | \alpha_{in} \rangle}{|\alpha_u|^2} \approx |S_{iu}|^2 \text{ for } i \in \{u, d_1, d_2\}. \quad (3.83)$$

This quantity is accessible in the lab since it amounts to measuring the classical reflexion and transmission coefficients of the interface when a coherent state is sent toward the interface from the upstream region. Even though this feature is not triggered by quantum vacuum fluctuations it is still a manifestation of the Hawking effect. To understand this point one must compare the scenarios whether  $\omega$  is in  $[\omega_{gap}, \omega_{max}]$  or not. In the latter case, energy conservation is simply  $|S_{uu}|^2 |\alpha_u|^2 + |S_{d_1u}|^2 |\alpha_u|^2 = |\alpha_u|^2$  and reflects that each of the output channels carries a fraction of the incoming energy. While when  $\omega \in [\omega_{gap}, \omega_{max}]$  the same condition reads  $|S_{uu}|^2 |\alpha_u|^2 + |S_{d_1u}|^2 |\alpha_u|^2 - |S_{d_2u}|^2 |\alpha_u|^2 = |\alpha_u|^2$  due to the negative energy mode. This directly implies  $|S_{uu}|^2 |\alpha_u|^2 + |S_{d_1u}|^2 |\alpha_u|^2 \geq |\alpha_u|^2$  which means that the two positive energy channels carry more energy than what was injected, the excess being compensated by the negative energy mode. This amplification means that the incoming coherent state extracted energy from the transcritical region by exciting a negative energy mode. This is the same argument that led to the prediction of rotational superradiance in black hole physics [\[41\]](#) as well as in classical electromagnetic systems [\[83\]](#).

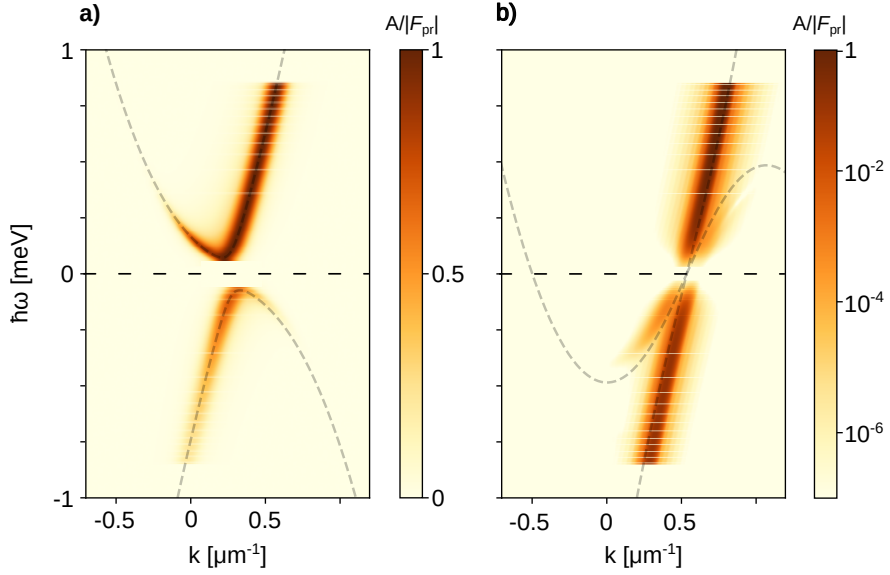


Fig. 3.5 Numerical simulation of scattering of a coherent probe on a transcritical fluid. **a)** amplitudes upstream. **b)** amplitudes downstream. The amplitudes  $A$  are normalized to the probe peak  $|F_{\text{pr}}|$ .

### 3.5 Numerical study of stimulated emission

Building on the methods developed in [44], we numerically studied the scattering of a coherent probe in a transcritical fluid featuring an acoustic horizon. The result is shown in Figure 3.5.

The amplitudes upstream and downstream are normalized to the peak amplitude of the probe. Note that this is different from the peak amplitude of the phonons created by the probe that then propagate towards the horizon before scattering onto it, so this procedure does not allow the evaluation of scattering coefficients  $|S_{u\alpha}|$  directly. However, it allows a qualitative comparison between the amplitudes in the reflected and transmitted modes.

We see that the amplitude in the reflected mode is strong at low  $\omega$  and decreases to an almost constant value ( $\approx 10^{-3}$ ) before  $\omega_{\text{max}}$ . The same is true for transmission into the negative energy mode (the amplitude is dominated by its complex conjugate according to Bogoliubov theory). In that frequency interval, transmission into the positive energy mode is low. After the reflection (and transmission into the negative energy mode) dies out, most of the probe amplitude is transmitted into the positive energy mode.

As discussed above, reflection upstream and the accompanying transmission into the negative-energy mode downstream are the hallmarks of amplification by the Hawking effect. The ability to explore scattering in the transcritical flow with a monochromatic coherent state thus provides us with a way to contrast various regimes of scattering, i.e. when there is Hawking emission or not.

### 3.6 Conclusion

In this chapter, we have explored the theoretical framework underlying the observation of Hawking radiation in a polariton quantum fluid. Starting from the Gross-Pitaevskii equation,

we derived the Bogoliubov spectrum of collective excitations, highlighting the rich variety of regimes depending on the fluid's density, velocity, and interaction strength. We demonstrated how the interplay between positive- and negative-energy modes leads to the possibility of particle creation at a transcritical interface, analogous to the Hawking effect in black hole physics.

The quantization of Bogoliubov modes revealed the fundamental role of the scattering matrix in describing the mixing of positive- and negative-norm modes at the horizon. This mixing not only enables spontaneous emission from vacuum but also provides a framework to study stimulated emission, where coherent input states amplify the Hawking-like radiation. Importantly, we showed that the amplification of outgoing modes is driven by the presence of negative-energy modes.

These results establish a theoretical foundation for the experimental investigation of analog Hawking radiation in polariton systems. By leveraging the properties of polariton fluids, such as their out-of-equilibrium nature and tunable parameters, this platform offers a promising avenue to probe fundamental aspects of quantum field theory in curved spacetime. In the next chapter, we will focus on the experimental implementation of these concepts and the challenges associated with observing Hawking radiation in practice.



## Chapter 4

# Optical generation and spectroscopy of arbitrary acoustic horizons

The previous chapter showed that the creation of a sonic horizon in a polariton fluid can lead to spontaneous emission of Bogoliubov modes provided the downstream region exhibits a collective excitation spectrum with negative-energy modes. Furthermore, it was shown that the strength of the emitted signal depends strongly on the curvature of the horizon, or in other words, its steepness. To ensure that such an effect is in principle observable in the laboratory, one needs to fully characterize the mean field of the fluid and locally probe its excitation spectrum. This chapter is dedicated to the description of the full optical generation of arbitrary transcritical fluids as well as the characterization of the excitation spectrum on both sides of the horizon. The measurement of this spectrum revealed for the first time negative-energy modes in a supersonic quantum fluid, validating the possibility to observe particle creation in a polariton fluid.

The first part of the chapter will focus on the generation of mean fields with arbitrary velocity profiles through the shaping of the pump laser phase. In the second part, we will present the pump-probe spectroscopy method used to locally measure the collective excitation spectrum, as well as the results obtained for several transonic fluids with different parameters. The results obtained are reported in [32].

### 4.1 Optical generation of an arbitrary fluid velocity field

We use the coordinates  $x$  and  $y$  to describe the microcavity plane. As explained in [chapter 2](#), translational invariance in the  $xy$ -plane ensure in-plane momentum conservation along photon absorption, while the wavevectors along the  $z$  direction are fixed by the cavity and quantum well lengths. Furthermore, in this experiment, the laser beam is set to be quasi-resonant with the lower polariton branch. As a consequence, the transverse phase of the laser is directly imprinted on the polariton field. Indeed, in the low wavevector limit, the lower polariton branch can be safely approximated by a parabola, namely :

$$\omega_{LP}(\mathbf{k}) = \omega_{LP}^0 + \frac{\hbar k^2}{2m_{LP}}. \quad (4.1)$$

The group velocity of a polariton is then  $\mathbf{v} = \frac{\partial \omega_{LP}}{\partial k} = \frac{\hbar \mathbf{k}}{m_{LP}} = \frac{\hbar \mathbf{k}_p}{m_{LP}}$  where  $k_p$  is the in-plane wavevector of the pump laser. In the case of a plane wave we can write  $k_p = \vec{\nabla}\theta(\mathbf{r})$  where  $\theta(r)$  is the spatial phase. This can safely be generalized to more complex spatial phase profiles, which provides a direct link between the driving laser phase and the velocity of the fluid :

$$\mathbf{v} = \frac{\hbar \vec{\nabla}\theta(\mathbf{r})}{m_{LP}}. \quad (4.2)$$

#### 4.1.1 Waterfall configuration

A first realization of a 1D acoustic black hole in a polaritonic system was done in [57] with the so-called waterfall configuration. The setup was composed of a microcavity etched to be one-dimensional (a microwire), and a defect was added in the middle of the wire to act as an external attractive potential and force the polariton flow to accelerate. The pump only illuminated the region upstream of the defect. The downstream region of the flow was then made of polaritons that propagate ballistically and whose speed is fixed by the interaction energy in the upstream region. Even though this configuration provides a natural fluid acceleration, the horizon geometry depends strongly on the defect shape and cannot be tuned easily. Furthermore, the collective excitation spectrum and the presence of negative-energy modes were not investigated, which prevented from concluding on the nature of the signal observed in the experiment. In this chapter, we present a different approach to generate such flows with an effective 1D fluid fully optically created, as well as a full characterization of the Bogoliubov spectrum.

#### 4.1.2 Target velocity profile

Before analyzing whether the fluid exceeds a critical velocity, the primary objective is to generate a flow exhibiting two homogeneous regions separated by a sharp transition, each characterized by a well-defined velocity. For clarity, the region preceding the transition will be referred to as the upstream region, with velocity  $v_{up}$  while the region following the transition will be designated as the downstream region, with velocity  $v_d$ . To model this configuration, a target velocity profile is defined as follows:

$$v(x) = \frac{v_d - v_{up}}{2} \tanh\left(\frac{x - x_h}{w_h}\right) + \frac{v_{up} + v_d}{2} \quad (4.3)$$

where  $x_h$  and  $w_h$  are the position and width of the transition respectively. This profile is represented in [Figure 4.1 a\)](#). One can then verify that :

$$\lim_{x-x_h \ll -w_h} v(x) = v_{up}, \quad (4.4a)$$

$$\lim_{x-x_h \gg +w_h} v(x) = v_d. \quad (4.4b)$$

Such a velocity profile provides great flexibility in the choice of the upstream and downstream velocities as well as the steepness and the position of the transition. From this, one can determine the phase that must be imprinted on the pump laser to generate such a flow profile by simple integration of [Equation 4.3](#), which gives :

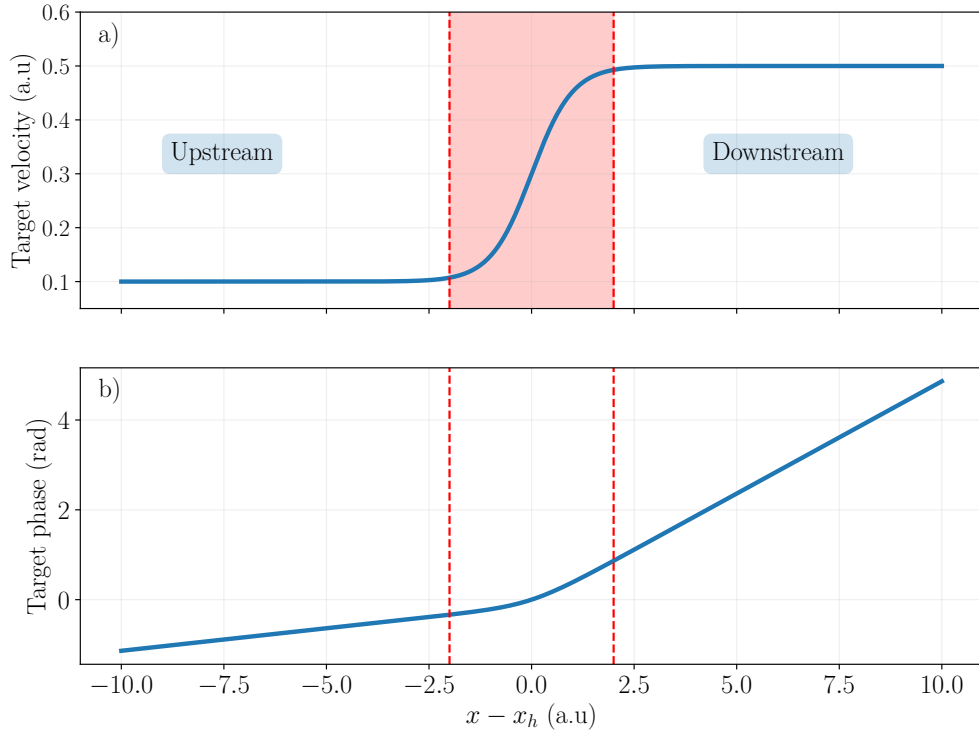


Fig. 4.1 **a)** Target velocity profile for input parameters  $v_{up} = 0.1$ ,  $v_d = 0.5$ ,  $x_h = 0$  and  $w_h = 1$  in arbitrary units. The red shaded area represents the transition region. **b)** Corresponding phase profile to be imprinted on the pump laser.

$$\phi(x) = \frac{m_{LP}}{\hbar} \int v(x) dx = \frac{m_{LP}}{\hbar} \left( \frac{v_d - v_{up}}{2} w_h \ln(\cosh\left(\frac{x - x_h}{w_h}\right)) + \frac{v_{up} + v_d}{2} x \right). \quad (4.5)$$

The latter is plotted in **Figure 4.1 b)**. The derivative of this curve at the position  $x$  corresponds to the local wavevector of the pump laser, or equivalently, this curve provides a cut of the wavefront of the driving laser. Indeed, the wavefront is defined as the surface of constant phase of the beam. Notably, considering that the driving laser also possesses a wavevector along the  $z$  direction, determined by the resonance conditions, the isophase surfaces of the total laser phase  $\theta_{laser}$  are given by:

$$\begin{aligned} \theta_{laser}(r) &= k_z z + \phi(x) = cst \\ &= \frac{2\pi n_{cav}}{\lambda_0} z + \theta(x) = cst, \end{aligned} \quad (4.6)$$

which is inverted as  $z \propto \phi(x)$ . Making a fluid with the desired velocity field then reduces to be able to imprint the phase given by **Equation 4.11** on the laser that resonantly excites the

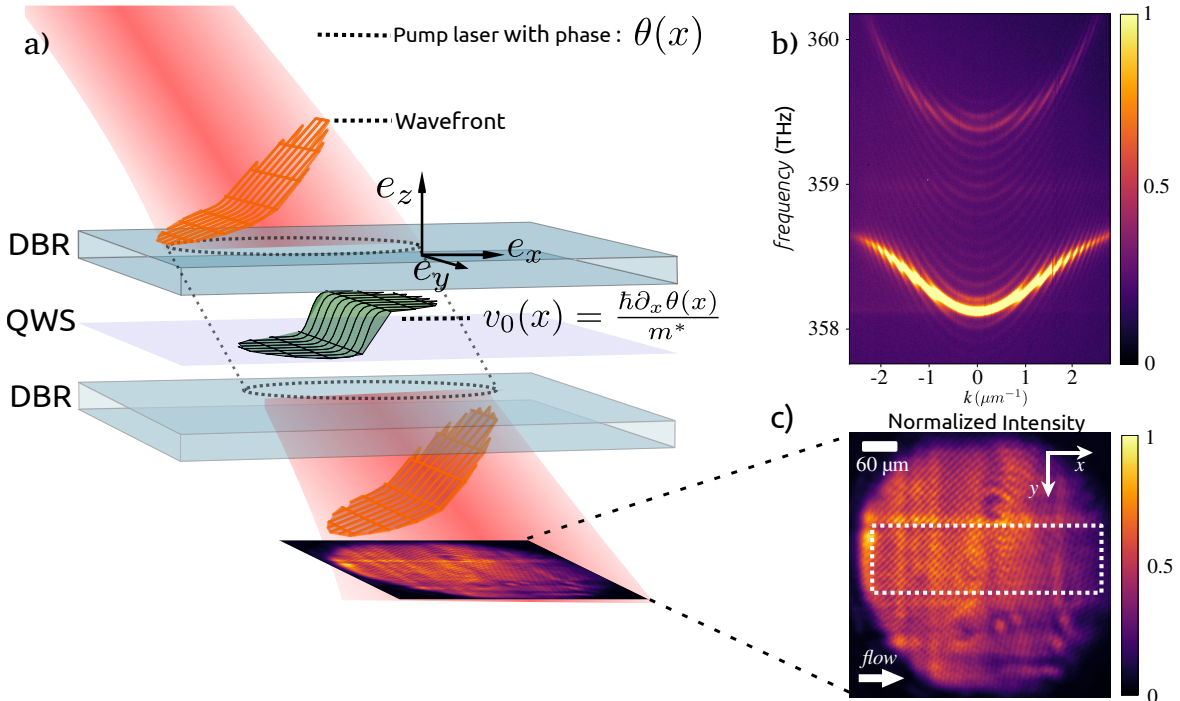


Fig. 4.2 Simplified scheme of the generation of a transonic fluid. **a)** The pump laser is shaped with the target phase profile and sent on the microcavity. The corresponding fluid velocity field is represented by the black surface lying on the Quantum Wells (QWs). **e)** The outgoing photons are collected and the sample plane is imaged on a CCD camera to obtain the fluid density map. **b)** Measured Lower and Upper polariton dispersion at the working point C5 – D6 (see Figure 4.5) at which the experiment was run. By fitting these dispersions, the effective LP mass can be extracted  $m_{LP} = 7.0 \times 10^{-35} \text{ kg}$

fluid. As we will see in the next section, this can be done with a Spatial Light Modulator (SLM).

A simplified scheme showing how the printing of the target wavefront in the sample plane creates the desired flow is presented in Figure 4.2 a). To verify that the fluid has the expected phase, we use the off-axis interferometry method whose principle is explained in subsection A.1.2 As an example, the measured phase corresponding to the mean field displayed in Figure 4.2 b) is shown in Figure 4.3.

**Controlling the local intensity.** Being able to modify on demand the intensity of the pump laser along with the phase is also crucial since the polariton fluid density, and thus the regime of collective excitations, depends on the input intensity as explained in chapter 3. Notably, if the system operates at the turning point of the upper bistability loop, it exhibits a linear collective excitation spectrum, and the speed of sound is directly linked to the detuning of the laser with respect to the lower polariton branch as  $gn + g_r n_r = \delta(k_p)$ . More generally, the possibility to move onto the higher branch of the bistability enables control over the gap opening in the Bogoliubov spectrum, transitioning from a linear, massless spectrum to a parabolic, massive one. Once again, this can be achieved using the SLM by locally adjusting

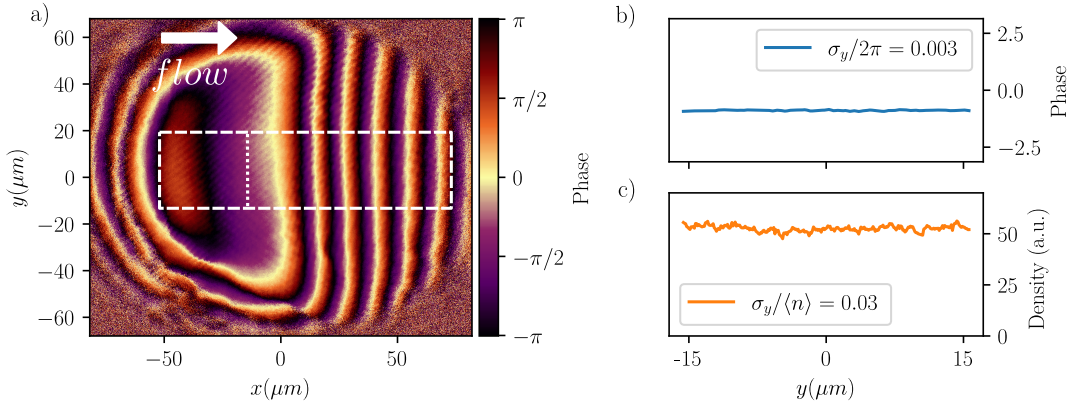


Fig. 4.3 **a)** Measured phase of the mean field shown in Figure 4.2. The curvature of the fringes present in the upstream region is due to the nonlinear self-focusing. The region of interest in which we assume translational invariance is represented by the white dashed rectangle. **b)** Cut of the phase in the  $y$  direction represented by the dotted white line in the rectangle. The variation to the phase with respect to  $2\pi$  is equal to 0.3%. **c)** Cut of the intensity of the mean field in the  $y$  direction at the same location as **b)**. The corresponding relative intensity variation is equal to 0.3%.

the depth of the phase grating under the target phase profile, as explained in subsection A.1.4. This adjustment reduces the number of photons directed into the first diffracted order. This method is widely used to create top-hat intensity profiles and is of significant interest in metrology and cold-atom experiments to minimize systematic effects [55].

To summarize, it is possible to generate and monitor a fluid with arbitrary density and velocity flow by shaping the pump laser both in phase and intensity. We hence have a full optical way to create effective spacetimes on which we can study the propagation of the collective excitations of the fluid near the transition region.

### 4.1.3 Effective 1D fluid

So far, the description of the fluid both in velocity and density was one-dimensional despite the fluid is actually a 2D system. This assumption relies on the fact that the fluid wavefunction is invariant under translation in the  $y$  direction in the region of interest represented by the white dashed rectangle of Figure 4.3. This area is about  $130 \mu m$  long and  $30 - 40 \mu m$  wide. Cuts of both the phase and density in the direction orthogonal to the propagation are shown in Figure 4.3 b) and c). Periodic modulations are present because of back reflection on the protection screen of the camera sensor and are present even without passing through the sample. These modulations can be removed using Fourier filtering which allows to compute the variation of the phase with respect to  $2\pi$ ,  $\sigma_y^{ph}/2\pi = 0.3\%$  as well as the relative intensity variation  $\sigma_y^I/\langle I \rangle = 3\%$ . As a consequence, we can safely assume that the fluid is effectively 1D in the region of interest. This is in contrast with the work [57] previously mentioned. In the present configuration, the shape of the horizon is fixed by the phase of the exciting laser and can be tuned at will, which is crucial to study the effect of the horizon steepness

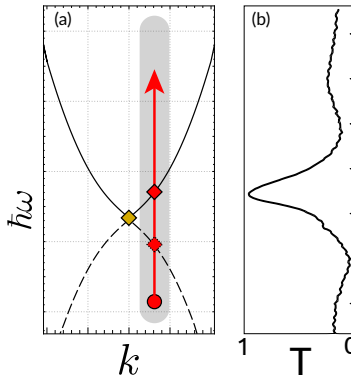


Fig. 4.4 Simplified scheme of the pump-probe spectroscopy method. **a)** At a given in plane wavevector represented by the red arrow, the probe frequency is scanned around the mean field frequency and is transmitted when it resonates with the Bogoliubov branch. **b)** Typical transmission spectrum of the probe at the wavevector shown in **a**).

on the emitted signals. Moreover, the presence of the pump laser in the downstream region brings a significant advantage : the velocity of the fluid can be changed as will and does not depend on the interaction energy of the upstream region, allowing the study of many fluid configurations.

## 4.2 Experimental spectroscopy of the collective excitation spectrum

The analog of the Hawking radiation in a polariton fluid is the spontaneous emission of Bogoliubov modes from the horizon. When the system is operating at the turning point of the bistability, the Bogoliubov spectrum is gapless and linear which enables the definition of a speed of sound  $c_s = \sqrt{\hbar g n / m_{LP}}$  and speak without ambiguity of sonic excitation in the low wavevector limit. In this regime, the condition to observe negative-energy modes coincides with the fluid being supersonic, as explained in the previous chapter. However, creating a stable fluid at the turning point is quite challenging and the measurement of the spectrum linearity requires experimental techniques that are hard to implement on a moving fluid [21]. Nevertheless, linearity is not mandatory to observe Hawking radiation since it only requires the mixing between positive and negative-energy modes which can be achieved without operating at the turning point. Besides, a gap opening in the Bogoliubov spectrum brings new physics since it widens the study of quasiparticle creation to the case of massive particles. In this section, we discard the necessity to have sonic excitations and measure the presence of negative-energy modes in a wide range of fluid configurations exploring various asymptotic velocities and horizon steepness.

### 4.2.1 High resolution pump-probe spectroscopy method

The measurement of the collective excitations spectrum consists in scanning the mean field resonance by measuring the transmission of a weak probe laser at different incidence angles.

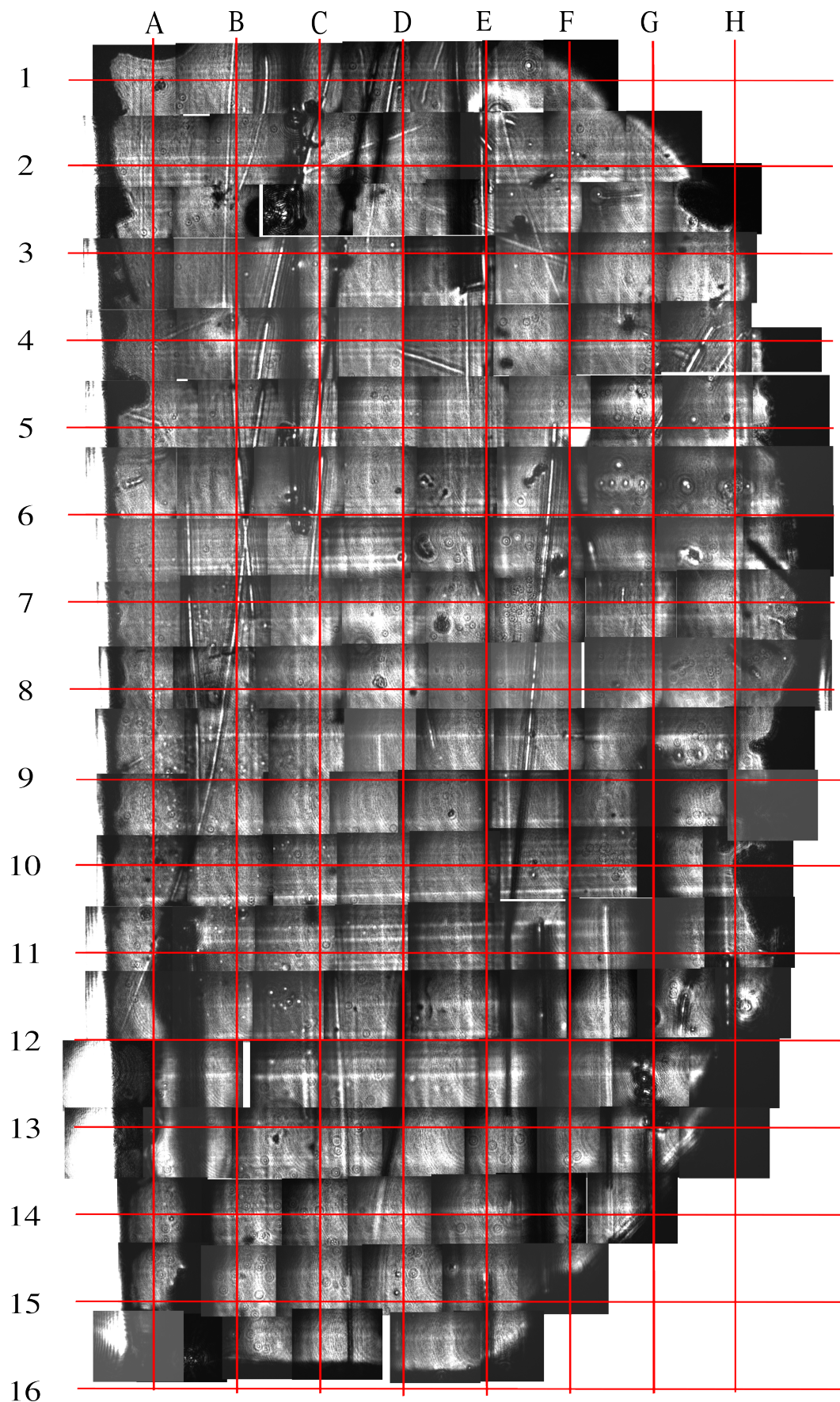


Fig. 4.5 Map of the sample used in this experiment.

First, a polariton fluid is created with a driving laser as described in the previous section. A probe laser is then sent on the sample with a well defined incidence angle corresponding to a precise in plane wavevector, as explained in [section 2.1](#). The frequency of the probe is then scanned around the mean field frequency. When the probe frequency matches the frequency of a collective excitation mode, the probe laser gets transmitted by the cavity and can be detected. Frequency scans are then repeated for different incidence angles providing each time a transmission spectrum of the probe as shown in [Figure 4.4](#). To make sure that we are in the weak perturbation regime the intensity of the probe is set two orders of magnitude below that of the pump. To collect only the signal emitted in the perturbation mode, a tunable pinhole is placed in the Fourier plane of the collection path and tracks the probe in-plane wavevector position to filter out the unwanted photons. Finally, the probe intensity is modulated at  $f_{mod}$  in order to isolate its transmission from the very strong signal of the pump. The remaining light is then sent on a photodiode connected to a Spectrum analyzer that demodulates the signal at  $f_{mod}$  to obtain the transmission spectrum. In the end, all the scans are put together to reconstruct the full Bogoliubov dispersion as typically shown in [Figure 4.7](#).

### 4.3 Experimental setup

The setup used in this experiment is shown in [??](#). The sample is a microcavity consisting of three InGaAs quantum wells sandwiched between two highly reflecting planar GaAs-AlGaAs Bragg mirrors as described in [chapter 2](#). To optimize the light-matter coupling, the quantum wells, separated by GaAs barriers, are located at the three antinodes of the cavity, which has a finesse of the order of 3000. A complete map of this sample is shown in [Figure 4.5](#). This map enables to perform an experiment over several days at the same working point and to overcome the problem due to daily cooling and warming procedures imposed by the open-cycle cryostat. The experiment described in this chapter was run on the working point C5 – D6. The set-up is divided in three main paths, the pump path, the probe path and the collection path.

- **The pump path** represented by the blue box is used to create the steady states of the experiment. The polariton fluid is generated by a circularly polarized CW Ti:Sapphire laser with a sub-MHz linewidth. This laser frequency can be precisely tuned around the LP resonance energy centered around 836 nm in our sample. An acousto-optic modulator (AOM) together with a Proportional-integral-derivative feedback on the AOM driving RF are used to stabilize the laser intensity and ensure that the experiment is constantly run at a single fluid density. The stabilized Gaussian beam is reflected on the spatial light modulator (SLM), which imprints the target phase  $\theta_p(x) = \int v_0(x)dx$  that determines the fluid velocity  $v_0(x)$  at each point. The SLM plane is imaged on the input plane of the cavity with two focal-length matched telescopes ( $2f - 2f$  configuration).
- **The probe path** represented by the red box is used to measure the collective excitation spectrum. The probe is another tunable CW Ti:Sapphire laser with the same polarization as the pump beam. The probe is sent on the sample with a well-defined incidence angle controlled by another SLM on which a tunable step blazed grating is imprinted.

The frequency of the laser is scanned over 220 GHz around the mean field frequency and monitored by a high resolution wavemeter. An AOM and a Proportional-integral-derivative feedback are also used to both stabilize the intensity along the scan and apply a  $f_{mod} = 5$  MHz intensity modulation.

- **The collection path** located after the sample is used to collect the output signals coming from the fluid. A microscope objective sends the outgoing field on a 50:50 BS. One part is directed to an optical system to make the image both in real and momentum space of the field. For both lasers, a pick-up is made after their respective AOM to have a phase reference and perform off-axis interferometry measurement. Another part is sent to the apparatus described in [Figure 4.1.3](#) to measure the transmission spectrum of the probe. The tunable pinhole is made with a DMD and is placed in the Fourier plan of a lens, selecting only photons arriving at the position of the pinhole and sending them to the collection photodiode. Given the relative size of the probe mode and the size of a pixel of the DMD, the resolution of the pinhole can go down to  $\delta k = 0.0005 \mu\text{m}^{-1}$ . The collection photodiode is then connected to a spectrum analyzer set in zero span at  $f_{mod}$  to demodulate the signal and obtain the transmission spectrum of the probe. On both path a set of  $\lambda/4$ ,  $\lambda/2$  and *PBS* allows to control and filter the polarization of the signal.

**Scan resonances analysis.** The maximum value and the linewidth of the probe transmission and reflection peaks are directly related to the real and imaginary parts of the energy  $\hbar\omega_b$  of the Bogoliubov dispersion relation. If we consider plane wave like excitations

$$\psi_{LP}(t) \propto \exp(-i\omega_b t) = \exp(-i\Re(\omega_b)t) \cdot \exp(i\Im(\omega_b)t), \quad (4.7)$$

one easily verifies by taking its temporal Fourier transform that its spectral density has the following Lorentz-distribution law

$$I(\omega) = |\psi_{LP}(\omega)|^2 \propto \frac{1}{(\omega - \Re(\omega_b))^2 + \left(\frac{\Im(\omega_b)}{2}\right)^2}. \quad (4.8)$$

At each probe wavevector  $k_{pr}$  the transmission spectrum  $I_{k_{pr}}(\omega)$  is fitted with a Lorentzian function to extract the real and imaginary parts of the Bogoliubov dispersion  $\omega_b(k_{pr})$

## 4.4 Experimental results

### 4.4.1 Homogeneous fluid

We first study homogeneous fluids with non-zero velocities to see the effect of the Doppler shift on the collective excitations spectrum. In this section, the pump is a gaussian beam which creates fluid having a spatial extension of approximately 150  $\mu\text{m}$ . The input angle of the pump is controlled in the same way as the probe by printing a tunable step blazed grating on the SLM. In each measurement, the effective detuning  $\delta(k_p) = \omega_p - \omega_{LP}^0 - \hbar k_p^2 / 2m_{LP}$  is high enough to be in the bistable regime and the input pump intensity is chosen so the

system operates on the higher branch of the hysteresis curve quite far from the turning point. The probe is set to be two order of magnitude weaker than the pump and it has the same spatial extension and polarization.

**Direct normal branch measurement.** We create a set of homogeneous fluids with increasing in plane wavevectors  $k_p$  while keeping the pump frequency constant. For each fluid, we use the pump-probe spectroscopy method to measure the probe transmission spectrum as shown in [Figure 4.7](#). The DMD is programmed to display pinholes that track the wavevector of the probe laser along the scans. In this case the system measures the direct transmission of the probe. The first measurement **a)** is made with the pump laser turned off which means in the absence of interactions within the sample. The probe transmission then scans the bare cavity resonances and recovers the parabolic shape at low wavevector of LP branch. From this measurement we extract the detuning between the pump laser and the LP branch at zero wavevector  $\delta(0) = 33$  GHz. The blueshift due to interaction lifts the dispersion **a)** to higher energies whereas the Doppler shift modifies the resonances according to  $\omega' = \omega + \mathbf{v}_p \delta \mathbf{k}$  where  $\mathbf{v}_p$  is the fluid velocity  $\mathbf{v}_p = \hbar \mathbf{k}_p / m_{LP}$ . As the fluid velocity increases, the branch is bent and moved toward the pump wavevector. For  $k_p \geq 0.3$  we already see some resonances lying under the pump energy. As explained in the previous chapter, the energy sign of a collective mode is given by :

$$\text{sign}(E) = \text{sign}(\omega_B) \times \text{sign}(\|\delta\psi\|_B) \quad (4.9)$$

where  $\|\delta\psi\|_B$  is the norm of the mode defined in [Equation 3.24](#) and  $\text{sign}(\omega_B)$  is taken with respect to the pump energy. Since the normal branch has a positive norm, the resonances located below the pump frequency are negative-energy modes. As it can be seen, the ghost branch is not visible through direct excitation. This feature has a double origin : first the ghost branch is not optically resonant with the cavity which makes photon injection difficult at its energy. Secondly, the Bogoliubov coefficient  $v_k$  of the negative norm branch is very small compared to  $u_k$ . In the presence of a coherent state like the probe, the population then scale as  $v_k^2 |\alpha|^2 \ll u_k^2 |\alpha|^2$  where  $\alpha$  is the intracavity amplitude of the probe.

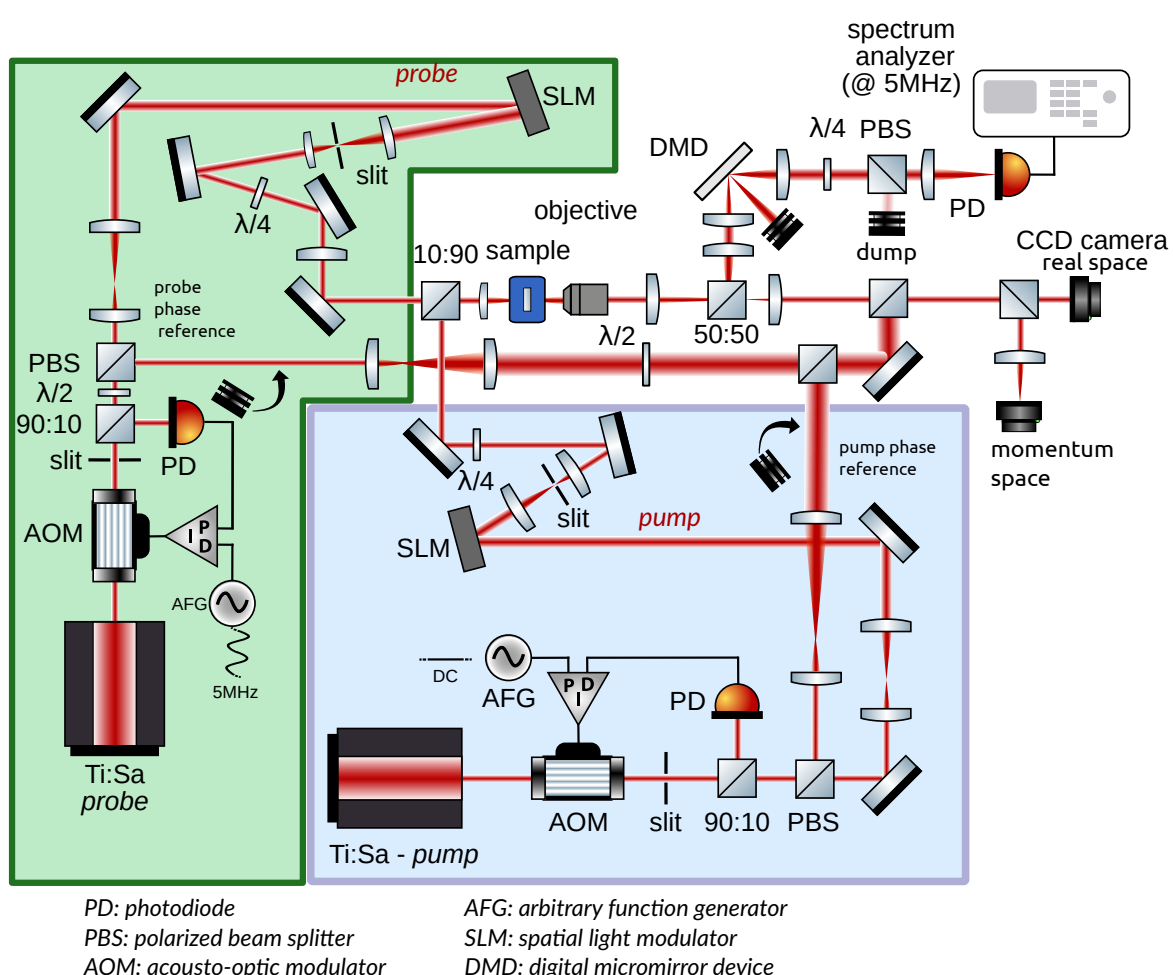


Fig. 4.6 Experimental setup

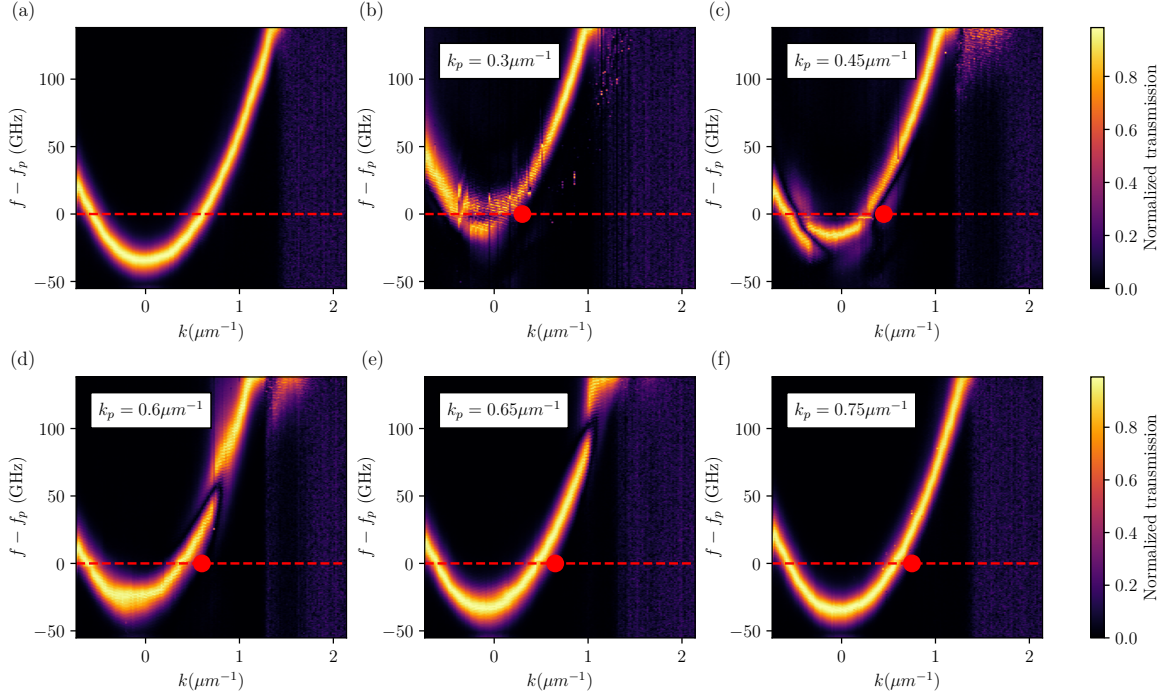


Fig. 4.7 a) Bare cavity dispersion measurement with the pump-probe spectroscopy method in the absence of fluid. The parabolic shape of the Lower Polariton branch is observed. The red dashed line represent the mean field frequency that was kept constant for all the measurements. From this we can measure the detuning between the pump laser and the LP branch at  $k = 0$ ,  $\delta(0) = 33$  GHz. b), c), d), e) and f) measured Bogoliubov normal branches for homogeneous fluid with velocities 0.75, 0.98, 1.23, 1.29 and  $1.43 \mu\text{m ps}^{-1}$  respectively, corresponding to the pump wavevector values in the inset of each figure.

**Ghost branch indirect measurement.** To overcome the difficulty to directly excite the ghost branch, we take advantage of the strong nonlinearities of the system to induce population through four wave mixing process. Indeed, because of the bosonic nature of Bogoliubov excitations, the occupation of the normal branch in the probe wavevector mode should stimulate the parametric conversion of two pump polaritons into a Bogoliubov pair with opposite wavevectors and energies with respect to the pump, namely :

$$(k_p, k_p) \rightarrow (k_p + \Delta k, k_p - \Delta k), \quad (4.10a)$$

$$(\omega_p, \omega_p) \rightarrow (\omega_p + \Delta\omega, \omega_p - \Delta\omega). \quad (4.10b)$$

The emission in the ghost branch is then boosted by a factor  $(u_k v_k)^2 |\alpha|^2$  [34]. In practice, this measurement can be done by changing the positions of the tunable pinhole so it tracks wavevectors opposite to the probe with respect to the pump. More precisely, when a scan at  $k_{pr} = k_p + \Delta k$  is made, the pinhole is set at  $k_{pr} = k_p - \Delta k$  to collect the signal emitted in the conjugate mode.

Here we create again a homogeneous fluid with wavevector  $k_p = 0.6 \mu\text{m}^{-1}$ . We then

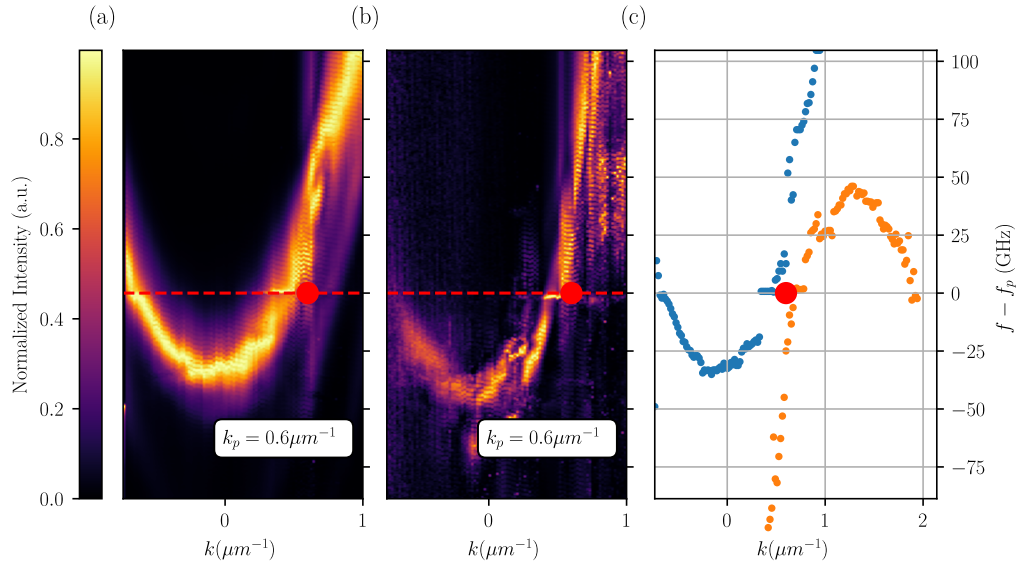


Fig. 4.8 **a)** Direct measurement of the normal branch of the Bogoliubov spectrum for a homogeneous fluid with in plane wavevector  $k_p = 0.6 \mu\text{m}^{-1}$ . **b)** Indirect measurement of the ghost branch of the Bogoliubov spectrum for the same fluid. **c)** Extracted resonance energy for each probe wavevector. The blue points are extracted from the direct measurement and correspond directly to the resonances of **a)**. The orange points are extracted from the indirect measurement. Each couple  $(k_{pr}, \omega)$  extracted from **b)** is symmetrized around the pump position in phase space  $(k_p, \omega_p)$  to account for FWM process.

perform direct measurement of the normal branch and indirect measurement of the ghost branch. The results are shown in Figure 4.8 **a)** and **b)** respectively. The modulations on the right side of the direct measurement come from interferences in the substrate of the sample that act as a low Q-factor Fabry-Pérot [21] microcavity. Each scan is normalized to its own maximum for the sake of clarity but the strength of the indirect signals is approximatively 1% – 10% of the direct one. The noise present on several scans of **b)** corresponds to parasitic signals coming from other scatterings process that may send photons at the position of the pinhole and that, in the case of direct measurement, are negligible with respect to the resonance. The reason why the ghost branch does not appear as the symmetric counterpart of the normal branch is because the axis  $k$  and  $f - f_p$  represent the wavevector and frequency of the injected probe and not the emitted signal. However, the pinhole positions first ensure us that the signal is emitted in the opposite wavevector mode. To verify that it is also symmetric in frequency, we send the photons collected through the pinhole into a spectrometer to measure their energy. This two tests allow to confirm that the signals taken through indirect measurement in **b)** indeed come from the ghost branch. As a consequence, it is possible to symmetrize the indirect data around the pump wavevector and energy to plot the full collective excitation spectrum shown in Figure 4.8 **c**). First, one can check that the two branches are indeed symmetric with respect to the pump represented by the red dot.

This measurement is an additional proof that for fluid velocities high enough, negative-

energy modes can be excited on both positive (normal) and negative (ghost) norm branches. It is worth noticing that this experiment was not conducted at the turning point of the bistability loop, which did not prevent the observation of negative-energy modes. This relaxes the experimental constraints to observe Hawking radiation in a polariton fluid and broadens the original analogy made for sonic excitation in a supersonic fluid. More specifically, a fluid exhibiting a sharp transition between a region supporting positive-energy modes and another supporting negative-energy modes is expected to emit of correlated Bogoliubov modes at the transition. These modes are not necessarily phonons and the velocity to exceed to observe them is not necessarily the speed of sound, but rather a critical velocity that depends more generally on the fluid parameters. This statement is actually more general and broadens the range of experimental configurations at which Hawking radiation can be observed. In the following we will rather speak of transcritical flow and critical velocity instead of "sonic".

#### 4.4.2 Smooth transition geometry

We first study a smooth transition between the sub and supercritical flow regions. We implement the target velocity profile :

$$\phi(x) = \frac{m_{LP}}{\hbar} \int v(x) dx = \frac{m_{LP}}{\hbar} \left( \frac{v_d - v_{up}}{2} w_h \ln(\cosh\left(\frac{x - x_h}{w_h}\right)) + \frac{v_{up} + v_d}{2} x \right). \quad (4.11)$$

with a transition width  $w_H = 20 \mu\text{m}$ . We study three profiles, with three values for the up- and downstream flow velocities  $v_u$  and  $v_d$ . All the measurements are made with  $\delta(0) = 56 \text{ GHz} \rightarrow \hbar\delta(0) = 0.2 \text{ meV}$ . At this detuning the system is in the bistable regime in both the upstream and downstream regions with a spatial extension of  $120 \mu\text{m}$ . For each configuration, the phase of the created fluid is measured by off-axis interferometry as described in subsection A.1.2. By unwrapping the phase profile, as the one typically shown in Figure 4.9 a), and taking the gradient in the  $x$  direction, we obtain the fluid velocity profile  $v(x)$ . The measured velocity profiles are represented by the solid lines in Figure 4.9 b) showing three different asymptotic downstream velocities  $v_d$  with a single upstream velocity  $v_u$ . To selectively measure the upstream or downstream region the diameter of the probe beam is reduced to half the spatial extension of the fluid and the probe is focused on the region of interest. The corresponding excitation spectra are shown in Figure 4.9 c)-f). The upstream region is shown in Figure 4.9 c) and the downstream regions in Figure 4.9 d)-f).

##### 4.4.2.1 Speed of sound measurement

Even though the system does not operate in a regime of sonic collective excitation, we call  $c_s = \sqrt{\hbar g n / m_{LP}}$  the speed of sound for the sake of clarity. The value of  $gn$  is extracted from the simultaneous fit of the normal and ghost branch of each spectrum with the Bogoliubov dispersion relation :

$$\omega_b^\pm(\delta k) = -\frac{i\gamma}{2} + v_0(x)\delta k(x) \pm \sqrt{\left(\frac{\hbar\delta k(x)^2}{2m^*} - \delta(k_p) + 2gn(x) + g_r n_r\right)^2 - (gn(x))^2} \quad (4.12)$$

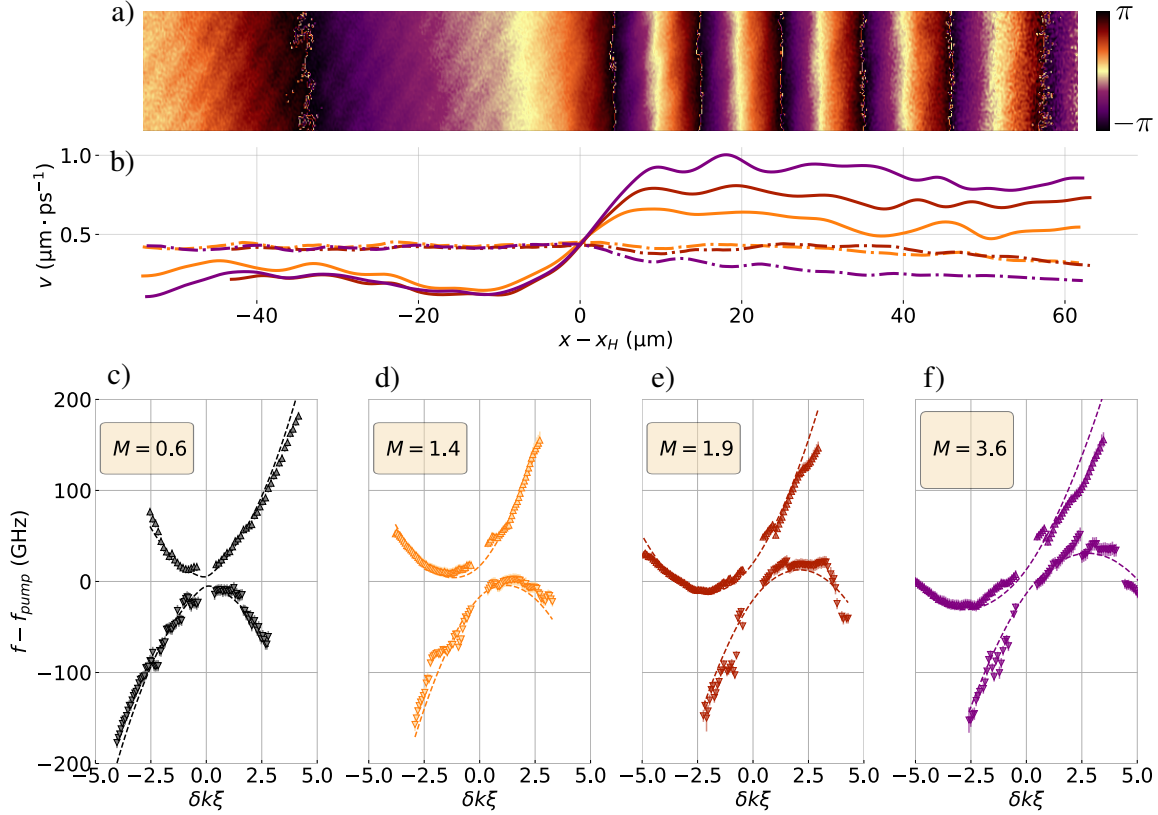


Fig. 4.9 **Smooth horizon.** a) Typical measured phase of the fluid  $\theta(x)$  inside the region of interest as defined in Figure 4.3. b) Fluid velocity profiles. Solid lines,  $v_0(x)$ ; dot-dashed lines,  $c_s(x)$ . Orange,  $M_u = 0.6$  and  $M_d = 1.4$ ; red,  $M_u = 0.4$  and  $M_d = 1.9$ ; purple  $M_u = 0.5$  and  $M_d = 3.6$ . **Excitation spectra** Eq. (4.12): c) typical upstream region; d)-f) downstream region. Up-triangles, positive-norm branch  $\omega_B^+$ ; down-triangles, negative-norm branch  $\omega_B^-$ ; dashed lines, fit obtained with free  $gn$  as a free parameter. Error bars (mostly of same size as the triangles) come from the uncertainty in the determination of the center of the lorentzian function used to fit each scan and from lambdameter used to measure the probe energy

with  $\delta k(x) = k - k_p(x)$ . The only unknown parameters in this equation are  $gn$  and  $g_r n_r$ . However, by taking the steady states solution of the Gross Pitaevskii equation coupled to a reservoir Equation 2.4.2 we obtain  $n_r \propto n$ . Based on the work [19; 21] made on the same sample. We use the value  $g_r n_r \approx 1.84 gn$  of work [21] and end with a single free parameter  $gn$  to fit the spectra. The fit are represented by the colored dashed line in Figure 4.9. The output of the fit gives in fact a value of  $gn(r_{pr})$  where  $r_{pr}$  is the position of the probe. However, this value can serve as calibration to reconstruct the full  $gn(r)$  profile. Indeed, we can safely assume that the output measured intensity is proportional to the fluid density as  $I_{\text{out}}(r) = an(r)$  and that  $a$  is a constant that depend on the exciton photon detuning through the hopfield coefficients and complex cavity parameters. Nonetheless, given the spatial extension of the fluid  $w \approx 120 \mu\text{m}$  with respect to the wedge of the sample  $0.04 \mu\text{eV} \mu\text{m}^{-1}$ , these parameters can be considered as constant in the region of interest. We can then calibrate the speed of

sound measurement through :

$$c_s(r) = \sqrt{\frac{I_{out}(r)}{I_{out}(r_{pr})}} c_s(r_{pr}). \quad (4.13)$$

The  $c_s(x)$  map obtained for the different configurations is represented by the dashed lines in [Figure 4.9 b](#)). The speed of sound is found to be quite constant, which yields a smooth transition between the upstream and downstream regions.

#### 4.4.2.2 Critical velocity

In conservative fluids, sub- and supercritical flows are discriminated by the Mach number  $M := v_0/c_s = 1$ . Instead, in our driven-dissipative fluid, the minimum velocity to have a supercritical dispersion is larger than  $c_s$  because of the gap opening in the spectrum. As a result, the condition  $M = 1$ , which defines the acoustic horizon in the hydrodynamic limit does not necessarily coincide with the condition to excite negative-energy waves in the system. In other words, the position at which the velocities exceed  $c_s$  in [Figure 4.9 b](#)) does not define the horizon of the fluid. Indeed, when the system does not operate at the turning point of the bistability we have  $gn > \delta(k_p) - g_r n_r$ , which opens a gap in the dispersion. We rewrite the dispersion in the laboratory frame in a form that allows us to easily identify the effect of the gap on the spectrum,

$$\begin{aligned} \omega_B^\pm(\delta k) &= v_0(x)\delta k(x) - i\frac{\gamma}{2} \pm \left[ \left( \frac{\hbar\delta k(x)^2}{2m_{LP}} \right)^2 + \frac{\hbar\delta k(x)^2}{m_{LP}}(2gn_0 - \delta(k_p) + g_r n_r) \right. \\ &\quad \left. + (gn_0 - \delta(k_p) + g_r n_r)(3gn_0 - \delta(k_p) + g_r n_r) \right]^{-1/2} \\ &= v_0(x)\delta k(x) - i\frac{\gamma}{2} \pm \sqrt{\left( \frac{\hbar\delta k(x)^2}{2m_{LP}} \right)^2 + c_B^2 \delta k(x)^2 + m_{det}^2 c_B^4} \end{aligned} \quad (4.14)$$

where we defined :

$$c_B = \sqrt{\frac{\hbar(2gn_0 - \delta(k_p) + g_r n_r)}{m_{LP}}}, \quad (4.15a)$$

$$m_{det} = m_{LP} \frac{\sqrt{(gn_0 - \delta(k_p) + g_r n_r)(3gn_0 - \delta(k_p) + g_r n_r)}}{(2gn_0 - \delta(k_p) + g_r n_r)}. \quad (4.15b)$$

These two quantities have a well-defined physical meaning as explained in [chapter 3](#). On the one hand,  $m_{det}c_B^2$  is the energy of  $k = 0$  modes of the fluctuation field  $\delta\psi$ , introducing a mass gap which vanishes when the system operates at the turning point of the bistability. On the other hand, [Equation 3.9](#) is a hyperbolic partial differential equation whose characteristic curves in a fluid at rest are given by  $|\mathbf{x}| = c_B t$ . These characteristic curves limit the speed at which the excitations can propagate information, defining the sound cones in full analogy to light cones. However, due to the mass gap, the propagation speed of a given bogoliubov mode is  $v_g = d\omega/dk \leq c_B$ . To clarify this point, we plot a typical gapped Bogoliubov spectrum in

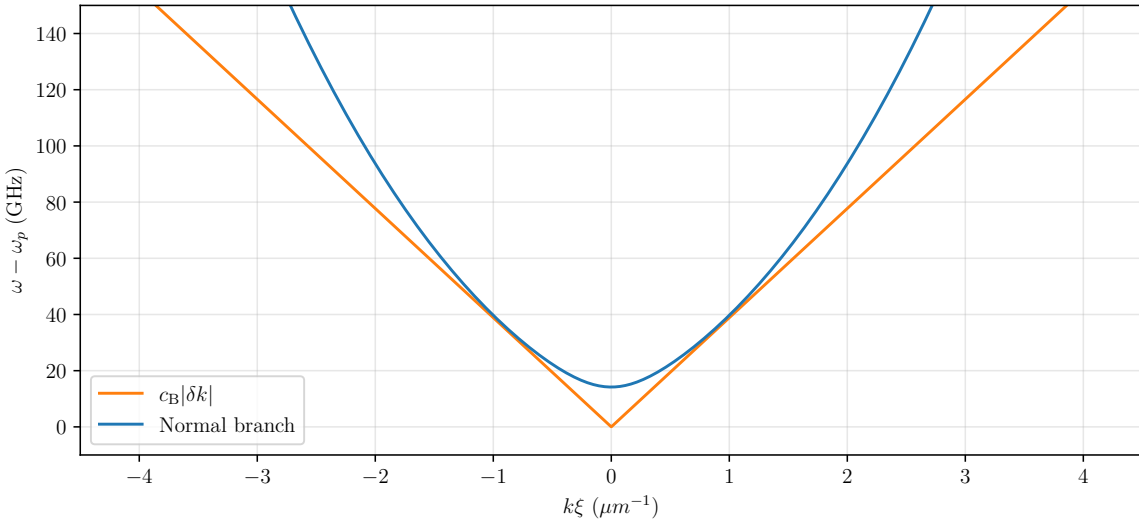


Fig. 4.10 Typical gapped Bogoliubov spectrum in the fluid frame. The parameters are arbitrarily chosen as  $\delta = 29$  GHz,  $gn_0 = 32$  GHz and the  $k$  axis is normalized to the inverse of the healing length  $1/\xi$  with  $\xi = 2.7\text{ }\mu\text{m}$ . Only the normal branch is represented by the solid blue line. The sound cone  $c_B|\delta k|$  is represented by the orange solid line.

**Figure 4.10** as well as the corresponding sound cone  $c_B|\delta k|$  as functions of the wavevector  $\delta k$  normalized to the inverse of the healing length  $1/\xi$ . As visible, for  $|\delta k\xi| < 1$ , the group velocities of the Bogoliubov modes are smaller than  $c_B$ . The latter can then be seen as the limiting speed of propagation of low wavevector perturbations. This is also in analogy to the propagation of modes of a massive relativistic scalar field, which travel at subluminal speeds, reaching only the speed of light in the limit of infinite momentum. From [Equation 4.14](#) we see that the field mass  $m_{\text{det}}$  increases  $|\text{Re}(\omega_B^{/\pm})|$  at all  $k$ , meaning that the critical velocity to have a Doppler effect large enough to excite negative-energy waves is larger than  $c_s$ . As explained in [chapter 3](#), for a fluid with a given set of parameters, changing the pump wavevector  $k_p$  while keeping the other parameters constant—the pump frequency and intensity—changes the spectrum itself because it modifies the detuning  $\delta(k_p)$  and the effective interaction energy  $gn$  through the bistability curve. It is subsequently difficult to derive a general expression for the critical velocity.

In practice, we compute numerically the normal branch  $\omega_B^+(\delta k)$  spectrum for different values of  $k_p$  and  $gn$  while keeping the zero momentum detuning constant and equal to  $\delta(0) = 56$  GHz as in the experiment. On each computed spectrum, we verify if it exhibits negative frequency values. We obtain the map shown in [Figure 4.11](#), indicating if a fluid with given velocity and interaction energy is super-critical. The points **cd**), **e**) and **f**) correspond to the measured spectrum of [Figure 4.9](#). As it can be seen, the upstream region and downstream region with the smaller velocity do not lie in the super-critical regime whereas **e**) and **f**) do. This is in agreement with the fact that the critical velocity is larger than the speed of sound since all the regime yielding super-critical flows are located on the right side of the black dashed line corresponding to the acoustic case  $c_s = \hbar k_p/m_{LP} = \sqrt{\hbar gn/m_{LP}}$ .

Moreover, the map predicts that configuration **d)** is subcritical despite a Mach number  $M_d = 1.34$  greater than one.

**Cutoff spatial frequency.** The absence of experimental data points at wavevectors  $\delta k < 0.10\mu m^{-1}$  is a consequence of the finite size of the probe beam  $\delta_x = 60\mu m$  which fixes the spatial extension of the probe in momentum space scaling as  $2\pi/\delta_x = 0.10\mu m^{-1}$ . At very small wavevector, the probe and its conjugate counterpart start to overlap and photons coming from both branches are collected by the pinhole. This prevents the effective discrimination between the two modes in the output signal of the photodiode. In practice, the cutoff frequency is computed by a simple optical Rayleigh criterion stating that two points are resolved if the distance between them is larger than the FWHM of the point spread function. In our case this directly gives  $\delta k_{cut} = 2\pi/\delta_x = 0.10\mu m^{-1}$ .

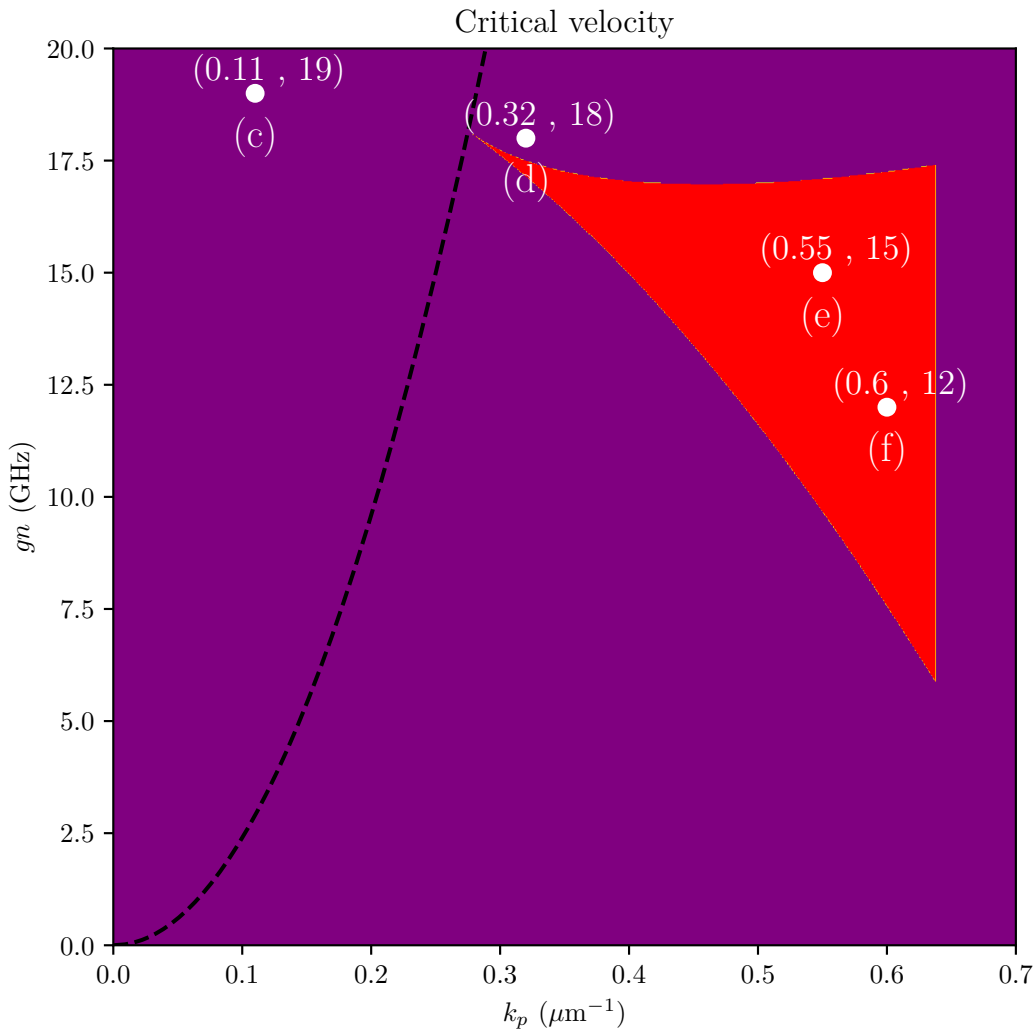


Fig. 4.11 Critical velocity map as a function of  $k_p$  and  $gn$  while the reservoir contribution was fixed as  $g_r n_r = 1.84gn$  and the detuning at zero wavevector kept equal to  $\delta(0) = 56$ . For each couple  $(k_p, gn)$  the Bogoliubov spectrum [Equation 4.12](#) is computed : the red area corresponds to super critical flows and the purple one to subcritical flows. The points **cd**), **e**) and **f**) correspond to the measured spectrum of [Figure 4.9](#). The black dashed line represents the acoustic case where the critical velocity coincides with the speed of sound  $c_s = \hbar k_s / m_{LP} = \sqrt{\hbar g n / m_{LP}}$

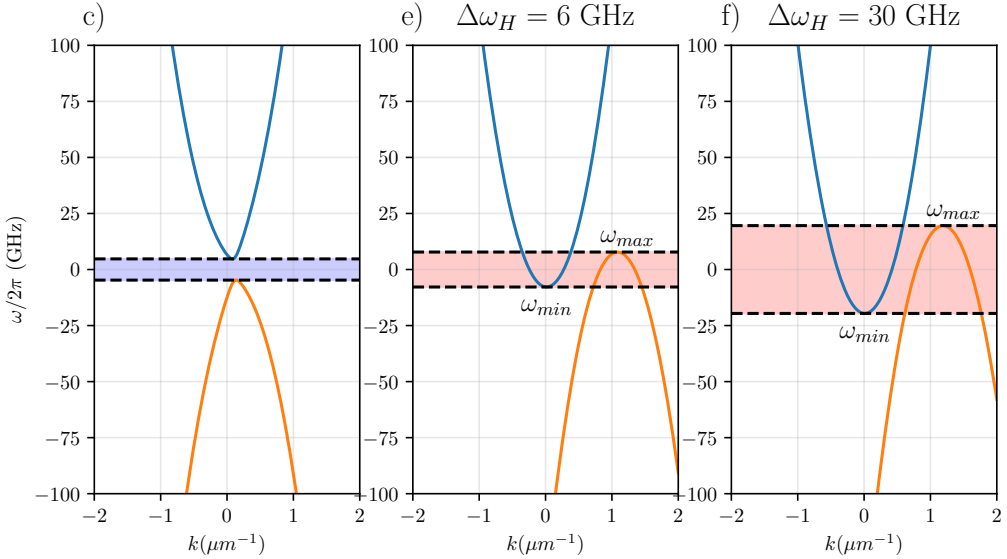


Fig. 4.12 c), e), f) analytical Bogoliubov dispersion corresponding to the fit of Figure 4.9 c), e) and f). The red color in e) and f) represents the frequency range at which negative-energy modes are available. The blue colored range in c) represents non-propagative modes that lies in the gap. The frequency range  $\Delta\omega_H$  in which positive-negative frequency mixing are displayed above each plot.

#### 4.4.2.3 Paired emission frequency range

The paired emission of correlated mode at the horizon requires the mixing of positive and negative-energy modes. Consequently, the finite velocity in the downstream region sets a maximum frequency at which the effect can occur [? ]. This frequency is given by the maximum energy of the negative-energy modes that can be excited in the downstream region and is ultimately set by the asymptotic downstream velocity  $v_d$  and the interaction energy  $gn$ . Increasing this range results in a larger number of correlated pairs emitted and is expected to enhance the overall correlation signal [? ]. In Figure 4.12 we plot the analytical Bogoliubov dispersion corresponding to the measurement of Figure 4.9 c), e) and f). Paired emission is then possible in the red range of Figure 4.12 where negative-energy modes can mix with the positive-energy mode of the upstream spectrum, located outside the gap represented in blue.

The overall frequency range at which Hawking emission is possible is given by :

$$\Delta\omega_H := 2\omega_{max} - \Delta\omega_{gap} \quad (4.16)$$

where  $\omega_{max}$  is the maximum energy of the negative-energy modes that can be excited in the downstream region and  $\Delta\omega_{gap}$  the width of the gap in the upstream spectrum. We measure  $\Delta\omega_H=6$  GHz for the e) configuration and 30 GHz for the fastest flow. Hence, by changing the asymptotic downstream speed our system enables tuning the number of states available for paired emission. Let us now show that we can control another crucial parameter of the Hawking radiation, the steepness of the horizon.

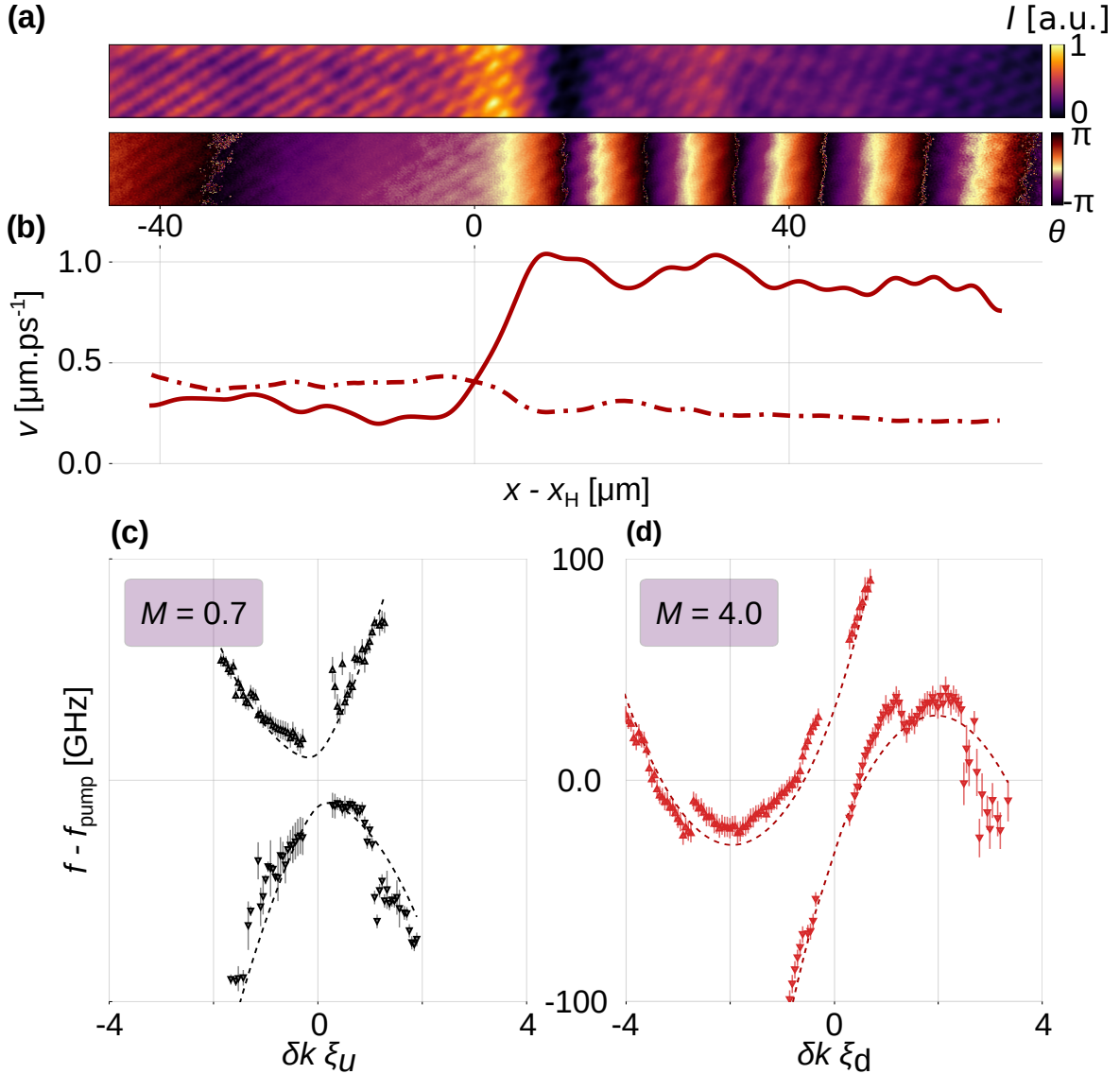


Fig. 4.13 **Steep horizon.** (a) Measured fluid density (top) and phase (bottom). (b) Measured fluid velocity profile. Solid line,  $v_0(x)$ ; dashed line,  $c_s(x)$ . **Excitation spectra** Eq. (4.12): (c) upstream region. (d) downstream region; dashed lines, fit with free parameter  $gn$ . Error bars represent the uncertainty in the determination of the center of the lorentzian when each scan is fitted by a lorentzian function to find the resonance energy. The  $M$  values in the inset of each spectrum is the computed Mach number in the corresponding region.

### 4.4.3 Steep horizon geometry

The sharpness of the transition is a crucial parameter to study the strength of correlation of the emitted modes. It can be evaluated with the following equation :

$$\kappa := \frac{1}{2c_s(x)} \frac{d}{dx} [v_0^2(x) - c_s^2(x)]|_{x_H}, \quad (4.17)$$

the hydrodynamic equivalent to surface gravity [7]. However, the discussion in the previous section pointed out that the position  $x_H$  at which the fluid velocity exceeds the speed of sound does not define the horizon of the fluid, the derivative in the definition of  $\kappa$  should then be taken at the position where the critical velocity is reached and involves the critical velocity instead of  $c_s$ . In practice this brings only a rather correction to the value of  $\kappa$ .

**Increasing the surface gravity.** The steepness of the horizon can be tuned in two ways. First, by reducing the width of the transition  $w_H$  in the target velocity profile. Second, by taking advantage of the dependence of the bistability cycle on the effective detuning  $\delta(k_p)$ . As shown in [Figure 2.12 b\)](#) the value of  $gn$  with a fixed input intensity increases linearly with the effective detuning until the turning point is reached. More precisely, when the pump wavevector is increased,  $\delta(k_p) = \omega_p - \omega_{LP}^{(0)} - \hbar k_p^2 / 2m_{LP}$  decreases and so does  $gn$  as shown in [Figure 4.14](#). In some sense the microcavity naturally reduces the density of the fluid when the pump wavevector is increased, moving the laser away from resonance. In practice, we tune wisely the energy of the pump laser and the asymptotic upstream and downstream target waveveectors. The different values of  $\delta(k_{up})$  and  $\delta(k_d)$  can lead to region with different  $gn$  values as shown on [Figure 4.14](#).

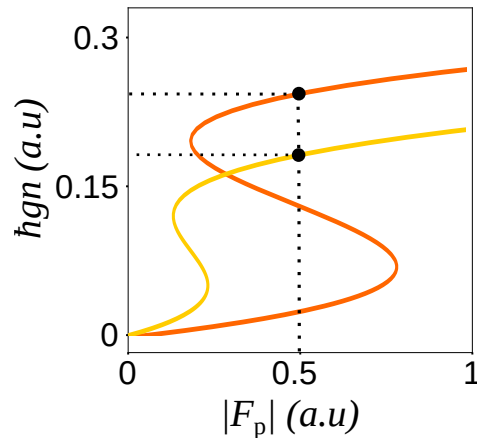


Fig. 4.14 *Bistability cycle for two different values of the effective detuning  $\delta(k_p^{(1)})$  (yellow)  $\leq \delta(k_p^{(2)})$  (orange) when  $k_p^{(2)} \leq k_p^{(1)}$ . The vertical dashed line represents the input intensity of the pump laser whereas the black dots represent the operating points of the system for each detuning. The region with the higher wavevector yields a lower  $gn$  value.*

Here we exploit this phenomenology and implement the target profile [Equation 4.3](#) with a large difference between  $v_d$  and  $v_u$ , a transition width  $w_H = 20 \mu\text{m}$  and a detuning  $\delta(0) = 71 \text{ GHz} \rightarrow \hbar\delta(0) = 0.3 \text{ meV}$  [Figure 4.13 \(b\)](#) shows  $v_0(x)$  (solid lines) as well as  $c_s(x)$

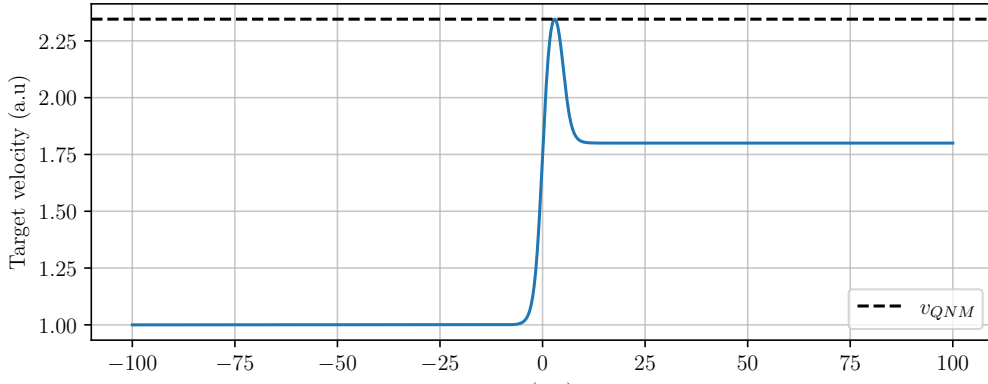


Fig. 4.15 Typical QNM target velocity profile.

(dot-dashed lines). The two supercritical fluids created in the smooth configuration shown in [Figure 4.9](#) have an horizon steepness  $\kappa$  of  $0.07 \text{ ps}^{-1}$  (red) and  $0.08 \text{ ps}^{-1}$  (purple). In contrast, in the steep geometry implemented here we compute  $\kappa = 0.11 \text{ ps}^{-1}$ . The excitation spectra are shown in [Figure 4.13 c\)](#) and [d\)](#). The frequency range at which paired emission is possible is roughly the same than in the smooth case f)  $\Delta\omega_H = 28 \text{ GHz}$  whereas the horizon steepness gets increased by 25%. A steep horizon is interesting in the context of Hawking radiation because it is expected to enhance the strength of the paired emission at the interface and subsequently facilitate its measurement.

This independent tuning of  $\kappa$  and the paired emission spectrum is not possible in conservative quantum fluids such as atomic BECs, for example. In these systems, the fluid velocity is kept constant, and the horizon is typically created by engineering both the trapping potential and the interaction constant which modifies the chemical potentials in each region  $\mu_{u,d} = g_{u,d} n_0$  and subsequently the speed of sound. In order to suppress spurious effects coming from the potential step the potential is chosen to exactly compensate the spatial jump in the Hartree energy  $\mu_u + V_u = \mu_d + V_d$  [63]. This condition then fixes the asymptotic values of the speed of sound in each region. In contrast, due to its out of equilibrium nature and the resonant pumping of the polariton fluid, the fluid parameters can be tuned at will through the pump engineering. The fine control over the waterfall horizon geometry we demonstrate here is interesting to test recent tunneling models for the Hawking effect [62].

#### 4.4.4 Quasi-normal mode configuration

The target velocity profile [Equation 4.3](#) can be modified to create complex horizon geometry by imprinting a velocity peak in the transition region. More precisely, we define the *Quasi-Normal Mode* (QNM) target velocity profile as :

$$v(x) = \frac{v_{QNM} - v_{up}}{2} \tanh\left(\frac{x - x_1}{w_1}\right) + \frac{v_d - v_{QNM}}{2} \tanh\left(\frac{x - x_2}{w_2}\right) + \frac{v_{up} + v_d}{2} \quad (4.18)$$

where  $v_{QNM}$  is the velocity of the peak,  $v_{up}$  and  $v_d$  are the upstream and downstream velocities,  $x_1$  and  $x_2$  are the position of the first and second transition and  $w_1$  and  $w_2$  are their

width. The typical corresponding shape is shown in [Figure 4.15](#). With the same asymptotic parameters as in the smooth horizon configuration of [Figure 4.9 e\)](#) we create a fluid with the QNM target velocity profile.

First, the asymptotic velocities are as expected, not modified by the presence of the peak, while the surface gravity is greatly enhanced as  $\kappa = 0.19 \text{ ps}^{-1}$ , almost twice the value obtained in the steep configuration. But the most peculiar feature of the QNM configuration is the density dip that comes with the velocity peak. For the reason explained in the previous section, the velocity peak imprinted here is associated with a density dip. As the dip is surrounded by two regions of higher density, it forms an effective resonator for Bogoliubov excitation. This leads to the appearance of a metastable excitation mode of  $\delta\psi$  called a quasi-normal mode: here specifically, a negative-energy standing wave can establish itself inside the resonator (at  $\omega_{\text{QNM}} > \max(\omega_B^-|_{x>x_H})$ ) and tunnel-couple with positive-energy propagating waves on either side [44]. As a result, the Hawking spectrum is predicted to peak at the frequency of the quasi-normal mode, bearing signatures of the near-horizon geometry. In some sense, the QNM configuration is a quantum analogue of the black hole ringdown phase, where the black hole emits gravitational waves with characteristic frequency and damping time [10] that depend on its parameters.

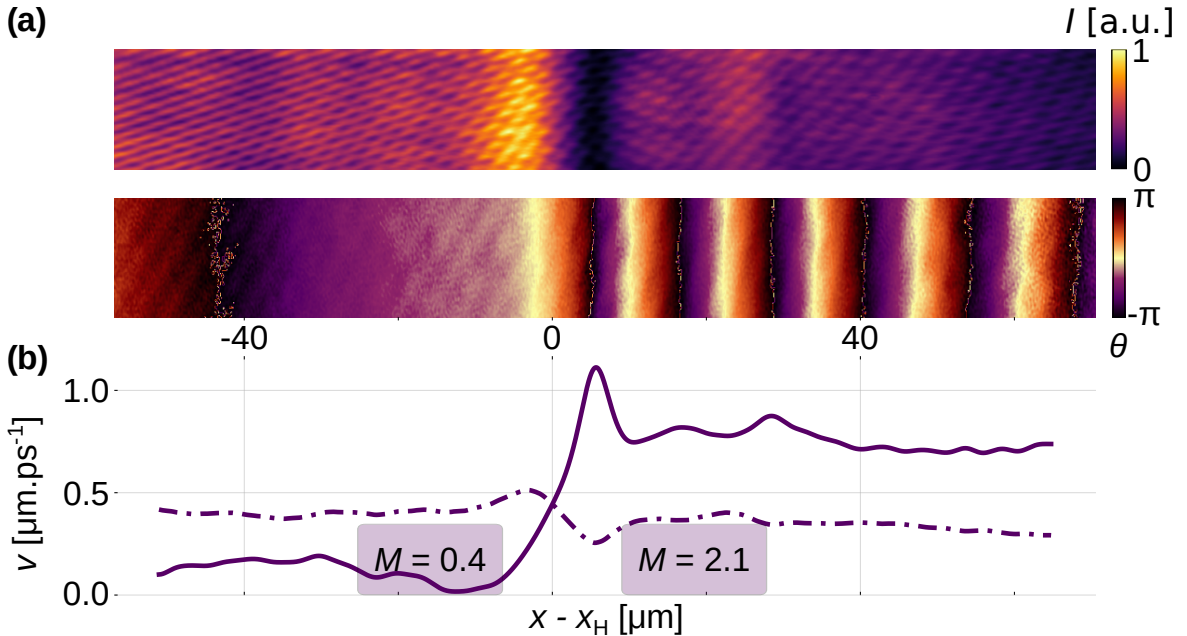


Fig. 4.16 **Quasi-normal mode horizon.** (a) Measured fluid density (top) and phase (bottom). (b) Measured fluid velocity profile. Solid line,  $v_0(x)$ ; dashed line,  $c_s(x)$ .

## 4.5 Conclusion

We demonstrated full optical generation and characterization of the mean field with arbitrary velocity profiles in a polariton fluid, which act as an effectively curved spacetime for Bogoliubov excitations. In each configuration, we were able to measure the collective excitations spectrum of the fluid and state if Hawking radiation could be observed or not. We showed that the critical velocity to observe negative-energy modes is not necessarily the speed of sound but rather a critical velocity that depends on the fluid parameters. This widens the range of experimental configurations at which particle creation can be observed. The great versatility of our experimental methods also showed that the steepness of the horizon can be controlled independently of the paired emission spectrum. Finally, we demonstrated the possibility of creating complex horizon geometry that could yield peculiar behaviors like Quasi Normal Modes. The great advantage of the system presented here is the large range of field theory scenarios that can be tested in a single setup. Even though transcritical polariton fluids are not completely encapsulating what truly happens at a black hole horizon, it is a great platform to study effects predicted by quantum field theory in curved spacetime, regardless they were originally thought for black holes or not.



## Chapter 5

# Experimental observation of stimulated Hawking radiation in a polariton quantum fluid

In the previous chapter, we demonstrated the experimental realization of a transcritical flow in a polariton quantum fluid through precise optical pump shaping. This allowed us to engineer the fluid's density and velocity profiles to form a transcritical region, a key ingredient for the emergence of a sonic horizon. Furthermore, we presented experimental evidence of negative-energy modes in this region, confirming the necessary conditions for the observation of the Hawking effect.

Building on these achievements, this chapter focuses on the experimental observation of stimulated Hawking radiation in a polariton fluid. Stimulated emission provides a controlled way to probe the Hawking effect by injecting a coherent state into the upstream region and measuring its scattering into outgoing modes. This approach allows us to directly study the amplification of positive-energy modes and the role of negative-energy modes in the transcritical region. The experimental realization of stimulated Hawking radiation involves several key steps. First, we describe the setup used to inject coherent states into the polariton fluid and the techniques employed to measure the outgoing modes. Next, we introduce a method to analyze the scattered modes. Although the scattering matrix is not directly measured, this approach reveals clear signatures of amplification, providing indirect evidence of the underlying scattering process. Finally, we present the results of these measurements, discuss the agreement with theoretical predictions and the robustness of the stimulated Hawking effect. The results presented in this chapter not only validate the theoretical predictions of stimulated emission but also establish a pathway toward the observation of spontaneous Hawking radiation. By leveraging the unique properties of polariton fluids, this work demonstrates the potential of these systems as a platform for exploring fundamental aspects of quantum field theory in curved spacetime and beyond.

### 5.1 Interferometric measurement of the scattering matrix

We aim at solving the scattering problem of a coherent state injected in the upstream region impinging on the horizon. This approach is complementary to what has already been done in

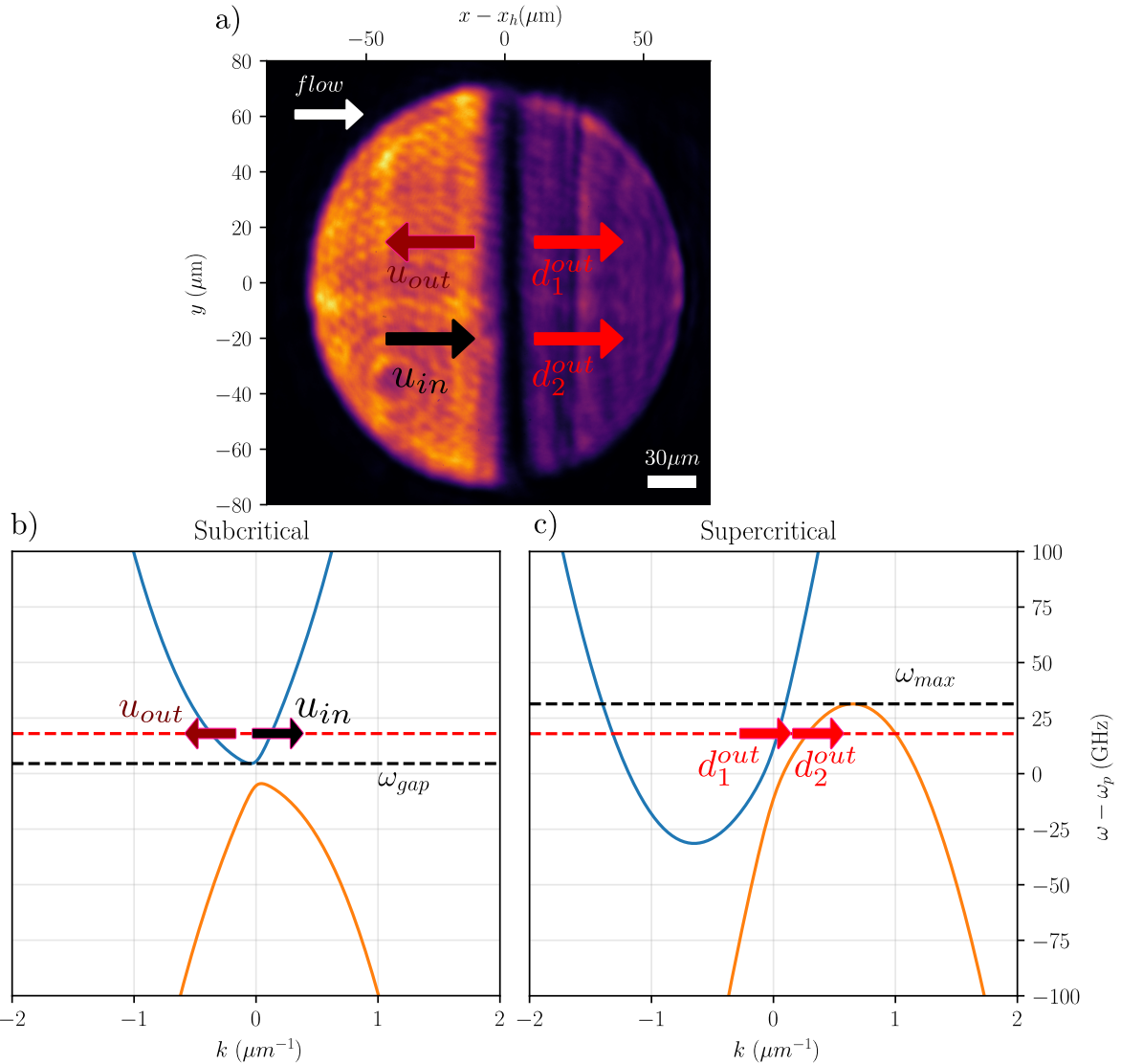


Fig. 5.1 **a)** Real space image of a transcritical flow of polaritons with detuning  $\delta(0) = 29\text{GHz}$  and wavevectors  $k_u = 0.2\mu\text{m}^{-1}$  and  $k_d = 0.6\mu\text{m}^{-1}$ . The black arrow represents the impinging mode  $u_{in}$  while the blue arrows represent the outgoing modes  $u_{out}$ ,  $d_1^{out}$  and  $d_2^{out}$ . The direction of the arrow reflects the sign of the group velocity of each mode. **b)** Typical analytical Bogoliubov dispersion relation in the upstream subcritical region. The arrows correspond to the modes displayed on the left side of **a**). **c)** Typical analytical Bogoliubov dispersion relation in the downstream supercritical region. The arrows correspond to the modes displayed on the right side of **a**)

the hydrodynamical experiment [29] in which the stimulating field came from the transcritical region.

### 5.1.1 Challenges of the measurement

Let us take a transcritical flow of polaritons with a typical density profile shown in [Figure 5.1 a\)](#). The bright region on the left corresponds to the upstream subcritical region, while the other side of the interface is the transcritical region. Typical analytical spectra corresponding to each region are shown in [b\)](#) and [c\)](#). The previous chapter evidenced that it is possible to locally excite the Bogoliubov dispersion by shining a weak probe laser at the right couple  $(\omega, k)$ . Consider then a coherent state  $|\alpha_{in}\rangle$  in the  $u_{in}$  mode of [b\)](#) that is, an upstream mode that impinges on the interface. If its frequency  $\omega_{in}$  is within  $[\omega_{gap}, \omega_{max}]$  we expect to measure one reflected mode  $u_{out}$  and two transmitted modes  $d_1^{out}$  and  $d_2^{out}$ . The latter is the negative energy mode responsible for Hawking radiation. Each of these modes has a different wavevector  $k_i$ .

Experimentally, this situation corresponds to four distinct optical signals exiting the sample at different angles, or equivalently, to four spatially separated spots in the Fourier plane of the cavity. To illustrate the inherent challenges associated with such measurements, we present in [Figure 5.2 b\)](#) the typical expected locations of the scattered signals in the Fourier plane corresponding to the fluid configuration of [Figure 5.1 a\)](#). The two bright spots correspond to the regions of the fluid characterized by the wavevectors  $k_u$  and  $k_d$ .

First, the expected position of the mode  $d_1^{out}$  nearly coincides with the pump signal in the downstream region. Since the probe intensity must remain at least two orders of magnitude lower than that of the pump to preserve the perturbative regime, the resulting signal-to-noise ratio is extremely low. Consequently, a direct measurement of the  $d_1^{out}$  at wavevectors close to that of the pump mode becomes unfeasible.

Second, in addition to the desired signals at frequency  $\omega_{in}$ , all modes are subject to four-wave mixing processes due to nonlinear interactions with the pumped polaritons. As a result, depending on the fluid parameters, the conjugate modes generated by these interactions may spatially overlap with the reflected or transmitted modes. For example, as illustrated in [Figure 5.2](#), the conjugate of the injected mode  $u_{in}$  appears at the same location in momentum space as the reflected mode  $u_{out}$ . Consequently, prevents a clear distinction between the two contributions.

The central challenge of this measurement is thus to detect weak signals on top of a strong background while ensuring that these signals originate from genuine transmission and reflection at the interface –rather than from spurious scattering events or nonlinear mixing. Therefore, the critical experimental objective is to optimize the signal-to-noise ratio, where “noise” refers to all undesired signals. This is achieved by acting on two main experimental parameters:

- **Enhancement of the signal:** As discussed in the previous chapter, this can be accomplished by increasing the steepness of the horizon.
- **Suppression of the pump background:** The photonic nature of the system allows us to exploit two key properties of light: polarization and coherence. Polarization filtering can be applied in the detection path, while coherence enables the use of interferometric techniques, as will be detailed in the following section.

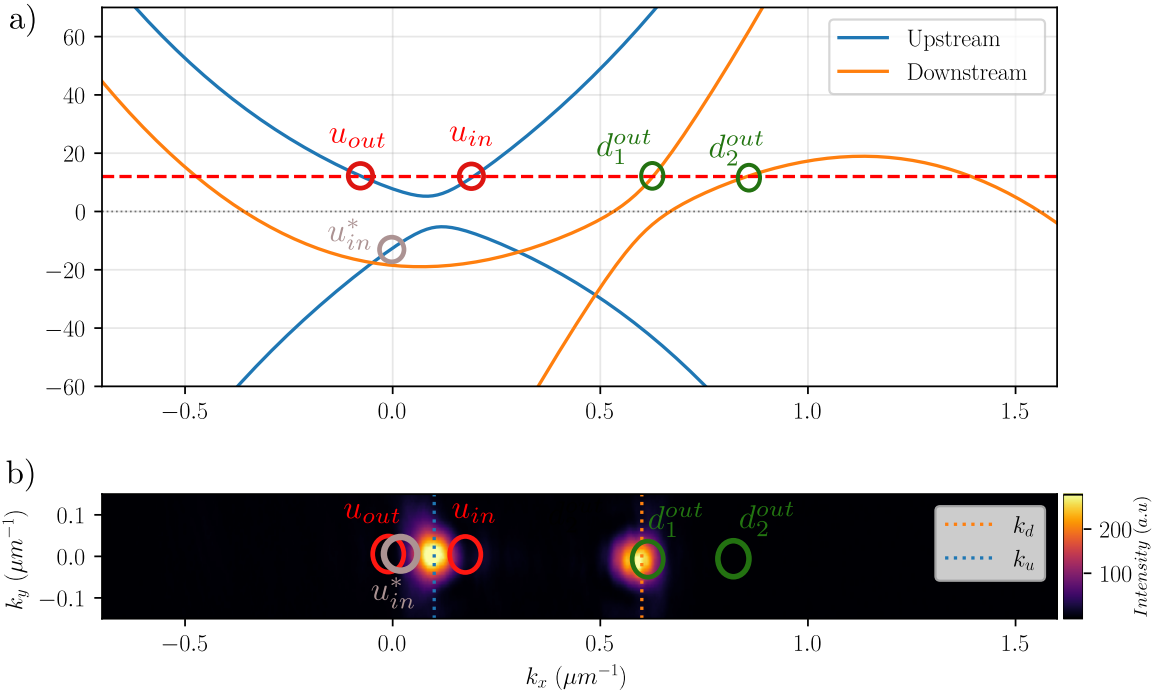


Fig. 5.2 **a)** Analytical Bogoliubov dispersion of both regions calculated with the parameters of the fluid of Figure 5.1 a). To show what happens in practice, the two dispersions are plotted in the same graph as a function of the wavevector in the laboratory frame. The upstream dispersion is centered at  $k_u$  while the downstream one is centered at  $k_d$ . The red dashed line corresponds to the energy of the injected mode. The wavevectors of the reflected-transmitted modes are obtained at the intersections of this line with the Bogoliubov branches and reported in the momentum space **b)**. The red (resp. green) circle represents the expected location of the upstream (resp. downstream) modes. Finally, the grey circle represents the conjugate of the injected signal resulting from four-wave mixing. **b)** Momentum space of Figure 5.1 a): the two bright spots correspond to the two regions of the fluid with wavevectors  $k_u$  and  $k_d$ . The colored circle are reported from **a)**.

**Electronic filtering.** One possible strategy to suppress the pump background is inspired by the method used to measure the excitation spectrum in the previous chapter. By modulating the intensity of the probe beam at a frequency  $\omega_{\text{mod}}$  accessible in the electronic domain, the signal can later be demodulated, isolating the component arising from the probe-induced excitation. However, in the current context, what previously served as an advantage becomes a limitation. Indeed, the four-wave mixing signals also carry the modulation, thus failing to resolve overlapped modes as explained above. To overcome this, we turn to the optical domain, specifically to interference-based detection schemes.

### 5.1.2 Interferometric reconstruction of the scattered field

The measurement is based on the same interferometric technique previously employed to reconstruct the mean field. The key distinction here is that the method is now applied to the probe field instead. Although this adjustment is minor in practice, it represents a significant conceptual shift that enables a comprehensive characterization of the scattering problem. Before detailing its experimental implementation in the context of the scattering problem, we first examine the insights that such a measurement can provide.

We again consider the generic situation presented above, namely, a coherent state injected in the upstream region. The full optical field transmitted through the sample is composed of :

- The mean field  $\psi_0$  oscillating at the pump frequency  $\omega_p$
- The probe field oscillating at the probe frequency  $\omega_p + \omega_{in}$  resulting from the scattering of  $u_{in}$  on the interface.
- The conjugate field oscillating at the opposite of the probe frequency  $\omega_p - \omega_{in}$  resulting from the four-wave mixing of each  $\omega_p + \omega_{in}$  mode with the pump.

In what follows, we work in the pump rotating frame, whereby all frequencies are measured relative to  $\omega_p$ . When the probe field is superimposed with a phase reference beam at the probe frequency—obtained as a pick-off from the probe laser—the only components that generate interference fringes are those oscillating at  $+\omega_{in}$ . Each scattered mode is characterized by a distinct wavevector  $k_i$ , leading to a unique spatial frequency in the resulting interferogram. As an illustrative example, [Figure 5.3 a\)](#) displays two regions of such an interferogram. The first lies within the probe injection area, where the fringe spacing is inversely proportional to  $|\Delta k|$ , with  $\Delta k = k_{u_{in}} - k_{\text{ref}}$  denoting the wavevector mismatch between the injected mode and the reference beam. The second region is located downstream, beyond the probe injection area. The mere presence of interference fringes in this region already confirms that the injected mode has propagated through the interface, while the fringe spacing provides direct information about the wavevector of the transmitted mode.

To clarify this, we perform the spatial Fourier transforms of the two regions and show the result in [d\)](#). The signal near  $\Delta k = 0$  corresponds to the continuous background signal—primarily the pump field and the conjugate modes at  $-\omega_{in}$ —which do not interfere with the reference beam. It is the analog of the DC signal in electronics. The central peaks represent the spatial frequencies of the propagating components in each region. Notably, the downstream region exhibits a higher wavevector, consistent with the scattering picture.

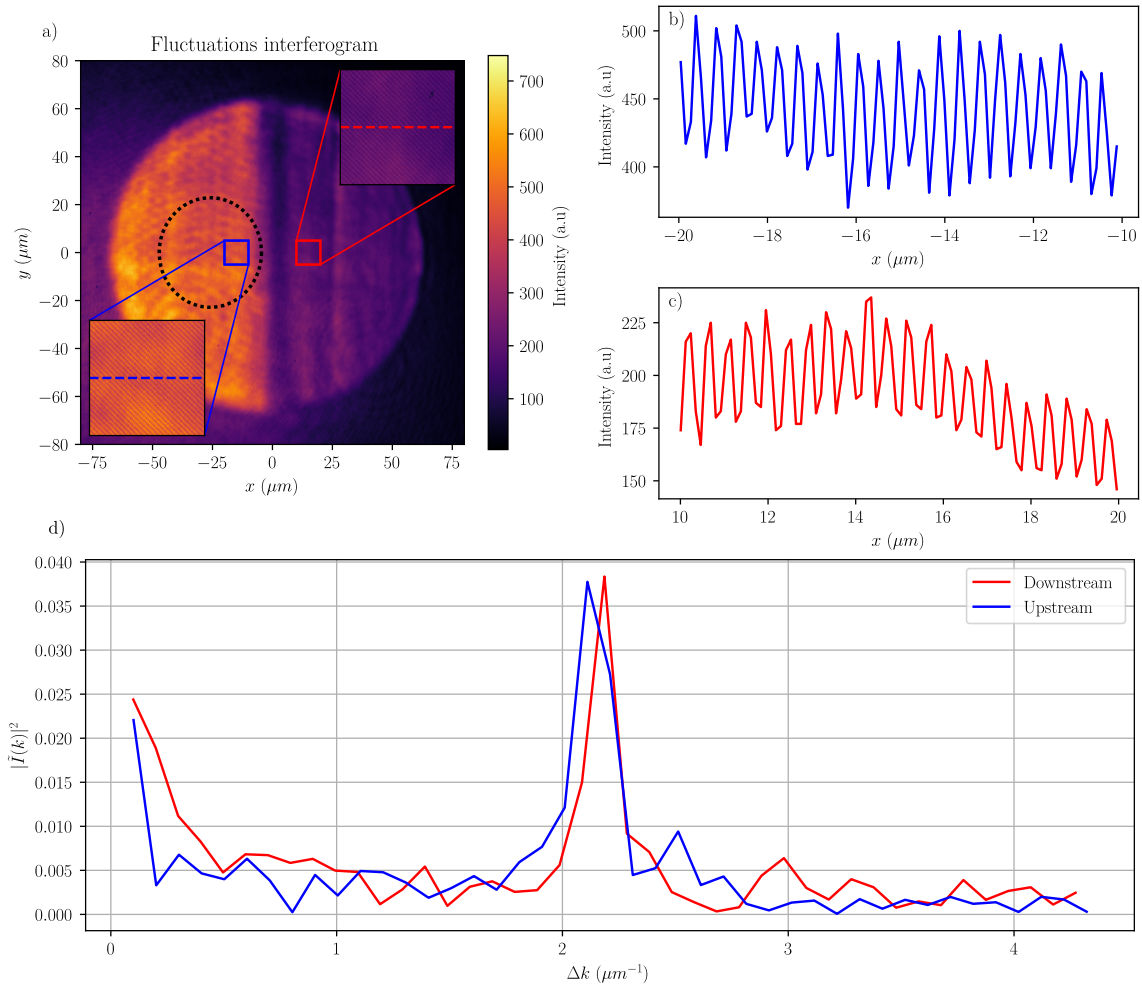


Fig. 5.3 **a)** Interferogram resulting from the superposition of Figure 5.1 **a)** and a reference beam from the probe laser. The black dashed circle represents the injected probe location. The red inset (resp. blue) is a zoom on the upstream (resp. downstream) region near the interface. **b)** Cut of the interferogram along the red dashed line of the red inset. **c)** Cut of the interferogram along the blue dashed line of the blue inset. **d)** Fourier transforms of the cuts **b)** and **c)**. The blue curve corresponds to the upstream region with spatial frequency  $\Delta k_u \approx 2.11 \mu\text{m}^{-1}$ . The red curve corresponds to the downstream region with spatial frequency  $\Delta k_d = 2.19 \mu\text{m}^{-1}$ .

This preliminary analysis already highlights the strength of the technique. By applying numerical masks at different spatial locations, one can selectively extract the Fourier components of the fluctuations. More generally, a single interferogram enables a full reconstruction of the probe field at the frequency of the injected perturbation. As a result, this method proves particularly well-suited for addressing the scattering problem, as it overcomes all the challenges previously outlined :

- Conjugate modes and background contributions from the pump are inherently filtered out, as they do not interfere with the reference beam and therefore do not generate fringes.
- Each scattered mode gives rise to a distinct spatial frequency in the interferogram, enabling their individual identification and selective extraction.
- The interference with the coherent reference beam enhances the signal-to-noise ratio, thereby facilitating the detection of weak scattered components.

The interferometric technique outlined above provides a powerful framework for reconstructing the probe field and isolating the scattered modes. By leveraging the distinct spatial frequencies of the scattered components and filtering out unwanted contributions, this method enables a precise characterization of the scattering process. In the following section, we detail the experimental implementation of this approach, focusing on the setup and procedures required to reconstruct the scattering matrix and extract the key parameters governing the stimulated Hawking effect.

## 5.2 Experimental implementation

The experiment is conducted in the same microcavity as in the previous chapter, operating at the same working point (C5-D6) and using an identical optical setup. However, whereas the previous measurements focused on characterizing the fluid's excitation spectrum, the present objective is to detect the scattered signals generated at the horizon interface. To this end, we first investigate configurations in which the horizon is as sharp as possible, even at the cost of significantly reducing the downstream density.

### 5.2.1 Ballistic configuration

This is accomplished by illuminating only the upstream region with the pump laser, set at a wavevector  $k_p = 0.02 \mu\text{m}^{-1}$ . As a result, the downstream region consists of polaritons propagating ballistically beyond the pumped area. The pump is detuned by  $\delta(0) = 26 \text{ GHz}$  in order to reach the high-density regime of optical bistability. Additionally, the Gaussian intensity profile of the pump beam is truncated into a half-disk shape with a diameter of  $150 \mu\text{m}$ , thereby generating a sharp intensity gradient at the edge of the pumped region. The resulting mean-field profile is presented in [Figure 5.4](#).

As shown on the corresponding intensity and velocity profiles [see [Figure 5.5 a\)](#)], the downstream region exhibits an exponentially decaying density accompanied by an increasing flow velocity. This behavior naturally arises from the conservation of current, as described by the continuity equation [3.1](#), in the absence of external pumping. More precisely, it can be

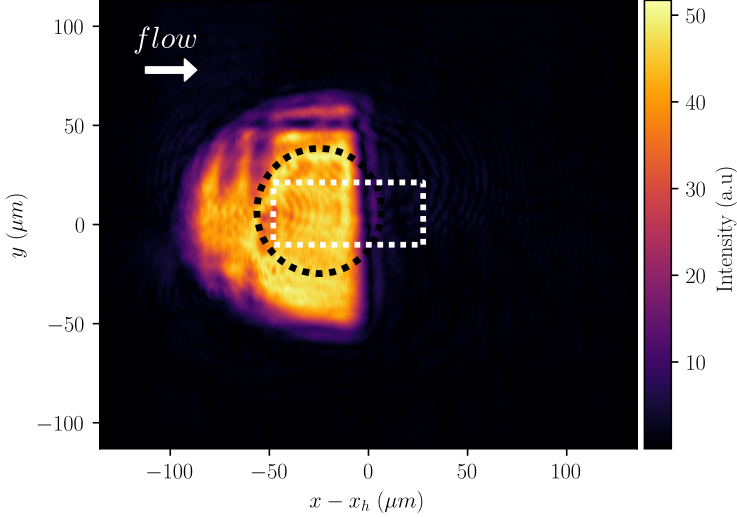


Fig. 5.4 **a)** Real space image of a transcritical flow of polaritons with detuning  $\delta(0) = 48$  GHz. The pump is shone only in the upstream region with wavevector  $k_p = 0.02 \mu\text{m}^{-1}$ . The downstream region is made of polaritons propagating ballistically. The black dashed circle represents the location of the injected probe while the white dashed rectangle represents the region of interest (ROI) for the density and velocity profiles.

shown that away from the pump spot in a slowly varying region where the quantum pressure can be neglected, the Gross Pitaevskii equation takes the form of a generalized Bernoulli equation for driven dissipative fluids. The wavefunction then takes the form [82]:

$$\psi_0(x \gg x_h) = \sqrt{n_0} e^{-\frac{x}{l_d}} e^{ik_{fluid}x}, \quad (5.1)$$

where  $1/l_d = \gamma_{LP}/2v_g$  is the spatial decaying rate resulting from the product between the fluid group velocity  $v_g = \hbar k_{fluid}/m_{LP}$  and the polariton lifetime  $1/\gamma_{LP}$ . The local wavevector of the polariton fluid  $k_{fluid}$  is determined by the equation:

$$\omega_p = \omega_{LP} + \frac{\hbar k_{fluid}^2}{2m} + gn_0(x) + g_r n_r(x). \quad (5.2)$$

Taking the low density limit  $gn_0, g_r n_r \rightarrow 0$ , the asymptotic value of  $k_{fluid}$  is fixed by the detuning  $\delta(0)$  in the pumped region as  $k_d := k_{fluid}(x \gg x_h) = \sqrt{2m\delta(0)/\hbar}$ . This evolution can also be intuitively understood through an optical analogy: photons propagating from the pumped region encounter a zone of lower polariton density, which corresponds to a higher effective refractive index. According to Snell-Descartes laws of refraction, the wavevectors of the photons are bent toward the normal of the interface, effectively resulting in an increase in the group velocity. The corresponding velocity profile measured by off-axis interferometry is depicted in [Figure 5.5 b\)](#). The horizon then forms spontaneously due to the simultaneous increase of the flow velocity and the decrease of the speed of sound.

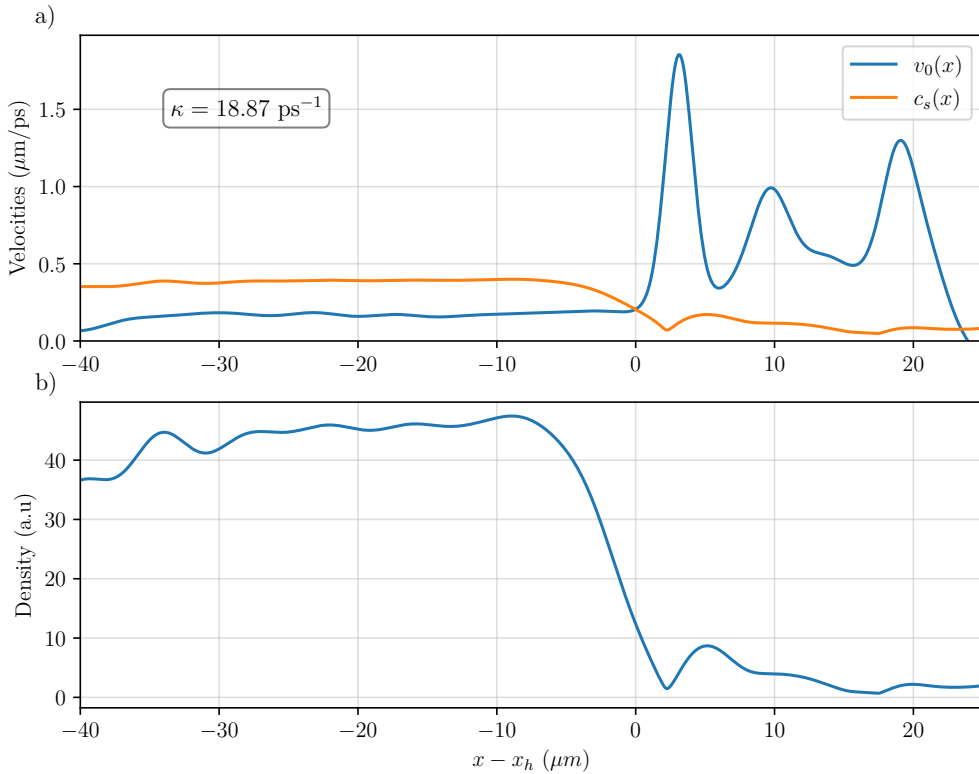


Fig. 5.5 **a)** *Density profile of the polariton fluid taken in the region of interest.* The profile is obtained by taking an average along the  $y$ -axis on the whole ROI represented by the white dashed rectangle of Figure 5.4. **b)** *Velocity profiles of the fluid in the ROI.* The blue curve corresponds to the velocity of the fluid obtained by off axis interferometry. The orange curve corresponds to  $c_s = \sqrt{gn_0/m_{LP}}$  calibrated from the value of  $gn_0$  fitted from the upstream Bogoliubov spectrum.

The speed of sound is calibrated with the same method as in chapter 4 from the Bogoliubov spectrum measurement shown in Figure 5.7. The latter allows to obtain the interaction energy  $gn_0 = 9.6 \pm 0.1 \text{ GHz}$ . In this configuration, the surface gravity is  $\kappa \approx 18 \text{ ps}^{-1}$ , which is two order of magnitude higher than what was obtained in the steepest horizon of the previous chapter. The price to pay for this enhancement is the appearance of oscillations in the downstream fluid density and velocity profiles. Indeed, since the pump is no longer present to fix the phase of the system and inject density, the fluid is more sensitive to fabrication defects in the microcavity, each of them acting as a scattering center.

### 5.2.2 Measurement of the Bogoliubov spectrum

In order to determine whether a detected signal originates from genuine scattering at the interface or from a spurious scattering event, we begin by characterizing the Bogoliubov excitation spectrum of the fluid in each region independently. This is done by employing

a technique mixing the high-resolution pump-probe spectroscopy detailed in the previous chapter and the interferometric technique described in the previous section.

First, the probe beam is centered in the upstream region close to the interface as represented by the black dashed circle in [Figure 5.4 a\)](#). A slight spatial overlap with the downstream region across the interface is voluntarily introduced to have access to the spectrum of both regions on a single frequency scan as we will see later. Then, the whole field is superimposed with a collimated phase reference beam originating from the probe laser. As a rule of thumb, the diameter of the reference is increased to be three times larger than the diameter of the probe beam in order to have the flattest possible phase front. The angle difference between the two beams is set to obtain the best spatial frequency resolution as explained in [subsection A.1.2](#).

Secondly, the wavevector of the probe beam is tuned from  $-1.0 \mu\text{m}^{-1}$  to  $1.0 \mu\text{m}^{-1}$  by 60 steps of  $\Delta k = 0.046 \mu\text{m}^{-1}$ . At each step, the probe frequency is scanned  $\pm 65 \text{ GHz}$  around the pump frequency. The main difference from the previous experiment lies in the detection scheme. In fact, instead of modulating the probe intensity to isolate the signal by electronic filtering, we use the aforementioned interferometric technique. A single frequency scan consists of a series of 80 interferograms recorded on a CCD camera. Then, a full dataset is made of  $80 \times 60$  interferograms, where each image has  $2056 \times 2464$  pixels encoded on 16 bits for the best dynamical range. In principle, the number of frames per scan could be increased by performing a longer energy scan, but this would result in a longer acquisition time. Compared to the 600 points per energy scan available with the previous technique, the present procedure then suffers from a lack of frequency resolution. However, frequency resolution turned out not to be a limitation, and this drawback is largely compensated for by the advantages of the interferometric technique. In particular, it allows one to measure almost all the relevant observables in a single data set, as we shall see now.

**Spectrum reconstruction.** For each interferogram, a Gaussian numerical mask of width  $40 \mu\text{m}$  is applied either in the upstream or downstream region to spatially isolate the area of interest (see [Figure 5.4](#)). A two-dimensional Fourier transform is then performed on the masked interferograms, yielding the fluctuation spectrum at the probe frequency within the selected region. Initially, our objective was to extract the Bogoliubov dispersion relation in each region, which, as discussed in the previous chapter, can be inferred from the transmission spectrum of the probe across the sample. To this end, an additional numerical pinhole (centered on the probe wavevector and with a radius matched to the probe spot) is applied in the Fourier domain of the interferogram, as illustrated in [Figure 5.6](#). The integral over the masked Fourier planes provides the transmission of the probe in the corresponding region.

In summary, for each probe configuration defined by the  $(k_{in}, \omega_{in})$  couple, this procedure yields the transmitted probe intensity  $I_{u,d}(k_{in}, \omega_{in})$  in both the upstream and the downstream regions. At this stage, the reason for positioning the probe beam so that it slightly overlaps with the downstream region becomes clear: it allows for the direct excitation of Bogoliubov modes with minimal influence from the interface. This is essential for benchmarking the dispersion relation of modes transmitted from upstream, and for confirming that they coincide with those excited locally in the downstream region. By repeating this procedure while varying the probe wavevector and frequency we obtain the Bogoliubov dispersion in each region, as shown in [Figure 5.7](#). As anticipated, only the normal branch is accessible via

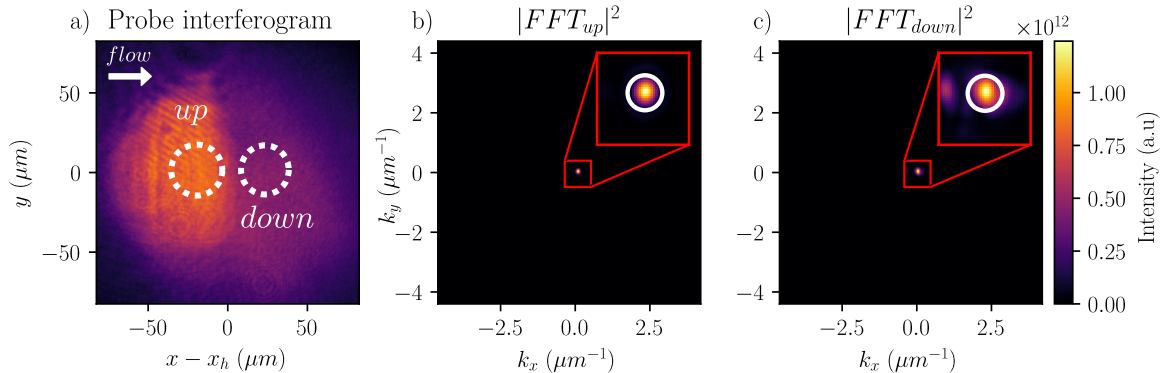


Fig. 5.6 **a)** **Probe interferogram.** The probe is located in the upstream region as in Figure 5.4. The white dashed circle represent the numerical mask applied to isolate each region. **b)** Shifted fourier transform of the masked interferogram of the upstream region. The red inset is a zoom on a  $0.2 \mu\text{m}^{-1}$  region around the probe spot where the solid white circle correspond to the numerical pinhole applied to isolate the probe signal. **c)** Shifted fourier transform of the masked interferogram of the downstream region. The red inset is a zoom on a  $0.2 \mu\text{m}^{-1}$  region around the probe spot where the solid white circle corresponds to the numerical pinhole applied to isolate the probe signal.

direct excitation. This is not a limitation since this method was specifically chosen for its ability to isolate positive frequency signals. In addition, knowledge of the normal branch alone is sufficient to reconstruct the full Bogoliubov spectrum, as its structure is intrinsically symmetric with respect to the pump. Moreover, the existence of the ghost branch, particularly its positive-frequency domain, which is essential for the Hawking effect in the supercritical regime, was established in the previous chapter. Consequently, we will not attempt to measure it in this experiment.

The upstream spectrum shown in Figure 5.7 a) exhibits a gap and a slight Doppler shift consistent with the pump wavevector in the upstream region  $k_p = 0.023 \mu\text{m}^{-1}$ . The data points are fitted with the Bogoliubov dispersion relation given in Equation 3.44 where  $gn_0$  is the only fitting parameter (the dark reservoir is handled in the same way as in the previous chapter ie set to  $g_r n_r = 1.84 gn$ ). We obtain  $gn_0 = 9.6 \pm 0.1 \text{ GHz}$  and find a good agreement of the model with the experimental points.

The downstream spectrum shown in Figure 5.7 b) features negative frequency modes, which is typical of a supercritical flow. In the absence of pumping, the system must satisfy the condition given in Equation 5.2, which can be recast in the form  $\delta(k_{fluid}) = gn_0 + g_r n_r$ . It is the counterpart of the turning point condition in the pumped region, implying that the Bogoliubov spectrum is expected to be linear far from the interface:

$$\omega_B(k) = v_d(k - k_d) \pm \sqrt{\frac{\hbar(k - k_d)^2}{2m_{LP}} \left( \frac{\hbar(k - k_d)^2}{2m_{LP}} + gn_0 \right)}, \quad (5.3)$$

where  $v_d = \hbar k_d / m_{LP}$  is the asymptotic velocity of the fluid measured by off-axis interferometry.

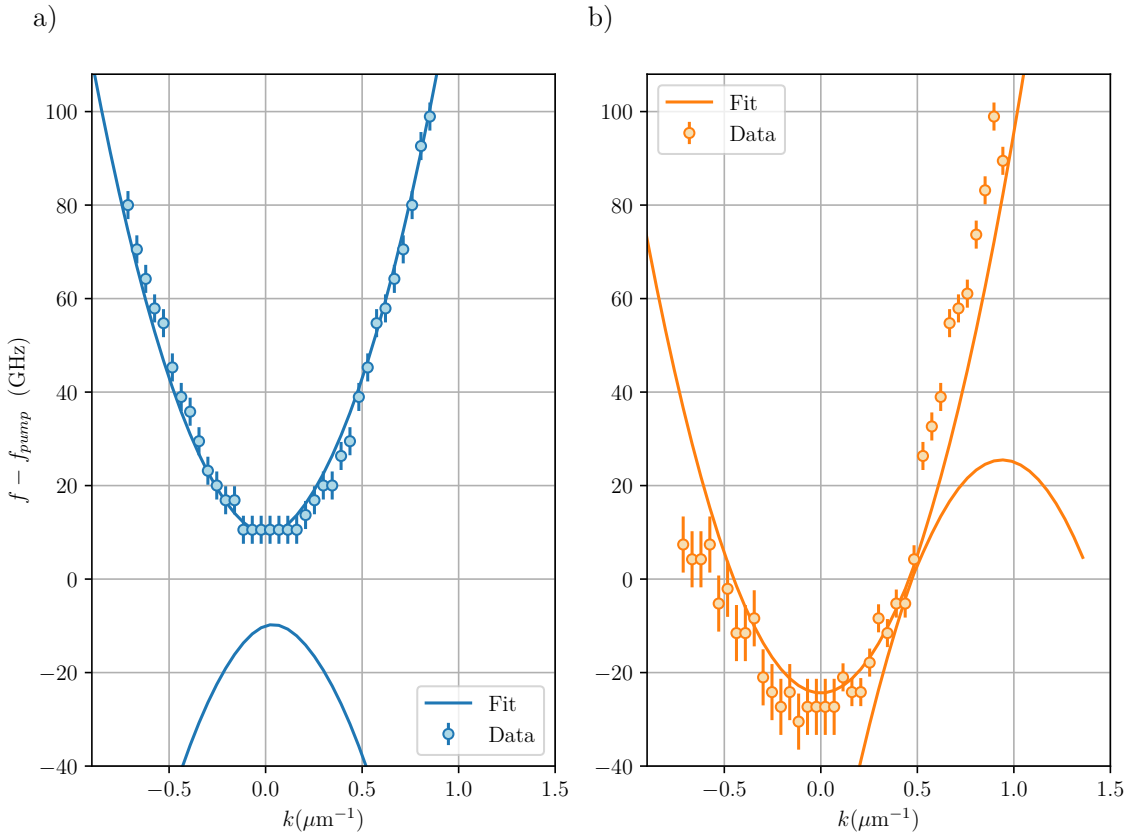


Fig. 5.7 **a)-b) Upstream-Downstream Bogoliubov spectrum.** The scattered points correspond to the maxima of the transmission spectrum of the probe in the upstream-downstream region. The blue-orange solid line is the analytical Bogoliubov dispersion plotted with the experimental parameters and the nonlinear interactions  $gn_0$  obtained from the fit of the data with the normal Bogoliubov branch. The upstream region fit gives  $gn_0 = 9.6 \pm 0.1$  GHz while in the downstream we obtain  $gn_0 = 1.2 \pm 0.01$  GHz. The vertical error bars mainly originate from the frequency resolution of the measurement.

The fit gives  $gn_0 = 1.20(1)$  GHz. As visible in [Figure 5.7 b](#)), the agreement is not as good as in the upstream region. This is because in the unpumped region, the fluid is no longer homogeneous close to the interface, as shown in [Figure 5.5 b](#)). Homogeneity is recovered far from the interface, where the density is low, implying that there is no fluid left to probe. Consequently, the measured signal comes mainly from the transient region, where looking for the Bogoliubov modes as plane waves is already an approximation. To obtain a better agreement between the theoretical curve and the experimental data, a complete diagonalization of the Bogoliubov matrix around the steady state would be necessary in this region to obtain the exact expected Bogoliubov spectrum. However, this is not the goal of this work, and the supercritical feature we are interested in remains robust against this approximation.

The shape of the spectrum in each region indicates the presence of an acoustic horizon. We can now turn to the measurement of the scattering matrix.

### 5.2.3 Observation of stimulated Hawking radiation

#### 5.2.3.1 Detection of the scattered modes

We analyze the emergence of transmitted or reflected modes resulting from the scattering of a perturbation impinging on the horizon from the upstream region, namely when the probe excites a  $u_{in}(k)$  mode.

For each  $k_{in}$ , we compute the Fourier transform of the probe interferogram in both the upstream and downstream regions, following the same separation procedure used for the reconstruction of the Bogoliubov spectrum. In contrast to the earlier analysis, we now apply a numerical anti-pinhole in the Fourier plane to suppress the intense contribution of the  $u_{in}$  mode at the probe position. A peak detection algorithm is then used to identify the positions of the scattered modes in the Fourier plane and to extract their wavevector. Each identified wavevector is compared with the Bogoliubov spectrum to confirm its physical relevance and to rule out spurious scattering events. This process is systematically repeated as the probe sequentially excites each  $u_{in}$  mode. The resulting scattering data are summarized in [Figure 5.8 a](#)). As observed, the  $(k, \omega)$  positions of the modes detected both in the upstream and downstream regions agree well with the Bogoliubov dispersions.

This measurement demonstrates that the interface scatters the incoming modes as expected from the Bogoliubov theory. However, the  $d2_{out}$  modes –that are expected on the ghost branch–are not detected in the downstream region. This is due to its negative norm: its amplitude mostly lies on the conjugate branch. Indeed, in the Bogoliubov basis the excited  $d2_{out}$  mode is written as :

$$\begin{pmatrix} u_{k_{d2}^{out}} \\ v_{k_{d2}^{out}} \end{pmatrix} e^{-i\omega_{prt}} = \begin{pmatrix} U_{k_{d2}^{out}} \\ V_{k_{d2}^{out}} \end{pmatrix} e^{ik_{d2}^{out}x} e^{-i\omega_{prt}}, \quad (5.4)$$

where  $\omega_{pr}$  is the probe frequency. According to [3.37](#), the corresponding fluctuation of the order parameter ie the physical quantity experimentally accessible, is :

$$\delta\psi_{d2_{out}}(x,t) = U_{k_{d2}^{out}} e^{ik_{d2}^{out}x} e^{-i\omega_{prt}} + V_{k_{d2}^{out}}^* e^{-ik_{d2}^{out}x} e^{i\omega_{prt}}. \quad (5.5)$$

Due to its negative norm the Bogoliubov amplitudes are  $\int |U_{k_{d2}^{out}}|^2 - |V_{k_{d2}^{out}}|^2 = -1$ , meaning that  $|V_{k_{d2}^{out}}|^2$  is significantly greater than  $|U_{k_{d2}^{out}}|^2$ . Consequently, its larger amplitude is at

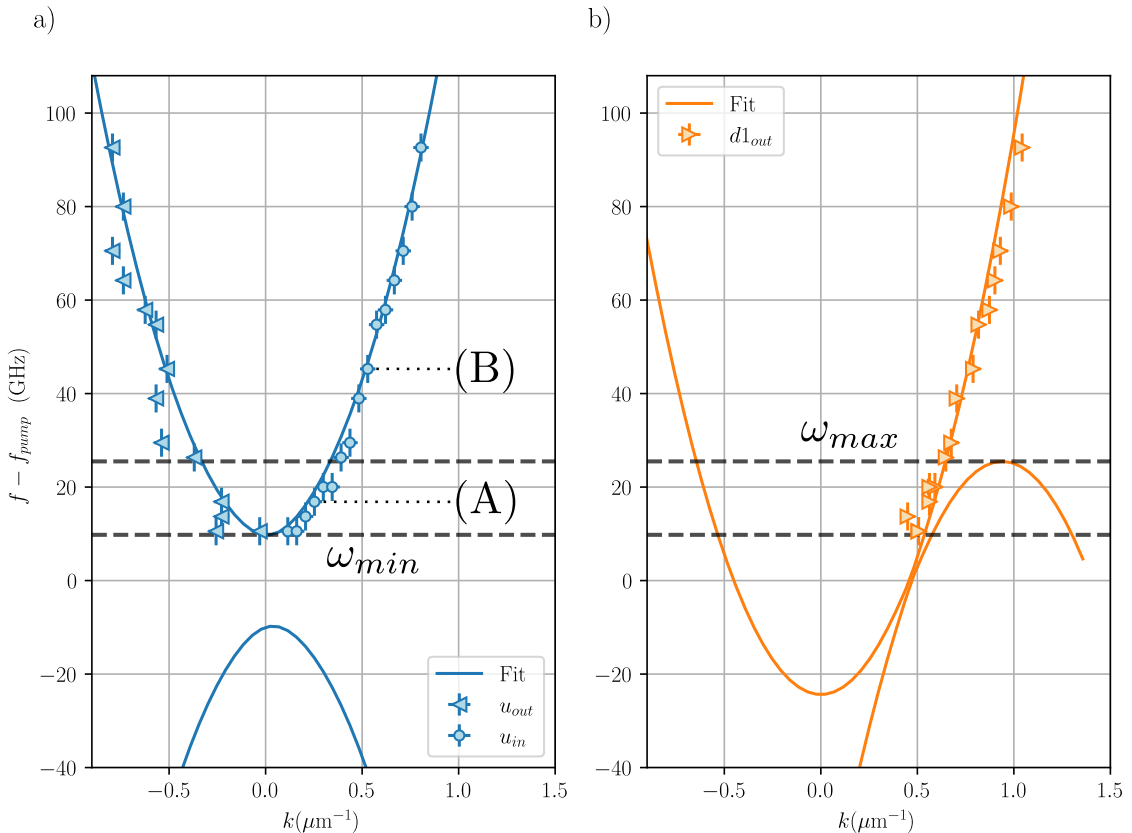


**Fig. 5.8 Reflection and transmission at the horizon.** **a)** **Measurement of the reflected modes  $u_{out}$**  The  $u_{in}$  modes excited by the probe are represented by the blue dots. The error bars are the same as in [Figure 5.7](#). For each  $u_{in}$  mode, the wavevectors of the maxima detected in the upstream region are represented by the blue left-oriented triangles. The error bars are the same than for the  $u_{in}$  modes with an additional contribution due to the resolution in momentum space ( $\Delta = 0.027 \mu\text{m}^{-1}$ ) in the peak detection algorithm. The blue solid line is the fit of the upstream Bogoliubov dispersion obtained in [Figure 5.7 a\)](#). The black dashed lines define the frequency range at which negative-positive energy mixing is possible. The specific configurations (A) and (B) are taken as examples for later comparison. The mode (A) lies in the negative-positive energy mixing frequency interval, while the mode (B) lies outside. **b)** **Measurement of the transmitted modes.** The wavevectors of the maxima detected in the downstream region are represented by the orange right-oriented triangles. The error bars are the same as in **a)**. The orange solid line is the fit of the downstream Bogoliubov dispersion obtained in [Figure 5.7 b\)](#).

opposite frequency and wavevector, namely, in the  $d2_{out}^*$  mode (on the normal branch at negative frequency). This explains why the interferometric technique, which can detect only modes at the probe frequency fails to detect the weak amplitude of the  $d2_{out}$  mode.

To measure amplitudes in  $d2_{out}^*$ , we use an imaging spectrometer Princeton Instruments SpectraPro SP-2750 mounted with a 1200 lines/mm grating together with a high sensitive CCD camera Teledyne PIXIS 1024. By imaging the Fourier plane of the entire field on the entrance slit of the spectrometer it is possible to directly obtain the spectrum of the fluid including both the pump and the probe contributions. As the pump is generally two orders of magnitude brighter than the probe, it quickly saturates the camera sensor, preventing the detection of weak probe signals. To overcome this issue, the pump is filtered out by a razor blade placed in real space, before the spectrometer. The blade is positioned so as to block the bright upstream region while letting the weak downstream region pass through. This allows setting a long exposure time without being blinded by the pump. A typical spectrum taken with a 4 seconds exposure time is shown in [Figure 5.9 a\)](#). By superimposing the image with the downstream Bogoliubov dispersion obtained earlier, the different modes are identified. Their positions are represented by colored dashed circles in [Figure 5.9 a\)](#).

Remarkably, an intensity peak is observed at the  $d2_{out}^*$  mode, as shown in the vertical cut in [Figure 5.9b\)](#). To confirm that this mode indeed originates from Hawking radiation, we verified that the peak disappears when the excited  $u_{in}$  mode lies outside the negative-positive energy mixing frequency interval.

Finally, an additional peak is observed at  $\omega = 2\omega_{probe}$  indicated by the green dashed circle in [Figure 5.9 a\)](#). We interpret it as the result of a four-wave mixing process where two  $d1_{out}$  polaritons scatter into a pump mode polariton and a higher energy mode:

$$\begin{aligned} (\omega_{pr}, \omega_{pr}) &\rightarrow (0, 2\omega_{pr}) \\ (k_{d1}^{out}, k_{d1}^{out}) &\rightarrow (k_{d1}^{out} - \Delta k, k_{d1}^{out} + \Delta k), \end{aligned} \quad (5.6)$$

where  $\Delta k = k_{d1}^{out} - k_d$  is the wavevector mismatch between the pump in the downstream region and the  $d1_{out}$  mode. This process arises as a consequence of bosonic stimulation resulting from the high occupancy of the pump state, while the linearity of the Bogoliubov spectrum ensures optimal phase matching.

The simultaneous detection of modes  $u_{out}$ ,  $d1_{out}$  and  $d2_{out}^*$  when the probe is exciting a  $u_{in}$  mode in the negative-positive energy mixing region is a convincing signature of stimulated Hawking radiation. Let us now turn to a more quantitative analysis and see whether reflection and transmission coefficients can be extracted from the data.

## 5.2.4 Toward the measurement of the scattering matrix

### 5.2.4.1 Input and output modes discrimination

In order to compute reflection and transmission coefficients, the input and output modes must be defined clearly. To do so, let us consider the perturbation field  $\delta\psi$  when a *in* mode is excited. In a first approach, we restrict our description to what is experimentally accessible

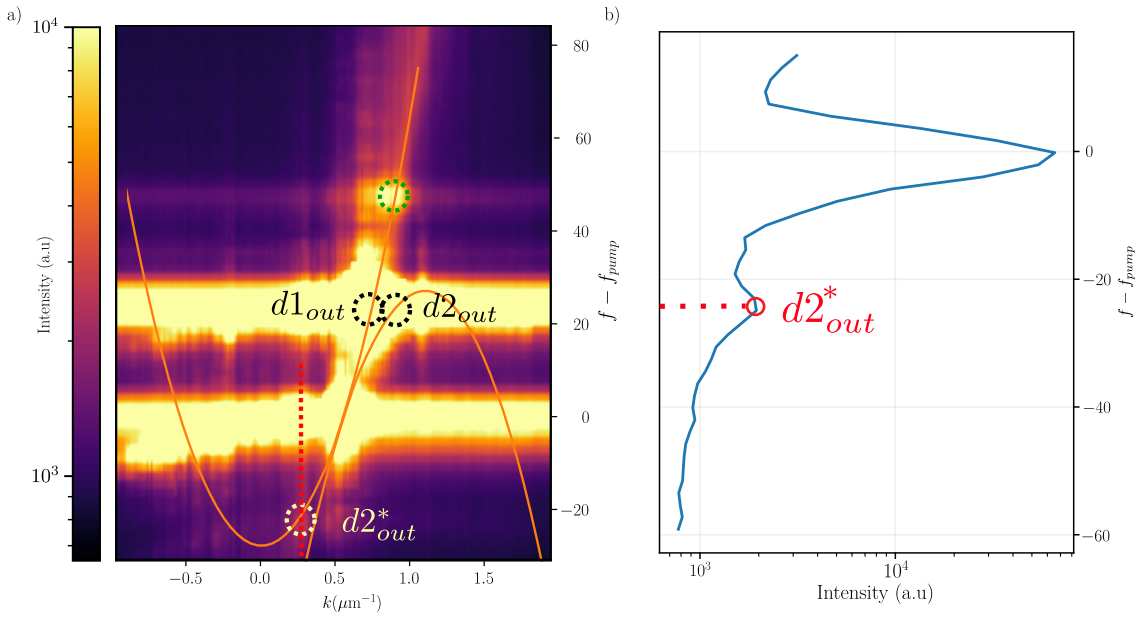


Fig. 5.9 **a)** *Spectrum of the downstream region of the fluid.* The spectrum is obtained by integrating over the whole downstream region of the fluid during 4 seconds with an imaging spectrometer. The orange solid line represents the fit of the Bogoliubov dispersion relation obtained in Figure 5.7 b). The dashed purple circles are the  $d1_{out}$  mode and the expected location of the  $d2_{out}$ . The orange dashed circle is the  $d2^*_{out}$  mode, conjugate of  $d2_{out}$ . The green dashed circle represents a higher order four-wave mixing at twice the probe frequency. The red dashed line indicates the energy cut made in the right subplot. **b)** *Vertical cut of the  $d2^*_{out}$  mode.* The intense peak on the right corresponds to the remaining pump contribution. The red dashed line is the  $d2^*_{out}$  mode energy.

with our interferometric method. Namely, the field at the probe frequency only. In a very general way, the wavefunction can be decomposed as follows:

$$\begin{aligned}\delta\psi(x,t) &= \delta\psi_{\text{in}}(x,t) + \delta\psi_{\text{res}}(x,t) \\ &= \delta\psi_{\text{in}}(x,t) + \delta\psi_{\text{scat}}(x,t) + \delta\psi_{\text{err}}(x,t).\end{aligned}\quad (5.7)$$

where  $\delta\psi_{\text{in}}$  is the ideal incoming mode ie a perfect gaussian of the form :

$$\delta\psi_{\text{in}} = Ae^{\frac{-(x-x_{\text{in}})^2}{w}} e^{ik_{\text{in}}x} \quad (5.8)$$

where  $w$  is the width of the mode and  $A$  its amplitude. Note that this is the continuous wave counterpart of the probe beam defined in the numerical study [35]. Conversely,  $\delta\psi_{\text{res}}$  is the residual field. The latter is made of all the other modes that are not in the *in* mode. The term  $\psi_{\text{scat}}$  represents all the scattering events that may occur in the fluid. In particular, it contains the outgoing modes  $u_{\text{out}}$ ,  $d_1^{\text{out}}$  and  $d_2^{\text{out}}$  that are the result of the scattering at the horizon. Furthermore, the residual field also accounts for deviations of the injected probe beam in the cavity from the perfect Gaussian beam defined by  $\delta\psi_{\text{in}}(x,t)$ . This contribution

$\delta\psi_{\text{err}}(x,t)$  is purely optical and can be thought of as a bias when  $\psi_{\text{in}}$  is extracted from the true probe beam, as we shall see now.

**Input mode.** The most reliable method to define the *in* mode while minimizing potential biases is to perform a Fourier transform of the perturbation field and apply a modal decomposition. Following the procedure outlined in the previous section, we first identify the amplitude peak of the injected mode, which constitutes the dominant contribution in Fourier space. Cuts along both axes of the detected peak are presented in [Figure 5.10 a\)](#) and [b\)](#). Noticeably, the peak is not perfectly symmetric and shows a slight elongation along the  $k_x$  direction. It remains unclear whether this asymmetry carries information about the scattering process itself or whether it merely results from the broadening induced by the fluid's motion. To address this ambiguity, we focus on the  $k_y$  direction, exploiting the translational invariance of the fluid along this axis, as discussed in [chapter 3](#).

The cut along the  $y$ -axis is then fitted with a one-dimensional Gaussian function of the form

$$f(k_y) = A \exp\left(-\frac{(k_y - k_y^0)^2}{2\sigma^2}\right)$$

The resulting fit is shown in [Figure 5.10 a\)](#), demonstrating excellent agreement with the data. The amplitude  $A$  and width  $\sigma$  obtained from the fit are then used to define a two-dimensional Gaussian function with the same amplitude and width, centered on the wavevector  $\mathbf{k} = (k_x^0, k_y^0) = (k_{\text{in}}, 0)$ :

$$A_{\text{fit}}(k_x, k_y) = A \exp\left(-\frac{(k_x - k_x^0)^2}{2\sigma^2} - \frac{(k_y - k_y^0)^2}{2\sigma^2}\right). \quad (5.9)$$

To end the definition of the input mode complex field, we need to provide it with a phase. To do so, we look at the phase of the  $\delta\tilde{\psi}$  in the vicinity of the peak. Close to the maximum amplitude, the phase is well defined and is approximated by a planar surface by fitting the signal with a function of the form  $\theta_{\text{fit}}(k_x, k_y) = x_0 k_x + y_0 k_y + c$  where  $x_0$ ,  $y_0$  and  $c$  are the fitting parameters. These encode the position of the *in* mode in real space. This fitting procedure is equivalent to neglecting any curvature in the mode wavefront or, in other words, to assume that the mode has a plane wave phase. Of course, fluctuations around this ideal phase are expected and may contain information about the scattering process. To take this into account, we perform a last step that consists of projecting the overall field  $\delta\tilde{\psi}$  on the ideal input mode we just defined, ie,  $\delta\tilde{\psi}_{\text{fit}}(\mathbf{k}) = A_{\text{fit}}(\mathbf{k}) \exp(i\theta_{\text{fit}}(\mathbf{k}))$ . The resulting field is given by :

$$\delta\tilde{\psi}_{\text{in}} = \langle \delta\tilde{\psi}_{\text{fit}} | \delta\tilde{\psi} \rangle \delta\tilde{\psi}_{\text{fit}}. \quad (5.10)$$

**Residual field.** From the above expression, we are able to define the residual field as the difference between the injected mode and the overall field  $\delta\tilde{\psi}_{\text{res}} = \delta\tilde{\psi} - \delta\tilde{\psi}_{\text{in}}$ . Note that the way  $\delta\tilde{\psi}_{\text{in}}$  is built through a scalar product ensures that the residual field is orthogonal to the *in* mode provided  $\delta\tilde{\psi}_{\text{fit}}$  is normalized:

$$\begin{aligned} \langle \delta\tilde{\psi}_{\text{in}} | \delta\tilde{\psi}_{\text{res}} \rangle &= \langle \delta\tilde{\psi}_{\text{fit}} | \delta\tilde{\psi} \rangle (\langle \delta\tilde{\psi}_{\text{fit}} | \delta\tilde{\psi} \rangle - \langle \delta\tilde{\psi}_{\text{fit}} | \delta\tilde{\psi}_{\text{in}} \rangle) \\ &= \langle \delta\tilde{\psi}_{\text{fit}} | \delta\tilde{\psi} \rangle (\langle \delta\tilde{\psi}_{\text{fit}} | \delta\tilde{\psi} \rangle - \langle \delta\tilde{\psi}_{\text{fit}} | \delta\tilde{\psi}_{\text{fit}} \rangle \langle \delta\tilde{\psi}_{\text{fit}} | \delta\tilde{\psi} \rangle) \\ &= 0. \end{aligned} \quad (5.11)$$

In this manner, the basis chosen for our description is as close as possible to the Bogoliubov plane wave basis explicitly specified in [chapter 3](#). This is a strong assumption that will be discussed in the following.

### 5.2.4.2 Real space analysis

In the previous section, the different modes involved in the scattering process were well separated in momentum space. In this modal picture, the natural procedure to obtain reflection and transmission coefficients seems to be the comparison between the amplitudes of the different modes in momentum space. Indeed, in an ideal situation where the only modes involved in the scattering process are the incoming and outgoing modes –or said differently where  $\delta\psi_{err} = 0$ – each mode results in a well-defined peak in the Fourier plane whose maximum and position are directly related to the amplitude and wavevector of the modes, respectively.

In the present case, the situation is quite different, as the residual field  $\delta\psi_{res}$  is not negligible. To illustrate this point, we performed the inverse Fourier transform of the fields and analyzed the resulting images in real space. The results are shown in [Figure 5.10 c\)](#) and [d\)](#). As expected, the input mode is very close to a perfect Gaussian beam since it was constructed precisely to be such. The residual field, on the other hand, is much more complex and contains spurious contributions. For example, the signal is not zero far from the interface in the upstream region as visible on the intensity cut in [Figure 5.10 e\)](#) near  $x \approx -60 \mu\text{m}$ . This would not be the case if  $\psi_{res}$  consisted solely of reflected or transmitted signals at the interface. More specifically, the profile in [e\)](#) would instead be composed of two decaying exponentials, both originating from the horizon. Indeed, the discussion made in [subsection 5.2.1](#) also holds for the Bogoliubov modes, meaning that the scattered modes –that are not supported by the probe laser– are exponentially damped with a characteristic length fixed by their group velocity and the polariton lifetime as in [Equation 5.2](#).

This demonstrates that the way we defined the *in* mode indeed introduces a bias. Therefore, a direct analysis in Fourier space would include many unwanted contributions, making quantitative analysis difficult. A more reliable method is to analyze the data locally in real space in the vicinity of the horizon. This is what is done in analytical works [35; 63] where the scattering matrix coefficients are computed from the continuity equations of the wavefunctions and their derivatives at the horizon [28]. This approach is particularly well suited to stationary flows, where the time variable is eliminated. It is the standard method used to solve textbook quantum mechanics problems [22], such as the scattering of a plane wave incident from  $-\infty$  by a potential barrier. In this case, the reflection and transmission coefficients can be obtained by taking the ratio of the complex amplitudes of the reflected and transmitted waves to the amplitude of the incoming one at the interface. Usually, this cannot be done experimentally since the field at a given position is a superposition of all the modes present. Consequently, unless having a perfect knowledge of the incoming mode both in phase and amplitude, an intensity measurement does not allow to discriminate between the different contributions because of the interference between them.

In our case, the interferometric method together with the procedure of separating the modes in momentum space and then performing the inverse Fourier transform allows analyzing the complex fields independently. However, a local analysis does not remove the spurious contributions of the residual field even in the vicinity of the interface.

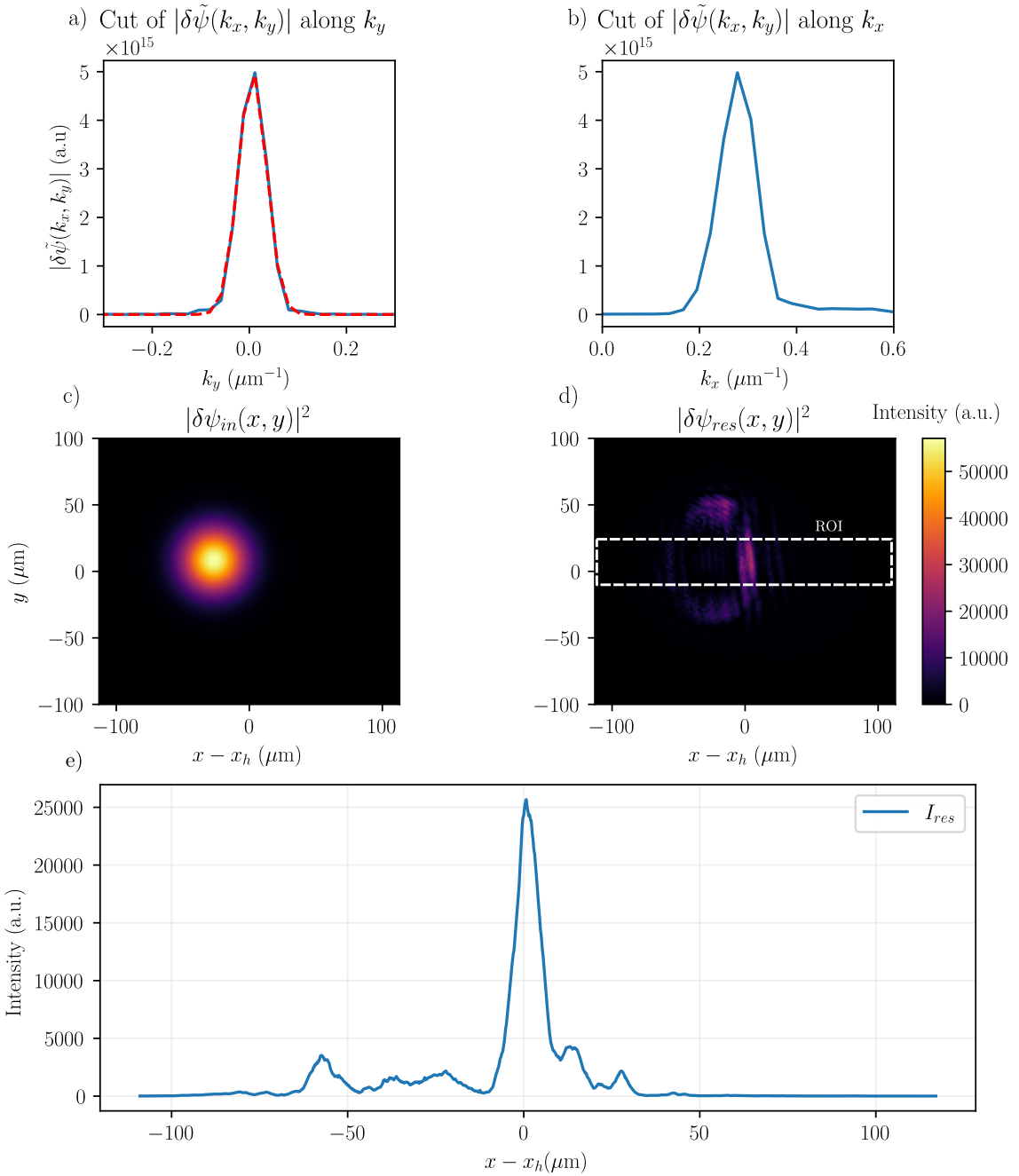


Fig. 5.10 **a) Cut of the injected mode in the  $k_y$  direction.** The blue curve is the data and the red dashed curve is the gaussian fit. The model has a R-squared value of 0.98. The amplitude  $A$  and width  $\sigma$  are extracted from the fit. **b) Cut of the injected mode in the  $k_x$  direction.** **c) Intensity of the constructed input mode in real space.** Obtained by applying the inverse fourier transform to  $\delta\psi_{in}(k_x, k_y)$ . **d) Intensity of the constructed residual field in real space.** Obtained by applying the inverse fourier transform to  $\delta\psi_{res}(k_x, k_y)$ . **e) Cut of the intensity of the residual field.** An average along the  $y$  axis is performed in the region of interest (ROI) defined by the white dashed rectangle of **d)**.

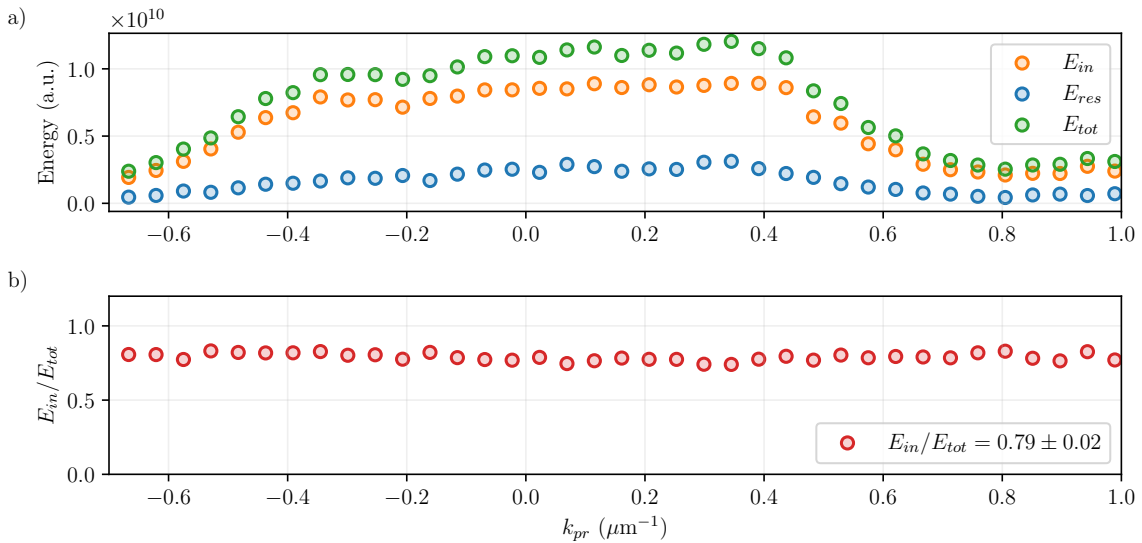


Fig. 5.11 **a)** **Energy budget.** The energy in the *in* mode (orange) the *res* mode (blue) and the total energy (green) are plotted as a function of the probe wavevector. **b)** **Ratio of the energy in the *in* mode with respect to the total energy.** The average value is 0.79 with a standard deviation of 0.02.

#### 5.2.4.3 Signature of amplification

Although the previous section highlighted the potential inaccuracies introduced by the modal decomposition, the method remains a robust and systematic approach to define the various modes, independently from specific experimental realizations. That is, the relative energy contribution of the *in* mode to the total energy remains invariant across different probe configurations, indicating that the bias in the field decomposition is effectively independent of which specific *in* mode is excited. To illustrate this point, we calculate the energy  $\int d\mathbf{r} |\delta\psi_i(\mathbf{r})|^2$  associated with each mode, as well as the total energy, as functions of the probe wavevector. The results are presented in Figure 5.11. The subpanel b) shows that the ratio  $E_{in}/E_{tot}$  remains approximately constant at 0.79 with a standard deviation of 0.02.

Moreover, it should be noted that the sum of the energies in the *in* and *out* modes precisely equals the total energy, as evident in a). Whereas this feature appeared obvious in momentum space since the modes were orthogonal by construction, it is less trivial in real space. In fact, the residual and scattered fields spatially overlap, giving rise to an interference term of the form  $\delta\psi_{res}^*(\mathbf{r})\delta\psi_{scat}(\mathbf{r})$ . In fact, this term sums up to zero when integrated over the whole space. This is a direct consequence of the Fourier transform isometry property which conserves the  $L^2$  scalar product.

To summarize, our method defines the input and output modes in a manner that is independent of the specific experimental realization. Consequently, variations in the relative contributions of individual modes across different configurations carry physical information about the interaction between the input mode and the interface.

To observe a signature of amplification, we compare two specific configurations: when the

input modes lie in the negative-positive energy mixing interval (configuration A) and when it lies outside of it (configuration B). The specific realizations taken for comparison are labeled in [Figure 5.8 a](#)). For both configurations, a cut of the intensity in the  $x$  direction is done for each mode. To smooth the data and enhance the signals, an average along the  $y$ -axis in the region of interest (ROI) defined by the white dashed rectangle of [Figure 5.10 d](#)) is performed. The results are shown in [Figure 5.12](#). The first observation is that, in both configurations, the residual mode yields an intensity spike at  $x = x_h$  reflecting that the residual field is in fact mostly located at the interface. However, the shape of the residual field is an additional proof that our mode decomposition was not perfect. Indeed, as explained in the previous section, if the residual field consisted solely of scattered modes, the resulting intensity profile would exhibit two decaying exponentials with distinct characteristic lengths. One oriented toward the upstream region with characteristic length  $l_u = v_u/2\gamma_{LP}$  where  $v_u$  is the  $u_{out}$  mode group velocity, and another oriented toward the downstream region corresponding primarily to  $d1_{out}$  with characteristic length  $l_d = v_d/2\gamma_{LP}$ . Furthermore, as remarkable in [Figure 5.8](#),  $|v_d|$  is always greater than  $|v_u|$  meaning that the upstream exponential should decrease faster than the downstream one. This is not what we observed and the displayed profile seems actually to present the opposite behavior. This being said, it does not prevent us from comparing the two configurations.

In configuration (B) the *res* mode intensity is significantly lower than the *in* mode and never exceeds it, whereas in configuration (A) where amplification is expected, the *res* mode intensity becomes larger than that of the *in* mode at the interface. For comparison purposes, we compute the intensity ratios at the interface for both cases. In configuration (B), we obtain  $I_{res}/I_{in} = 0.15$  while in configuration (A) we find  $I_{res}/I_{in} = 1.89$ . This suggests that whenever the input mode lies in the negative-positive energy mixing region, the relative contribution of the residual mode is significantly higher than when it lies outside this frequency interval, while the *in* mode remained the same.

To highlight that this enhancement arises from the Hawking effect, we computed this ratio for all the  $u_{in}$  mode. In each case, we take the left and right limit of the ratio  $I_{res}(x)/I_{in}(x)$  labeled  $L_u$  and  $L_d$  respectively :

$$\begin{aligned} L_u &:= \lim_{x \rightarrow x_H^-} I_{res}(x)/I_{in}(x) \\ L_d &:= \lim_{x \rightarrow x_H^+} I_{res}(x)/I_{in}(x) \end{aligned} \tag{5.12}$$

These coefficients embed contributions from the  $u_{out}$  and  $d1_{out}$  reflection and transmission and thus give information on the  $|S_{uu}|^2$  and  $|S_{d1u}|^2$  coefficients. The results are shown in [Figure 5.13 a](#)).

The error bars displayed come mainly from two sources: the uncertainty on the horizon position and the standard deviation of the energy ratio  $E_{in}/E_{tot}$  calculated above. Regarding the horizon position, it was initially defined as the position at which the speed of sound  $c_s = \sqrt{gn_0/m_{LP}}$  equals the fluid velocity  $\mathbf{v}_0$  while the previous chapter made clear that this velocity is not the relevant one to define the interface. Indeed the critical velocity  $v_c$  at which negative energy modes arise is greater than  $c_s$ . It means that computing the intensity ratios at  $x = x_h$  may introduce an error. Quantifying this uncertainty precisely is difficult since the discrepancy between  $v_c$  and  $c_s$  velocities does not follow a simple law and depends on the

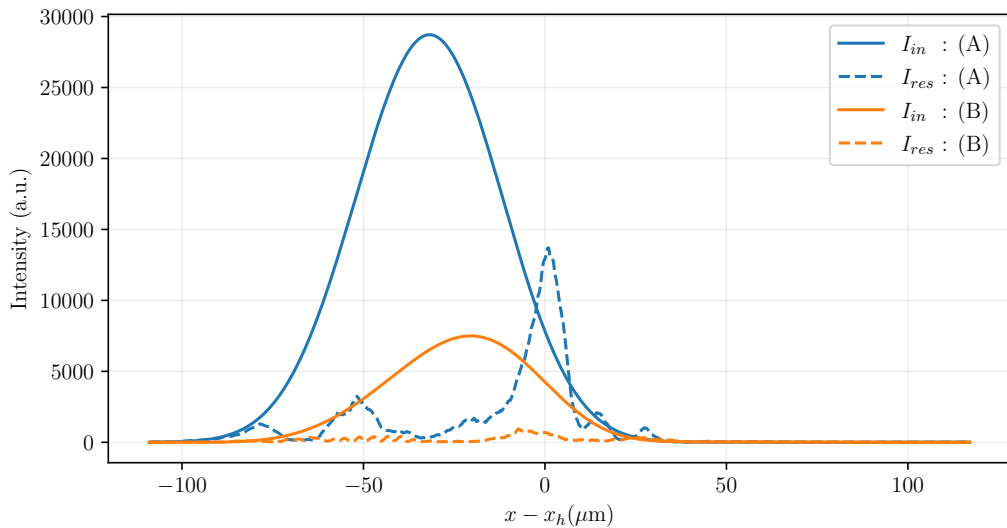


Fig. 5.12 a) **Intensity comparison.** Cuts along the  $x$  direction of the intensities of the *in* mode and the *res* mode for the two configurations (A) and (B). The blue color corresponds to the (A) configuration in which the input mode lies in the negative-positive energy mixing region while the orange color corresponds to the (B) configuration in which the input mode lies outside this region. The solid lines are the *in* mode intensities while the dashed lines are the *res* mode intensities.

fluids parameters. However, it is reasonable to assume that the horizon position lies within the upstream to downstream transition region of the fluid velocity (see Fig 5.5), which is of the order of  $\sigma_{x_h} = 5 \mu m$ . To propagate this uncertainty in the coefficients, we computed the intensity ratio at the left and right limits of position  $x_i$  where  $x_i \in [x_h - 5 \mu m, x_h + 5 \mu m]$ . Then, the mean values (resp. standard deviation) of the reflection and transmission coefficients are taken as the average (resp. standard deviation) of the left and right limits for all values of  $x_i$ .

The second main source of uncertainty comes from the energy ratio  $E_{in}/E_{tot}$ , which is computed from the energy budget shown in Figure 5.11 b). In other words, it ultimately originates from the procedure used to define the *in* and the *res* modes that, as already mentioned, is not perfect. Once again, it is complicated to report this uncertainty on our local measurements since it was initially obtained by integrating fields over the entire space for all configurations. We roughly estimate it by assuming that the relative error on the intensities is the same as the relative error on  $E_{in}/E_{tot}$  divided by the area corresponding to the full field of view over accessible with our imaging system that is  $226 \times 271 \mu m^2$ . In other words, this hypothesis correspond to consider that the error on  $\int |\delta\psi(r)|^2 dr$  is uniformly distributed over the integration area.

These two contributions are then added quadratically to obtain the final error bars shown in Figure 5.13 a).

**Analysis and discussion.** The first thing to notice is that the left and right limits of the intensity ratio are enhanced when the input mode lies in the negative-positive energy mixing

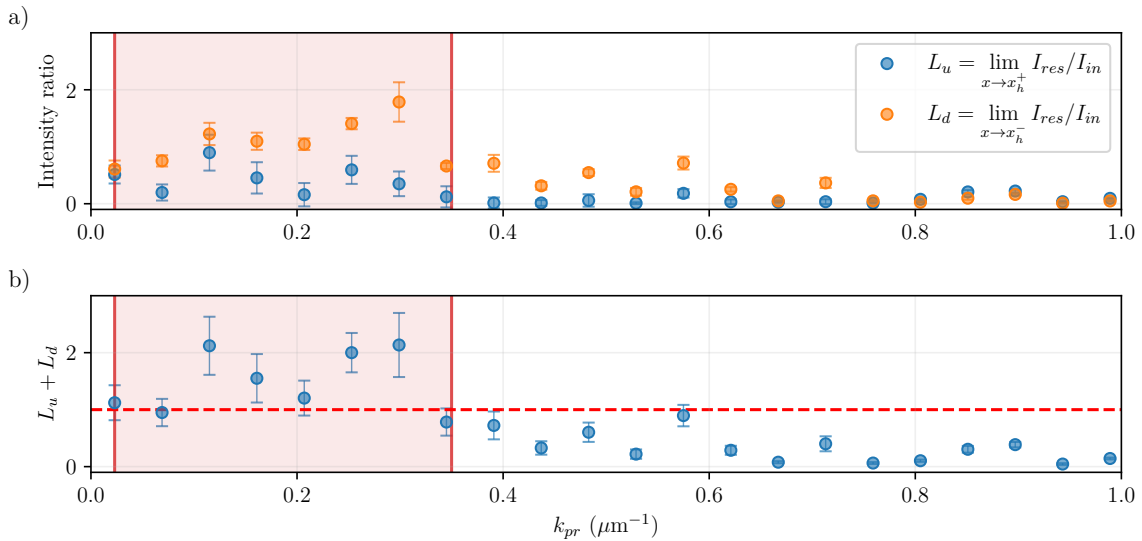


Fig. 5.13 **a) Intensity ratio.** Estimation of the reflection and transmission coefficients by taking the left and right limits of the intensity ratio  $I_{res}/I_{in}$  at the interface. The red colored region corresponds to the probe configurations where stimulated hawking radiation is expected. The error bars are calculated by taking into account uncertainties on the horizon position as well as the standard deviation of the energy ratio  $E_{in}/E_{tot}$ . **b) Sum of the reflection and transmission coefficients.** The error bars result from the quadratic sum of the relative error bars on the reflection and transmission coefficients. The red dashed line represent the line  $L_u + L_d = 1$ .

interval as shown in [Figure 5.13](#). This demonstrates that the contribution of the residual field is larger than in the other configurations and suggests that the scattering process is indeed different in this frequency interval. The sum of these two quantities is shown in [Figure 5.13 b\)](#). As visible, it can exceed one in the Hawking frequency range.

Together with the measurement of the  $d2_{out}^*$  modes presented in [Figure 5.9](#) these results provide a signature of amplification stemming from negative-positive energy mixing at the interface. However, as explained above, these values should not be quantitatively trusted and do not provide a direct measurement of the reflection and transmission coefficients despite all the efforts made to account for the discrepancies introduced by the mode decomposition. To obtain a quantitative measurement of the scattering coefficients, a better definition of the input modes is needed. Indeed, building the input mode from a Gaussian fit and a linear phase does not take into account the interplay between pumping, propagation and losses. A more accurate estimation would require a complete resolution of the Bogoliubov equation (3.18) by adding a force term to account for the probe laser injection.

From an experimental point of view, this can be done by placing the probe laser far enough from the interface in the upstream region so it does not interact with it. This would provide a direct way to compare the field with and without the interface, and any difference could be interpreted as a horizon feature. A second significant improvement would be to create a more homogeneous fluid in the unpumped region. This would reduce spurious scattering

events and make the plane wave approximation more reliable. This could be achieved either by finding a working point that is free of cavity impurities or by turning to the geometries created in the previous chapter where the pump intensity is finite everywhere. Finally, finding a way to measure  $d2_{out}^*$  and more generally, all the conjugate modes, with the same powerful interferometric method would allow a more straightforward comparison with the other modes, as well as real space information about their location, amplitude and phase. Implementing this method requires finding a phase reference at the conjugate frequency, which is phase locked with the probe laser. A possible solution would be to create two neighboring fluids with the same lasers, one for the experiment and one to create a reference beam through four-wave mixing. The advantage of this approach is that the reference beam would be naturally phase locked with the probe laser and directly at the conjugate frequency. Furthermore, having a local oscillator at the ghost branch frequency paves the way to quantum noise measurements such as homodyne detection and squeezing measurements [9].

### 5.3 Conclusion

In this chapter, we have presented the first experimental observation of stimulated Hawking radiation in a polariton quantum fluid. Using a fully optical approach, we demonstrated the ability to reconstruct the fluctuation field and detect scattered modes, providing evidence of negative-positive energy mixing at the interface. This mixing, a hallmark of the Hawking effect, was observed through the detection of outgoing modes and the conjugate mode  $d2_{out}^*$ , which together suggest amplification. Our measurement method, based on interferometric techniques, proved to be a powerful tool for isolating and analyzing the scattered modes. This approach highlights the versatility of the polaritonic platform, which, due to its optical nature, is particularly well-suited for such experiments. The results presented here pave the way for a more quantitative analysis of the scattering process, including the reconstruction of the scattering matrix. Such a complete measurement would be a significant step forward, enabling the study of correlations between emitted modes and providing deeper insights into the quantum nature of the Hawking effect. This work once again demonstrates the potential of polariton systems as a platform for exploring fundamental aspects of quantum field theory in curved spacetime. The combination of tunability, out-of-equilibrium properties, and full optical accessibility makes polariton fluids uniquely suited for analog gravity experiments, offering a promising avenue for future studies of quantum effects at analog horizons.

# **Chapter 6**

## **Bogoliubov modes correlations in a polariton quantum fluid**

The study of collective excitations in quantum fluids is fundamental to understand nonequilibrium dynamics and many-body interactions. Furthermore, the analog Hawking radiation on which this work is focused, is expected to create non classical correlations between Bogoliubov modes, the event horizon acting as a two mode squeezer [9]. The simplest manifestation of paired correlated emission can be observed in the density fluctuations second order correlation function [39; 44; 57; 70]. This observable exhibits a correlation pattern in the density fluctuations of the fluid on both side of the horizon. Yet, this has been done only numerically in polaritonic system since the experiment would require to resolve the polariton lifetime  $\sim 10\text{ps}$ . However the strong photonic component of this system suggests that correlations between collective excitations modes must have an optical signature that could be addressed with all the tools developed in quantum optics. In this work, we report the first experimental measurement of correlations between collective excitation modes—Bogoliubov modes—in a static and homogeneous quantum fluid of microcavity exciton-polaritons. By using a balanced detection set-up, we measure intensity correlation between the normal and ghost branches, probing the fluctuation dynamics of the polariton fluid and extracting the spectral correlations of Bogoliubov excitations. We observe a clear enhancement of the intensity correlations when the polariton fluid operates near the turning point of the bistability due to the emergence of correlated phonon-like excitations. These correlations, seeded by quantum and thermal fluctuations, provide insights into the role of the nonlinear and phononic interactions in the collective excitations of a polariton quantum fluid.

### **6.1 Quantum noise of an electromagnetic field**

#### **6.1.1 Standard quantum limit**

Let us first consider a mode of the electromagnetic field with a frequency  $\omega$ , quantized within a box of volume  $V$ . At a fixed point in space, the electric field can be expressed using the photon creation and annihilation operators :

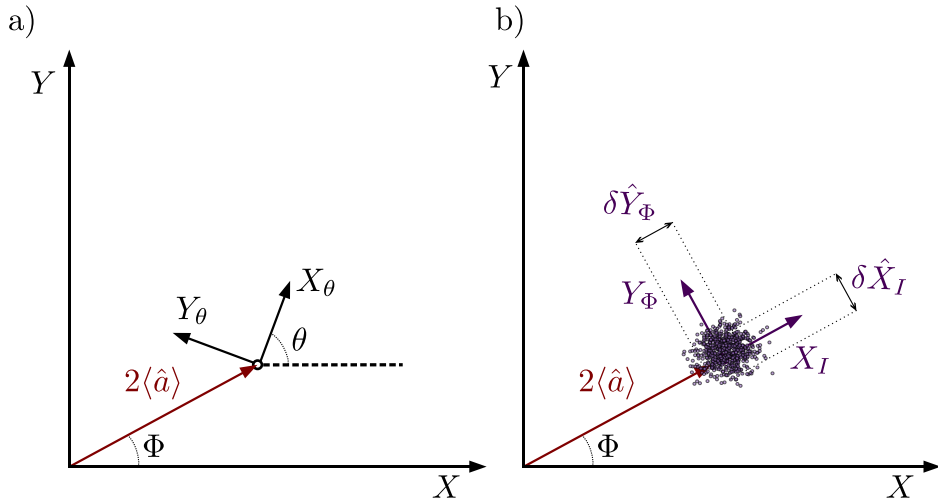


Fig. 6.1 **a)** Fresnel representation of a classical state. **b)** Quantum representation of the quadrature operators. The cloud of points around the mean value ( $\langle \hat{X} \rangle, \langle \hat{Y} \rangle$ ) represents several measurements of the same quantum state. The area of the cloud is bounded from below by the Heisenberg uncertainty principle. The quadratures  $\hat{X}_I$  and  $\hat{Y}_\Phi$  are the amplitude and phase quadratures respectively.

$$\begin{aligned}\hat{E}(t) &= E_0 (\hat{a}e^{-i\omega t} + \hat{a}^\dagger e^{i\omega t}) \\ &= E_0 (\hat{X} \cos(\omega t) + \hat{Y} \sin(\omega t))\end{aligned}\tag{6.1}$$

where we introduced the quadrature operators  $\hat{X}$  and  $\hat{Y}$  defined as :

$$\hat{X} = (\hat{a} + \hat{a}^\dagger) \quad \text{and} \quad \hat{Y} = i(\hat{a}^\dagger - \hat{a}).\tag{6.2}$$

The amplitude of the field  $E_0 = \sqrt{\frac{\hbar\omega}{2\epsilon_0 V}}$  where  $\epsilon_0$  is the vacuum permittivity, corresponds to the electric field of a single photon with energy  $\hbar\omega$  in the quantization volume  $V$ . For a classical field,  $X$  and  $Y$  are real numbers and correspond to the real and imaginary parts of the complex field amplitude in the Fresnel representation as visible in [Figure 6.1 a\)](#). In quantum mechanics, the quadrature operators are conjugate variables. Indeed, by using the commutation relation of the photon creation and annihilation operators  $[\hat{a}, \hat{a}^\dagger] = 1$ , we obtain :

$$[\hat{X}, \hat{Y}] = 2i.\tag{6.3}$$

Consequently, the quadrature operators are non-commuting variables and cannot be simultaneously measured with arbitrary precision. This is a direct consequence of the Heisenberg uncertainty principle stating that the product of the uncertainties in the two quadrature measurements is bounded from below by a constant value. More precisely, the variances

$\Delta X^2 = \langle \hat{X}^2 \rangle - \langle \hat{X} \rangle^2$  and  $\Delta Y^2 = \langle \hat{Y}^2 \rangle - \langle \hat{Y} \rangle^2$  must satisfy the inequality :

$$\Delta X^2 \Delta Y^2 \geq 1 \quad (6.4)$$

In contrast with the classical case, the vector  $(\langle \hat{X} \rangle, \langle \hat{Y} \rangle)$  representing the expectation values of the operators is associated with uncertainties whose area is bounded by the Heisenberg principle. The state most closely resembling a classical field is the one in which the fluctuations in both quadratures saturate [Equation 6.4](#). In this case, the uncertainty area assumes a circular shape with a diameter  $E_0$  in the phase space, as illustrated in [Figure 6.1 b\)](#). In this figure, the field and its fluctuations are not represented on the same scale; a laser field comprises a very large number of photons, whereas the fluctuations are much smaller. Such a minimum uncertainty state is referred to as a coherent state while the corresponding fluctuations define the standard quantum fluctuations. Coherent state are typically produced by a laser way above threshold and are the eigenvector of the annihilation operator  $\hat{a}$ .

### 6.1.2 Intensity and phase fluctuations

The choice of a given set of quadrature operators is arbitrary and corresponds to a choice of phase reference. Moving to another set of operators  $\hat{X}_\theta, \hat{Y}_\theta$  consists in a rotation in the phase space :

$$\hat{X}_\theta = \hat{X} \cos(\theta) + \hat{Y} \sin(\theta) \quad \text{and} \quad \hat{Y}_\theta = -\hat{X} \sin(\theta) + \hat{Y} \cos(\theta). \quad (6.5)$$

The rotated operators satisfy the same commutation relation [6.3](#) and the uncertainty relation [6.4](#) remains valid. However, a particular choice of quadratures is often made in the context of quantum optics [38] which consists in choosing  $\theta = \Phi$  where  $\Phi$  is the phase of the mean field  $\langle \hat{a} \rangle = |\hat{a}|e^{i\Phi}$ . The fluctuations of the corresponding quadrature operators that we call  $\hat{X}_I$  and  $\hat{Y}_\phi$  are then proportional to intensity and phase fluctuations respectively as shown in [Figure 6.1 b\)](#). In the case of a laser beam, the standard quantum limit is also referred to as the shot noise limit and corresponds to a poissonian statistics in the photon arrival time [38]. Indeed, the measurement of the intensity of a laser beam is subject to statistical noise scaling as the square root of the mean number of photons in the beam.

$$\Delta \hat{N}^2 = \langle \hat{N} \rangle \quad (6.6)$$

From an experimental point of view, this relation is helpful since it provides a direct way to infer the standard quantum limit from an intensity measurement.

### 6.1.3 Squeezed states

While vacuum fluctuations serve as a reference for quantum fluctuations, there is nevertheless no fundamental restriction against obtaining states in which the fluctuations of a given quadrature,  $\hat{X}_\theta$ , are reduced below the standard quantum limit. Indeed, the Heisenberg inequality pertains to the product of uncertainties. This inequality remains satisfied provided that the fluctuations in the orthogonal quadrature  $\hat{Y}_\theta$  increase accordingly. Graphically, their representation is obtained by squeezing the uncertainty area along the direction of

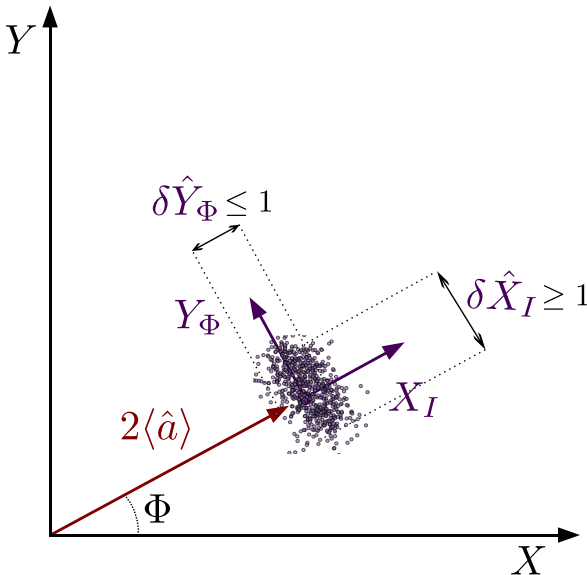


Fig. 6.2 Representation of a squeezed state in the phase space. The uncertainty area is squeezed below the SQL along the  $\hat{Y}_\Phi$  phase quadrature and correspondingly stretched along the  $\hat{X}_I$  intensity quadrature. The uncertainty area is still bounded by the Heisenberg uncertainty principle.

the quadrature  $\hat{X}_\theta$  and stretching it along the direction of  $\hat{Y}_\theta$ . A typical representation of such a state in the phase space is shown in ???. The resulting states are referred to as a squeezed state, and are of great interest in quantum optics as they can be used to enhance the sensitivity of measurements. As an example, phase squeezed state are used in LIGO-VIRGO infrastructures to resolve the infinitesimal displacements of the interferometer mirrors induced by the gravitational waves.

## 6.2 Photodetection

A photodetector is a device that converts the energy of a photon into an electrical signal. The most common type of photodetector is the photodiode, which operates by generating a current in response to the absorption of photons. In principle, such devices allows to acquire and process all the information contained in the electromagnetic field by electronic means. However, an optical field oscillates at hundreds of terahertz, which is far beyond the bandwidth of any electronic device. A photodiode can thus only provide a time-averaged signal, which is proportional to the intensity of the field. More precisely, the mean value of the photo-current  $\bar{i}$  is proportionnal to the incoming photon flux as :

$$\bar{i} = \eta e \frac{P}{\hbar\omega} \quad (6.7)$$

where  $\eta$  is the quantum efficiency of the photodetector,  $e$  is the electron charge,  $P$  is the power of the incoming light and  $\hbar\omega$  is the energy of a single photon. In the ideal case  $\eta = 1$  where 100% of the photons are converted into electrons the current statistics reproduce exactly the

statistics of the incoming light. However, in practice, the quantum efficiency is always less than one and the photodetector introduces losses that add to the photonic losses that the incoming beam may have already undergone. Such losses are random events and subsequently lead any statistics to become Poissonian when they are large enough.

This being said, an incoming photon flux shot noise limited will produce a photocurrent that also follows a Poissonian statistics. For a mean number of electron  $N_e$  produced by the photodetector, the variance is :

$$\Delta N_e^2 = N_e. \quad (6.8)$$

From which we deduce the variance of the photocurrent on a time interval  $\Delta t$  :

$$\Delta i^2 = \frac{e^2 \Delta N_e^2}{\Delta t^2} = \frac{e^2 N_e}{\Delta t^2}. \quad (6.9)$$

Furthermore, by writing  $N_e = \bar{i} \Delta t / e$  we obtain :

$$\Delta i^2 = \frac{e \bar{i}}{\Delta t}. \quad (6.10)$$

This relation shows that the variance of the photocurrent is inversely proportional to the time interval over which the current is measured. In the frequency domain it means that the variance is proportional to the bandwidth of the measurement apparatus  $\delta f = 1/2\Delta t$ . Furthermore, in the case where the latter can be modeled by a narrow band-pass filter centered on an analysis frequency  $\omega_c$  it can be shown [20] that the variance of the photocurrent is related to its power spectral density (PSD) as :

$$\Delta i^2 = 2\delta f S_i(\omega). \quad (6.11)$$

This is precisely how a spectrum analyzer works. It measures the power spectral density of the photocurrent  $S_i(\omega)$  by integrating its variance over a given bandwidth  $\delta f$  usually limited by the resolution bandwidth (RBW) of the spectrum analyzer. At the end, we have a way to measure the power spectral density of the incoming light field by measuring the variance of the photocurrent. Let us now see how such a device can be used to measure the correlations between two fields.

### 6.3 Balanced detection

Intensity balanced detection is a common detection scheme used to suppress the classical noise commonly present in optical measurements and measure the intensity noise of a beam. The basic principle of this technique is to use two photodetectors, each measuring the intensity of an optical field, and to subtract their output photo-currents. If the two beams share the same classical noise, the subtraction will cancel it out, leaving only the quantum correlations. A representation of the balanced detection scheme is shown in [Figure 6.3](#). Usually, these kind of apparatus are also able to measure the sum of the two photo-currents which is proportional to the total noise of the two beams. However, as we will see in the next section, measuring the difference together with the individual photo-currents is sufficient to obtain the correlation function of the two fields.

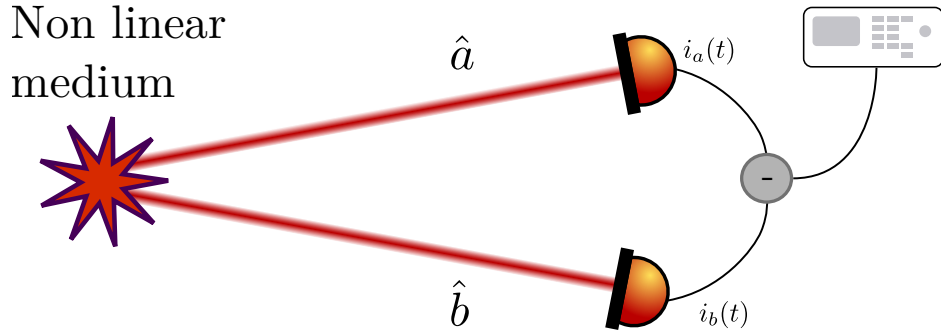


Fig. 6.3 *Balanced detection scheme. Example of a typical nonlinear medium producing two modes of the electromagnetic field  $\hat{a}$  and  $\hat{b}$ . Each of them is sent to a photodiode that produces a photo-current carrying the noise of the beams. The output photo-currents are then subtracted to cancel the classical noise and sent into a spectrum analyzer.*

### 6.3.1 Difference measurement

Let us consider two fields  $\hat{a}$  and  $\hat{b}$  impinging on two photodetectors as shown in Figure 6.3. Their respective intensities are given by their number operator  $\hat{N}_a = \hat{a}^\dagger \hat{a}$  and  $\hat{N}_b = \hat{b}^\dagger \hat{b}$ . We are interested in the intensity difference operator  $\hat{N}_-$  defined as :

$$\hat{N}_- = \hat{a}^\dagger \hat{a} - \hat{b}^\dagger \hat{b}. \quad (6.12)$$

As explained above, it is convenient to linearize each operator around its mean value :

$$\begin{aligned} \hat{a} &= |\alpha| e^{i\Phi} + \delta \hat{a} \\ \hat{b} &= |\beta| e^{i\Psi} + \delta \hat{b} \end{aligned} \quad (6.13)$$

where  $|\alpha| e^{i\Phi}$  and  $|\beta| e^{i\Psi}$  are the mean values of the two fields and  $\delta \hat{a}$  and  $\delta \hat{b}$  are their respective fluctuations. The difference operator can then be expressed to first order in the fluctuations as :

$$\begin{aligned} \hat{N}_- &= (|\alpha|^2 e^{i\Phi} + \delta \hat{a}^\dagger)(|\alpha| e^{i\Phi} + \delta \hat{a}) - (|\beta|^2 e^{i\Psi} + \delta \hat{b}^\dagger)(|\beta| e^{i\Psi} + \delta \hat{b}) \\ &= |\alpha|^2 - |\beta|^2 + (|\alpha| \delta \hat{X}_a^\Phi + |\beta| \delta \hat{X}_b^\Psi) \end{aligned} \quad (6.14)$$

The mean value  $\langle N_- \rangle = |\alpha|^2 - |\beta|^2$  provides information about the average intensity difference between the two beams. In the balanced case—that is, when this difference vanishes—the fluctuations of the difference can be expressed as:

$$\delta \hat{N}_- = |\alpha| (\delta \hat{X}_a^\Phi - \delta \hat{X}_b^\Psi). \quad (6.15)$$

If the two fields are intensity correlated, the fluctuations of the difference operator is reduced. The case where  $\langle N_- \rangle \neq 0$  requires a more detailed analysis. In particular, it should be noted that in this situation, the individual quantum noise of each mode plays a role in the measurement of correlations. For further discussion, one can refer to [72]. In practice, we will measure the variance of the difference operator as we will see in the next section.

## 6.4 Correlations in continuous-variables quantum optics

As a very general statement, two quantities are said to be correlated if they ultimately originate from the same source or quantum process. In this case, a knowledge of one of the two quantities gives informations about the other. Take the example of a two photons emission by a non linear process such as a Type II spontaneous parametric down conversion (SPDC). Their correlations is of several natures. The first and most obvious one is temporal in the sense that the two photons are emitted at the same time. This can be quantified by looking at the second order intensity correlation function  $g^{(2)}(t,t')$ , which is the probability of detecting a photon at time  $t$  and another one at time  $t'$  [12]. They can also be correlated through their polarization meaning that if one photon is detected in a given polarization, the other one will be detected in the orthogonal polarization. Reversing the picture, the measurement of a given type of correlations can thus provide informations about the quantum nature of the process that generated them.

### 6.4.1 Correlation function.

Let us consider a quantum operator evolving in time  $\hat{f}(t)$ . The autocorrelation of  $\hat{f}$  at time  $t$  and  $t'$  is defined as :

$$C_{\hat{f}}(t,t') = \langle \hat{f}(t)\hat{f}(t') \rangle = \langle \delta\hat{f}(t)\delta\hat{f}(t') \rangle \quad (6.16)$$

where  $\delta\hat{f}(t) = \hat{f}(t) - \langle \hat{f}(t) \rangle$  is the fluctuation of the operator around its expectation value. If the process at stake is stationary,  $\langle \hat{f}(t) \rangle$  does not depend on  $t$  and the correlation function depends only on the time difference  $\tau = t - t'$  [5]. In this case, the Wiener-Khinchin theorem states that the autocorrelation function is related to the spectral density of the field  $S_{\hat{f}}(\omega)$  by a Fourier transform [20] :

$$S_{\hat{f}}(\omega) = \int_{-\infty}^{+\infty} C_{\hat{f}}(\tau) e^{-i\omega\tau} d\tau. \quad (6.17)$$

In the same manner, it is possible to define the cross-correlation between two operators  $\hat{f}_a$  and  $\hat{f}_b$  as :

$$C_{\hat{f}_a, \hat{f}_b}(t, t') = \langle \hat{f}_a(t)\hat{f}_b(t') \rangle = \langle \delta\hat{f}_a(t)\delta\hat{f}_b(t') \rangle \quad (6.18)$$

The corresponding cross power spectral density (for stationary processes) is given by the Fourier transform of this correlation function :

$$S_{ab}(\omega) = \int_{-\infty}^{+\infty} C_{ab}(\tau) e^{i\omega\tau} d\tau \quad (6.19)$$

If we are now interested in the autocorrelation of the difference operator  $\hat{N}_-$  defined in [Equation 6.12](#), one can express the PSD of the difference operator as [5] :

$$S_-(\omega) = S_a(\omega) + S_b(\omega) - 2S_{ab}(\omega). \quad (6.20)$$

where  $S_a(\omega)$  and  $S_b(\omega)$  are the power spectral densities of the number operators  $\hat{N}_a$  and  $\hat{N}_b$  respectively. From this, we define the normalized cross-correlation function between the two operators as :

$$C_{ab}(\omega) = \frac{S_{ab}(\omega)}{\sqrt{S_a(\omega)S_b(\omega)}}. \quad (6.21)$$

The PSD of the difference operator can then be expressed in terms of the normalized cross-correlation function as :

$$S_-(\omega) = S_a(\omega) + S_b(\omega) - 2\sqrt{S_a(\omega)S_b(\omega)}C_{ab}(\omega). \quad (6.22)$$

Due to the Cauchy-Schwarz inequality,  $C_{ab}$  is bounded between  $-1$  and  $1$ . A value of  $C_{ab}(\omega) = 1$  indicates that the two operators are perfectly correlated, while  $C_{ab}(\omega) = -1$  indicates that they are perfectly anti-correlated.

Finally, if we invert [Equation 6.22](#), we can express the normalized cross-correlation in terms of the PSDs as :

$$C_{ab}(\omega) = \frac{S_-(\omega) - S_a(\omega) - S_b(\omega)}{-2\sqrt{S_a(\omega)S_b(\omega)}}. \quad (6.23)$$

By measuring the PSD of the difference operator  $S_-(\omega)$  and the individual PSDs  $S_a(\omega)$  and  $S_b(\omega)$ , we can thus obtain the normalized cross-correlation function  $C_{ab}(\omega)$  between the two operators.

#### 6.4.2 Bogoliubov modes correlations

Let us now consider a static homogeneous polariton fluid created by a pump with frequency and wavevector  $(\omega_p, k_p)$ , operating on the high density branch of the bistability curve as we did in the previous chapters. We set our description in the rotating frame of the pump laser so that in the following we will drop the pump frequency  $\omega_p$  and wavevector  $k_p$ . A given bogoliubov mode at  $(k, \omega)$  on the normal branch, and its conjugate mode at  $(-k, -\omega)$  on the ghost branch, are expected to be correlated. Indeed, they ultimately result from a four-wave mixing process that is the parametric scattering of two pump polaritons into two Bogoliubov modes at  $(k, \omega)$  and  $(-k, -\omega)$ . More precisely, the phase matching and energy conservation conditions of the four-wave mixing process read as :

$$(0,0) + (0,0) \rightarrow (k, \omega) + (-k, -\omega). \quad (6.24)$$

**Bogoliubov coefficients.** According to the Bogoliubov theory, the Bogoliubov amplitudes  $u_k$  and  $v_k$  related to the normal branch mode and the ghost branch mode respectively are given by [15; 60] :

$$u_k = \sqrt{\frac{1}{2} \left( \frac{\epsilon_k + gn_0}{\omega_B^+(k)} + 1 \right)}, \quad (6.25)$$

$$v_k = -\sqrt{\frac{1}{2} \left( \frac{\epsilon_k + gn_0}{\omega_B^+(k)} - 1 \right)}. \quad (6.26)$$

where  $gn_0$  is the interaction energy,  $\epsilon_k = \hbar k^2/2m_{LP}$  is the kinetic energy with  $m_{LP}$  the polaritons effective mass, and  $\omega_B^+(k)$  is the positive norm Bogoliubov frequency that we remind here :

$$\omega_B^+(k) = \sqrt{\left(\frac{\hbar k^2}{2m_{LP}} - \delta + 2gn_0\right)^2 - (gn_0)^2} \quad (6.27)$$

with  $\delta = \omega_p - \omega_{LP}$  the detuning between the pump laser and the polariton resonance frequency  $\omega_{LP}$  at zero wavevector. Note that the reservoir contribution was not taken into account without loss of generality since its contribution can be absorbed in the detuning  $\delta$ .

**Stimulated emission.** The Bogoliubov modes can be probed by injecting a weak probe laser beam at a specific wavevector  $k_{pr}$  and frequency  $\omega_{pr}$ , chosen to be resonant with the mode at  $(k_{pr}, \omega_{pr})$  on the normal branch, as in previous experiments.

As explained in [chapter 4](#), this results in the stimulation of a four-wave mixing process, leading to the emission of two optical beams at  $(k_{pr}, \omega_{pr})$  and  $(-k_{pr}, -\omega_{pr})$ . Using the input-output formalism [34], one can compute the expected intensities of the emitted beams on the normal and ghost branches as:

$$\begin{aligned} I_N(k_{pr}, \omega_{pr}) &= |u_{k_{pr}}|^4 |\alpha|^2 \text{ for the normal branch} \\ I_G(-k_{pr}, -\omega_{pr}) &= |v_{k_{pr}} u_{k_{pr}}|^2 |\alpha|^2 \text{ for the ghost branch.} \end{aligned} \quad (6.28)$$

where  $|\alpha|^2$  is the intracavity probe intensity. This two intensities are expected to yield high correlation since they result from a nonlinear four-wave mixing process [36; 66]. Measuring this correlation is the goal of this experiment.

By computing the ratio of the two intensities, we can eliminate the probe contribution and obtain the Bogoliubov coefficients ratio  $u_{k_{pr}}^2/v_{k_{pr}}^2$ . The asymptotic behavior of this ratio is then expected to scale as [15]. :

$$\begin{aligned} \frac{u_{k_{pr}}^2}{v_{k_{pr}}^2} &\sim \frac{\hbar^2 k^4}{m_{LP}^2 g^2 n_0^2} && \text{when } k_{pr} \rightarrow +\infty \\ &\sim 1 && \text{when } k_{pr} \rightarrow 0. \end{aligned} \quad (6.29)$$

As a result, the beams on the normal and ghost branches are balanced at low wavevectors, which is expected to enhance the correlations between the two beams, as will be discussed in the following section.

## 6.5 Experimental implementation

The set up used is similar to the one used in the previous experiment with the addition of a balanced detection scheme that will be detailed in the next section. The microcavity is the same as the one used in the previous chapters but the experiment is runned at the working point B10-C10 (see [Figure 4.5](#)).

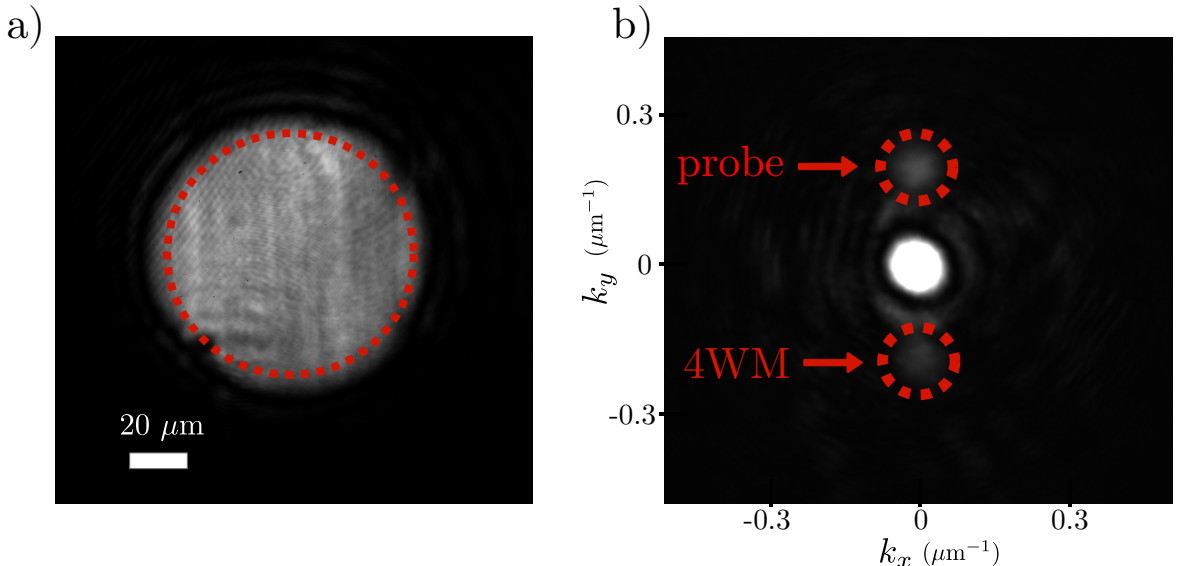


Fig. 6.4 **a)** Real space image of a polariton fluid operating on the high density branch of the bistability loop. The image is taken at the working point B10-C10. The red dashed circle represents the pinhole applied to the image to filter out the signal coming from the edges of the fluid. **b)** Corresponding  $k$ -space image of the polariton fluid when a weak probe is exciting the normal branch at  $k_{pr} = 0.2 \mu\text{m}^{-1}$ . The direct transmission of the probe is pointed out by the red arrow on top of the image while its four wave mixing signal is visible at  $-k_{pr}$ . The red dashed circles represent the pinholes applied in the Fourier plane to isolate each signal before sending it to the balanced detection scheme.

### 6.5.1 Bogoliubov coefficients measurement

We create a static polariton fluid by shinning a pump laser beam of diameter  $w = 100 \mu\text{m}$  at normal incidence on the microcavity ie at  $k_p = 0$ . The laser is detuned from the polariton resonance by  $\delta = 35 \text{ GHz}$  in order to operate in a bistable regime. The pump laser is  $\sigma_+$  polarized in order to excite a single polariton population [1]. A typical real space image of the polariton fluid is shown in Figure 6.4 a).

To begin with, the collective excitation spectrum of the fluid is measured with the same method than in chapter 4. The pump laser intensity is set to operate close to the turning point of the higher branch of the bistability loop but sufficiently far from it to have a stable polariton fluid. The normal branch shown in Figure 6.5 a) is measured through direct excitation ie by placing pinholes that track the probe wavevector in the Fourier space at each energy scan. Conversely, the ghost branch shown in b) is measured through 4WM excitation meaning that the pinholes are systematically positioned at the opposed wavevector  $-k_{pr}$ . At each couple  $(k, \omega)$  and  $(-k, -\omega)$  the corresponding intensities are measured by fitting the resonance peaks by a Lorentzian function. As outlined by the previous section, by then computing the ratio of the two quantities, the probe contribution disappears and we can have acces to the Bogoliubov coefficients ratio  $u_{k_{pr}}^2/v_{k_{pr}}^2$ . Figure 6.5 c) shows this ratio as a function of the probe wavevector  $k_{pr}$ . At low wavevector, the ratio tends to a constant

value which is expected from the Bogoliubov theory as explained in the previous section. A quantitative value of this value can non be extracted from the data because at low wavevector the measurement method does not allow to discriminate the two conjugated modes. However, one can appreciate that the ratio is close to one which is consistent with the theoretical prediction. At high wavevector  $u_{k_{pr}}^2/v_{k_{pr}}^2$  is expected to follow a  $k^4$  law as previously explained. To discuss this feature, we take the data for  $|k_{pr}| > 1/\xi \approx 0.35 \mu\text{m}^{-1}$  and fit them with a power law of the form  $ak^\beta$  with  $a$  and  $\beta$  as fitting parameter. The healing length  $\xi = 3 \mu\text{m}$  is estimated from the detuning  $\delta = 35 \text{ GHz}$  which is slightly lower than the interaction energy  $gn_0$  since the system operates close to the turning point of the bistability loop.

The resulting fit are represented by the red dashed line in [Figure 6.5 c\)](#). The fit gives a value of  $\beta = 3.74 \pm 0.5$  for negative wavevector whereas for positive wavevector we obtain  $\beta = 1.47 \pm 0.5$ . The first value is consistent with the Bogoliubov theory prediction of  $\beta = 4$  while the second one is not. The uncertainty on  $\beta$  is of 13% for  $k < 0$  and 34% for  $k > 0$ . This asymmetry between the two branches is not well understood and may be due to a sample effect that is not perfectly isotropic. Indeed, as explained in [chapter 4](#), the sample exhibits a so called wedge which can be understood as a small tilt of the microcavity DBR mirrors. This creates a direction along which the photon resonance energy increases as a function of the cavity width. This breaking of symmetry may result in a  $k$ -dependent efficiency of the emission that is not taken into account in the initial model. A way to verify this hypothesis would be to precisely characterize the wedge as well as the  $k$ -dependance of the DBR reflectivity and run numerical simulations of angle and energy resolved emission.

It is worth noticing that at low wavevector  $|k_{pr}| < 0.5 \mu\text{m}^{-1}$  where  $k$  and  $-k$  are closer to each other, symmetry between the branch is restored which support the anisotropy hypothesis we just made.

**Bogoliubov coefficients.** The Bogoliubov coefficients  $u_{k_{pr}}$  and  $v_{k_{pr}}$  can be separately extracted from the ratio  $u^2/v^2$  by using the normalization condition  $u^2 - v^2 = 1$ . The results are shown in [Figure 6.5 d\)](#). While we observe a clear enhancement of both coefficients at low wavevector, we do not observe the  $1/k$  divergence expected from the Bogoliubov theory. This is not due to the incapacity of the experimental method to disinguish between the normal and the ghost the modes a low wavevector. Indeed, such a divergence should be observed in the overall intensity collected by the pinhole. In fact, in the litterature [15; 58; 60], the  $1/k$  behavior is computed for a homogeneous and infinite condensate. In practice, eventhough the polariton fluid is homogeneous it has a finite size of  $w = 100 \mu\text{m}$ . The latter, limits the minimum wavevector that can be probed to  $k_{min} = \pi/w \approx 0.03 \mu\text{m}^{-1}$ . In other words, it is not possible to excite modes that correspond to interactions ranges greater than the size of the fluid.

In view of measuring correlations between the Bogoliubov modes, the validation that the emissions in the two branches become balanced at low wavevector suggests that correlations should increase in this regime [72]. This is precisely what we observe as we will see in the next section.

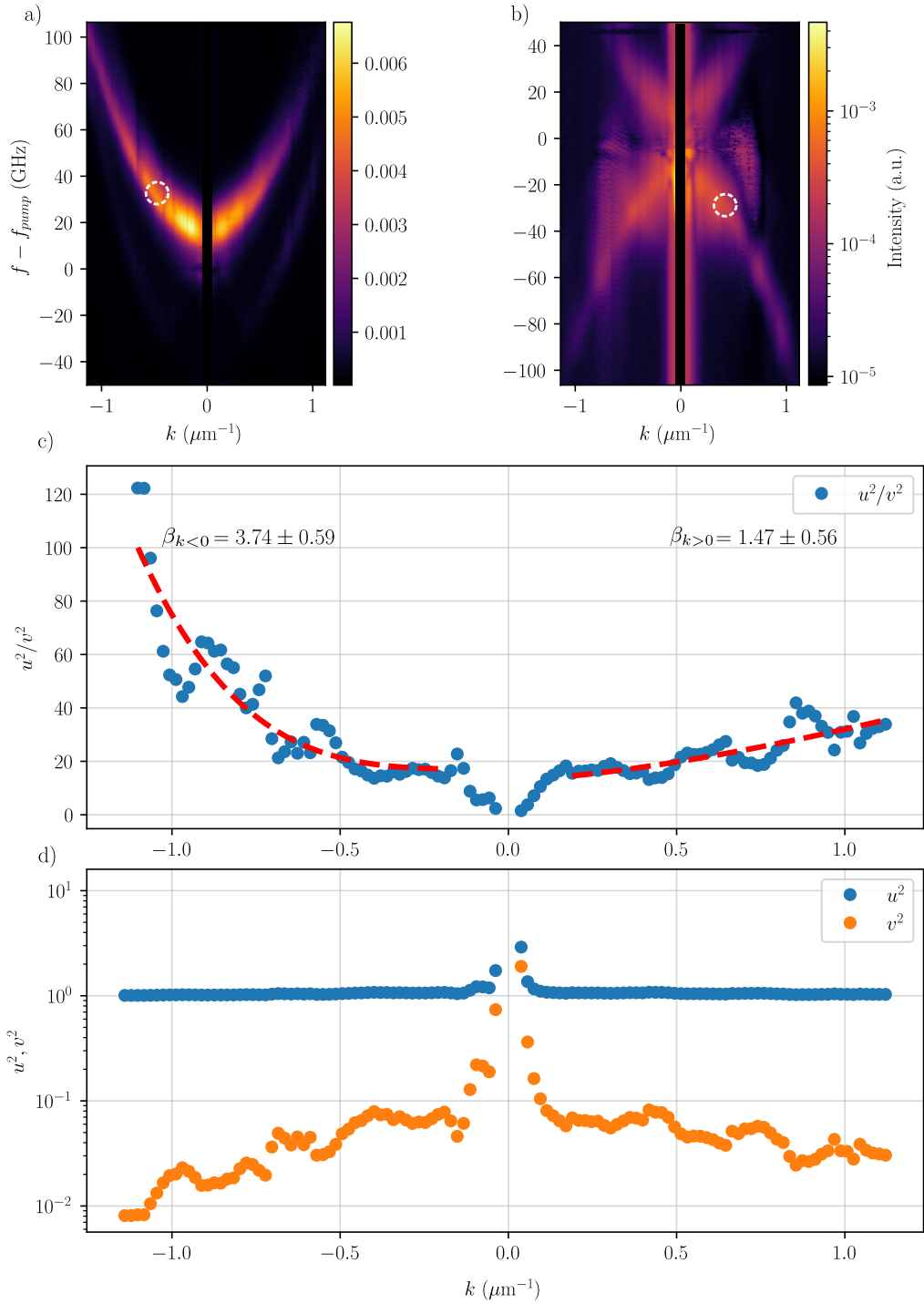


Fig. 6.5 **Bogoliubov dispersion measurement.** **a)** Normal branch measurement. **b)** Ghost branch measurement. As explained in chapter 4, the black solid rectangle centered at  $k = 0$  on both plots represents the region where the two conjugate modes start to overlap in the  $k$ -space and thus cannot be resolved. The white dashed circles represent two conjugated bogoliubov modes whose emission are compared to extract the Bogoliubov coefficients  $u$  and  $v$ .

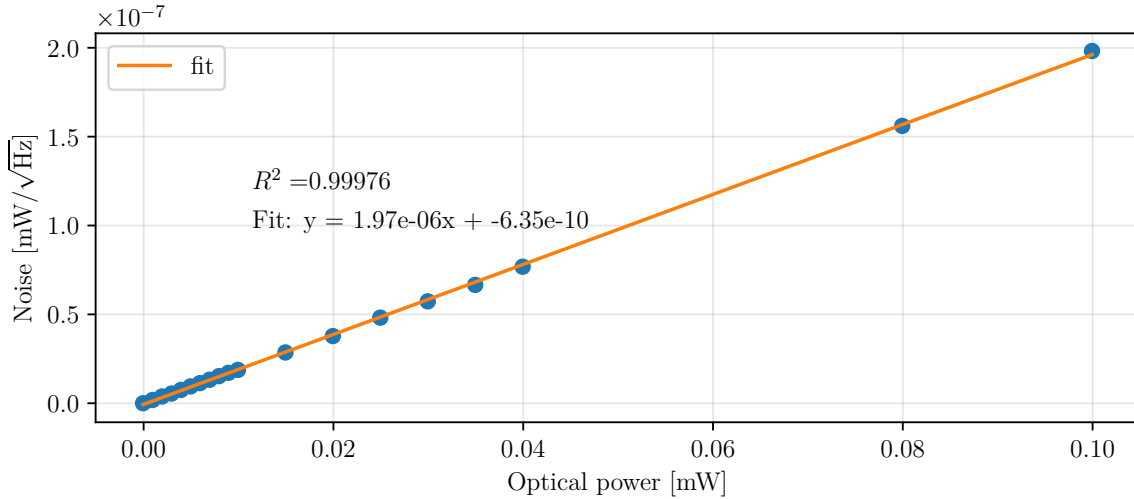


Fig. 6.6 *Shot noise calibration.* The variance of the photocurrent is measured as a function of the laser power. The dark noise of the apparatus measurement has been subtracted. The linear fit gives the coefficient relating the intensity of the laser and the shot noise level.

## 6.5.2 Bogoliubov modes correlations

### 6.5.2.1 Shot noise calibration

Since we are interested in measuring correlations produced by the non linear four wave mixing process, it is necessary to make sure that both the lasers injected in the microcavity don't introduce any classical noise in the system. Indeed, as explained in [72], if the laser used to stimulate non linear effect carry classical noise, both of the emitted beam will be classically correlated which will result in a strong noise reduction in the difference photocurrent and artificially enhance the correlations. To verify that the lasers are shot noise limited, we send one of them on a half wave plate followed by a polarizing beam splitter (PBS). This enables to precisely balance the two outputs of the PBS before sending them to the balanced detection scheme and make sure that any classical noise is cancelled out. Then, the intensity of the laser is ramped up. At each intensity value, the PSD is measured by a spectrum analyzer in order to determine the linear relation between the laser power and the intensity variance. Since all the classical noise has been removed, this variance reflects the poissonian statistics stemming from the intrinsic quantum noise of the lasers as explained in the previous section. As this statistic is universal, there is no need to make the measurement for the two lasers and the linear coefficient relating intensity and noise is fixed by the measurement apparatus [5].

The results are presented in Figure 6.6. As expected, the variance of the photocurrent is linear with the laser power. This calibration curve is then used to make sure that the lasers are shot noise limited by verifying that, for a given laser power its power spectral density falls on the calibration curve. Of course, the settings of the spectrum analyzer as well as the photodetector must be exactly the same as the ones used for the calibration process. Since the quantum noise is a white noise, the calibration as well as the experiment can be in principle done at any frequency. However, it is convenient to chose an analysis frequency at

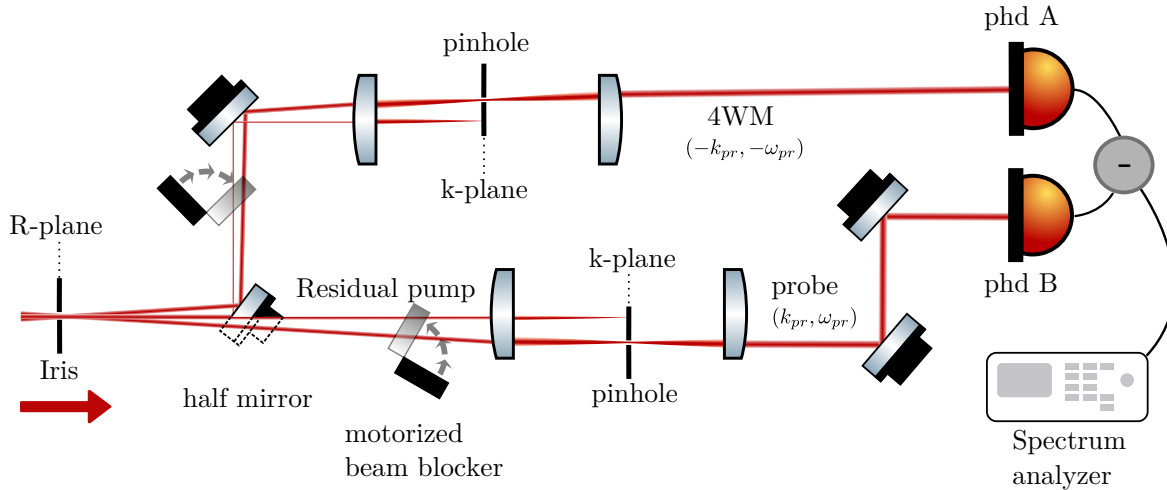


Fig. 6.7 Experimental set up used to measure the correlations between Bogoliubov modes. The red arrow represent the propagation direction of the light. The first real space filtering is done with an adjustable iris diaphragm while the filterings in Fourier space are done with pinholes of diameter  $w = 300 \mu\text{m}$  to match the size of the probe. A motorized beam blocker is placed on each optical path to measure the noise of each beam separately. The focal lengths of the lenses are chosen to magnify the image so its matches the size of the photodiodes sensors that are  $d = 800 \mu\text{m}$  in diameter. The two photodiodes are connected to a spectrum analyzer in zero span mode at 1.5 MHz. The resolution bandwidth (RBW) and the video bandwidth (VBW) are set to 100 kHz.

least in the MHz range to the  $1/f$  electronic noise as well as classical noises like vibrations while staying in the photodetector bandwidth of few MHz. These vibrations are mainly due to the vacuum pump connected to the cryostat whose frequency do not exceed hundreds of kilohertz. Further increasing the analysis frequency mean that the photodetector bandwidth must be accordingly increased which would result in a reduction of the apparatus gain and thus of the signal to noise ratio. To have the best compromise between these constraints, the calibration and the experiment were done at 1.5 MHz.

Using the calibration curve, we verified that both of the lasers used in the experiment are shot noise limited thus ensuring that no classical noise is introduced in the system.

The photodiodes used in this experiment are industrial Thorlabs PDB450A photodiodes with adjustable gain. The latter is set to  $10^4$  in order to have a bandwidth of 4 MHz. The spectrum analyzer is a RIGOL DSA-815 in zero span mode at 1.5 MHz. The resolution bandwidth (RBW) as well as the video bandwidth (VBW) are set to 100 kHz in order to have a good compromise between the signal to noise ratio and the measurement time. The sweep time is set to 100 ms.

### 6.5.2.2 Balanced detection

Once the polariton fluid is established, we fix the probe wavevector to  $k_{pr} = 0.2 \mu\text{m}^{-1}$  and tune the laser frequency to be resonant with the normal branch of the bogoliubov dispersion. The field outgoing the microcavity is then directed to a balanced detection setup, illustrated

in [Figure 6.7](#). To measure the correlations between the Bogoliubov modes, it is essential to isolate the two conjugate modes from each other but also from the pump.

If the photodiodes collect residual light from the pump, the detection scheme may yield a spurious non-zero correlation even in the absence of the probe. Indeed, although the pump laser generating the mean field is shot-noise limited, the photonic component of the polariton fluid escaping the microcavity is not. This excess noise originates from the Kerr effect inside the cavity, which leads to self-phase modulation of the polariton field. As a result, additional intensity and phase fluctuations are introduced in the fluid. If one spatially isolate two region of the fluid, the fluctuations in the mean field will be correlated, leading to a non-zero correlation signal in the balanced detection scheme. However, these correlations do not stem from the nonlinear scattering process under investigation, but rather from the single mode character of the polariton fluid as demonstrated in [\[4\]](#).

To prevent this, we first proceed to a filtering of the polariton fluid in real space as shown in [Figure 6.7](#). The real space image of the polariton fluid is filtered using a pinhole of diameter  $w = 100 \mu\text{m}$ , which is the same as the pump beam diameter. The purpose of this filtering is to remove the light coming from the edges of the polariton fluid, which, as explained in the previous chapter, expels polaritons at high momentum and may yield a spurious signal in the detection scheme. The filtered image is then left to propagate, allowing the Bogoliubov signals at  $k_{\text{pr}}$  and  $-k_{\text{pr}}$ , as well as the mean field at  $k = 0$ , to become spatially separated in the far field. Then, a half mirror is used to split the light into two paths as shown in [Figure 6.7](#). At this stage, both paths still contain mean field photons. To remove them, another filtering is applied in the Fourier plane to isolate the Bogoliubov modes as shown in [Figure 6.4 b\)](#). This picture shows the whole  $k$ -space image for the sake of clarity, but in practice, the top and bottom halves belong to two different paths of the balanced detection scheme.

**Experiment check.** To validate that the apparatus is able to measure correlations between the Bogoliubov modes and is not only measuring the single mode character of the polariton fluid [\[4\]](#), we inject two probe beams in the system in order to generate two independent four wave mixing processes. Both of them come from the same laser : one has a non zero wavevector along the  $x$ -axis ( $k_x = 0.2, k_y = 0$ ) while the other one has a non zero wavevector along the  $y$ -axis ( $k_x = 0, k_y = 0.2$ ). For the sake of clarity we label  $k_{x,y}$  the modes directly excited by the probe and  $k_{x,y}^*$  their conjugate counterpart. The energy of the laser is again set to be resonant with the normal branch of the Bogoliubov dispersion. Each of the two probe beams generates its own conjugate mode at its respective opposite wavevector as shown in [Figure 6.8](#). One can notice that the modes along the  $y$ -axis are less intense than these along  $x$  despite the input size and intensity of the two beam is the same. This once again supports the idea that the emission efficiency in one mode or the other is  $k$ -dependent.

The verification consists in measuring the correlations between two conjugate modes and compare it to the correlation between two modes that are not. If the measurement is dominated by pump contributions one should measure the same result for both cases. To do so, we rotate the half mirror by  $45^\circ$  around its normal axis in order to separate the top left part of the field from the bottom right part and send them to the two optical paths. The separation is explicated by the diagonal purple dashed line in [Figure 6.8](#). Then, depending on which couple we want to measure the correlations, we place the pinholes in the Fourier plane

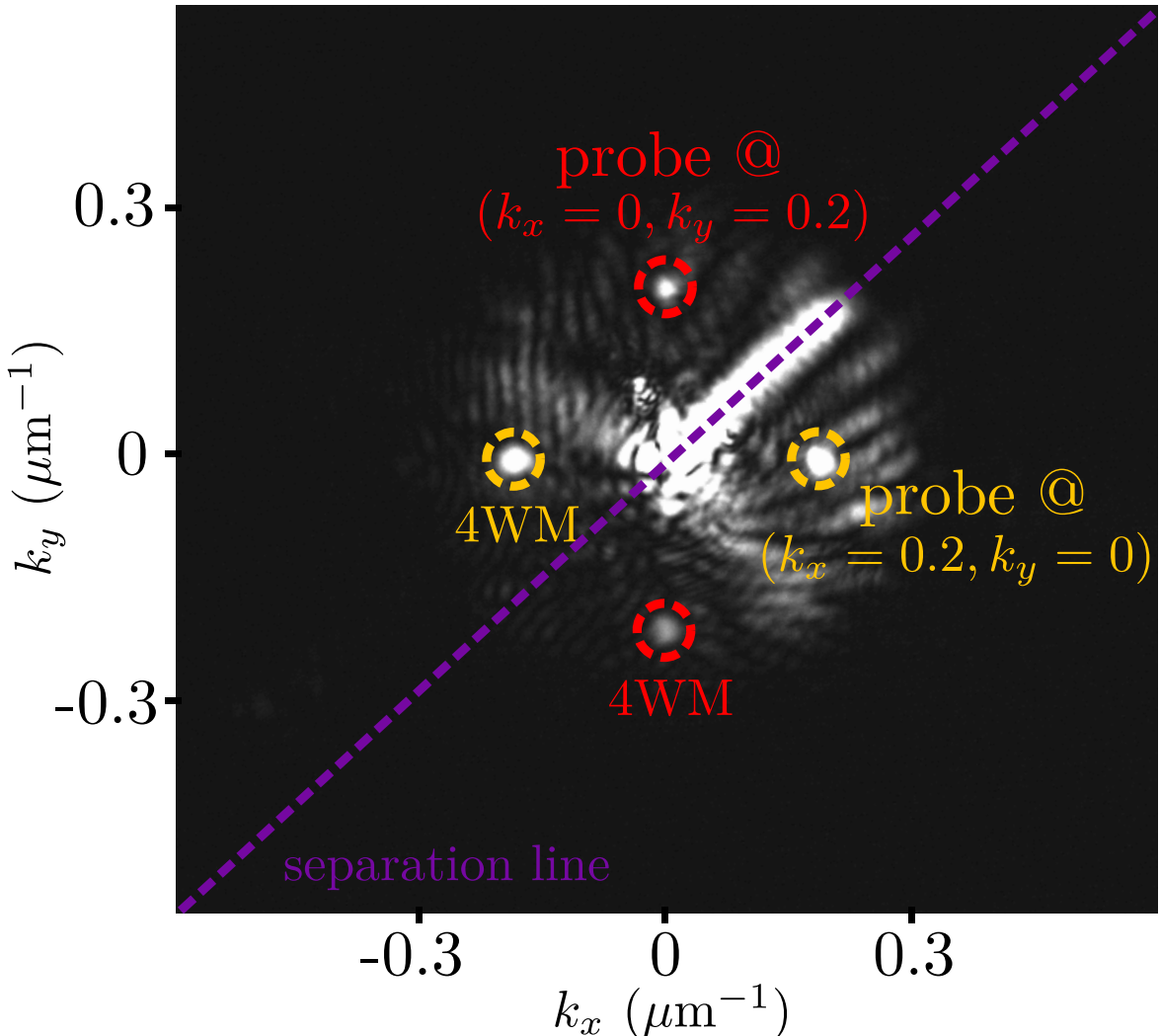


**Fig. 6.8 Fourier plane of the field with two probe beams injected in the system.** The two beams are injected at  $k_{pr} = (0.2, 0)$  and  $k_{pr} = (0, 0.2)$ . The red dashed circle represent the conjugate mode along the  $y$ -axis and the yellow dashed circles the modes along the  $x$ -direction. The half mirror is rotated by  $45^\circ$  to separate the top left and right bottom part of the field which is represented by the purple dashed line. The pinholes are placed in the Fourier plane at the appropriate wavevector to measure the correlations between two conjugate modes or between two modes that are not conjugate.

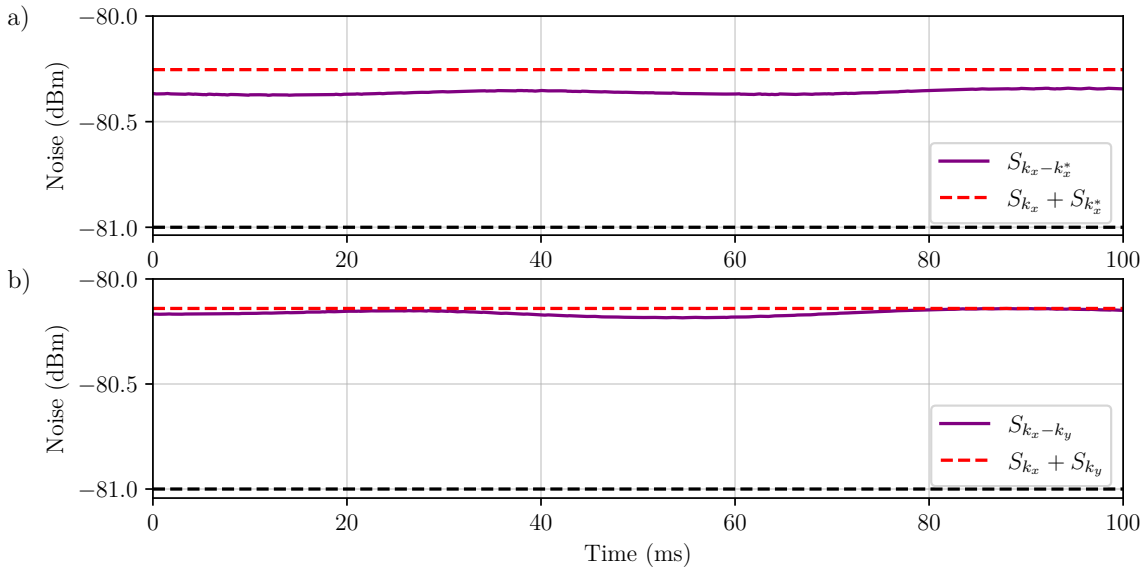


Fig. 6.9 *Sanity check correlation measurement.* **a)** Power spectral density of the photocurrent difference for two conjugate modes  $k_x$  and  $k_x^*$ . **b)** Power spectral density of the photocurrent difference for two modes that are not conjugated  $k_x$  and  $k_y$ . To smooth the date is noise is averaged on 10 sweeps of the spectrum analyzer. In both panels, the red dashed line represents the sum of the two individual photocurrent power spectral density as if they were not correlated. The black dashed line is the dark electronic noise of the apparatus.

at the appropriate wavevector. The results are shown in Figure 6.9. The panel **a)** displays the PSD of the photocurrent difference for the two conjugate modes  $k_x$  and  $k_x^*$  while **b)** shows the same measurement for the two modes  $k_y$  and  $k_y^*$ . A simple way to infer if the beams are correlated is to compare the difference PSD to the sum of the individual PSDs as if they were not correlated. As visible, in the first case **a)**, the difference PSD is below the sum of the individual PSDs, which indicates that the two modes are correlated. In contrast, in the second case **b)**, the difference PSD is superimposed to the sum of the individual PSDs, which indicates that the two modes are not correlated.

More precisely, we measure a correlation coefficient  $C_{k_x, k_x^*} = 0.11 \pm 0.01$  for the first case and  $C_{k_x, k_y^*} = 0.01 \pm 0.005$  for the second one. The error bars are estimated from the standard deviation of the PSDs over the swipe time of the spectrum analyzer. This result confirms that modes originating from the same four wave mixing process are correlated while modes originating from different processes are not and that the measurement is not dominated mean field contributions.

### 6.5.2.3 Correlations measurement

The previous section showed that the efficiency of the emission in a given mode appear to be  $k$ -dependent. As a consequence, studying correlations for different probe wavevectors might not be the best way to investigate the Bogoliubov modes correlations. Instead, we propose to focus on the correlations as a function of the operating point of the polariton fluid on the

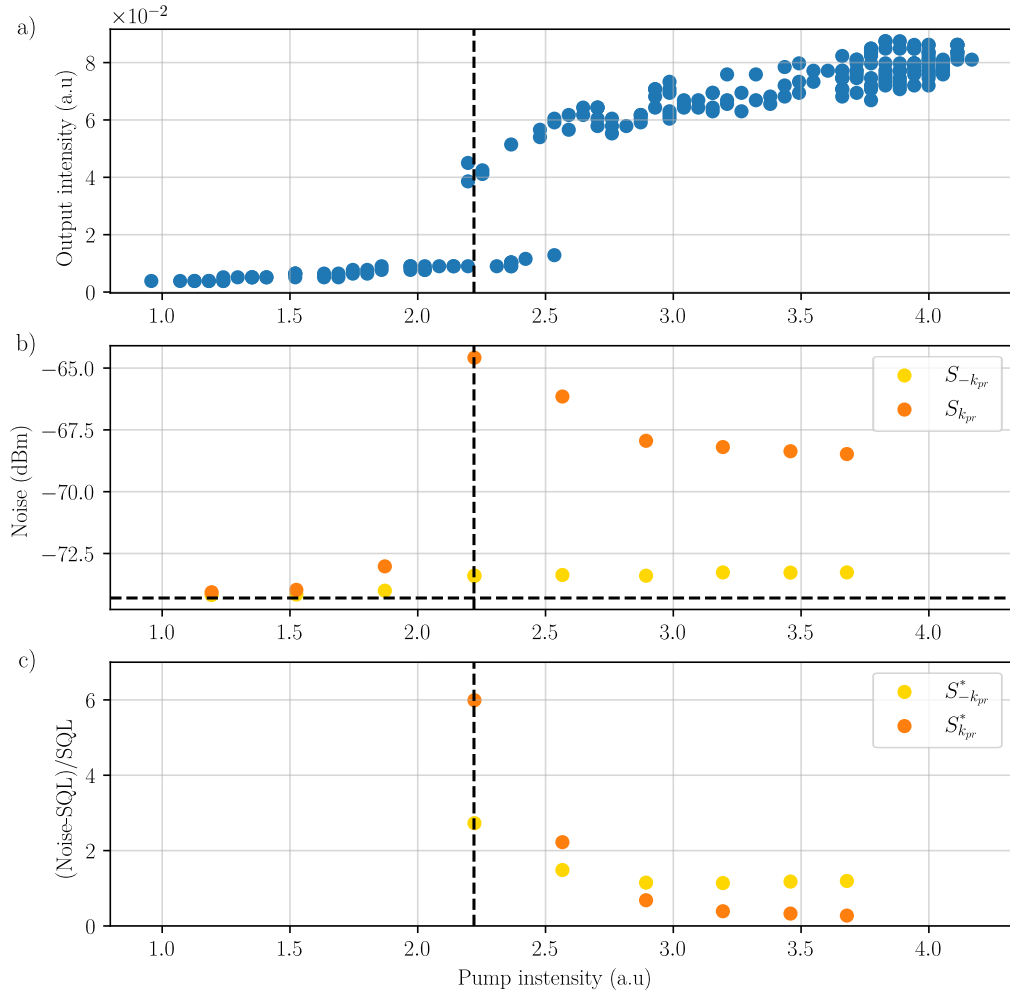


Fig. 6.10 **a)** Measured bistability loop of the static polariton fluid at the working point B10-C10 with detuning  $\delta = 35$  GHz. The vertical black dashed line on all plots indicates the turning point of the bistability loop. **b)** Measurement of the individual noises of the two conjugate modes  $k_{pr}$  and  $-k_{pr}$  as a function of the pump power. The horizontal black dashed line represent the dark noise of the apparatus. **c)** Excess noises of the two conjugate modes normalized to their respective shot noise calculated from the calibration curve of Figure 6.6. The points at pump power below the turning point are not shown because they were too weak to be measured and fall in the dark noise of the apparatus.

higher branch of the bistability loop.

To do so, we fix the probe wavevector to  $k_{pr} = (0 \ 0.2 \mu\text{m}^{-1})$  and set the pump intensity to operate on the high density branch of the hysteresis curve. Then the pump power is ramped down toward the turning point of the bistability loop. In terms of collective excitation, the system goes from a parabolic gapped dispersion to a linear gapless one as explained in chapter 4.

At each pump power, the probe frequency is tuned to stay resonant with the normal branch Bogoliubov mode at  $k_{pr}$ . The correlations between the two conjugate mode are then measured the same way as in the previous section. We start by analyzing the noise of each mode based on [Figure 6.10](#). The first plot in [Figure 6.10 a\)](#) shows the bistability loop of the polariton fluid under investigation. The measurement of the individual noises is displayed in [Figure 6.10 b\)](#). The normal branch mode is much more noisy than its conjugate counterpart. This is mainly due to the power unbalance between the two modes. To compare them on the same scale we normalize their excess noise to their respective shot noise calculated from the calibration curve of ?? and plot the result in [Figure 6.10 c\)](#). The normalized excess noise are labelled  $S_{k_{pr}, -k_{pr}}^*$  for the sake of clarity. Both exhibit excess noise due to nonlinear interactions [4]. Then the noises increase significantly when the system approaches the turning point. This is a typical feature of critical points and phase transitions in physical systems. For example, such behavior is very similar to what happens in an OPO configuration just below threshold [84] : the amplitude quadrature of the signal and idler drastically increase in a correlated way leading to the formation of two modes squeezed state.

In a second time we measure the noise of the difference photocurrent and compute the corresponding correlation in [Figure 6.11](#). In order to easily see the evolution of the correlations, we also plot the sum of the individual noises as if they were not correlated like we did previously. When the system is far from the turning point and is not even bistable, the difference PSD is almost superimposed to the sum of the individual PSDs which, as shown in [Figure 6.11](#). This behavior indicates a low correlation between the two modes ( $C_{k_{pr}, -k_{pr}} \approx 0.02$ ). When the system gets closer to the turning point, the difference PSD becomes lower than the sum of the individual PSDs and the correlation increases to reach a maximum value of  $C_{k_{pr}, -k_{pr}} = 0.61 \pm 0.05$  near the turning point. It is likely that the correlations would further increase if we were able to operate even closer to the turning point. However, this is not possible in practice because at this point the system becomes unstable and any fluctuation makes the system fall back to the low density branch of the bistability loop.

Furthermore, if we refer to the ideal linear amplifier model [8], increasing the amount of nonlinearity in order to increase the gain of the four wave mixing process should in principle enhance the correlations as well. In a polariton system, this can be achieved by increasing the detuning  $\delta$  between the pump laser and the polariton resonance. However, this implies high pump laser power to remain in the bistable regime and, up to a certain point, the laser starts to heat the sample which in turn results in a reduction of the non linearity and thus of the correlations [66].

To finish with, one could think that balancing the signals by attenuating the normal branch mode would allow to increase the correlations. In fact the work [67] showed that rather than balancing the beam intensities, correlations could be enhanced by balancing the individual noises of the two modes. However, in our case the two intensities and two individual noises differ by a factor 10 and 7 respectively. In any case such an attenuation introduce too much losses on the normal branch mode and makes its intensity statistic tend to a poissonian distribution which suppresses the correlations at the same time.

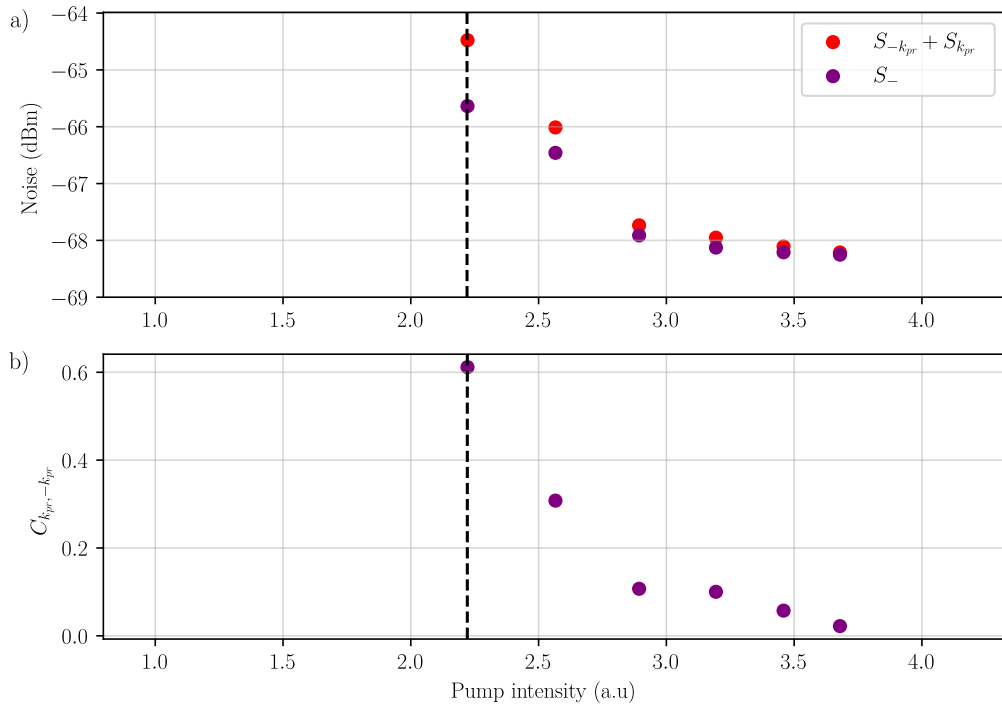


Fig. 6.11 Correlations between Bogoliubov modes as a function of the pump power. **a)** Measurement of the difference photocurrent noise. The latter is represented by the purple dots while the red dots indicates the sum of the individual noises as if they were not correlated. **b)** Correlation coefficient  $C_{k_{pr}, -k_{pr}}$  between the two conjugate modes as a function of the pump power.

## 6.6 Conclusion

In this chapter, we have investigated the correlations between Bogoliubov modes in a polariton quantum fluid. By employing a balanced detection scheme, we were able to measure the intensity correlations between the normal and ghost branches of the Bogoliubov dispersion. The experimental results demonstrate that these correlations are seeded by the nonlinear four-wave mixing process intrinsic to the polariton system.

We first validated the experimental setup by ensuring that the lasers used in the experiment were shot-noise limited and that the balanced detection scheme was capable of isolating quantum correlations from classical noise. An experiment check confirmed that the measured correlations were indeed due to the nonlinear scattering process and not dominated by residual pump contributions or single-mode effects.

The analysis of the Bogoliubov coefficients revealed that the emission in the normal and ghost branches becomes balanced at low wavevectors, despite showing an asymmetry suggesting a  $k$ -dependence in the emission efficiency. Furthermore, we observed that the correlations increase significantly as the system approaches the turning point of the bistability loop, where the four-wave mixing process is the most efficient. This behavior highlights the critical role of the bistable regime in amplifying quantum correlations.

The maximum correlation coefficient measured was  $C_{k_{pr}, -k_{pr}} = 0.61 \pm 0.05$ , achieved near the turning point of the bistability loop. This result demonstrates the potential of polariton systems for generating strongly correlated quantum states, which could be further optimized by operating closer to the turning point or by tuning the system parameters to enhance the nonlinear gain.



# Chapter 7

## Conclusion

In this thesis, we have explored the physics of microcavity polaritons and their application to analog gravity, with a particular focus on the Hawking effect in polariton quantum fluids. By combining theoretical and experimental approaches, we have demonstrated the versatility of this platform for studying quantum field theory in effectively curved spacetimes.

We began by presenting the microcavity polariton system, detailing its unique properties as a hybrid light-matter quasiparticle. This was followed by a theoretical investigation of the Hawking effect in polariton quantum fluids, where we showed how the Bogoliubov excitations in these systems can mimic the behavior of quantum fields in curved spacetime. This theoretical framework provided the foundation for designing experiments to study analog gravity effects.

A key achievement of this work was the demonstration of the tunability of polariton systems, which allowed us to effectively create curved spacetime geometries. By carefully controlling the system parameters, we were able to engineer conditions that emulate event horizons and study the associated analog gravity phenomena. This tunability highlights the potential of polariton systems as a flexible platform for exploring a wide range of analog gravity effects.

We then reported the first observation of stimulated Hawking radiation in a polariton quantum fluid. By injecting a weak probe beam, we stimulated the emission of Bogoliubov modes and observed their properties, providing direct evidence of the analog Hawking effect in this system. This result represents a significant step forward in the experimental study of analog gravity.

Finally, we focused on the measurement of correlations between Bogoliubov modes. By analyzing the intensity correlations, we gained insights into the underlying quantum processes driving the analog Hawking effect. This work paves the way toward the measurement of quantum correlations between modes emitted by an analog horizon, a crucial step for exploring the quantum nature of analog gravity phenomena.

In conclusion, this thesis has demonstrated the potential of microcavity polariton systems as a platform for studying analog gravity and quantum field theory in curved spacetime. The results presented here open new avenues for investigating quantum correlations and non-classical effects in analog horizons, bridging the gap between condensed matter physics and fundamental questions in quantum gravity.



# **Appendices**



## Appendix A

# Mean field shaping and monitoring

### A.1 Phase printing

Controlling precisely the phase of a laser beam is a common but challenging task in optics. The most basic way to do it is by applying spatial filtering in the fourier plane of a lens. The phase of the beam after a second collimating lens is then given by the convolution product of the beam phase and the mask inverse fourier transform. This method then show its limits when one wants to generate complex phase profile since its depend on the mask form. A way to overcome this problem is the use of Digital Micromirror Device (DMD) which is an array of micro-mirrors that can be individually controlled to reflect the light or not. By putting this array in the fourier plan of a lens it is possible to create spatial filtering with arbitrary shapes. However, this method suffers from high losses and diffraction of the light on the individual mirrors that tend to add unwanted noise. This being said, DMD are very powerfull devices and allow to do a great amount of things at low cost. A wide range of possible methods are referenced in the great work [61].

#### A.1.1 Spatial light modulator.

In this work, we use a Spatial Light Modulator (SLM) which is a liquid crystal display that can be used to modulate the phase of a laser beam. The principle is to apply a voltage on each pixel of the SLM to change the orientation of the liquid crystal molecules. The phase shift is then given by the difference of the optical path of light going through the different pixels as shown in [Figure A.1](#).

By shinning a flat phase collimated beam on the SLM which displays the target phase profile the beam gets reflected carrying the desired wavefront. However the efficiency of the SLM is not perfect and whenever light is shone on it, some photons might not see it and not be phase modulated. To overcome this difficulty, we first write a blazed phase grating on the SLM screen on top of which the wanted profile is set. All the photons that did interact with the liquid crystals are then mostly diffracted on the first order of the grating. Doing so, an efficiency of 60-70% can be reached. This contrast with the usual 80% usually claimed on manufacturer datasheets that actually correspond to the efficiency in all orders. A typical phase profile encoded on the SLM is shown in [Figure A.2](#). A gray value of zero correspond to no shift while 255 corresponds to  $2\pi$ . The gray map corresponding to the target phase

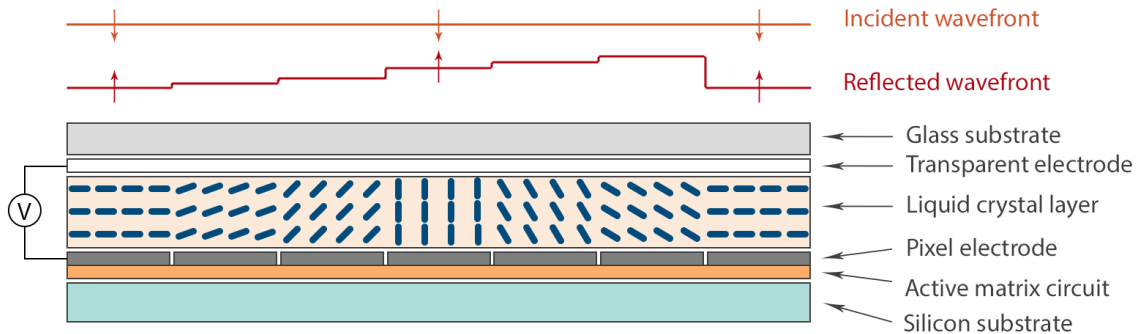


Fig. A.1 *Principle of a Spatial Light Modulator.*

profile has been unwrapped for the sake of clarity and is shown in [Figure A.2 c](#)). The final gray map displayed on the SLM screen is represented in [Figure A.2 e](#)).

To imprint precisely the resulting wavefront in the cavity plane two  $2f - 2f$  optical telescopes are used in series to image the SLM screen with an overall demagnification of 1/130 while avoiding short focal length that would introduce optical aberrations. An adjustable slit is placed in the fourier plane of the first telescope to filter out the unwanted diffracted orders.

### A.1.2 Phase measurement

### A.1.3 Off axis interferometry

The principle is the following : the beam whose phase is to be measured is recombined on a CCD camera with a flat phase reference beam. An angle is voluntary introduced between the two beam to create an interference pattern on the camera plane. The phase difference between the two beams is then encoded in the size of the fringes and can be recovered by performing a fourier transform on the interferogram and demodulate the signal around the satellite peak created by the angle between the two beams [51].

### A.1.4 Controlling the local intensity

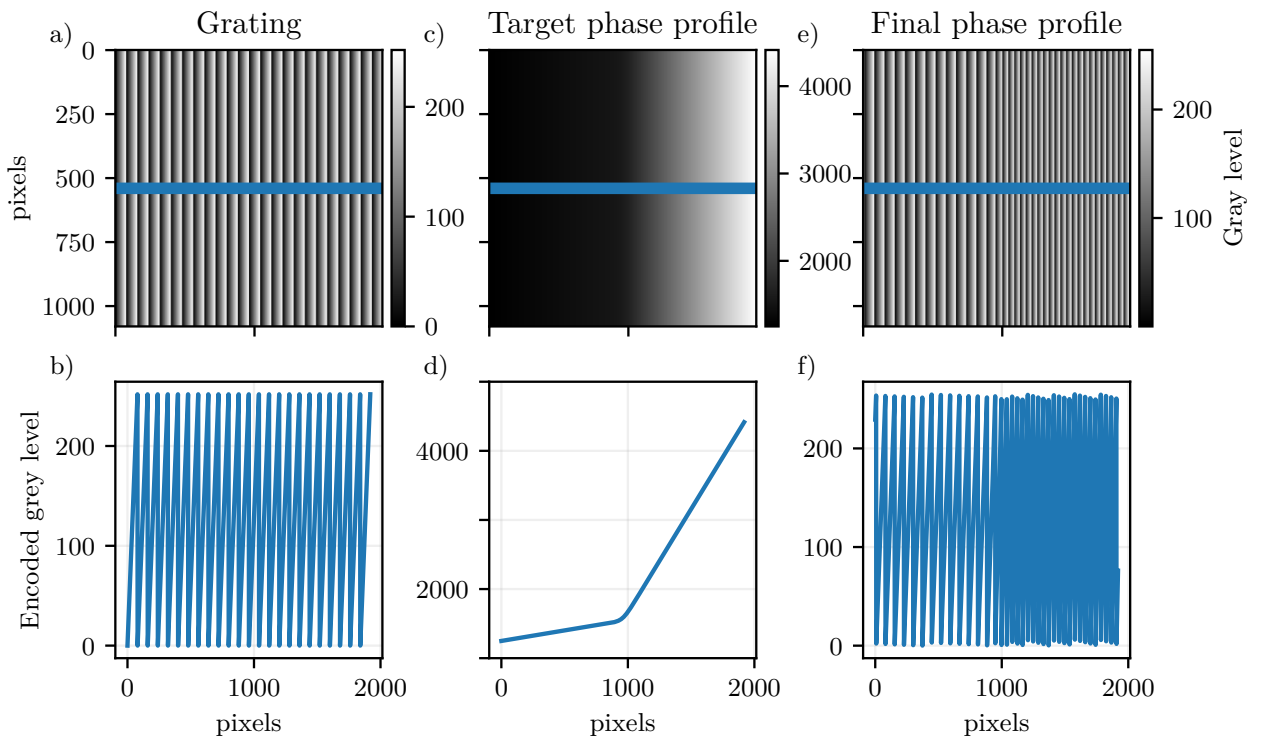


Fig. A.2 *Typical profile encoded on the SLM to generate the target velocity profile. a) Gray map of a phase blazed grating encoded on the SLM screen and b) corresponding cut in the  $x$  direction. c) Unwrapped grey map of the target phase profile and d) corresponding cut in the  $x$  direction. e) Final gray map encoded on the SLM screen and f) corresponding cut in the  $x$  direction. This map is the sum of the blazed grating and the target phase profile modulus 255.*



# Bibliography

- [1] “Exciton polaritons in microcavities”. URL <http://dx.doi.org/10.1007/978-3-642-24186-4>. Cited page 136
- [2] Ivan AMELIO, Anna MINGUZZI, Maxime RICHARD & Iacopo CARUSOTTO 2020. “Galilean boosts and superfluidity of resonantly driven polariton fluids in the presence of an incoherent reservoir”. *Phys. Rev. Res.* **2**, p. 023158. Cited page 57
- [3] Alberto AMO, Jérôme LEFRÈRE, Simon PIGEON, Claire ADRADOS, Cristiano CIUTI, Iacopo CARUSOTTO, Romuald HOUDRÉ, Elisabeth GIACOBINO & Alberto BRAMATI. “Superfluidity of polaritons in semiconductor microcavities”. *Nat. Phys.* **5**(11), p. 805–810. Cited pages 37, 60, and 63
- [4] A. BAAS, J.-Ph. KARR, M. ROMANELLI, A. BRAMATI & E. GIACOBINO 2006. “Quantum degeneracy of microcavity polaritons”. *Phys. Rev. Lett.* **96**, p. 176401. Cited pages 141 and 145
- [5] H.A. BACHOR 1998. *A Guide to Experiments in Quantum Optics*. ISBN 978-3-527-29298-1. URL <https://books.google.fr/books?id=6vhAAQAAIAAJ>. Cited pages 133 and 139
- [6] C. BARCELÓ, S. LIBERATI & M. VISSER 2011. “Analogue Gravity”. *Living Reviews in Relativity* **14**, p. 3. Cited page 48
- [7] Carlos BARCELÓ, Stefano LIBERATI, Sebastiano SONEGO & Matt VISSER. “Hawking-like radiation does not require a trapped region”. *Physical Review Letters* **97**(17). Cited page 98
- [8] Robert W. BOYD 2008. *Nonlinear Optics, Third Edition* (USA) 3rd édition. ISBN 0123694701. Cited page 145
- [9] Anthony J. BRADY, Ivan AGULLO & Dimitrios KRANAS 2022. “Symplectic circuits, entanglement, and stimulated hawking radiation in analogue gravity”. *Phys. Rev. D* **106**, p. 105021. Cited pages 72, 126, and 127
- [10] Richard BRITO, Vitor CARDOSO & Paolo PANI. “Superradiance”. *arXiv:1501.06570 [astro-ph, physics:gr-qc, physics:hep-ph, physics:hep-th, physics:physics]* **906**. Cited page 100
- [11] Richard BRITO, Vitor CARDOSO & Paolo PANI 2020. *Superradiance: New Frontiers in Black Hole Physics Lecture Notes in Physics*, tome 971 (Springer International Publishing, Cham). ISBN 978-3-030-46621-3 978-3-030-46622-0. URL <http://dx.doi.org/10.1007/978-3-030-46622-0>. Cited page 70
- [12] BROWN, R. & TWISS, R. 1956. “Correlation between photons in two coherent beams of light.” *Nature* **177**, p. 27–29. Cited page 133

- [13] Iacopo CARUSOTTO & Cristiano CIUTI 2013. “Quantum fluids of light”. *Rev. Mod. Phys.* **85**(1), p. 299–366. Cited pages 32 and 36
- [14] Iacopo CARUSOTTO, Serena FAGNOCCHI, Alessio RECATI, Roberto BALBINOT & Alessandro FABBRI. “Numerical observation of hawking radiation from acoustic black holes in atomic bose-einstein condensates”. *New Journal of Physics* **10**(10), p. 103 001. Cited page 71
- [15] Y. CASTIN 2001. *Bose-Einstein Condensates in Atomic Gases: Simple Theoretical Results* (Springer Berlin Heidelberg, Berlin, Heidelberg). ISBN 978-3-540-45338-3. Cited pages 49, 50, 52, 56, 69, 134, 135, and 137
- [16] Y. CASTIN & R. DUM 1998. “Low-temperature bose-einstein condensates in time-dependent traps: Beyond the  $u(1)$  symmetry-breaking approach”. *Phys. Rev. A* **57**, p. 3008–3021. Cited page 69
- [17] C. CIUTI, V. SAVONA, C. PIERMAROCCHI, A. QUATTROPANI & P. SCHWENDIMANN 1998. “Role of the exchange of carriers in elastic exciton-exciton scattering in quantum wells”. *Phys. Rev. B* **58**, p. 7926–7933. Cited pages 23 and 24
- [18] F. CLAUDE, M. J. JACQUET, I. CARUSOTTO, Q. GLORIEUX, E. GIACOBINO & A. BRAMATI 2023. “Spectrum of collective excitations of a quantum fluid of polaritons”. *Phys. Rev. B* **107**, p. 174 507. Cited pages 37 and 60
- [19] F. CLAUDE, M. J. JACQUET, R. USCIATI, I. CARUSOTTO, E. GIACOBINO, A. BRAMATI & Q. GLORIEUX 2022. “High-Resolution Coherent Probe Spectroscopy of a Polariton Quantum Fluid”. *Physical Review Letters* **129**(10), p. 103 601. Publisher: American Physical Society. Cited pages 30, 37, 52, 58, 60, and 91
- [20] Fabre CLAUDE. “Quantum fluctuations in light beams”. Cited pages 131 and 133
- [21] Ferdinand CLAUDE 2022. *High resolution coherent spectroscopy of a polariton fluid : Bogoliubov modes, non equilibrium phase transitions and turbulence*. Theses Sorbonne Université. URL <https://theses.hal.science/tel-04009505>. Cited pages 7, 29, 58, 60, 82, 89, and 91
- [22] C. COHEN-TANNOUDJI, B. DIU & F. LALOE 2018. *Mécanique Quantique - Tome 1: Nouvelle édition* (EDP sciences). ISBN 978-2-7598-2285-0. URL <https://books.google.fr/books?id=9KxxDwAAQBAJ>. Cited page 120
- [23] C. COHEN-TANNOUDJI, B. DIU & F. LALOE 2018. *Mécanique Quantique - Tome 2: Nouvelle édition* (EDP sciences). ISBN 978-2-7598-2285-0. URL <https://books.google.fr/books?id=9KxxDwAAQBAJ>. Cited page 23
- [24] Claude COHEN-TANNOUDJI, Jacques DUPONT-ROC & Gilbert GRYNBERG. *Photons and atoms: introduction to quantum electrodynamics*. Physics textbook. Nachdr. édition. ISBN 978-0-471-18433-1. Cited page 28
- [25] M. COMBESCOT, M. A. DUPERTUIS & O. BETBEDER-MATIBET 2007. “Polariton-polariton scattering: Exact results through a novel approach”. *Europhysics Letters* **79**(1), p. 17 001. Cited pages 21, 23, 24, and 31
- [26] Monique COMBESCOT & Shiao SHIUE-YUAN. *Excitons and Cooper Pairs Two Composite Bosons in Many-Body Physics*. 1st ed édition. ISBN 9780191815287. Cited pages 10, 12, 14, 15, 18, and 23
- [27] DE BROGLIE, LOUIS 1925. “Recherches sur la théorie des quanta”.

- Ann. Phys.* **10**(3), p. 22–128. Cited page 34
- [28] Adrià DELHOM, Killian GUERRERO, Paula CALIZAYA CABRERA, Kévin FALQUE, Alberto BRAMATI, Anthony J. BRADY, Maxime J. JACQUET & Ivan AGULLO 2024. “Entanglement from superradiance and rotating quantum fluids of light”. *Phys. Rev. D* **109**, p. 105 024. Cited pages 70 and 120
- [29] Léo-Paul EUVÉ, Scott ROBERTSON, Nicolas JAMES, Alessandro FABBRI & Germain ROUSSEAU 2020. “Scattering of co-current surface waves on an analogue black hole”. *Phys. Rev. Lett.* **124**, p. 141 101. Cited page 105
- [30] Alessandro FABBRI & Carlos MAYORAL. “Steplike discontinuities in bose-einstein condensates and hawking radiation: The hydrodynamic limit”. *Physical Review D* **83**(12). Cited page 68
- [31] Alessandro FABBRI & Nicolas PAVLOFF. “Momentum correlations as signature of sonic hawking radiation in bose-einstein condensates”. *SciPost Phys.* **4**(4), p. 019. Cited page 73
- [32] Kévin FALQUE, Adrià DELHOM, Quentin GLORIEUX, Elisabeth GIACOBINO, Alberto BRAMATI & Maxime J JACQUET 2024. “Polariton fluids as quantum field theory simulators on tailored curved spacetimes”. [2311.01392](https://arxiv.org/abs/2311.01392) URL <https://arxiv.org/abs/2311.01392>. Cited page 77
- [33] M. FOX 2010. *Optical Properties of Solids- Second Edition* (Oxford University Press). Cited page 18
- [34] Irénée FRÉROT, Amit VASHISHT, Martina MORASSI, Aristide LEMAÎTRE, Sylvain RAVETS, Jacqueline BLOCH, Anna MINGUZZI & Maxime RICHARD 2023. “Bogoliubov excitations driven by thermal lattice phonons in a quantum fluid of light”. *Phys. Rev. X* **13**, p. 041 058. Cited pages 24, 61, 88, and 135
- [35] Dario GERACE & Iacopo CARUSOTTO 2012. “Analog hawking radiation from an acoustic black hole in a flowing polariton superfluid”. *Phys. Rev. B* **86**(14), p. 144 505. Cited pages 118 and 120
- [36] Quentin GLORIEUX, Luca GUIDONI, Samuel GUIBAL, Jean-Pierre LIKFORMAN & Thomas COUDREAU 2011. “Quantum correlations by four-wave mixing in an atomic vapor in a nonamplifying regime: Quantum beam splitter for photons”. *Phys. Rev. A* **84**, p. 053 826. Cited page 135
- [37] E P GROSS 1961. “Structure of a quantized vortex in boson systems”. *Nuovo Cimento (Italy) Divided into Nuovo Cimento A and Nuovo Cimento B* **10**(10). Cited page 35
- [38] Gilbert GRYNBERG, Alain ASPECT & Claude FABRE. *Introduction to Quantum Optics*. Cited pages 38, 39, and 129
- [39] Pjotrs GRĪSSINS, Hai Son NGUYEN, Jacqueline BLOCH, Alberto AMO & Iacopo CARUSOTTO. “Theoretical study of stimulated and spontaneous hawking effects from an acoustic black hole in a hydrodynamically flowing fluid of light”. *Phys. Rev. B* **94**(14), p. 144 518. Cited page 127
- [40] Dominik HANGLEITER, Jacques CAROLAN & Karim P. Y. THÉBAULT 2022. *Analogue Quantum Simulation: A New Instrument for Scientific Understanding* (Springer International Publishing, Cham). ISBN 978-3-030-87215-1 978-3-030-87216-8. URL

- <http://dx.doi.org/10.1007/978-3-030-87216-8>. Cited page 70
- [41] S. W. HAWKING. “Black holes in general relativity”. *Communications in Mathematical Physics* **25**(2), p. 152–166. Cited pages 48, 71, and 73
- [42] J. J. HOPFIELD. “Theory of the contribution of excitons to the complex dielectric constant of crystals”. *Physical Review* **112**(5), p. 1555–1567. Cited page 27
- [43] M. ISOARD & N. PAVLOFF. “Quantum fluctuations close to an acoustic horizon in a bose-einstein condensate”. *arXiv:1909.02509 [cond-mat, physics:gr-qc]*. Cited page 71
- [44] M.J. JACQUET, L. GIACOMELLI, Q. VALNAIS, M. JOLY, F. CLAUDE, E. GIACOBINO, Q. GLORIEUX, I. CARUSOTTO & A. BRAMATI 2023. “Quantum Vacuum Excitation of a Quasinormal Mode in an Analog Model of Black Hole Spacetime”. *Physical Review Letters* **130**, p. 111 501. Cited pages 71, 74, 100, and 127
- [45] JOFFRE, M., HULIN, D., MIGUS, A., MYSYROWICZ, A. & ANTONETTI, A. 1987. “Subpicosecond excitonic optical nonlinearities in quantum wells”. *Rev. Phys. Appl. (Paris)* **22**(12), p. 1705–1709. Cited page 24
- [46] J. KASPRZAK, M. RICHARD, S. KUNDERMANN, A. BAAS, P. JEAMBRUN, J. M. J. KEELING, F. M. MARCHETTI, M. H. SZYMAŃSKA, R. ANDRÉ, J. L. STAELHIL *et al.* “Bose-einstein condensation of exciton polaritons”. *Nature* **443**(7110), p. 409–414. Cited pages 37 and 38
- [47] Charles KITTEL. *Introduction to solid state physics*. 8th ed édition. ISBN 978-0-471-41526-8. Cited pages 10 and 19
- [48] L. LANDAU 1941. “Theory of the superfluidity of helium ii”. *Phys. Rev.* **60**, p. 356–358. Cited page 56
- [49] A. Von LEHMEN, D. S. CHEMLA, J. E. ZUCKER & J. P. HERITAGE 1986. “Optical stark effect on excitons in gaas quantum wells”. *Opt. Lett.* **11**(10), p. 609–611. Cited page 24
- [50] Giovanni LERARIO, Anne MAÎTRE, Rajiv BODDEDA, Quentin GLORIEUX, Elisabeth GIACOBINO, Simon PIGEON & Alberto BRAMATI 2020. “Vortex-stream generation and enhanced propagation in a polariton superfluid”. *Phys. Rev. Res.* **2**, p. 023 049. Cited page 37
- [51] Michael LIEBLING, Thierry BLU & Michael UNSER. “Complex-wave retrieval from a single off-axis hologram”. *J. Opt. Soc. Am. A* **21**(3), p. 367. Cited page 154
- [52] T. C. H. LIEW, A. V. KAVOKIN & I. A. SHELYKH 2008. “Optical circuits based on polariton neurons in semiconductor microcavities”. *Phys. Rev. Lett.* **101**, p. 016 402. Cited page 30
- [53] Anne MAITRE. *Generation, propagation and control of quantized vortices and dark solitons in polariton superfluids*. Thèse de doctorat. URL <https://theses.hal.science/tel-03147158>. Cited pages 26, 31, 37, and 60
- [54] Jean-Michel MÉNARD, C. POELLMANN, Michael PORER, U. LEIERSEDER, Élisabeth GALOPIN, Aristide LEMAÎTRE, Alberto AMO, Jacqueline BLOCH & Rupert HUBER 2014. “Revealing the dark side of a bright exciton-polariton condensate”. *Nature Communications* **5**. Cited page 36
- [55] N. MIELEC, M. ALTORIO, R. SAPAM, D. HORVILLE, D. HOLLEVILLE, L. A. SIDORENKOVA, A. LANDRAGIN & R. GEIGER 2018. “Atom interferometry with top-hat

- laser beams". *Applied Physics Letters* **113**(16), p. 161 108. Cited page 81
- [56] A. MYSYROWICZ, D. HULIN, A. ANTONETTI, A. MIGUS, W. T. MASSELINK & H. MORKOÇ 1986. "dressed excitons" in a multiple-quantum-well structure: Evidence for an optical stark effect with femtosecond response time". *Phys. Rev. Lett.* **56**, p. 2748–2751. Cited page 24
- [57] H.S. NGUYEN, D. GERACE, I. CARUSOTTO, D. SANVITTO, E. GALOPIN, A. LEMAÎTRE, I. SAGNES, J. BLOCH & A. AMO. "Acoustic black hole in a stationary hydrodynamic flow of microcavity polaritons". *Phys. Rev. Lett.* **114**(3), p. 036 402. Cited pages 71, 78, 81, and 127
- [58] Christopher PETHICK & Henrik SMITH 2008. *Bose-Einstein condensation in dilute gases* (Cambridge university press, Cambridge) 2nd ed édition. ISBN 978-0-521-84651-6. Cited pages 49, 53, and 137
- [59] Lev P PITAEVSKII 1961. "Vortex lines in an imperfect bose gas". *Sov. Phys. JETP* **13**(2), p. 451–454. Cited page 35
- [60] Lev P. PITAEVSKIY & Sandro STRINGARI 2016. *Bose-Einstein condensation and superfluidity*. Numéro 164 dans International series of monographs on physics. Reprinted (with corrections) édition. ISBN 978-0-19-875888-4. Cited pages 34, 134, and 137
- [61] S. POPOFF. "Wavefront shaping". <https://www.wavefrontshaping.net/>. Cited page 153
- [62] Francesco Del PORRO, Stefano LIBERATI & Marc SCHNEIDER 2024. "Tunneling method for hawking quanta in analogue gravity". *arXiv:2406.14603* . Cited page 99
- [63] A. RECATI, N. PAVLOFF & I. CARUSOTTO. "Bogoliubov theory of acoustic hawking radiation in bose-einstein condensates". *Phys. Rev. A* **80**(4), p. 043 603. Cited pages 68, 69, 71, 99, and 120
- [64] G. ROCHAT, C. CIUTI, V. SAVONA, C. PIERMAROCCHI, A. QUATTROPANI & P. SCHWENDIMANN 2000. "Excitonic bloch equations for a two-dimensional system of interacting excitons". *Phys. Rev. B* **61**, p. 13 856–13 862. Cited page 24
- [65] G. ROCHAT, C. CIUTI, V. SAVONA, C. PIERMAROCCHI, A. QUATTROPANI & P. SCHWENDIMANN 2000. "Excitonic bloch equations for a two-dimensional system of interacting excitons". *Phys. Rev. B* **61**, p. 13 856–13 862. Cited page 32
- [66] M. ROMANELLI, C. LEYDER, J. Ph. KARR, E. GIACOBINO & A. BRAMATI 2007. "Four wave mixing oscillation in a semiconductor microcavity: Generation of two correlated polariton populations". *Phys. Rev. Lett.* **98**, p. 106 401. Cited pages 135 and 145
- [67] Marco ROMANELLI, Elisabeth GIACOBINO & Alberto BRAMATI 2004. "Optimal intensity noise reduction in multimode vertical-cavity surface-emitting lasers by polarization-selective attenuation". *Opt. Lett.* **29**(14), p. 1629–1631. Cited page 145
- [68] Germain ROUSSEAU, Christian MATHIS, Philippe MAÏSSA, Thomas G PHILBIN & Ulf LEONHARDT. "Observation of negative-frequency waves in a water tank: a classical analogue to the hawking effect?" *New Journal of Physics* **10**(5), p. 053 015. Cited page 45
- [69] Elena ROZAS, Evgeny SEDOV, Yannik BRUNE, Sven HÖFLING, Alexey KAVOKIN & Marc ASSMANN 2023. "Polariton–dark exciton interactions in bistable semiconductor microcavities". *Phys. Rev. B* **108**, p. 165 411. Cited page 40

- [70] Jeff STEINHAUER. “Observation of quantum hawking radiation and its entanglement in an analogue black hole”. *Nature Physics* **12**(10), p. 959–965. Cited pages 71 and 127
- [71] Petr STEPANOV, Ivan AMELIO, Jean-Guy ROUSSET, Jacqueline BLOCH, Aristide LEMAÎTRE, Alberto AMO, Anna MINGUZZI, Iacopo CARUSOTTO & Maxime RICHARD. “Dispersion relation of the collective excitations in a resonantly driven polariton fluid”. *Nat Commun* **10**(1), p. 1–8. Cited pages 36, 37, 40, and 60
- [72] Nicolas TREPS & Claude FABRE 2005. “Criteria of quantum correlation in the measurement of continuous variables in optics”. *Hal open science- Laser Physics* **15**(2), p. 187. Cited pages 132, 137, and 139
- [73] W. G. UNRUH . “Experimental black-hole evaporation?” *Physical Review Letters* **46**(21), p. 1351–1353. Cited page 46
- [74] W. G. UNRUH . “!notes on black-hole evaporation”. *Physical Review D* **14**(4), p. 870–892. Cited page 70
- [75] William UNRUH & Ralf SCHÜTZHOLD. “Universality of the hawking effect”. *Physical Review D* **71**(2). Cited page 70
- [76] Tunemaru USUI 1960. “Excitations in a high density electron gas. i:”. *Progress of Theoretical Physics* **23**(5), p. 787–798. Cited page 32
- [77] S. UTSUNOMIYA, L. TIAN, G. ROUMPOS, C. W. LAI, N. KUMADA, T. FUJISAWA, M. KUWATA-GONOKAMI, A. LÖFFLER, S. HÖFLING, A. FORCHEL *et al.* “Observation of bogoliubov excitations in exciton-polariton condensates”. *Nature Physics* **4**(9), p. 700–705. Cited page 30
- [78] S. UTSUNOMIYA, L. TIAN, G. ROUMPOS, C. W. LAI, N. KUMADA, T. FUJISAWA, M. KUWATA-GONOKAMI, A. LÖFFLER, S. HÖFLING, A. FORCHEL *et al.* 2008. “Observation of Bogoliubov excitations in exciton-polariton condensates”. *Nature Physics* **4**(9), p. 700–705. Cited page 60
- [79] Robert M. WALD 1994. *Quantum field theory in curved spacetime and black hole thermodynamics*. Chicago lectures in physics (University of Chicago Press). ISBN 978-0-226-46766-3. Cited page 70
- [80] Silke WEINFURTNER, Edmund W. TEDFORD, Matthew C. J. PENRICE, William G. UNRUH & Gregory A. LAWRENCE. “Measurement of stimulated hawking emission in an analogue system”. *Physical Review Letters* **106**(2), p. 021 302. Cited page 45
- [81] C. WEISBUCH & .J RARITY 1996. *Microcavities and Photonic Bandgaps: Physics and Applications*. ISBN 978-94-009-0313-5. URL <https://link.springer.com/book/10.1007/978-94-009-0313-5>. Cited pages 9, 10, and 21
- [82] Michiel WOUTERS, Iacopo CARUSOTTO & Cristiano CIUTI 2008. “Spatial and spectral shape of inhomogeneous nonequilibrium exciton-polariton condensates”. *Phys. Rev. B* **77**, p. 115 340. Cited page 110
- [83] Ya. B. ZEL'DOVICH. *Pis'ma Zh. Eksp. Teor. Fiz.* **12**, p. 443. Cited page 73
- [84] Yun ZHANG, Kazuhiro HAYASAKA & Katsuyuki KASAI 2006. “Generation of two-mode bright squeezed light using a noise-suppressed amplified diode laser”. *Opt. Express* **14**(26), p. 13 083–13 088. Cited page 145



---

**Sujet : Etude expérimentale de la radiation de Hawking stimulée et correlations entre modes de Bogoliubov dans un fluide quantique de polaritons.**

---

**Résumé :** Ce manuscrit est dédié à l'étude expérimentale de la radiation de Hawking stimulée dans un fluide quantique de polaritons en microcavité ainsi qu'au correlations d'intensité entre modes d'excitations collectives du système.

Dans un premier temps, nous établissons le cadre théorique nécessaire à la compréhension des fluides de polaritons. En partant de l'équation de Gross-Pitaevskii, nous dérivons le spectre de Bogoliubov des excitations collectives et analysons les régimes dynamiques en fonction de la densité, de la vitesse et des interactions du fluide. Cette analyse met en évidence le rôle clé des modes d'énergie positive et négative dans la création de particules analogues à l'effet Hawking.

Ensuite, nous présentons la réalisation expérimentale d'un écoulement transcritique dans un fluide de polaritons, obtenue grâce à un façonnage précis du pompage optique. Cette configuration permet de créer une région transcritique, essentielle pour l'apparition d'un horizon sonore. Nous démontrons également la présence de modes d'énergie négative dans cette région, confirmant les conditions nécessaires à l'observation de l'effet Hawking. Cette étude permet notamment d'étendre le cadre dans lequel il est possible d'observer des phénomènes de création de particules à des configurations où le spectre de Bogoliubov n'est pas nécessairement linéaire et comprend des excitations massives. Sur cette base, nous réalisons l'observation expérimentale de l'émission stimulée du rayonnement de Hawking. En injectant un état cohérent dans la région amont et en mesurant les modes diffusés, nous mettons en évidence une signature du mélange des énergies positives et négatives à l'interface. Bien que nos résultats ne constituent pas encore une mesure quantitative complète de la matrice de diffusion, ils démontrent la puissance des techniques optiques utilisées pour reconstruire le champ de fluctuations et analyser les modes diffusés.

Enfin, nous explorons les corrélations entre les modes d'excitations collectives dans le cas d'un fluide au repos en vue d'une étude plus approfondie des aspects quantiques de l'effet Hawking. Nous discutons également des perspectives offertes par les fluides de polaritons pour des expériences de gravité analogue, grâce à leur nature optique, leur caractère hors équilibre et leur grande flexibilité. Cette thèse présente la première mesure expérimentale de l'effet Hawking stimulé et met en évidence le potentiel des systèmes polaritoniques comme plateforme expérimentale pour étudier des phénomènes fondamentaux de la physique des champs quantiques en espace temps courbés, ouvrant ainsi la voie à de nouvelles investigations sur les effets quantiques aux horizons analogiques.

**Mots clés :** Optique quantique, fluides quantiques de lumière, superfluidité, contrôle tout optique, gravité analogue, rayonnement de Hawking, création de particules, théorie des champs, espace-temps courbe, trous noirs, corrélation, détection balancée

---

**Subject : Experimental study of stimulated Hawking radiation and Bogoliubov modes correlations in a quantum fluid of polaritons.**

---

**Abstract:** This thesis is devoted to the experimental investigation of stimulated Hawking radiation in a quantum fluid of polaritons within a microcavity, as well as the analysis of intensity correlations between collective excitation modes in the system. Initially, a comprehensive theoretical framework is established to describe polariton fluids. Beginning with the Gross-Pitaevskii equation, the Bogoliubov spectrum of collective excitations is derived, enabling a detailed examination of the dynamic regimes as a function of fluid density, velocity, and interaction strength. This theoretical analysis underscores the important role of positive and negative energy modes in the formation of particle analogs associated with the Hawking effect.

Subsequently, the thesis presents the experimental realization of a transcritical flow in a polariton fluid, achieved through precise optical pumping engineering. This configuration facilitates the formation of a transcritical region, a necessary condition for the emergence of a sonic horizon. The presence of negative energy modes in this region is experimentally confirmed, verifying the conditions required for the manifestation of the Hawking effect. Notably, this study extends the scope of particle creation phenomena to configurations where the Bogoliubov spectrum is not strictly linear and yields massive excitations.

Building upon these findings, the thesis reports the experimental observation of stimulated Hawking radiation. By injecting a coherent state into the upstream region and analyzing the scattered modes, a signature of energy mixing at the interface between positive and negative modes is identified. While these results do not yet constitute a comprehensive quantitative measurement of the scattering matrix, they demonstrate the efficacy of optical techniques in reconstructing the fluctuation field and characterizing the scattered modes.

Lastly, the thesis explores the correlation dynamics between collective excitation modes in a stationary fluid as a preliminary step toward a more rigorous investigation of the quantum aspects of the Hawking effect. Additionally, it discusses the potential of polariton fluids as a versatile experimental platform for analog gravity studies, given their optical nature, non-equilibrium dynamics, and high tunability.

Overall, this work presents the first experimental demonstration of stimulated Hawking radiation in a polariton system and underscores the viability of such systems for probing fundamental phenomena in quantum field theory within curved spacetime, thus opening new avenues for the exploration of quantum effects at analog horizons.

**Keywords :** Quantum optics, quantum fluids of light, quantum fluids, superfluidity, full optical control, analogue gravity, hawking radiation , particles creation, quantum field theory, curved spacetime, black holes, correlation, balanced detection

---